Methods in Modelling of Composite Materials with Microstructure

by

Ryan Barrage

A thesis
presented to the University of Waterloo
in fulfillment of the
thesis requirement for the degree of
Doctor of Philosphy
in
Civil Engineering

Waterloo, Ontario, Canada, 2022

Examining Committee Membership

The following served on the Examining Committee for this thesis. The decision of the Examining Committee is by majority vote.

External Examiner:

Leszek Sudak
Professor, Department of Mechanical and Manufacturing Engineering
University of Calgary

Supervisors:

Maria Anna Polak
Professor, Department of Civil & Environmental Engineering
University of Waterloo

Stanislav Potapenko
Professor, Department of Civil & Environmental Engineering
University of Waterloo

Internal Members:

Wei Chau Xie
Professor, Department of Civil & Environmental Engineering
University of Waterloo

Mahesh Pandey

Professor, Department of Civil & Environmental Engineering

University of Waterloo

Internal-External Member:

Tais Sigaeva

Assistant Professor, Department of Systems Design Engineering

University of Waterloo

Author's Declaration

I hereby declare that I am the sole author of this thesis. This is a true copy of the thesis, including any required final revisions, as accepted by my examiners.

I understand that my thesis may be made electronically available to the public.

Abstract

Composite material properties are dependent on their microstructure. To adequately model these materials, a revised formulation of elasticity that accounts for microstructural effects must be considered. Size dependent behaviour is an inherent property of such materials, resulting in a need for non-classical continuum theories for adequate characterization.

The modelling of bi-material composites is investigated, with emphasis on how material microstructure impacts the overall behaviour of continua. The work aims to provide mathematical models capable of predicting the homogenized material response under specified loads given known constituent properties, for eventual use in creating design provisions, integration into numerical simulations, and further applications in materials research. Specifically, this thesis considers Cosserat (micropolar) elasticity to model microstructural effects.

Fiber reinforced composites with unidirectional fibers are modelled as transversely isotropic materials under the framework of Cosserat elasticity. The model assumes a periodic microstructure and develops a boundary condition to account for the periodicity. The governing equations for plane strain are developed, with the conditions for existence and uniqueness of the solution established.

A three-dimensional model for an exponentially graded composite with microstructural effects is developed under the framework of Cosserat elasticity. The mixed boundary value problem is formulated and existence and uniqueness of a weak solution is established for use in accordance with the finite element method. The finite element formulation is developed and integrated into the commercial software Abaqus through a user developed element, with an associated post processing code for output visualization. Given a lack

of elastic constants from experiments, validation is partially obtained through recovery of the classical limit. Following this, a conceptual extension to demonstrate a proof of concept is applied, with conclusions drawn based on the results. Recommendations for future extensions of the model are provided.

Acknowledgements

I would like to first thank my supervisors, Dr. Maria Anna Polak and Dr. Stanislav Potapenko, for their continuous guidance, and support in conducting meaningful research.

I would next like to thank my colleagues in the Polak Army, for always providing helpful feedback in my research. I would like to thank Graeme Milligan, who shared my struggles with modelling in Abaqus, and for our countless research discussions, without which several obstacles could not have been overcome.

I would also like to thank Sam and Astrit, for helping me solve various technical difficulties, our engaging discussions, and their constant support.

Finally I would like to thank my family for their support, and my wife, for ensuring I remained sane through difficult times.

Dedication

To Paola.

Table of Contents

List of Figures

List of Tables

List of Symbols

δ_{ij}	Kroenicker delta
ε_{ijk}	Alternating tensor components
σ_{ij}	Stress tensor components
$\vec{\boldsymbol{X}}$	Body force vector
ρ	Density
$\vec{\boldsymbol{a}}$	Acceleration vector
$\vec{\boldsymbol{Y}}$	Body moment vector
A_{ijkl}	Rank 4 tensor components
$\vec{\boldsymbol{u}}$	Displacement vector
ϵ_{ij}	Classical strain tensor components
λ, μ	Lamé constants
E	Young's modulus
ν	Poisson's ratio
$\vec{\boldsymbol{n}}$	Unit outward normal
$\vec{\boldsymbol{t}}$	Traction vector
U_0	Internal energy density
$\vec{\boldsymbol{\varphi}}$	Microrotation vector
$\mathcal{U}$	Internal energy

$\mathcal{K}$	Kinetic energy
$\mathcal{L}$	Power of external forces
$\mathcal{Q}$	Non-mechanical power
γ_{ij}	Cosserat strain tensor components
$\varkappa_{ij}$	Twist tensor components
μ_{ij}	Couple-stress tensor components
$\alpha, \beta, \gamma, \epsilon$	Cosserat elastic constants
$\vec{\boldsymbol{m}}$	Moment traction vector
$\vec{\boldsymbol{x}}$	Position vector
$\vec{\boldsymbol{G}}$	Grading vector
W	Work done
$\vec{\boldsymbol{p_v}}, \vec{\boldsymbol{m_v}}$	Body stress/couple-stress vectors
$\vec{\boldsymbol{p_s}}, \vec{\boldsymbol{m_s}}$	Surface stress/couple-stress vectors
$\vec{\boldsymbol{U}}$	Grouped displacement/microrotation vector
$\boldsymbol{\mathcal{E}}$	Grouped deformation tensor
$\boldsymbol{\Sigma}$	Grouped stress/couple-stress tensor
$\underline{\boldsymbol{C}}$	Grouped stiffness matrix
$\vec{\boldsymbol{T}}_{\boldsymbol{v}}, \vec{\boldsymbol{T}}_{\boldsymbol{v}}$	Grouped body stress/couple-stress vectors
$\vec{\boldsymbol{T}}_{\boldsymbol{s}}, \vec{\boldsymbol{T}}_{\boldsymbol{s}}$	Grouped surface stress/couple-stress vectors

Chapter 1

Introduction

1.1 Problem Statement

Composites are a class of materials in which two or more constituent materials are bonded together to form a continuum. The resulting material generally possesses material properties different from the individual constituents, with most synthesized composites being tailored for specific applications. Some examples of synthesized composites include concrete, reinforced rubber, and polycrystalline aggregates [1], with most applications appearing in the automotive, aviation, and construction industries.

Since composites are formed by combining two or more materials with different properties, the nature by which they are combined plays an important role in determining the mechanical behaviour of the new material. A relatively new technique, called functional grading, has become a topic of great interest due to the designer's ability to tailor the mechanical properties of the material to suit the desired application. Functional grading

involves creating a gradient in the material properties of the composite to achieve desired behaviour as a function of position. Such an example would be the need to have a portion of a beam be more ductile, with another region requiring less ductility. The mixture of the constituents can be altered (volume fraction, etc.) to achieve this gradient in properties, resulting in the desired behaviour. Common functional grades include stepwise, polynomial, power law, periodic, and exponential. Examples of functionally graded composite materials include high performance tennis rackets, bamboo, human tooth enamel, and thermal shielding. Composite materials that do not have a functional grading, but rather are a perfect mixture of the constituents can still be considered functionally graded materials, with the grading considered as a constant function.

Within the field of structural engineering, fiber reinforced polymers (FRPs) are being considered for a variety of applications. Most FRP materials fall under the umbrella of functionally graded materials, with the grading being constant (a perfect mixture). Some applications include using FRP as internal reinforcement for concrete structures, as the material provides the necessary tensile strength, and does not corrode as traditional steel reinforcement does. Furthermore, there is increasing interest in using FRP materials for the construction of structural elements, due to their beneficial properties. Offshore wind turbines suffer deterioration to corrosion as saltwater facilitates the oxidation process [2], making FRPs a prime alternative in constructing the turbine structure. Composite materials are also of great interest to the field of Nanotechnology, as most new nanomaterials are composite materials. Due to the rising interest in these materials, there is a fundamental need to understand their behaviour.

Most composites have a microstructure that is statistically uniform, resulting in a macroscopically homogeneous material [3]. These composite materials typically fail under ex-

treme working conditions through the separation of the fibers and matrix – a process known as delamination or debonding [4, 5]. This process is a result of significant shear stresses occurring at the interface at which two materials with vastly different properties are bonded [6]. The mathematical modelling of debonding processes in composite materials is challenging in nature due to the interface conditions (high stress concentrations). Considering a representative unit cell in which the matrix contains a single fibrous inclusion, one must include a model for the bond between the matrix and the inclusion, which presents several issues in terms of the solvability of the governing systems. Due to these mathematical challenges, most models assume perfect bond between the fiber and matrix, which simplifies the conditions for continuity of the homogenized medium, but does not accurately represent the physical processes involved.

Over the past few decades, functionally graded materials (FGM), have been used to address the issue of debonding due to stress concentrations elegantly. FGMs vary their elastic properties with position, creating a smooth gradient that eliminates high stress concentrations and interface conditions [6]. The elimination of sharp interfaces, where failure is typically initiated, forms a class of materials with desirable properties (heat /corrosion resistant) [5, 7] that are able to withstand extreme conditions (high temperature gradients, stress concentrations, etc.) [4, 8, 9]. FGMs are classified as microscopically inhomogeneous materials with engineered gradients of composition and structure, resulting in tailored properties in the preferred orientation [5, 10]. The desired properties are obtained by spatially varying the volume fractions of the constituents in a preferred direction. FGMs can occur in nature, with bones being a notable example [11].

1.2 Research Significance, Objectives, and Thesis Outline

Since composite materials are heavily dependent on their microstructure (further illustrated in Chapter 2), a formulation of elasticity that accounts for microstructural effects must be considered. Size dependent behaviour is an inherent property of such materials, resulting in a need for non-classical continuum theories for adequate characterization.

The modelling of bi-material composites will be investigated in this work, with emphasis on how material microstructure impacts the overall behaviour of the continuum. The goal of the research is to provide mathematical models capable of predicting the homogenized material response under specified loads given known constituent properties, for eventual use in creating design provisions, integration into numerical simulations, and further applications in materials research.

1.2.1 Research Objectives

The main objective of the proposed research is to devise mathematical models to describe the behaviour of bimaterial composites, with particular emphasis on microstructural effects using Cosserat (micropolar) elasticity. The research will be composed of two sections: transversely isotropic composites (sub class of orthotropic materials), and functionally graded isotropic composites.

The modelling of transversely isotropic composites will focus on developing the governing equations for FRPs with unidirectional fibers, with specific research tasks as follows:

- Develop constitutive relations for homogenized, transversely isotropic, Cosserat composite

  Consider Eringen's constitutive relations (general elasticity with microrotational degrees of freedom, discussed in Chapter 2) for a general anisotropic elastic continuum with microstructure and reduce the relations to the transversely isotropic case. Specifically, develop the stress/strain, couple stress/twist relations for the material, reducing the number of unknown elastic constants by exploiting plane symmetries in the stress/couple stress states.

- Set up homogenization scheme and develop boundary conditions for the representative unit cell

  Use the proposed stress/strain relations in conjunction with a periodic representative unit cell to develop boundary conditions for the microstructure. Specifically, obtain periodic traction conditions on the unit cell, and use a variational principle on the potential energy of the system to develop a boundary condition linking the microscale to the macroscale.

- Pose the equilibrium in cylindrical coordinates and discuss simplifying assumptions (plane strain)

  Use force and moment equilibrium to develop a system of 6 coupled partial differential equations in cylindrical coordinates to describe the homogenized continuum. Reduce the problem complexity to 3 coupled equations by considering the case of plane strain.

- Present the conditions for solving the system, and discuss limitations in obtaining a solution

  Present the conditions for uniform ellipticity and positive strain energy density, noting that measurement of elastic constants is required to guarantee ellipticity. Measurement of the elastic constants is beyond the scope of this work, leaving the solution of the system for future works.

The modelling of isotropically graded composites will focus on developing and solving the governing equations for exponentially graded composite materials:

- Obtain governing system of equations for exponentially graded system with microstructure

  Consider Nowacki's constitutive relations (isotropic equations of elasticity for a system with microrotational degrees of freedom) for an isotropic continuum with 6 variable elastic coefficients and derive the equilibrium equations for the general three-dimensional case.

- Set up boundary value problem for exponentially graded continuum

  Use the force/moment equilibrium equations to obtain the corresponding boundary value problem. Prove ellipticity of the resulting system of partial differential equations with variable coefficients, obtaining the conditions for existence and uniqueness of the solutions.

- Obtain a weak solution to the governing system and implement into commercial finite element analysis (FEA) software

Using the commercial FEA software Abaqus [12], a user, micropolar, exponentially graded, element will be designed to implement the weak-form solution to the governing equations.

- Use developed model in conjunction with fictitious material parameters to illustrate applicability, and future use in the industry

  Considering fictitious elastic properties for a homogenized composite (since micropolar elastic constants are currently not available), conceptual application of the model will be demonstrated under various loading cases as a proof of concept for future works.

1.2.2 Thesis Outline

Following the introduction (Chapter 1), where the research objectives and outline of the thesis are presented, Chapter 2 outlines discrepancies found between the classical elasticity model and observed phenomena in specific materials with notable microstructure. Consequently, the importance of Cosserat elasticity theory is discussed, along with a comparative introduction to Cosserat elasticity theory, with appropriate preliminaries in functional analysis.

Chapter 3 discusses the modelling of transversely isotropic composites with unidirectional fiber reinforcement, and formulates the governing equations in the framework of Cosserat elasticity. The solvability of the equations is also addressed.

Chapter 4 presents a Cosserat elasticity model for an exponentially graded material, sets up the governing system of differential equations, and proceeds to solve the energetic

equivalent using the finite element method. The finite element solution is implemented into commercial software, with several numerical examples considered to demonstrate the applicability.

Finally, Chapter 5 outlines some conclusions drawn from the presented work, with recommendations provided for extensions to the foundations laid out in the thesis.

Chapter 2

Literature Review

2.1 Limitations of Classical Theory

At a small enough scale, all materials have a defined microstructure. For many practical purposes however, the most common models used to describe materials paint them as continuous media. This assumption holds true in most cases, as many of the commonly used materials in industry possess microstructure at a small enough scale that the effects on the macroscopic behaviour are negligible. This is not true for all materials however, and the rising popularity of tailor-made materials brings new challenges to material modelling as these emerging materials often possess non-negligible microstructure [13]. Rueger and Lakes [14] show that for some materials, slender cylinders appear to be stiffer than what classical elasticity theory predicts, citing size effect as the key contributing factor. They also find a similar size effect in the bending of thin plates, and in predicting the stress concentration factor around a hole. Their findings suggest that in the case of small holes (or cracks), the deformation induced spills over to corner regions, and through the use

of holography, show that strain concentrations exist in those corner regions. Classical elasticity theory predicts no deformation in those corner regions, suggesting a need for modification to the existing theory. Both authors suggest that the length scale of the specimen may play an important role in the prevalence of these effects, and warrant further investigation.

One particular avenue for the use of functionally graded materials is to attempt to seamlessly integrate prosthetics or inclusions into the human skeletal structure. For example, metal plating is a common inclusion. The issue with such inclusions is that a discontinuity is introduced, whereby the material properties of the bone differ from those of the plate, introducing stress concentrations at the interface that can be problematic. A means of mitigating this issue would be to grade the inclusion in such a manner that it can provide the necessary strength, with a smooth transition towards the material properties of bone at the interface. Furthermore, in orthopaedic surgery, it is common practice to introduce screw holes into a bone. Stress concentrations arise around holes, and the stress concentration can be expressed through a stress concentration factor calculated by taking the ratio of the maximum stress to nominal stress in classical elasticity theory. Yoon and Katz [15] discuss the effects of strain gradients on fatigue and fracture strength of materials, and how grain size influences the accuracy of the results in comparison to experimental measurements [16]. Their findings suggest that the higher the strain gradient across the specimen, the higher the fatigue strength. Furthermore, they suggest that fracture in brittle materials, as well as the onset of static yielding in ductile materials, occur at higher loads than what is predicted using classical stress concentration factors. Their findings suggest a need to incorporate strain gradient effects into the governing elasticity theory for certain materials, namely bone.

While materials like sands and gravel are composed of distinct particles that interact with each other, classical continuum models are often used to describe such media. The interaction between these distinct particles presents in the form of internal force transmission, which is averaged over a sufficiently large volume to generate a continuous description. These models typically neglect transmission of moments between the particles, as in most materials, these contact moments produce negligible macroscopic effects. With granular materials, as those mentioned above, these contact moments are not negligible with regards to macroscopic behaviour, due to the large size of the material point, or grain. With such materials however, at the microscopic scale, local behaviour is governed by Coulomb's law, in which contact shear force cannot overcome a certain threshold, and that such contacts are only active in compression [17]. These principles account for the complex behaviour of sands, which is typically not well captured by macroscopic elastoplastic models. The micromechanical models in question introduce internal parameters to attempt to account for the limitations, such as plastic deformation and hardening variables, which are typically not clearly defined. Calvetti et al. [17] performed tests on small circular rods or material where the grain size is comparable to the length of the specimen, and found that as the test time elapsed, the standard deviation between classical prediction and measurements grew larger for the rotational degrees of freedom, suggesting the possibility of rotations at a microscopic level being kinematically independent from translations.

By design, many composites consist of stiff, finite sized elastic inclusions within a resin matrix [18]. Prior to curing, the contrast in properties between the fiber and matrix is very large, to the extent where under loads associated with forming the desired shape, the individual fibers deform and bend independently, carrying localized moments [19]. Sakhaei et. al [18] illustrate how neglecting these localized contributions in modelling results in the bending mechanics of the composite becoming highly mesh dependent when discretized.

They observe wrinkles forming in the corner radius of a thick composite part under consolidation, and suggest a need to include localized bending mechanics into existing theory of elastoplasticity. Lakes and Drugan [20] also show how in the bending of a composite (square cross-section) with non-negligible microstructure, a sigmoidal deformation of the lateral surfaces arises in addition to the usual tilt, exhibiting the same behaviour observed by Sakhaei et. al. The authors' observations suggest a need for further investigation into how the micromechanics of materials can play an important role in the governing macroscopic behaviour, and the need to identify the microscopic quantities at play.

Fleck et al [21] discussed the results of tests on metals and ceramics in which the indentation hardness of the materials increases with decreasing indenter size. They suggest that fine-grained metals are stronger than coarse grained ones, with the effect becoming more pronounced with decreasing grain size or indent size, suggesting a size effect. Furthermore, they tested both thin and thick wires under torsion and determined that the thin wires required substantially higher torsions to cause an equivalent amount of rotation. In addition, Xu et al [22] illustrate how the flexural properties (stiffness) of zirconia ceramics increase with decreasing specimen height. They highlight how the macroscopic dimension of the object, in relation to the size of the material microstructure, can lead to a larger deviation in predictions by classical elasticity theory.

Huang and Xu [23] further discuss the relationship between microstructural properties and observable size effects. They highlight the link between characteristic lengths in granular media and macroscopic properties, namely stating that the aforementioned characteristic lengths are proportional to the microstructure length (grain size). They further note that the material properties are linked to these characteristic lengths, displaying size effect in the over all macroscopic behaviour. Moreover, Lakes and Benedict [24] discuss bending and

torsion experiments on cylinders of various size in which size effects on the apparent stiffness where observed. They further supported these findings through their own experimental program, testing human compact bone, which has been shown to behave in a non-classical manner.

Diepolder, Mannl, and Lippman [25] extend this idea by testing metals to observe microstructural effects. The authors tested solid cylindrical aluminium specimens, as well as thin-walled aluminium specimens. Their findings showed that metallic grains undergo a shear deformation along the crystalline slip planes, whose orientation influences global deformation. As a result, they note that the grains show an individual rotation that can deviate considerably from the classical rotation, and that these rotations are delayed with respect to the rotation of the overall torsional flow field, denoting kinematic independence.

2.2 Significance of Cosserat Theory in Modelling Microstructural Effects

To attempt to address the discrepancies observed between classical elasticity theory and experiments in which microstructural effects prevail, the micropolar (Cosserat) theory of elasticity has experienced a re-emergence since its introduction by the Cosserat brothers in 1909 [26]. Mora and Wass [27] succinctly state that the Cosserat theory is a good starting point for the characterization of materials that exhibit these effects, since it introduces a length scale that is not present in classical continuum theories. These effects take into account force-like quantities that develop in bodies when strain gradients exist, and consider rotations on the microstructure scale to be kinematically independent from displacements in their continuum description. As a result of incorporating these effects, Cosserat theory

of elasticity inherently includes a length scale [13] in its formulation, which can account for the observed size effects. This enriched continuum model takes into account 6 degrees of freedom, three classical displacements, as well as three microrotations. The spatial gradients of these rotations result in internal curvature measures, which form work conjugates [18] to the resulting internal bending moments.

Furthermore, equilibrium of a material point denotes a transfer of moments in addition to axial forces (classical), which gives rise to the kinematically independent microrotations. Considering moment equilibrium for a body, one can see that the addition of these degrees of freedom gives rise to stress-like quantities [15], known as couple stress, which consist of a couple per unit area. The addition of these terms in the moment equilibrium equations result in the stress tensor being asymmetric, contrasting classical, symmetric stress tensors.

Cosserat theory has been shown to address some of the discrepancies observed between classical theory and experiments. Most notably, Cosserat theory shows better agreement with experiments in the prediction of stresses in materials with microstructure. In particular, the analytical solutions for stress concentrations around holes (circular and elliptic) display smaller stress concentration factors when compared to classical calculations, matching more closely with experiments [16]. Size effect is also predicted in the torsion and bending of rods, as the elastic modulus of the rods increases with decreasing size [22, 28]; this size effect is not captured in classical elasticity theory. This gives rise to the notion that the Cosserat continuum model can be useful in modelling heterogeneous materials in which the size of the heterogeneity is reasonably comparable to the size of the structure [29], and can be a useful too to regularize numerical computations where classical analysis methods break down.

Three examples from the literature are presented to demonstrate the predictive capabilities

of Cosserat elasticity for the aforementioned materials.

First, an experimental investigation by Park and Lakes [30] on wet bone (soft tissue) is presented. Bone tissue is a complex material that exhibits fibrous, porous, and particulate microstructures at different length scales. Experimental investigations have determined that the stress concentration factor for bone is much lower than the predictions made by classical elasticity. The authors aimed to present the predictive power of the Cosserat micropolar model in capturing the complex microstructural effects through a series of experiments. They performed experiments to determine the distribution of strain on the lateral surfaces of prismatic, square cross-section bars of wet (soft) and dry bone in torsion.

To analyse the results, the authors compared the experimental data to theory as follows. They converted the obtained strain data along the boundary of the sample to the tensorial shear strain element ϵ_{zy}, and normalized the results by dividing by the angle of twist per unit length, and by the width of the specimen. These results were compared to classical, theoretical strain distributions, and Cosserat predictions. The difference between the theoretical predictions arises from the fact that classically, the strain distribution is independent of the elastic constants, whereas in Cosserat elasticity, the distribution exhibits a dependence. Previous experiments by Yang and Lakes [31] demonstrated measurement of the elastic constants through the method of size effects, which involved some curve fitting assumptions. Measurement of the Cosserat elastic constants remains a challenge, and is rather difficult without certain relations between constants being assumed.

Figures 2.1a and 2.1b compare the experimental results to theoretical predictions for dry bone samples, and wet bone samples with different techniques used to hydrate the samples. Figure 2.1a displays results for bone hydrated by placing the sample in a humid

environment for 5 days, then immersing it in water for 10 hours. Figure 2.1b displays results for a sample directly immersed in water for 12 hours. The results show that dry bone behaves as a classical material, while wet bone, regardless of the hydration method, displays non-classical effects better predicted by Cosserat elasticity theory. The authors

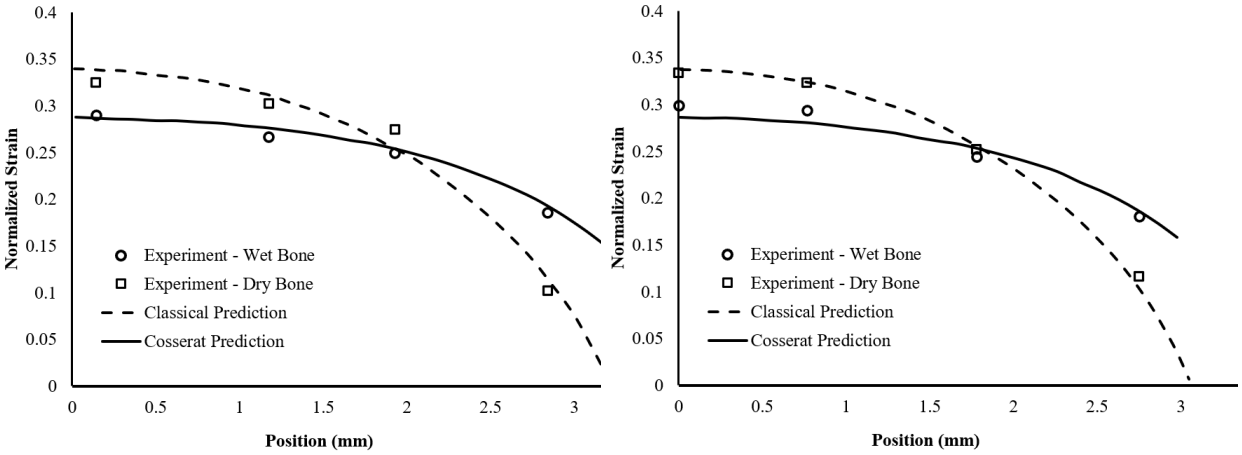

Figure 2.1: (a) Dry bone compared to specimen left in a humid environment for 5 days, then immersed in water for 10 hours (b) Dry bone compared to specimen directly immersed in water for 12 hours [30]

posit that the osteonal architecture of the compact human bone is the physical mechanism responsible for these Cosserat elastic effects, with the properties of the cementitious substance between osteons suggested as the specific mechanism involved. Hydration of the substance changes the compliance of the composite, resulting in macroscopic behavioural changes as a result of the microstructural changes. The authors also observed a size effect in their investigations, where the length scale of the microstructure in comparison to the structural size of the specimen is related to the prevalence of the Cosserat effects.

Another example of non-classical effects that can be predicted by Cosserat elasticity is

observed in reticulated foams by Lakes [32]. The author tested bars of open-cell polymer foam with a square cross-section in torsion, and observed that warping of the cross-section was reduced by a factor of approximately four (Figure 2.2) in comparison to the classical predictions, but was shown to agree with the predictions made by Cosserat elasticity. The author tested bars with a square cross-section 25 mm wide, and plotted the normalized warp (warp divided by angle of twist per unit length, and bar width squared) versus position along the bar cross section. In a Cosserat solid, the strain redistributes towards

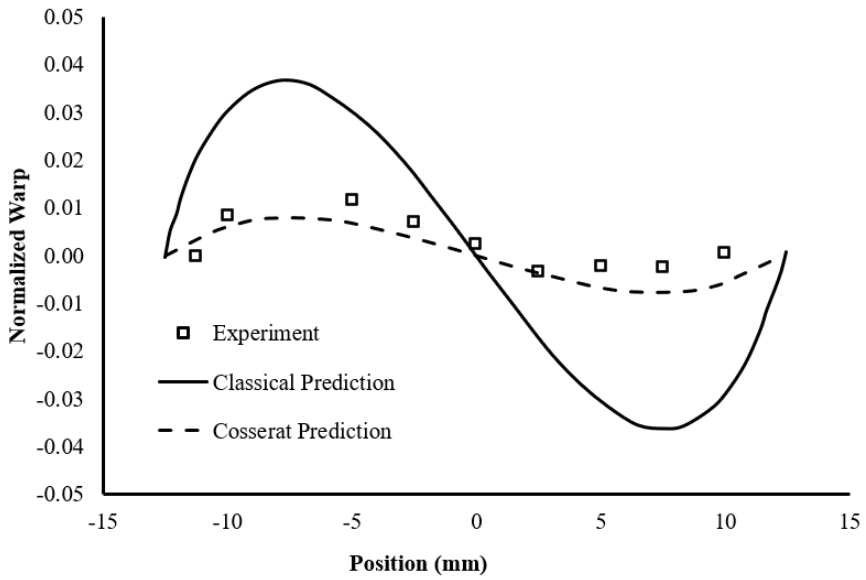

Figure 2.2: Warping of square cross-section for open-cell foam beam in torsion [32]

the corner regions, which in classical elasticity theory, are predicted to have zero stress and strain. As a result, the peak strain is reduced in comparison with classical predictions. The rationale for this difference is well explained by the authors, and is a result of the symmetry of the stress tensor in classical elasticity theory. Since the shear stresses must be symmetric, and the corners of the square-cross section are joined by two free surfaces that undergo zero shear stress, the strain must be zero. However, due to twisting of the

bar, there must be warping, specifically away from the corners. Since Cosserat elasticity does not have a symmetry of the stress tensor (due to the presence of couple stresses), the stresses and strains at the corners can be non-zero, reducing the warping in regions away from the corners. This constitutes a redistribution, explaining the reduction in observed peak stress from classical predictions.

Lastly, to further illustrate how Cosserat (micropolar) elasticity can capture the microstructural/size effects that are not well captured by classical elasticity, a well-known experiment by Rueger and Lakes [14] is discussed.

The authors tested corrugated nylon tubing, with an inner diameter of 3.18 mm, outer diameter of 6.7 mm, and density of approximately 0.26 g/cm^3. The lengths of the tubes were cut to be approximately three times the average diameter of the sample. The authors tested 4 samples, consisting of a single tube, an array of three tubes arranged in a triangular pattern, seven tubes arranged in a hexagonal pattern, and 19 tubes arranged in a hexagonal pattern (Figure 2.3).

The authors determined the torsional and bending rigidity of the specimens using a broadband viscoelastic spectrometer. The Poisson's ratio of the specimens was determined through compression testing by measuring the transverse strain with a micrometer.

The specimens were treated as isotropic, which has been shown to be a good approximation given the size of the specimens and loading cases examined. As such, the experimental data could be compared to exact analytical solutions to the Cosserat governing equations involving Bessel functions.

In lieu of directly measuring the Cosserat elastic constants, the authors measured micropolar engineering constants to indirectly obtain a means of computing the 4 non-classical elastic constants. Two sets of tests were conducted, in which the torsional rigidity and bending rigidity of the specimens were measured, and compared to both classical and Cosserat elasticity predictions.

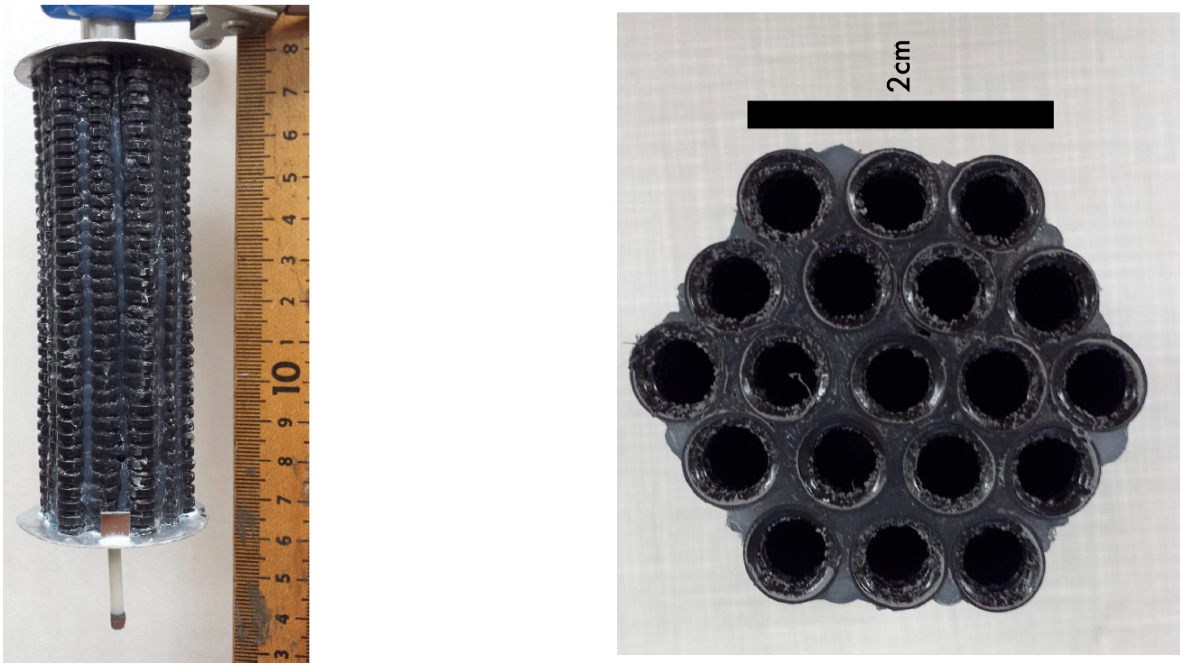

(a) (b)

Figure 2.3: (a) Largest specimen of aligned corrugated tubing and silicone rubber matrix composite (b) Cross section of largest sample [14]

Classically, the torsional rigidity of a circular specimen is given by

$$\frac{M}{\theta} = G\left[\frac{\pi}{2}r^4\right], \tag{2.2.1}$$

with a normalized rigidity ratio defined as

$$\Omega = \frac{\frac{M}{\theta}}{G\left[\frac{\pi}{2}r^4\right]} = 1, \tag{2.2.2}$$

where M is the applied moment, θ is the angular displacement, G is the shear modulus, and r is the radius of the specimen.

In Cosserat elasticity, the torsional rigity is dependent on inherent size effects, and therefore Ω is not a constant value. The authors' results are shown in Figure 2.4, with the points showing experimental values for the different specimens, and the curve denoting the predictions made using Cosserat elasticity theory.

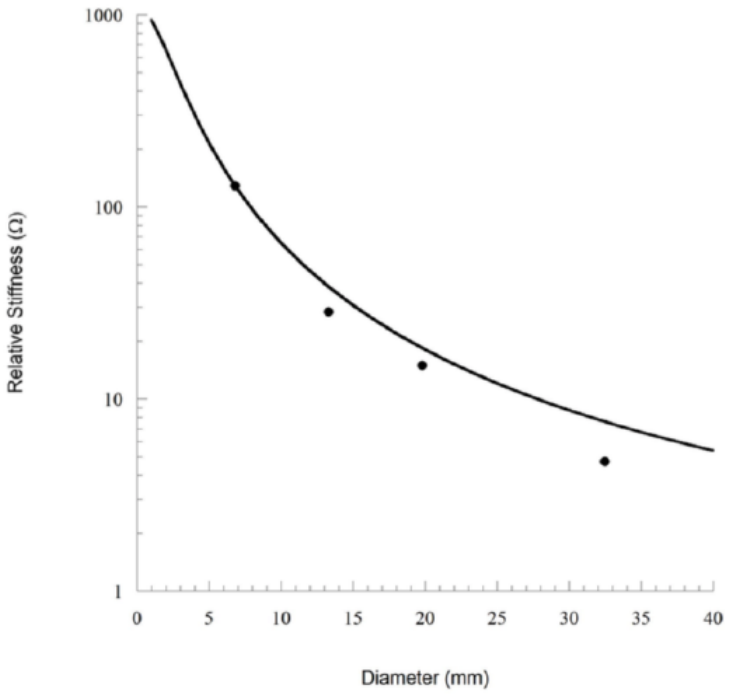

Figure 2.4: Size effects for corrugated tubing specimens in torsion [14]

Figure 2.4 shows close agreement between Cosserat elasticity and the experiment,

whereas the classical prediction of $\Omega = 1$, deviates from the experiments. It is however important to note that as the diameter increases, the experimental data appears to converge towards the classical prediction of $\Omega = 1$; this suggests that classical elasticity fails to capture the inherent size effects present.

In a similar manner, the authors tested the specimens in bending. The classical bending rigidity of a circular specimen is given by

$$\frac{M}{\theta} = E\left[\frac{\pi}{4}r^4\right], \tag{2.2.3}$$

with a normalized rigidity ratio (recycling the variable Ω) defined as

$$\Omega = \frac{\frac{M}{\theta}}{E\left[\frac{\pi}{4}r^4\right]} = 1, \tag{2.2.4}$$

where E is the Young's modulus of the specimen.

Similar to the case of torsion, in Cosserat elasticity, the bending rigity is dependent on inherent size effects, and is not a constant value. The authors' results are shown in Figure 2.5, with the points showing experimental values for the different specimens, and the curve denoting the predictions made using Cosserat elasticity theory.

Figure 2.5 shows close agreement between Cosserat elasticity and the experiment, whereas the classical prediction of $\Omega = 1$, deviates from the experiments. Once more, one can observe that as the diameter increases, the experimental data appears to converge towards the classical prediction of $\Omega = 1$.

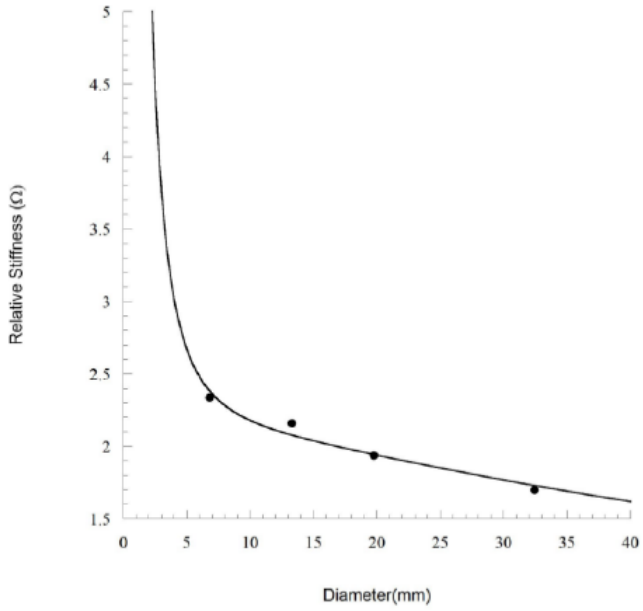

Figure 2.5: Size effects for corrugated tubing specimens in bending [14]

The above experiment, as well as others discussed in this section, suggest that Cosserat elasticity provides a good model for predicting size effects, as well as microstructural influences on macroscopic behaviour, where classical elasticity theory fails to do so. The Cosserat model for elasticity will therefore be adopted in this work to model functionally graded materials, and those with significant microstructure.

While many examples depicting deviations between the classical and Cosserat formulations in materials with microstructure exist, most of them assume values for the Cosserat elastic constants to do so. Experimental analysis can detect the presence of micropolar effects, but calculation of the elastic constants is less than straightforward [24]. This is largely due to the scale at which measurements must be made, as they are on the scale of the microstructure. Measurement techniques however continue to evolve, and the scale at which measurements can be performed continues to approach the

required scale. In the meantime, it is of great importance to analyze the governing boundary value problems in preparation for the arrival of the material constants [16, 33].

2.3 Mathematical Preliminaries

2.3.1 Tensor Calculus

Throughout what follows, tensor and index notation are utilized to describe quantities of interest (stresses, displacements, elastic matrices, etc.). The tensors used cover 3 spatial dimensions with indices assuming values 1,2, and 3. Repeated indices denote a summation from 1 to 3 as per the Einstein summation convention, unless stated otherwise.

For example, the tensorial contraction

$$A_i = B_{ij}C_j \tag{2.3.1}$$

denotes a 3×1 column vector $\vec{\boldsymbol{A}}$ with components A_i, which are calculated by

$$A_i = B_{ij}C_j = \sum_{j=1}^{3} B_{ij}C_j \tag{2.3.2}$$

The standard Kroenecker delta is a special tensor, with components defined by

$$\delta_{ij} = \begin{cases} 0, & \text{if } i \neq j \\ 1, & \text{if } i = j \end{cases} \tag{2.3.3}$$

The alternating, or permutation, tensor is another special tensor, defined by

$$\varepsilon_{ijk} = \begin{cases} 1 & \text{if } (i,j,k) \text{ is } (1,2,3),(2,3,1), \text{ or } (3,1,2) \\ -1 & \text{if } (i,j,k) \text{ is } (3,2,1),(1,3,2), \text{ or } (2,1,3) \\ 0 & \text{if } i=j, \text{ or } j=k, \text{ or } k=i \end{cases} \tag{2.3.4}$$

Differentiation with respect to a coordinate x_α is denoted by $(...)_{,\alpha}$.

$\mathcal{M}_{mxn}$ denotes the space of $(m \times n)$ matrices, where $\mathcal{I}_n$ denotes the identity matrix in $\mathcal{M}_{nxn}$.

Assessing the definiteness of a matrix will be required in this work. Sylvester's criterion [34] provides a useful means of assessing the definiteness of a symmetric matrix.

Theorem 2.3.1. *Given an $n \times n$ symmetric matrix M with entries $m_{ij} = m_{ji}$, such that*

$$M = \begin{bmatrix} m_{11} & \cdots & m_{1n} \\ \vdots & \ddots & \vdots \\ m_{n1} & \cdots & m_{1n} \end{bmatrix},$$

let $M^{(l)}$ denote the $l \times l$ submatrix obtained from the top left corner of M, such that

$$M^{(1)} = [m_{11}], \qquad M^{(2)} = \begin{bmatrix} m_{11} & m_{12} \\ m_{21} & m_{22} \end{bmatrix}, M^{(l)} = \begin{bmatrix} m_{11} & \cdots & m_{1l} \\ \vdots & \ddots & \vdots \\ m_{l1} & \cdots & m_{1l} \end{bmatrix}, \qquad M^{(n)} = M$$

Let Δ_l represent the determinant of submatrix $M^{(l)}$, such that $\Delta_l = det(M^{(l)})$. Sylvester's criteron states that

- *M is positive definite if and only if $\Delta_1 > 0, \Delta_2 > 0, ..., \Delta_n > 0$.*
- *M is negative definite if and only if $(-1)^1\Delta_1 > 0, (-1)^2\Delta_2 > 0, ..., (-1)^n\Delta_n > 0$.*

2.3.2 Relevant Functional Spaces and Theorems

Let V denote a real Hilbert space [35], equipped with inner product $(\cdot,\cdot)_V$, and norm $\|\cdot\|_V$. Let V' denote the topological dual, with the $V' \times V$ duality pairing $\langle\cdot,\cdot\rangle$.

For any $f \in V'$, the standard dual norm is defined as

$$\|f\|_{V'} = \sup_{\|v\|_V=1, v\in V} \left|\langle f, v\rangle\right| \tag{2.3.5}$$

Let the Banach space of bounded linear maps between Hilbert spaces V_1 and V_2 be given by $\mathcal{L}(V_1, V_2)$, with its associated norm defined as

$$\|T\|_{\mathcal{L}(V_1,V_2)} = \sup_{\|v\|_{V_1}=1, v\in V_1} \|Tv\|_{V_2} \tag{2.3.6}$$

Let $L^2(\Omega)$ be the Lebesgue space of square integrable functions, over a domain $\Omega \in \mathbb{R}^n$, with Euclidean volume element dx, and inner product

$$(u, v)_{L^2} = \int_\Omega uvdx, \tag{2.3.7}$$

and norm $\|u\|_{L^2}^2 = (u, u)_{L^2}$. Since this work will look to solve partial differential equations through the Finite Element Method, in which weak forms of the governing equations are

defined, and thus weak form solutions are sought, it is important to consider the definition of Sobolev spaces.

Let $k \in \mathbb{N}, \leq p \leq \infty$. The Sobolev space $W^{k,p}(\Omega)$ is defined to be the set of functions $f \in \Omega$ such that the mixed partial derivative

$$f^{(\alpha)} = \frac{\partial^{|\alpha|} f}{\partial x_1^{\alpha_1} \cdots \partial x_n^{\alpha_n}} \tag{2.3.8}$$

exists weakly in $L^p(\Omega)$ for every multi-index α with $|\alpha| \leq k$.

To say that a derivative exists weakly means that it is a generalization of the derivative of a function for functions that are not assumed to be differentiable, but only integrable. In the Finite Element Method, differential equations are converted to integral form, and as such, weak differentiation becomes relevant.

The Sobolev space $W^{k,2}(\Omega)$ is also referred to as $H^k(\Omega)$, and will be referred to often in this work. Specifically, the Sobolev space $H^1(\Omega)$, will be considered. $H^1(\Omega)$ is the Sobolev space of all vector fields on Ω , once weakly differentiable, that lie in $L^2(\Omega)$.

The Sobolev space $H^1(\Omega)$ is equipped with the inner product

$$(u, v)_{H^1} = \int_\Omega (\nabla u \cdot \nabla v + uv)\, dx \tag{2.3.9}$$

Within the context of solving systems of partial differential equations, the following theorems will be useful.

Consider a general second order partial differential equation of the form

$$Lu = f \tag{2.3.10}$$

where L is a linear differential operator of the form

$$Lu = -\sum_{i,j=1}^{n} \partial_i \left(a_{ij} \partial_j u \right) + \sum_{i=1}^{n} \partial_i \left(b_i u \right) + cu \tag{2.3.11}$$

and define the associated bi-linear form

$$a : H^1(\Omega) \times H^1(\Omega) \to \mathbb{R} \tag{2.3.12}$$

by

$$a(u,v) = \int_\Omega \left\{ \sum_{i,j=1}^{n} a_{ij} \partial_i u \partial_j v - \sum_{i=1}^{n} b_i u \partial_i v + cuv \right\}, \tag{2.3.13}$$

such that

$$a_{ij}, b_i, c \in L^\infty(\Omega), \quad a_{ij} = a_{ji}, \tag{2.3.14}$$

where $H^1(\Omega)$ is a standard Sobolev space.

Theorem 2.3.2. *(Korn's Inequality [36]) Let a be a bi-linear form on $H^1(\Omega)$ defined in (2.3.13), where the coefficients satisfy (2.3.14) and the uniform ellipticity condition.*

Then there exist constants $C_1, C_2 > 0$ *and* $\gamma \in \mathbb{R}$ *such that for all* $u, v \in H^1(\Omega)$ *[36]*

$$C_1\|u\|^2_{H^1_0} \leq a(u,u) + \gamma\|u\|^2_{L^2} \tag{2.3.15}$$

$$\left|a(u,v)\right| \leq C_2\|u\|_{H^1_0}\|v\|_{H^1_0} \tag{2.3.16}$$

Theorem 2.3.3. *(Lax-Milgram) Let* $\mathscr{H}$ *be a Hilbert space with inner product* $< \cdot, \cdot >: \mathscr{H} \times \mathscr{H} \to \mathbb{R}$*, and let* $a : \mathscr{H} \times \mathscr{H} \to \mathbb{R}$ *be a bi-linear form on* $\mathscr{H}$*. Assume there exist constants* $C_1, C_2 > 0$ *such that [36]*

$$C_1\|u\|^2 \leq a(u,u), \quad \left|a(u,v)\right| \leq C_2\|u\|\|v\| \qquad \textit{for all } u,v \in \mathscr{H}. \tag{2.3.17}$$

Then for every bounded linear functional $f : \mathscr{H} \to \mathbb{R}$*, there exists a unique* $u \in \mathscr{H}$ *such that*

$$< f, v >= a(u,v) \qquad \textit{for all } v \in \mathscr{H}. \tag{2.3.18}$$

Typically, problems in linear elasticity theory are solved over domains Ω with smooth geometry, and as such, solutions of the class C^n are sought. However, in cases where the geometry of the boundary is complex, this is not possible. In such cases, one can decompose the domain Ω into the union of sufficiently smooth, geometrically elementary subdomains, with analogous boundary value problems formulated over each subdomain [36, 37]. The requirement for the smoothness of the boundary is Hölder continuity, defined below.

Let Ω be an open set in $\mathbb{R}^n$, with $0 < \alpha \leq 1$, and non-negative integer $k \in \mathbb{N}$. The (uniform) Hölder spaces $C^{k,\alpha}(\Omega)$ consist of functions whose k-th order derivatives are

uniformly Hölder continuous with exponent α in Ω.

Lastly, due to the computational implementation of the obtained solutions in this work, a discussion on the well-posedness and stability of the solution is warranted. For a system 2.3.10 with form 2.3.11 and associated bi-linear operator $a(u, v)$ (equation 2.3.13), the system of partial differential equations is well-posed (in the sense of Hadamard [38]) if

- for each choice of data, a solution exists in some sense.
- for each choice of data, the solution is unique in some sense.
- the map from the data to the solutions is continuous

The conditions therefore necessitate the existence and uniqueness of the solution to the system of partial differential equations, as well as the continuous dependence of the solutions u on the data f defined in problem 2.3.10. A problem satisfying the conditions of the Lax-Milgram theorem is guaranteed existence and uniqueness of the solution in the appropriate Sobolev space, as well as a continuous map from the solutions to the data. The condition requiring a continuous map from the solutions to the data can be written as

$$\|u\|_X \leq C\|f\|_Y \,, \tag{2.3.19}$$

for solution u and data f belonging to functional spaces X and Y. The continuity of the mapping from the data to the solutions in the given problem follows from the coercivity and continuity requirements for the Lax-Milgram theorem, given in 2.3.17, where the constant C from the inequality 2.3.19 is $\frac{1}{C_1}$ in 2.3.17. The solution to the given problem is therefore well-posed, subject to satisfying the requirements of the Lax-Milgram theorem.

2.4 Review of Classical Linear Elastostatics

The foundational principles of linear elasticity theory began with the works of Cauchy, Navier, and Green in the 18th century, with the concept first proposed by Robert Hooke in 1678. Their work centralized on developing a continuum model to describe how objects deform under prescribed loading conditions.

In many practical structural engineering applications, the goal of design is to minimize a structural element's deformations and ensure adequate strength under typical loads. As such, for many practical purposes, linear elasticity theory is used to model elastic bodies, with higher order strain terms neglected. Therefore, throughout what follows, discussion of elasticity theory will be limited to linear elasticity theory, which follows the small strain assumption.

This section aims to illustrate the steps for constructing boundary value problems in linear elastostatics, and ultimately the framework for solving them numerically. The goal of this outline will be to facilitate understanding of Chapters 3 and 4, which will employ the same methods to construct and solve the governing problems in Cosserat elasticity.

Classical elasticity theory begins with the assumption that a representative element within the material, with surface area dA_1, transfers internal loadings to a neighbouring element, with surface area dA_2, through the action of axial forces, or surface tractions (Figure 2.6). This transfer of forces results in the definition of a stress tensor, with components σ_{ij}.

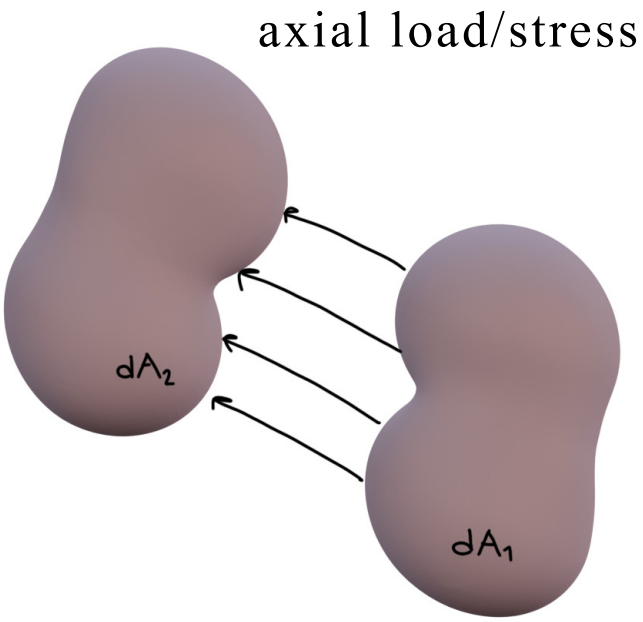

Figure 2.6: Internal transfer of loads between neighbouring continuum elements, classical elasticity

Due to the three-dimensional nature of the analysis, the stress tensor holds nine components in Cartesian coordinates. Each component of the stress tensor acts in a cardinal Cartesian direction, on a Cartesian plane projected from the element's volume, dV. Figure 2.7 illustrates the nine different stress components.

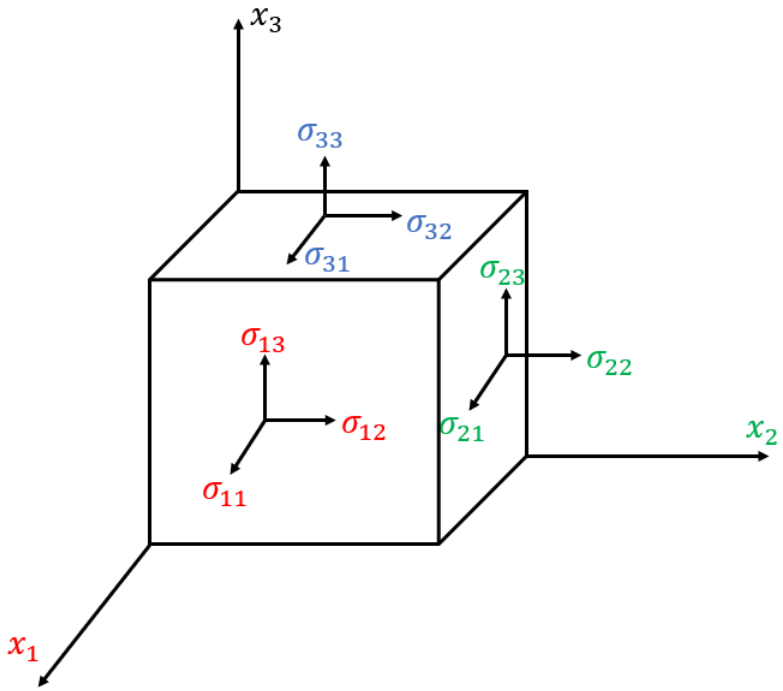

Figure 2.7: Stress tensor components in Cartesian coordinates

The resulting stress tensor components can be represented in matrix form by

$$\sigma_{ij} = \begin{bmatrix} \sigma_{11} & \sigma_{12} & \sigma_{13} \\ \sigma_{21} & \sigma_{22} & \sigma_{23} \\ \sigma_{31} & \sigma_{32} & \sigma_{33} \end{bmatrix}, \tag{2.4.1}$$

In conjunction with external body force densities, $\vec{\boldsymbol{X}} = (X_1, X_2, X_3)^T$ (force per unit volume), present on a continuum point, and the transfer of loads depicted in Figure 2.6, one can turn to equilibrium equations to analyse the mechanics of a continuum point. In what follows, temperature dependent effects will not be considered.

First, considering the balance of forces in each Cartesian direction, one obtains from

Newton's second law, and the Ostrogradski-Gauss transformation, that

$$\sigma_{ji,j} + X_i = \rho \frac{\partial^2 u_i}{\partial t^2}, \tag{2.4.2}$$

where u_i denotes the components of the material point's displacement in the ith direction, and ρ denotes the density.

Neglecting body forces, and considering the static case to analyse an elastostatic structure, the force equilibrium equations reduce to

$$\sigma_{ji,j} = 0 \tag{2.4.3}$$

Similarly, moment equilibrium equations can be developed for the static case, such that

$$\epsilon_{ijk}\sigma_{jk} + Y_i = 0, \tag{2.4.4}$$

where $\vec{Y} = (Y_1, Y_2, Y_3)^T$ denotes external body moment densities (moment per unit volume) and ϵ_{ijk} is the alternating/permutation tensor.

Once again, neglecting the action of body moments, the equations reduce to

$$\epsilon_{ijk}\sigma_{jk} = 0, \tag{2.4.5}$$

which yields an important result. Expanding equation (2.4.5) to its component form, one

can see that

$$\sigma_{12} - \sigma_{21} = 0, \tag{2.4.6}$$

$$\sigma_{31} - \sigma_{13} = 0, \tag{2.4.7}$$

$$\sigma_{23} - \sigma_{32} = 0, \tag{2.4.8}$$

which signifies that the components of the stress tensor are symmetric. This property of the stress tensor yields six independent components of stress, and allows usage of the convenient Voigt notation. Symmetry of the stress tensor simplifies the analysis of the governing equations of elasticity, reducing the complexity of the ensuing system of differential equations.

When seeking to solve the equations of elastostatics analytically, it is convenient to formulate the governing system of differential equations in terms of material point displacements, as it results in fewer unknown quantities to solve for. To accomplish this, constitutive relations relating stresses to measures of deformation (strain, ε_{ij}), and relations between these measures and material point displacements ($\vec{u}$), must first be introduced. Many approaches exist to develop the constitutive relations, with the most notable stemming from relations between the Helmholtz free energy and strain energy, with differentiation resulting in the general constitutive response. Since the development of constitutive relations is not the goal of this work, a simpler analogue will be discussed to introduce the concept.

For a continuous elastic material, the stresses and strains within the body are related through an analogue to Hooke's spring law, treating the material points as a series of interconnected springs. Instead of a spring extension/compression, and restorative force,

the deformation, or strain, is treated as an analogue to the extension/compression of the spring, with the analogue for the restorative force being the stress. In a similar manner to Hooke's law for springs, the two quantities are related to each other through constant values, analogous to the spring constant k. In particular, the constant values are stored in a rank 4 tensor, whose components are the elastic constants. In its most general form, Hooke's law can be written as

$$\sigma_{ij} = A_{ijkl}\varepsilon_{kl}, \tag{2.4.9}$$

where the components of the rank 4 tensor A_{ijkl} are represented by a matrix of 81 independent constants, representing the elastic properties of a given material. The symmetry of the stress tensor, obtained from equation (2.4.5) leads to many of these constants being dependent on each other, reducing the total number of independent constants to 21. Further symmetries can be exploited to reduce the remaining number of independent constants to the simplest case (2 independent constants), known as isotropic elasticity. In such a formulation, the material properties are the same in any given direction. To illustrate the necessary concepts, the isotropic case will be considered in the proceeding discussion.

Moreover, the components of strain can be related to the material point displacements ($\vec{u} = (u_1, u_2, u_3)$), through

$$\varepsilon_{ij} = \frac{1}{2}\left(u_{j,i} + u_{i,j}\right) \tag{2.4.10}$$

Taking all of these definitions into consideration, a system of 3 differential equations in terms of the 3 components of displacement can be developed. The simplest of these

systems is known as the Navier-Cauchy equations, which represent the aforementioned isotropic case, with two independent material constants (Lamé constants λ, μ). The Navier-Cauchy equations are

$$\mu u_{i,jj} + (\mu + \lambda) u_{j,ji} = 0, \tag{2.4.11}$$

where one would look to solve for the unknown displacement field. Measuring the Lamé constants directly through experiments is highly impractical. As a result, indirect measures relating the Lamé constants, known as engineering constants, are often measured instead. In the case of linear isotropic elasticity, these constants are known as Young's modulus ($E = \frac{\mu(3\lambda+2\mu)}{\lambda+\mu}$) and Poisson's ratio ($\nu = \frac{\lambda}{2(\lambda+\mu)}$).

With all the relevant governing equations in place, typical boundary value problems of elastostatics can be constructed.

Considering an isotropic, linear elastic body, in equilibrium, under the action of imposed tractions and displacements, the equilibrium equations can be formulated such that

$$\begin{aligned} \mu u_{i,jj} + (\mu + \lambda) u_{j,ji} &= 0 \\ \Rightarrow \underline{\boldsymbol{L}}\vec{\boldsymbol{u}} &= \vec{\boldsymbol{0}} \end{aligned} \tag{2.4.12}$$

where $\vec{\boldsymbol{u}} = (u_1, u_2, u_3)^T$ is the vector of unknown displacements to be solved for, $\vec{\boldsymbol{0}}$ is the 3×1 null matrix, and $\underline{\boldsymbol{L}}$ is the 3×3 matrix differential operator. Populating the appropriate vectors, the system of differential equations can be written as

$$\begin{bmatrix} \lambda\xi_1^2 & (\lambda+\mu)\,\xi_1\xi_2 & (\lambda+\mu)\,\xi_1\xi_3 \\ (\lambda+\mu)\,\xi_2\xi_1 & \lambda\xi_2^2 & (\lambda+\mu)\,\xi_2\xi_3 \\ (\lambda+\mu)\,\xi_3\xi_1 & (\lambda+\mu)\,\xi_3\xi_2 & \lambda\xi_3^2 \end{bmatrix} \begin{bmatrix} u_1 \\ u_2 \\ u_3 \end{bmatrix} = \begin{bmatrix} 0 \\ 0 \\ 0 \end{bmatrix} \tag{2.4.13}$$

where the quantities ξ_i correspond to the differentiation operation $\frac{\partial}{\partial x_i}$. It is important to note that the displacements are twice continuously differentiable, or C^2, which results in the order of the differentiation being interchangeable.

In addition to defining the differential operator, the tractions, through the boundary stress operator, must also be defined. Defining a unit outward normal to the body, $\vec{\boldsymbol{n}} = (n_1, n_2, n_3)^T$, we can write the stress vector acting on a surface element with unit normal $\vec{\boldsymbol{n}}$ as

$$t_j = \sigma_{ij} n_i \tag{2.4.14}$$

in which the stress components can be written in terms of displacements, to obtain the tractions in the form

$$\vec{\boldsymbol{t}} = \underline{\boldsymbol{T}}\vec{\boldsymbol{u}} \tag{2.4.15}$$

The populated boundary stress operator $\underline{\boldsymbol{T}}$ is

$$\underline{\boldsymbol{T}} = \begin{bmatrix} (2\mu+\lambda)\, n_1\xi_1 + \mu\,(n_2\xi_2 + n_3\xi_3) & \lambda n_1\xi_2 + \mu n_2\xi_1 & \lambda n_1\xi_3 + \mu n_3\xi_1 \\ \lambda n_2\xi_1 + \mu n_1\xi_2 & (2\mu+\lambda)\, n_2\xi_2 + \mu\,(n_1\xi_1 + n_3\xi_3) & \lambda n_2\xi_3 + \mu n_3\xi_2 \\ \lambda n_3\xi_1 + \mu n_1\xi_3 & \lambda n_3\xi_2 + \mu n_2\xi_3 & (2\mu+\lambda)\, n_3\xi_3 + \mu\,(n_1\xi_1 + n_2\xi_2) \end{bmatrix} \tag{2.4.16}$$

The boundary value problem can now be formulated, such that

$$\begin{aligned} \underline{\boldsymbol{L}}\vec{\boldsymbol{u}} &= \underline{\mathbf{0}} \quad \text{in } \Omega, \\ \vec{\boldsymbol{u}} &= \vec{\tilde{\boldsymbol{u}}} \quad \text{on } \partial\Omega_1, \\ \vec{\boldsymbol{t}} &= \vec{\tilde{\boldsymbol{t}}} \quad \text{on } \partial\Omega_2, \end{aligned} \tag{2.4.17}$$

where $\vec{\tilde{\boldsymbol{u}}}$ is the displacement vector, prescribed on the Dirichlet part of the boundary $\partial\Omega_1$, and $\vec{\tilde{\boldsymbol{t}}}$ is the traction vector, prescribed on the Neumann part of the boundary $\partial\Omega_2$.

Ideally, one would look to solve the system of differential equations analytically, to obtain an exact form of the solution. In some of the more complex cases where standard techniques fail, this is either impractical, or not possible. As such, numerical approximation techniques such as the Finite Element Method, or Boundary Element Method are employed to approximate the solution (weak solution) in the appropriate functional space, usually a Sobolev space. The governing equations and associated boundary value problems in this work will be solved numerically, and as such, approximate solution techniques will be discussed to frame the necessary context.

Solving such a system can be done in many ways, with the first step involving existence and uniqueness theorems, discussed at length by Payne and Knops [39], to prove that the

solution exists in the required functional space. In Chapter 4, this work aims to find weak solutions in the appropriate Sobolev space, so that the Finite Element Method can be employed. To prove that such a solution exists, the Lax-Milgram theorem, in conjunction with a proof of uniform ellipticity for the system (2.4.12) will be employed.

To show that the system (2.4.12) is uniformly elliptic, it is sufficient to prove that the matrix $\underline{\boldsymbol{L}}$, retaining only terms with higher order derivatives, is invertible for all $\xi_i \neq 0$ [40]. Since the matrix $\underline{\boldsymbol{L}}$ contains only higher order derivative terms, one can check for invertibility by considering its determinant, such that

$$det(\underline{\boldsymbol{L}}) = \mu^2 \left(3\lambda + 2\mu\right) \xi_1^2 \xi_2^2 \xi_3^2 \tag{2.4.18}$$

It is clear that in order to satisfy the condition for invertibility, and hence uniform ellipticity, that $\mu \neq 0$ and $(3\lambda + 2\mu) \neq 0$. To show that the elastic constants satisfy the required properties, one must look towards energy considerations.

One important restriction that must be placed on linear elastic systems is the requirement of positive strain energy. In the absence of dissipative forces, an elastic body will maintain conservation of energy. This means that forces acting on an elastic body will cause it to deform, with the deformation energy (known as strain energy) being stored in the body as elastic potential energy. Once the action of the forces is removed, the body will release the stored potential energy to return to its undeformed state. As such, to be a physically valid elastic medium, the strain energy stored within a body must be positive, or zero in the case of no deformation; the strain energy stored in an elastic body cannot be negative. This is an important requirement in elasticity theory, as it places restrictions on the elastic material constants, and aids in developing existence

and uniqueness theorems for the governing boundary value problems.

As such, one can refer to an important quantity in the field of elasticity theory, known as the internal energy density. For a general linear elastic body, the internal energy density at a point is given by

$$U_0 = \frac{1}{2}\sigma_{ij}\varepsilon_{ij} \tag{2.4.19}$$

Within the realm of isotropic, linear elasticity, equation (2.4.19) assumes a quadratic form, and is by definition positive definite. Through its positive-definiteness, restrictions on the Lamé constants are imposed, such that

$$\mu > 0, \qquad 2\mu + 3\lambda > 0 \tag{2.4.20}$$

With the above restrictions, one can now say that the invertibility condition is satisfied, and hence the system (2.4.12) is uniformly elliptic. With uniform ellipticity in place, one can now turn to the Lax-Milgram theorem to show that a unique solution to the boundary value problem exists in the Sobolev space $H^1(\Omega)$.

Using Theorems (2.3.2) and (2.3.3), and the fact that L is shown to be a uniformly elliptic operator, it follows that a unique solution to the boundary value problem (2.4.12) exists in the Sobolev space $H^1(\Omega)$.

Given that a unique solution exists in the Sobolev space $H^1(\Omega)$, one can now proceed to solve the system using the Finite Element Method.

2.5 Review of Cosserat Linear Elastostatics

Following the procedures outlined in Section 2.4, a brief introduction to Cosserat elasticity will be outlined.

In a similar manner to Section 2.4, temperature dependent effects will not be considered. Cosserat elasticity theory differs to classical elasticity as a result on one, fundamental assumption. Unlike the classical assumption in which a representative element within the material, with surface area dA_1, transfers internal loadings to a neighbouring element, with surface area dA_2, through the action of forces, Cosserat elasticity also assumes that internal loads are transferred through the action of moments (Figure 2.8). This transfer of forces results in the definition of a stress tensor, with components σ_{ij}, and a couple-stress tensor, with components μ_{ij}. Whereas in the classical case the transfer of loads between elements gives rise to material point displacements, the transfer of loads through moments in the case of Cosserat elasticity gives rise to material point rotations/orientations, known as microrotations ($\vec{\boldsymbol{\varphi}}$), which are kinematically independent from displacements. These microrotations give rise to another deformation measure called twist, which can be viewed as a rotational analogue to classical strain measures. It is important to note however that twists are kinematically independent to strains.

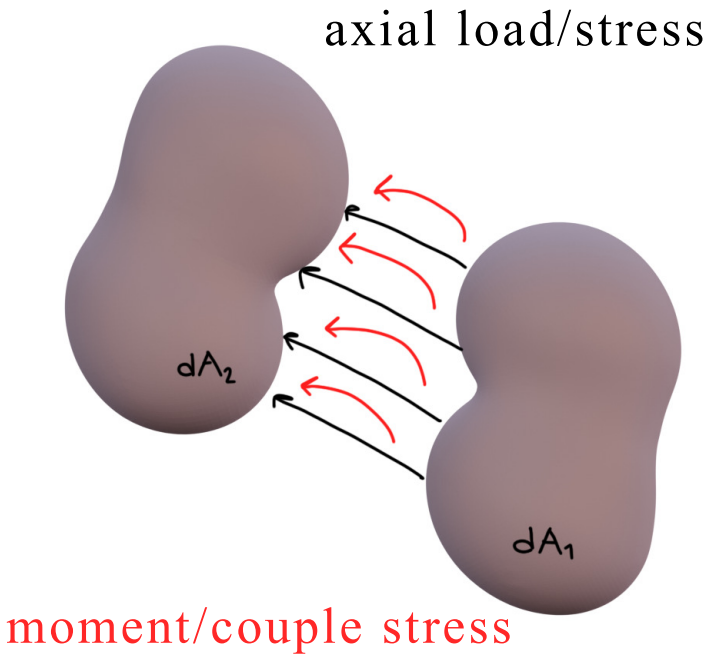

Figure 2.8: Internal transfer of loads between neighbouring continuum elements, Cosserat elasticity

In the three-dimensional case, both the stress, and couple-stress, tensors hold nine components in Cartesian coordinates. Each component of the tensors acts in a cardinal Cartesian direction, on a Cartesian plane projected from the element's volume, dV. Figure 2.9 illustrates the nine different stress, and couple-stress components.

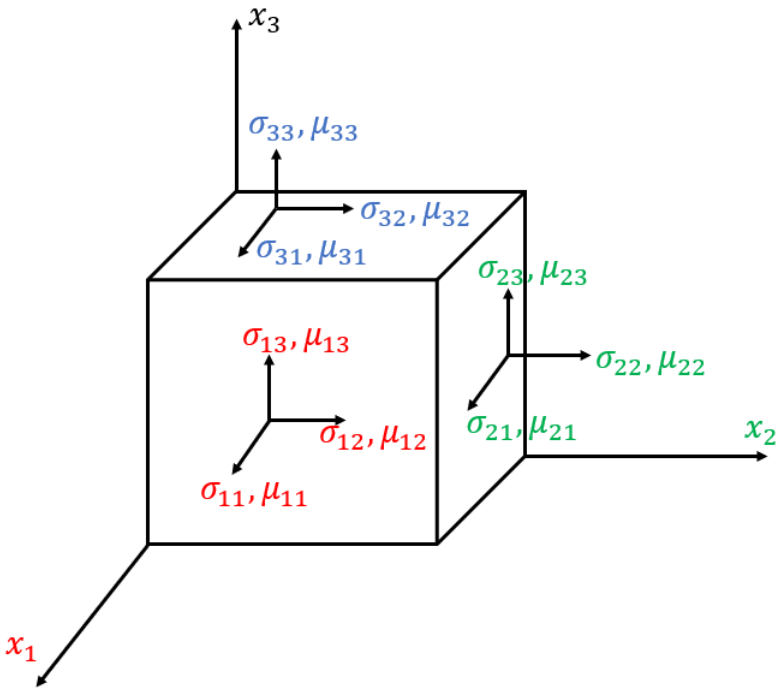

Figure 2.9: Stress/Couple-stress tensor components in Cartesian coordinates

The resulting tensor components can be represented in matrix form by

$$\sigma_{ij} = \begin{bmatrix} \sigma_{11} & \sigma_{12} & \sigma_{13} \\ \sigma_{21} & \sigma_{22} & \sigma_{23} \\ \sigma_{31} & \sigma_{32} & \sigma_{33} \end{bmatrix}, \tag{2.5.1}$$

$$\mu_{ij} = \begin{bmatrix} \mu_{11} & \mu_{12} & \mu_{13} \\ \mu_{21} & \mu_{22} & \mu_{23} \\ \mu_{31} & \mu_{32} & \mu_{33} \end{bmatrix}, \tag{2.5.2}$$

In conjunction with external body force densities and moments respectively,
$\vec{\boldsymbol{X}} = (X_1, X_2, X_3)^T$ (force per unit volume) and $\vec{\boldsymbol{Y}} = (Y_1, Y_2, Y_3)^T$ (moment per unit

volume), present on a continuum point, and the transfer of loads depicted in Figure 2.8, one can turn to equilibrium equations to analyse the mechanics of a continuum point. As in Section 2.4, temperature dependent effects will not be considered.

To remove the temperature dependence, the following assumptions are made

- Assume no heat sources in body
- Assume no heat flow from exterior
- Slow internal heat exchange during deformation (adiabatic)

In contrast to the Hookean analogy used to obtain the constitutive response in Section 2.4, this section will follow the energetic approach used by Eringen [42, 43] to develop the constitutive equations, along with the assumption of material frame-indifference, where microrotation of a material point is considered as rigid only, and not constrained to macro rotation at that point.

For such a system, Eringen considers conservation of energy through the contributions of elastic potential, and kinetic energy. From conservation of energy over an entire body, one can obtain

$$\frac{d}{dt}\left(\mathcal{U}+\mathcal{K}\right)=\mathcal{L}+\dot{\mathcal{Q}} \tag{2.5.3}$$

where ($\mathcal{U}$ is the internal energy, $\mathcal{K}$ is the kinetic energy, $=\mathcal{L}$ is the power of external forces, $\mathcal{Q}$ is the non-mechanical power. Under the assumptions stated above, equation (2.5.3) reduces to

$$\frac{d}{dt}\left(\mathcal{U}+\mathcal{K}\right)=\mathcal{L}, \tag{2.5.4}$$

where at a given material point, the internal energy density rate (internal energy per unit volume, per unit time) is given by

$$\dot{U}_0 = \sigma_{ji}\dot{\gamma_{ji}} + \mu_{ji}\dot{\varkappa_{ji}} \tag{2.5.5}$$

The above energy density rate defines σ_{ji} as the components of the stress tensor, γ_{ji} as the components of the strain tensor (different from the classical equivalent due to the inclusion of microrotations), μ_{ji} as the components of the couple stress tensor, $\varkappa_{ji}$ as the components of the twist tensor (local rotational equivalent to strain), with time differentiation denoted by the overhead dot.

Expanding $U_0\left(\gamma_{ji}, \varkappa_{ji}\right)$ into a McLaurin series about the undeformed state ($\gamma_{ji}, \varkappa_{ji} = 0$), one obtains

$$\begin{aligned} U_0\left(\gamma_{ji}, \varkappa_{ji}\right) =& U_0^* + \left(\frac{\partial U_0}{\partial \gamma_{ji}}\right)_0 \gamma_{ji} + \left(\frac{\partial U_0}{\partial \varkappa_{ji}}\right)_0 \varkappa_{ji} \\ &+ \frac{1}{2}\left[\left(\frac{\partial^2 U_0}{\partial \gamma_{ji}\partial \gamma_{kl}}\right)_0 \gamma_{ji}\gamma_{kl} + 2\left(\frac{\partial^2 U_0}{\partial \gamma_{ji}\partial \varkappa_{kl}}\right)_0 \gamma_{ji}\varkappa_{kl} + \left(\frac{\partial^2 U_0}{\partial \varkappa_{ji}\partial \gamma_{kl}}\right)_0 \varkappa_{ji}\varkappa_{kl}\right] \\ &+ \textit{higher order terms} \end{aligned} \tag{2.5.6}$$

To constrain the system to fall under small deformation theory (linear elasticity), higher order terms are neglected, thus considering only small strains. The internal energy

density therefore reduces to

$$U_0\left(\gamma_{ji},\varkappa_{ji}\right)\approx U_0^*+\left(\frac{\partial U_0}{\partial\gamma_{ji}}\right)_0\gamma_{ji}+\left(\frac{\partial U_0}{\partial\varkappa_{ji}}\right)_0\varkappa_{ji} \\ +\frac{1}{2}\left[\left(\frac{\partial^2U_0}{\partial\gamma_{ji}\partial\gamma_{kl}}\right)_0\gamma_{ji}\gamma_{kl}+2\left(\frac{\partial^2U_0}{\partial\gamma_{ji}\partial\varkappa_{kl}}\right)_0\gamma_{ji}\varkappa_{kl}+\left(\frac{\partial^2U_0}{\partial\varkappa_{ji}\partial\gamma_{kl}}\right)_0\varkappa_{ji}\varkappa_{kl}\right] \tag{2.5.7}$$

Under the framework of linear elasticity, strains must be linear, so the following quantities can be defined

$$\sigma_{ji}=\frac{\partial U_0}{\partial\gamma_{ji}}, \tag{2.5.8}$$

$$\mu_{ji}=\frac{\partial U_0}{\partial\varkappa_{ji}} \tag{2.5.9}$$

Differentiating equation (2.5.7) with respect to strains and twists respectively, to obtain expressions for stress and couple stress corresponding to equations (2.5.8), (2.5.9), one obtains

$$\sigma_{ji}=\left(\frac{\partial U_0}{\partial\gamma_{ji}}\right)_0+\frac{1}{2}\left(\frac{\partial^2U_0}{\partial\gamma_{ji}\partial\gamma_{kl}}\right)_0\gamma_{kl}+\left(\frac{\partial^2U_0}{\partial\gamma_{ji}\partial\varkappa_{kl}}\right)_0\varkappa_{kl} \tag{2.5.10}$$

$$\mu_{ji}=\left(\frac{\partial U_0}{\partial\varkappa_{ji}}\right)_0+\frac{1}{2}\left(\frac{\partial^2U_0}{\partial\varkappa_{ji}\partial\varkappa_{kl}}\right)_0\varkappa_{kl}+\left(\frac{\partial^2U_0}{\partial\gamma_{ji}\partial\varkappa_{kl}}\right)_0\gamma_{ji} \tag{2.5.11}$$

To ensure that the stress and couple stress components vanish when deformation vanishes, the conditions that $\sigma_{ji},\mu_{ji}=0$ at $\gamma_{ji},\varkappa_{ji}=0$ can be imposed, resulting in

$$\left(\frac{\partial U_0}{\partial\gamma_{ji}}\right)_0,\left(\frac{\partial U_0}{\partial\varkappa_{ji}}\right)_0=0 \tag{2.5.12}$$

Without loss of generality, one can also impose $U_0^* = 0$, yielding

$$\sigma_{ji} = \frac{1}{2}\left(\frac{\partial^2 U_0}{\partial\gamma_{ji}\partial\gamma_{kl}}\right)_0 \gamma_{kl} + \left(\frac{\partial^2 U_0}{\partial\gamma_{ji}\partial\varkappa_{kl}}\right)_0 \varkappa_{kl} \tag{2.5.13}$$

$$\mu_{ji} = \frac{1}{2}\left(\frac{\partial^2 U_0}{\partial\varkappa_{ji}\partial\varkappa_{kl}}\right)_0 \varkappa_{kl} + \left(\frac{\partial^2 U_0}{\partial\gamma_{ji}\partial\varkappa_{kl}}\right)_0 \gamma_{ji} \tag{2.5.14}$$

The following tensors can now be introduced, with components

$$\frac{\partial^2 U_0}{\partial\gamma_{ji}\partial\gamma_{kl}} = a_{jikl}, \tag{2.5.15}$$

$$\frac{\partial^2 U_0}{\partial\gamma_{ji}\partial\varkappa_{kl}} = b_{jikl}, \tag{2.5.16}$$

$$\frac{\partial^2 U_0}{\partial\varkappa_{ji}\partial\varkappa_{kl}} = c_{jikl} \tag{2.5.17}$$

The expression for the internal energy density now reduces to

$$U_0\left(\gamma_{ji}, \varkappa_{ji}\right) = \frac{1}{2}a_{jikl}\gamma_{ji}\gamma_{kl} + b_{jikl}\gamma_{ji}\varkappa_{kl} + \frac{1}{2}c_{jikl}\varkappa_{ji}\varkappa_{kl} \tag{2.5.18}$$

The form of equation (2.5.18) implies symmetry conditions for the tensors with components a_{jikl} and c_{jikl} respectively [44], such that

$$a_{jikl} = a_{klij}, \quad c_{jikl} = c_{klij}$$

$$\Rightarrow \sigma_{ji} = \frac{1}{2}a_{jikl}\gamma_{kl} + b_{jikl}\varkappa_{kl} \tag{2.5.19}$$

$$\mu_{ji} = \frac{1}{2}c_{jikl}\varkappa_{kl} + b_{jikl}\gamma_{ji} \tag{2.5.20}$$

Absorbing the $\frac{1}{2}$ into the constants and relabelling the indices '$ji \to kl$' and '$kl \to ji$' in the tensor b_{jikl}, one obtains the constitutive law (Eringen's law) for a general anisotropic

medium

$$\sigma_{ji} = a_{jikl}\gamma_{kl} + b_{jikl}\varkappa_{kl} \tag{2.5.21}$$

$$\mu_{ji} = b_{klij}\gamma_{kl} + c_{jikl}\varkappa_{kl} \tag{2.5.22}$$

The rank 4 tensors with components $a_{ijkl}, b_{ijkl}, c_{ijkl}$ are represented by matrices each containing 81 independent constants, representing the elastic properties of a given material. This general form will be the starting point for the work conducted in Chapter 3.

Chapter 4 will however consider an isotropic medium with central symmetry, which leads to $b_{ijkl} = 0$. In such a case, the constitutive relations reduce to

$$\sigma_{ji} = a_{jikl}\gamma_{kl} \tag{2.5.23}$$

$$\mu_{ji} = c_{jikl}\varkappa_{kl} \tag{2.5.24}$$

Furthermore, exploiting the symmetries arising from the isotropic case, where a_{ijkl} and c_{ijkl} retain the same values in each coordinate system, the tensors assume the form of a general isotropic tensor of rank 4

$$a_{jikl} = (\mu + \alpha)\,\delta_{jk}\delta_{il} + (\mu - \alpha)\,\delta_{jl}\delta_{ik} + \lambda\delta_{ji}\delta_{kl} \tag{2.5.25}$$

$$c_{jikl} = (\gamma + \varepsilon)\,\delta_{jk}\delta_{il} + (\gamma - \varepsilon)\,\delta_{jl}\delta_{ik} + \beta\delta_{ji}\delta_{kl} \tag{2.5.26}$$

where $\mu, \lambda, \alpha, \beta, \gamma,\ \varepsilon$ are adiabatic constants.

Applying the isotropic tensors to the expression for internal energy density yields

$$U_0 = \frac{\mu+\alpha}{2}\gamma_{ji}\gamma_{ji} + \frac{\mu-\alpha}{2}\gamma_{ji}\gamma_{ij} + \frac{1}{2}\lambda\gamma_{kk}\gamma_{nn} + \frac{\gamma+\varepsilon}{2}\varkappa_{ji}\varkappa_{ji} + \frac{\gamma-\varepsilon}{2}\varkappa_{ji}\varkappa_{ij} + \frac{1}{2}\beta\varkappa_{kk}\varkappa_{nn} \tag{2.5.27}$$

Applying the isotropic tensors to equations (2.5.23) and (2.5.24) yields

$$\sigma_{ji} = \left[(\mu+\alpha)\,\delta_{jk}\delta_{il} + (\mu-\alpha)\,\delta_{jl}\delta_{ik} + \lambda\delta_{ji}\delta_{kl}\right]\gamma_{kl} \tag{2.5.28}$$

$$\mu_{ji} = \left[(\gamma+\varepsilon)\,\delta_{jk}\delta_{il} + (\gamma-\varepsilon)\,\delta_{jl}\delta_{ik} + \beta\delta_{ji}\delta_{kl}\right]\varkappa_{kl} \tag{2.5.29}$$

from which the final form for a linear isotropic Cosserat medium can be obtained.

$$\sigma_{ji} = (\mu+\alpha)\,\gamma_{ji} + (\mu-\alpha)\,\gamma_{ij} + \lambda\delta_{ji}\gamma_{kk} \tag{2.5.30}$$

$$\mu_{ji} = (\gamma+\varepsilon)\,\varkappa_{ji} + (\gamma-\varepsilon)\,\varkappa_{ij} + \beta\delta_{ji}\varkappa_{kk} \tag{2.5.31}$$

Equipped with constitutive relations, the deformation-displacement relations, as well as the equilibrium equations, must be formulated.

Starting with the definitions for strain and twist respectively, the tensor components take the form

$$\gamma_{ji} = u_{i,j} - \varepsilon_{kji}\varphi_k \tag{2.5.32}$$

$$\varkappa_{ji} = \varphi_{i,j} \tag{2.5.33}$$

The elastostatic equilibrium equations take a similar form to the classical case, with the difference arising in the balance of moments, where the effect of couple stresses takes

hold. The equilibrium equations for force and moment are, respectively,

$$\sigma_{ji,j} + X_i = 0, \tag{2.5.34}$$

$$\epsilon_{ijk}\sigma_{jk} + \mu_{ji,j} + Y_i = 0, \tag{2.5.35}$$

It is important to note that unlike the classical case, the moment equilibrium equations do not introduce symmetry to the stress tensor; this is a consequence of the presence of the couple stress tensor in the equation. As such, the stress, couple stress, strain, and twist tensors each contain 9 independent components.

Finally, analogously to the classical case, certain engineering constants can be obtained by relating the elastic constants to each other. The constants [45] are

$$\Psi = \frac{2\gamma}{2\gamma + \beta} \tag{2.5.36}$$

$$N = \sqrt{\frac{\alpha}{\mu + \alpha}} \tag{2.5.37}$$

$$l_b = \sqrt{\frac{\gamma + \varepsilon}{4\mu}} \tag{2.5.38}$$

$$l_t = \sqrt{\frac{\gamma}{\mu}} \tag{2.5.39}$$

$$E = \frac{\mu\left(3\lambda + 2\mu\right)}{\lambda + \mu} \tag{2.5.40}$$

$$\nu = \frac{\lambda}{2\left(\lambda + \mu\right)} \tag{2.5.41}$$

where E and ν are the well-known Young's modulus and Poisson's ratio, $N \in [0, 1]$ is the coupling number, $\Psi \in [0, \frac{3}{2}]$ is the polar ratio, and $l_b, l_t \geq 0$ are the characteristic lengths in bending and torsion, respectively.

Chapter 3

Modelling Fiber Reinforced Polymers with Unidirectional Fibers

Fiber Reinforced Polymers (FRPs) are becoming more prevalent in their use as internal reinforcement in concrete structures [46, 47]. Their high tensile strength, combined with their corrosion resistance places them as a viable alternative to traditional steel reinforcement [48, 49, 50, 51, 52].

For most practical applications in which FRPs are used as internal reinforcement to concrete, the reinforcing bars consist of a polymer resin matrix, with unidirectional fibers as reinforcement. Since the main purpose of concrete reinforcement is to carry tensile loads, it is sufficient to have the reinforcing bars be unidirectional in their tensile carrying capabilities. As such, FRPs can be characterized as transversely isotropic materials, with the unidirectional fibers representing the axis normal to the isotropic plane (Figure 3.1). With regards to classes of isotropy, transversely isotropic materials are a sub class of orthotropic materials, in which the material properties are symmetric about an axis that

is normal to a plane of isotropy. Furthermore, FRPs can be considered heterogeneous materials, due to their composite microstructure (polymer resin with fiber reinforcement). In this chapter, FRPs are modelled using the framework of Cosserat elasticity.

Several approaches exist to model heterogeneous Cosserat materials, including asymptotic expansion/perturbation methods [53, 54, 55, 56], and material symmetry group approaches [57]. In contrast to the aforementioned approaches, this work begins with a homogenized, transversely isotropic continuum, and introduces a two-scale displacement field to obtain the anisotropic material constants in terms of the constituent properties. The approach considered utilizes the homogenization procedure outlined by Wang and Pindera [58, 59] to obtain a homogeneous continuum comprised of unidirectional fibers and polymer matrix. The objective of this work is to develop (but not solve) a boundary value problem for the composite, for eventual use in the analysis of structures. Solving the boundary value problem depends on measurement of the homogenized elastic constants for a transversely isotropic material, which is outside of the scope of this work.

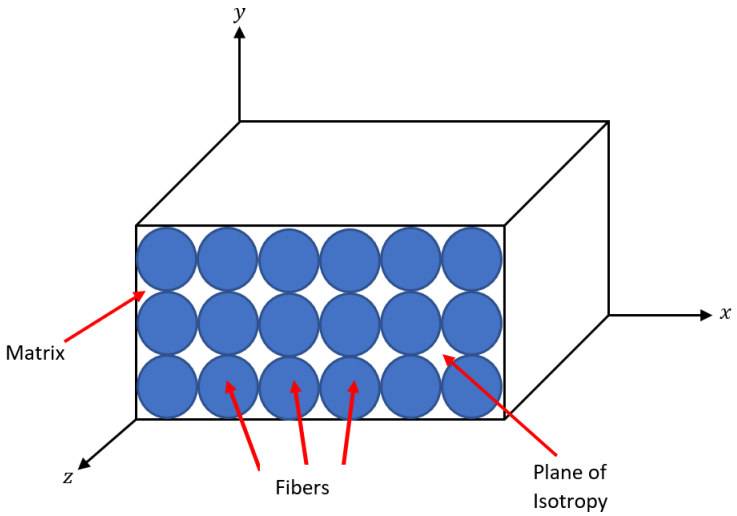

Figure 3.1: Transversely isotropic FRP

3.1 Constitutive Formulation - Transversely Isotropic Case

Since transversely isotropic materials exhibit symmetries in their material properties, one can exploit the symmetries to reduce the number of independent elastic material constants in the general Cosserat elasticity formulation. Mathematically, this can be accomplished by recognizing that elastic matrices containing the elastic material constants is invariant under certain coordinate transformations (planes/axes of symmetry).

By applying specific coordinate transformations to the constitutive equations, and equating the transformed and untransformed stresses, one can obtain a system of equations in terms of the elastic constants. The solution of the resulting equations will identify the dependent constants, thereby simplifying the elastic matrices to a form in which only independent material constants remain.

The development of the boundary value problem begins with establishing the constitutive law for a transversely isotropic material. Starting with the general, anisotropic form of Eringen's law (equations (2.5.21) and (2.5.22)) [42, 43],

$$\begin{cases} \sigma_{ij} = A_{ijkl}\gamma_{kl} + B_{ijkl}\varkappa_{kl} \\ \mu_{ij} = B_{klij}\gamma_{kl} + C_{ijkl}\varkappa_{kl}, \end{cases}$$

the symmetries can be modelled by implementing the following coordinate transformations independently. Taking the z-axis as the axis of the fibers, the plane of isotropy is the x-y plane.

First, the coordinate transformation (90° counterclockwise rotation about the z-axis, Figure 3.2)

$$\begin{aligned} x' &= y \\ y' &= -x \\ z' &= z \end{aligned} \tag{3.1.1}$$

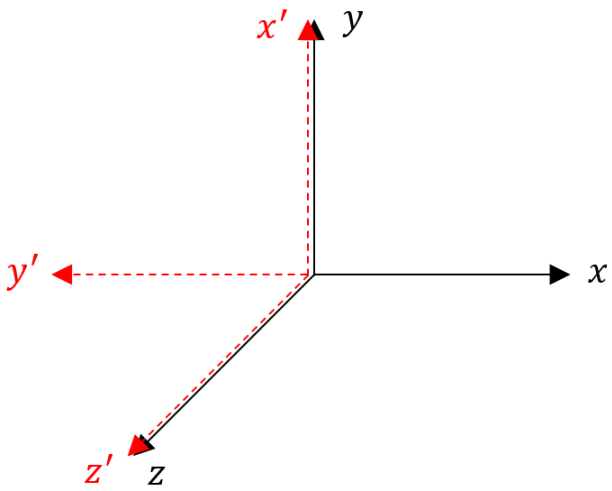

Figure 3.2: 90° counterclockwise rotation about the z-axis

is applied, where the z coordinate represents the the axis normal to the plane of isotropy. The transformation of the stress tensor, in column vector form, is shown below.

$$\vec{\boldsymbol{\sigma}} = \begin{bmatrix} \sigma_{11} \\ \sigma_{12} \\ \sigma_{13} \\ \sigma_{21} \\ \sigma_{22} \\ \sigma_{23} \\ \sigma_{31} \\ \sigma_{32} \\ \sigma_{33} \end{bmatrix}, \vec{\boldsymbol{\sigma'}} = \begin{bmatrix} \sigma_{22} \\ -\sigma_{21} \\ \sigma_{23} \\ -\sigma_{12} \\ \sigma_{11} \\ -\sigma_{13} \\ \sigma_{32} \\ -\sigma_{31} \\ \sigma_{33} \end{bmatrix} \tag{3.1.2}$$

The transformations for $\vec{\boldsymbol{\mu}}, \vec{\boldsymbol{\gamma}}$, and $\vec{\boldsymbol{\varkappa}}$ are identical. These transformed quantities are then substituted into the constitutive law. The corresponding quantities are equated (i.e. $\sigma_{11} = \sigma'_{11} = \sigma_{22}$) and written in terms of the deformations. A system of equations is then extracted by comparing the coefficients of the corresponding deformations on the left and right hand sides of the equation, preserving the required symmetries.

Next, the coordinate transformation (45° counterclockwise rotation about the z-axis, Figure 3.3)

$$\begin{aligned} x' &= \frac{x+y}{\sqrt{2}} \\ y' &= \frac{y-x}{\sqrt{2}} \\ z' &= z \end{aligned} \tag{3.1.3}$$

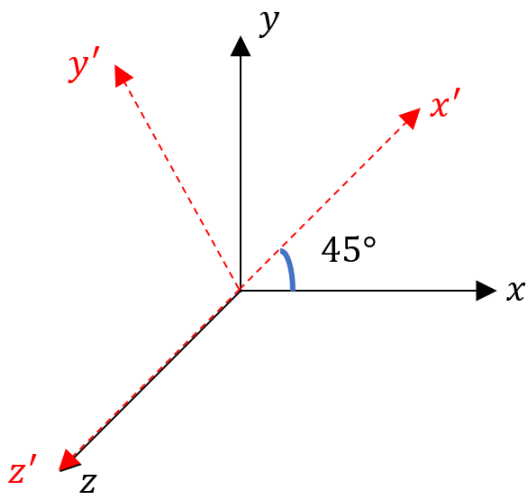

Figure 3.3: 45° counterclockwise rotation about the z-axis

is applied. The transformed stresses (and similarly, couple stresses and deformations) are

$$\vec{\boldsymbol{\sigma}'} = \begin{bmatrix} \frac{1}{2}(\sigma_{11} + \sigma_{12} + \sigma_{21} + \sigma_{22}) \\ \frac{1}{2}(-\sigma_{11} + \sigma_{12} - \sigma_{21} + \sigma_{22}) \\ \frac{1}{\sqrt{2}}(\sigma_{13} + \sigma_{23}) \\ \frac{1}{2}(-\sigma_{11} - \sigma_{12} + \sigma_{21} + \sigma_{22}) \\ \frac{1}{2}(\sigma_{11} - \sigma_{12} - \sigma_{21} + \sigma_{22}) \\ \frac{1}{\sqrt{2}}(-\sigma_{13} + \sigma_{23}) \\ \frac{1}{\sqrt{2}}(\sigma_{31} + \sigma_{32}) \\ \frac{1}{\sqrt{2}}(-\sigma_{31} + \sigma_{32}) \\ \sigma_{33} \end{bmatrix} \tag{3.1.4}$$

Once more, the symmetry of the tensors allows another set of equations, in terms of the elasticity constants, to be extracted.

By applying the two rotations, symmetries establishing the isotropic nature of the x-y

plane are established, while preserving the independent properties along the z-axis.

The resulting system of equations yields an over-constrained system of 648 equations. These equations are input into Maple, and solved to produce expressions for the remaining independent constants. The final (reduced) elasticity tensor components $A_{ijkl}, B_{ijkl}, C_{ijkl}$ are presented on the following pages. The resulting elastic matrices give rise to stress-deformation, and couple stress-deformation relationships through Eringen's law, and ultimately stress-displacement/microrotation, and couple stress-displacement/microrotation relations that define the governing differential equations.

$$\mathbf{A_{ijkl}} = \begin{bmatrix} A_{2222} & -A_{2221} & 0 & -A_{2212} & A_{2211} & 0 & 0 & 0 & A_{2233} \\ -A_{2122} & A_{2121} & 0 & -A_{2121} - A_{2211} + A_{2222} & -A_{2122} - A_{2212} - A_{2221} & 0 & 0 & 0 & -A_{2133} \\ 0 & 0 & A_{2323} & 0 & 0 & -A_{2313} & 0 & -A_{2331} & 0 \\ A_{2122} + A_{2212} + A_{2221} & -A_{2121} - A_{2211} + A_{2222} & 0 & A_{2121} & A_{2122} & 0 & 0 & 0 & A_{2133} \\ A_{2211} & A_{2212} & 0 & A_{2221} & A_{2222} & 0 & 0 & 0 & A_{2233} \\ 0 & 0 & A_{2313} & 0 & 0 & A_{2323} & A_{2331} & 0 & 0 \\ 0 & 0 & A_{3223} & 0 & 0 & -A_{3213} & A_{3232} & -A_{3231} & 0 \\ 0 & 0 & A_{3213} & 0 & 0 & A_{3223} & A_{3231} & A_{3232} & 0 \\ A_{3322} & -A_{3321} & 0 & A_{3321} & A_{3322} & 0 & 0 & 0 & A_{3333} \end{bmatrix}, \quad (58)$$

$$\mathbf{B_{ijkl}} = \begin{bmatrix} B_{2222} & -B_{2221} & 0 & -B_{2212} & -2B_{2212}+B_{2222} & 0 & 0 & 0 & B_{2233} \\ -B_{2122} & B_{2212} & 0 & B_{2212} & -B_{2122}-B_{2212}-B_{2221} & 0 & 0 & 0 & -B_{2133} \\ 0 & 0 & B_{2323} & 0 & 0 & -B_{2313} & 0 & -B_{2331} & 0 \\ B_{2122}+B_{2212}+B_{2221} & B_{2212} & 0 & B_{2212} & B_{2122} & 0 & 0 & 0 & B_{2133} \\ -2B_{2212}+B_{2222} & B_{2212} & 0 & B_{2221} & B_{2222} & 0 & 0 & 0 & B_{2233} \\ 0 & 0 & B_{2313} & 0 & 0 & B_{2323} & B_{2331} & 0 & 0 \\ 0 & 0 & B_{3223} & 0 & 0 & -B_{3213} & B_{3232} & -B_{3231} & 0 \\ 0 & 0 & B_{3213} & 0 & 0 & B_{3223} & B_{3231} & B_{3232} & 0 \\ B_{3322} & -B_{3321} & 0 & B_{3321} & B_{3322} & 0 & 0 & 0 & B_{3333} \end{bmatrix}, \tag{59}$$

$$\mathbf{C_{ijkl}} = \begin{bmatrix} C_{2222} & -C_{2221} & 0 & -C_{2212} & C_{2211} & 0 & 0 & 0 & C_{2233} \\ -C_{2122} & -\frac{1}{2}C_{2211} + \frac{1}{2}C_{2222} & 0 & -\frac{1}{2}C_{2211} + \frac{1}{2}C_{2222} & -C_{2122} - C_{2212} - C_{2221} & 0 & 0 & 0 & -C_{2133} \\ 0 & 0 & C_{2323} & 0 & 0 & -C_{2313} & C_{2332} & -C_{2331} & 0 \\ C_{2122} + C_{2212} + C_{2221} & -\frac{1}{2}C_{2211} + \frac{1}{2}C_{2222} & 0 & -\frac{1}{2}C_{2211} + \frac{1}{2}C_{2222} & C_{2122} & 0 & 0 & 0 & C_{2133} \\ C_{2211} & C_{2212} & 0 & C_{2221} & C_{2222} & 0 & 0 & 0 & C_{2233} \\ 0 & 0 & C_{2313} & 0 & 0 & C_{2323} & C_{2331} & C_{2332} & 0 \\ 0 & 0 & C_{3223} & 0 & 0 & -C_{3213} & C_{3232} & -C_{3231} & 0 \\ 0 & 0 & C_{3213} & 0 & 0 & C_{3223} & C_{3231} & C_{3232} & 0 \\ C_{3322} & -C_{3321} & 0 & C_{3321} & C_{3322} & 0 & 0 & 0 & C_{3333} \end{bmatrix}, \tag{60}$$

3.2 Homogenization Procedure

With the generalized constitutive law obtained in the form of the transversely isotropic elastic tensors, one can proceed with a discussion on homogenization of the representative volume element. The proposed homogenization approach will follow the scheme presented by Wang and Pindera [58] for a structure with hexagonal periodicity and transversely isotropic phases. The theory employs a Fourier series representation for the displacement fields in the fiber and matrix phases (2 scale displacement field used) in the cylindrical coordinate system that satisfies the equilibrium equations and continuity conditions in the unit cell's interior.

The approach relies on developing boundary conditions using a variational principle and the governing balance laws. This principle plays a key role in the employed unit cell solution, ensuring rapid convergence of the Fourier series coefficients with relatively few harmonic terms, yielding converged homogenized moduli and local stress fields with little computational effort.

The scheme presented by Wang and Pindera [58] for the homogenization of a fiber reinforced composite is outlined below. A hexagonal representative unit cell is used to model the micromechanical problem and relate the solution to the overall behaviour of the solid. The model for the hexagonal representative unit cell depicting the microstructure is shown in Figure 3.4.

The problem defines the global x_3 direction to be along the axis of the bar, with the x_1 and x_2 directions representing the horizontal and vertical axes respectively. Figure 3.4 shows the arbitrary location of the fiber within the unit cell, reinforcing the robustness of the approach with respect to fiber placement. The local coordinates of the fiber are y_1

and y_2, representing the horizontal and vertical axes respectively. The boundary of the unit cell is split into the six surfaces of the hexagon, labelled S_i, where $i = 1, 2, ..6$. The unit cell is loaded by homogenized strain components $\overline{\epsilon_{ij}}$.

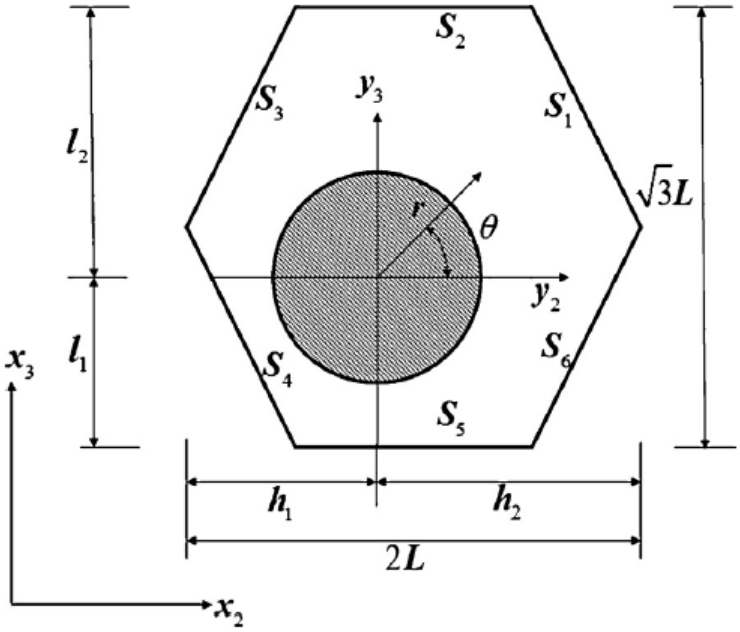

Figure 3.4: Hexagonal representative unit cell for a fiber reinforced composite [59]

3.3 Boundary Conditions

Section 3.3.1 outlines the procedure used by Wang and Pindera [58] to obtain the boundary condition for the classical case, with the extension to the Cosserat case presented in Section 3.3.2.

3.3.1 Classical Approach

The surface traction and displacement/rotation boundary conditions are defined as

$$\begin{cases} u_i = u_i^\circ, & \text{on } S_U \\ t_i = t_i^\circ, & \text{on } S_T \end{cases} \tag{3.3.1}$$

where u_i are the components of displacement within the unit cell, t_i are the components of the surface traction, and

$$\begin{cases} S_U \cup S_T = S & \text{, and} \\ S_U \cap S_T = \emptyset \end{cases} \tag{3.3.2}$$

The periodicity condition relates the tractions on different parts of the surface as follows

$$t_i(\vec{x_o} + \vec{d}) = -t_i(\vec{x_o}), \text{where } (\vec{x_o}, \vec{x_o} + \vec{d}) \in S \tag{3.3.3}$$

The most important boundary condition, which plays a key role in solving the unit cell problem, as well as relating the interior problem to the exterior problem is constructed using a variational principle. The energy functional proposed by Wang and Pindera [59] (labelled H_{D-P}) measures the difference in the deformation energy of the unit cell to the energy of the traction conditions of the surface S.

The energy functional proposed by Wang and Pindera is presented below; it considers the classical deformation measure (strain, with components ϵ_{ij}).

$$H_{D-P} = \frac{1}{2}\int_V \sigma_{ij}\epsilon_{ij}dV - \int_{S_U} t_i u_i^{\circ} dS - \int_{S_T} t_i^{\circ} u_i dS \tag{3.3.4}$$

The goal is to minimize the functional, thereby obtaining a boundary condition that satisfies the constraints of the unit cell and considers the periodicity of the problem. This follows from the principle of stationary total potential energy, which states that the function that extremizes the total potential energy will be one that satisfies equilibrium [61, 62, 63, 64]. That is to say, of the kinematically admissible solution states, the one that is required must satisfy the equilibrium equations and boundary conditions. As such, the required state must minimize the potential energy functional at stable equilibrium. Minimizing the functional consists of two parts. First, the first variation of the functional must vanish, thereby obtaining an extrememum of the functional. Next, the second variation must be shown to be non-negative, establishing the obtained extremum as a minimum.

To obtain the variation of a functional $F(\vec{x})$, one introduces the perturbation $\varepsilon\vec{x}$, with ε small, to the input of the functional, and constructs the Taylor expansion, such that

$$\delta F(\vec{x}) = F(\vec{x} + \varepsilon\vec{x}) - F(\vec{x}) \tag{3.3.5}$$

with

$$F(\vec{x} + \varepsilon\vec{x}) = F(\vec{x}) + \left.\frac{dF(\vec{x} + \varepsilon\vec{x})}{d\varepsilon}\right|_{\varepsilon=0} \varepsilon + \left.\frac{d^2F(\vec{x} + \varepsilon\vec{x})}{d\varepsilon^2}\right|_{\varepsilon=0} \varepsilon^2 + O(\varepsilon^3) \tag{3.3.6}$$

Considering the Taylor expansion, one can generalize the notion of derivatives to functionals.

To obtain the necessary variational terms, the following transformation will be required.

$$\begin{aligned}
\int_V \sigma_{ij}\epsilon_{ij}dV &= \int_V \sigma_{ij}(\frac{1}{2}u_{i,j} + \frac{1}{2}u_{j,i})dV \\
&= \int_V (\frac{1}{2}\sigma_{ij}u_{i,j} + \frac{1}{2}\sigma_{ij}u_{j,i})dV \\
&= \int_V (\frac{1}{2}\sigma_{ij}u_{i,j} + \frac{1}{2}\sigma_{ji}u_{j,i})dV, && \text{since } \sigma_{ji} = \sigma_{ij} \\
&= \int_V \sigma_{ij}u_{i,j}dV \\
&= \int_V \sigma_{ij}\frac{\partial u_i}{\partial x_j}dV \\
&= \int_V (\frac{\partial(\sigma_{ij}u_i)}{\partial x_j} - \frac{\partial\sigma_{ij}}{\partial x_j}u_i)dV \\
&= \int_V \frac{\partial\sigma_{ij}u_i}{\partial x_j}dV, && \text{since } \sigma_{ij,j} = 0 \\
&= \int_S (\sigma_{ij}u_i)n_j dS, && \text{by the Divergence theorem} \\
&= \int_S t_i u_i dS
\end{aligned}$$

This transformation leads to the expansion

$$\begin{aligned}\delta H_{D-P} &= H_{D-P}(u_i + \varepsilon u_i, t_i + \varepsilon t_i) - H_{D-P}(u_i, t_i) \\ &= \varepsilon[\int_{S_U} t_i(u_i - u_i^\circ)dS + \int_{S_T} u_i(t_i - t_i^\circ)dS] + \varepsilon^2[\frac{1}{2}\int_S t_i u_i dS]\end{aligned}$$

Considering the second variation as nothing more than the elastic strain energy, which is nonegative in classical elastostatics, one can conclude that the functional is minimized if the first variation vanishes.

Therefore, allowing the first variation to vanish leads to the boundary condition in its final form,

$$\int_{S_U} \delta t_i(u_i - u_i^\circ)dS + \int_{S_T} \delta u_i(t_i - t_i^\circ)dS = 0 \tag{3.3.7}$$

3.3.2 Cosserat Boundary Conditions

The surface traction and displacement/rotation boundary conditions are defined as

$$\begin{cases} u_i = u_i^\circ, & \text{on } S_U \\ t_i = t_i^\circ, & \text{on } S_T \end{cases} \tag{3.3.8}$$

where u_i are the components of displacement within the unit cell, t_i are the components of the surface traction, and

$$\begin{cases} S_U \cup S_T = S \quad \text{, and} \\ S_U \cap S_T = \emptyset \end{cases} \tag{3.3.9}$$

Furthermore, the moment traction and rotation boundary conditions are defined as

$$\begin{cases} \varphi_i = \varphi_i^\circ, \quad \text{on } S_\varphi \\ m_i = m_i^\circ, \quad \text{on } S_M \end{cases} \tag{3.3.10}$$

where φ_i are the components of rotation within the unit cell, m_i are the components of the moment traction, and

$$\begin{cases} S_\varphi \cup S_M = S \quad \text{, and} \\ S_\varphi \cap S_M = \emptyset \end{cases} \tag{3.3.11}$$

The periodicity condition relates the stress and moment tractions on different parts of the surface as follows

$$\begin{cases} t_i(\vec{x_o} + \vec{d}) = -t_i(\vec{x_o}), \\ m_i(\vec{x_o} + \vec{d}) = -m_i(\vec{x_o}), \quad (\vec{x_o}, \vec{x_o} + \vec{d}) \in S \end{cases} \tag{3.3.12}$$

The energy functional proposed by Wang and Pindera is modified to account for couple stresses and their influence on the micro-structure. The modified functional (labelled H_{D-P-M}) is

$$\begin{aligned} H_{D-P-M} =& \frac{1}{2}\int_V \sigma_{ij}\gamma_{ij}dV - \int_{S_U} t_i u_i^{\circ} dS - \int_{S_T} t_i^{\circ} u_i dS + \\ & \frac{1}{2}\int_V \mu_{ij}\varkappa_{ij}dV - \int_{S_\varphi} m_i \varphi_i^{\circ} dS - \int_{S_M} m_i^{\circ}\varphi_i dS, \end{aligned} \tag{3.3.13}$$

where γ_{ij} is the linear deformation (strain), $\varkappa_{ij}$ is the rotational deformation (twist), μ_{ij} is the couple stress, and φ_i is the micrororotation in the i^{th} direction.

The goal is, once again, to minimize the functional, thereby obtaining a boundary condition that satisfies the constraints of the unit cell and considers the periodicity of the problem.

In the case of Cosserat elasticity, this is accomplished using the transformations

$$\begin{aligned} \int_V \sigma_{ji}\gamma_{ji}dV &= \int_V \sigma_{ji}(u_{i,j} - \varepsilon_{jik}\varphi_k)dV \\ &= \int_V \{\sigma_{ji}\frac{\partial u_i}{\partial x_j} - \sigma_{ji}\varepsilon_{kji}\varphi_k\}dV \\ &= \int_V \{\frac{\partial(\sigma_{ji}u_i)}{\partial x_j} - \sigma_{ji,j}u_i\}dV - \int_V \sigma_{ji}\varepsilon_{kji}\varphi_k dV \\ &= \int_S \sigma_{ji}u_i n_j dS - \int_V \sigma_{ji}\varepsilon_{kji}\varphi_k dV \\ &= \int_S t_i u_i dS - \int_V \sigma_{ji}\varepsilon_{kji}\varphi_k dV \end{aligned} \tag{3.3.14}$$

where the Divergence Theorem, $\sigma_{ji,j} = 0$ (equilibrium), and $t_i = \sigma_{ji} n_j$ have been used, and

$$\begin{aligned}
\int_V \mu_{ji} \varkappa_{ji} dV &= \int_V \mu_{ji} \varphi_{i,j} dV \\
&= \int_V \{ \frac{\partial(\mu_{ji}\varphi_i)}{\partial x_j} - \mu_{ji,j}\varphi_i \} dV \\
&= \int_S \mu_{ji} \varphi_i n_j dS + \int_V \varepsilon_{ijk} \sigma_{jk} \varphi_i dV \\
&= \int_S m_i \varphi_i dS + \int_V \varepsilon_{ijk} \sigma_{jk} \varphi_i dV
\end{aligned} \tag{3.3.15}$$

where the Divergence Theorem, $\varepsilon_{ijk}\sigma_{jk} + \mu_{ji,j} = 0$ (equilibrium), and $m_i = \mu_{ji} n_j$ have been used.

The transformations in turn lead to

$$\begin{aligned}
\frac{1}{2}\int_V \mu_{ji}\varkappa_{ji} dV + \frac{1}{2}\int_V \sigma_{ji}\gamma_{ji} dV &= \frac{1}{2}\int_S t_i u_i dS + \frac{1}{2}\int_S m_i \varphi_i dS \\
&\quad - \frac{1}{2}\int_V \sigma_{ji}\varepsilon_{kji}\varphi_k dV + \frac{1}{2}\int_V \varepsilon_{ijk}\sigma_{jk}\varphi_i dV \\
&= \frac{1}{2}\int_S t_i u_i dS \\
&\quad + \frac{1}{2}\int_S m_i \varphi_i dS + \frac{1}{2}\int_V \{\varepsilon_{ijk}\sigma_{jk}\varphi_i - \sigma_{jk}\varepsilon_{ijk}\varphi_i\} dV \\
&= \frac{1}{2}\int_S t_i u_i dS + \frac{1}{2}\int_S m_i \varphi_i dS,
\end{aligned} \tag{3.3.16}$$

where $\frac{1}{2}\int_V \sigma_{ji}\varepsilon_{kji}\varphi_k dV = \frac{1}{2}\int_V \sigma_{jk}\varepsilon_{ijk}\varphi_i dV$ by relabelling indices $i \to k$ and $k \to i$.

Computing the variation of the energy functional yields

$$
\begin{aligned}
\delta H_{D-P-M} &= H_{D-P-M}(u_i+\varepsilon u_i, t_i+\varepsilon t_i, \varphi_i+\varepsilon\varphi_i, m_i+\varepsilon m_i) - H_{D-P-M}(u_i,t_i,\varphi_i,m_i) \\
&= \frac{1}{2}\int_S (t_i+\varepsilon t_i)(u_i+\varepsilon u_i)dS + \frac{1}{2}\int_S (m_i+\varepsilon m_i)(\varphi_i+\varepsilon\varphi_i)dS - \int_{S_U}(t_i+\varepsilon t_i)u_i^\circ dS - \\
&\int_{S_T} t_i^\circ(u_i+\varepsilon u_i)dS - \int_{S_\varphi}(m_i+\varepsilon m_i)\varphi_i^\circ dS - \int_{S_M} m_i^\circ(\varphi_i+\varepsilon\varphi_i)dS - \\
&\{\frac{1}{2}\int_S t_i u_i dS + \frac{1}{2}\int_S m_i\varphi_i dS - \int_{S_U} t_i u_i^\circ dS - \\
&\int_{S_T} t_i^\circ u_i dS - \int_{S_\varphi} m_i\varphi_i^\circ dS - \int_{S_M} m_i^\circ\varphi_i dS\} \\
&= \frac{1}{2}\int_S (t_i u_i + 2\varepsilon t_i u_i + \varepsilon^2 t_i u_i - t_i u_i)dS + \\
&\frac{1}{2}\int_S (m_i\varphi_i + 2\varepsilon m_i\varphi_i + \varepsilon^2 m_i\varphi_i - m_i\varphi_i)dS - \\
&\int_{S_U}(t_i u_i^\circ + \varepsilon t_i u_i^\circ - t_i u_i^\circ)dS - \\
&\int_{S_T}(t_i^\circ u_i + \varepsilon t_i^\circ u_i - t_i^\circ u_i)dS - \\
&\int_{S_\varphi}(m_i\varphi_i^\circ + \varepsilon m_i\varphi_i^\circ - m_i\varphi_i^\circ)dS - \\
&\int_{S_M}(m_i^\circ\varphi_i + \varepsilon m_i^\circ\varphi_i - m_i^\circ\varphi_i)dS \\
\Rightarrow \delta H_{D-P-M} &= \varepsilon[\int_{S_U} t_i(u_i-u_i^\circ)dS + \int_{S_T} u_i(t_i-t_i^\circ)dS + \int_{S_\varphi} m_i(\varphi_i-\varphi_i^\circ)dS \\
&+ \int_{S_M}\varphi_i(m_i-m_i^\circ)dS] + \varepsilon^2[\frac{1}{2}\int_S t_i u_i dS + \frac{1}{2}\int_S m_i\varphi_i dS]
\end{aligned}
\tag{3.3.17}
$$

Once more, allowing the first variation to vanish, the boundary condition is obtained in its final form,

$$\int_{S_U} \delta t_i(u_i - u_i^\circ)dS + \int_{S_T} \delta u_i(t_i - t_i^\circ)dS + \int_{S_\varphi} \delta m_i(\varphi_i - \varphi_i^\circ)dS + \int_{S_M} \delta\varphi_i(m_i - m_i^\circ)dS = 0 \tag{3.3.18}$$

3.4 Developing the Governing Equations

Following the procedure proposed by Wang and Pindera [58], the case of plane strain is considered to simplify the boundary value problem. FRP materials with unidirectional fibers, used as internal tensile reinforcement, can be treated under plane strain considerations, as the length of the bar is sufficiently long compared to its cross section.

The case of plane strain reduces the constitutive law to depend on 8 material constants, greatly simplifying the solution procedure. The resulting degrees of freedom that characterize the problem (shown in Figure 3.5) are now

$$\begin{aligned} \vec{\boldsymbol{u}} &= (u_1, u_2, 0), \\ \vec{\boldsymbol{\varphi}} &= (0, 0, \varphi_3), \end{aligned} \tag{3.4.1}$$

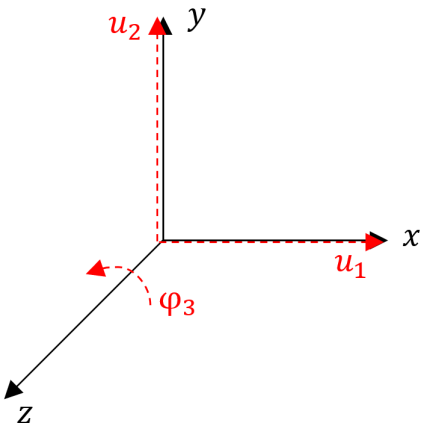

Figure 3.5: Plane strain degrees of freedom

with the stresses $\sigma_{13}, \sigma_{23}, \sigma_{31}, \sigma_{32}, \sigma_{33}, \mu_{11}, \mu_{12}, \mu_{21}, \mu_{22}, \mu_{31}, \mu_{32}, \mu_{33}$ all vanishing. The transversely isotropic constitutive law then reduces to

$$\boldsymbol{\sigma} = \begin{bmatrix} \sigma_{11} \\ \sigma_{12} \\ \sigma_{21} \\ \sigma_{22} \end{bmatrix} = \begin{bmatrix} A_{2222} & -A_{2221} & -A_{2212} & A_{2211} \\ -A_{2122} & A_{2121} & -A_{2121} - A_{2211} + A_{2222} & -A_{2122} - A_{2212} - A_{2221} \\ A_{2122} + A_{2212} + A_{2221} & -A_{2121} - A_{2211} + A_{2222} & A_{2121} & A_{2122} \\ A_{2211} & A_{2212} & A_{2221} & A_{2222} \end{bmatrix} \begin{bmatrix} \gamma_{11} \\ \gamma_{12} \\ \gamma_{21} \\ \gamma_{22} \end{bmatrix} \tag{3.4.2}$$

$$\boldsymbol{\mu} = \begin{bmatrix} \mu_{13} \\ \mu_{23} \end{bmatrix} = \begin{bmatrix} C_{2323} & -C_{2313} \\ C_{2313} & C_{2323} \end{bmatrix} \begin{bmatrix} \varkappa_{13} \\ \varkappa_{23} \end{bmatrix}, \tag{3.4.3}$$

with 8 independent elastic constants. The simplification leads to a reduction in the number of coupled differential equations from 6 to 3. The resulting equilibrium equations (neglecting body forces) are

$$\begin{cases} \sigma_{11,1} + \sigma_{21,2} = 0, \\ \sigma_{12,1} + \sigma_{22,2} = 0, \\ \mu_{13,1} + \mu_{23,2} + \sigma_{12} - \sigma_{21} = 0 \end{cases} \tag{3.4.4}$$

Substituting the constitutive law, as well as the following deformation-displacement relations,

$$\begin{cases} \gamma_{ij} = u_{j,i} - \varepsilon_{kij}\varphi_k \\ \varkappa_{ij} = \varphi_{j,i}, \end{cases}$$

the resulting system of partial differential equations (PDEs) in cartesian coordinates take the form

$$
\begin{cases}
A_{2222}\frac{\partial^2 u_1}{\partial x_1^2} + A_{2121}\frac{\partial^2 u_1}{\partial x_2^2} + (A_{2122} + A_{2221})\frac{\partial^2 u_1}{\partial x_2 \partial x_1} \\
+A_{2122}\frac{\partial^2 u_2}{\partial x_2^2} - A_{2221}\frac{\partial^2 u_2}{\partial x_1^2} + (-A_{2121} + A_{2222})\frac{\partial^2 u_2}{\partial x_2 \partial x_1} \\
+(-A_{2212} + A_{2221})\frac{\partial \varphi_3}{\partial x_1} + (2A_{2121} + A_{2211} - A_{2222})\frac{\partial \varphi_3}{\partial x_2} = 0, \\
\\
-A_{2122}\frac{\partial^2 u_1}{\partial x_1^2} + A_{2221}\frac{\partial^2 u_1}{\partial x_2^2} + (-A_{2121} + A_{2222})\frac{\partial^2 u_1}{\partial x_2 \partial x_1} \\
+A_{2222}\frac{\partial^2 u_2}{\partial x_2^2} + A_{2121}\frac{\partial^2 u_2}{\partial x_1^2} + (-A_{2122} - A_{2221})\frac{\partial^2 u_2}{\partial x_2 \partial x_1} \\
+(-2A_{2121} - A_{2211} + A_{2222})\frac{\partial \varphi_3}{\partial x_1} + (-A_{2212} + A_{2221})\frac{\partial \varphi_3}{\partial x_2} = 0, \\
\\
C_{2323}\frac{\partial^2 \varphi_3}{\partial x_1^2} + C_{2323}\frac{\partial^2 \varphi_3}{\partial x_2^2} + (-2A_{2122} - A_{2212} - A_{2221})\frac{\partial u_1}{\partial x_1} \\
+(-2A_{2121} - A_{2211} + A_{2222})\frac{\partial u_1}{\partial x_2} \\
+(2A_{2121} + A_{2211} - A_{2222})\frac{\partial u_2}{\partial x_1} + (-2A_{2122} - A_{2212} - A_{2221})\frac{\partial u_2}{\partial x_2} \\
+2(-2A_{2121} - A_{2211} + A_{2222})\varphi_3 = 0,
\end{cases}
\tag{3.4.5}
$$

Given the circular nature of the fiber, it is convenient to represent the differential equations in cylindrical coordinates, with the coordinate transformations defined as follows

$$
\begin{cases}
u_1 &= u_r \cos\theta - u_\theta \sin\theta, \\
u_2 &= u_r \sin\theta + u_\theta \cos\theta, \\
\varphi_3 &= \varphi_z
\end{cases}
\tag{3.4.6}
$$

The resulting system of PDEs is now

$$
\begin{cases}
(A_{2122}\sin\theta + A_{2222}\cos\theta)\frac{\partial^2 u_r}{\partial r^2} + \frac{(A_{2121}\cos\theta - A_{2221}\sin\theta)}{r^2}\frac{\partial^2 u_r}{\partial\theta^2} \\
+\frac{(A_{2121}\sin\theta + A_{2122}\cos\theta + A_{2221}\cos\theta - A_{2222}\sin\theta)}{r}\frac{\partial^2 u_r}{\partial r\partial\theta} \\
+\frac{(A_{2122}\sin\theta + A_{2222}\cos\theta)}{r}\frac{\partial u_r}{\partial r} + \frac{(-A_{2121}\sin\theta + A_{2122}\cos\theta - A_{2221}\cos\theta - A_{2222}\sin\theta)}{r^2}\frac{\partial u_r}{\partial\theta} \\
+\frac{(-A_{2122}\sin\theta - A_{2222}\cos\theta)}{r^2}u_r + \frac{(A_{2122}\cos\theta - A_{2222}\sin\theta)}{r^2}\frac{\partial^2 u_\theta}{\partial\theta^2} + (-A_{2121}\sin\theta - A_{2221}\cos\theta)\frac{\partial^2 u_\theta}{\partial r^2} \\
+\frac{(-A_{2121}\cos\theta + A_{2122}\sin\theta + A_{2221}\sin\theta + A_{2222}\cos\theta)}{r}\frac{\partial^2 u_\theta}{\partial r\partial\theta} \\
+\frac{(-A_{2121}\sin\theta - A_{2221}\cos\theta)}{r}\frac{\partial u_\theta}{\partial r} + \frac{(-A_{2121}\cos\theta - A_{2122}\sin\theta + A_{2221}\sin\theta - A_{2222}\cos\theta)}{r^2}\frac{\partial u_\theta}{\partial\theta} \\
+\frac{(A_{2121}\sin\theta + A_{2221}\cos\theta)}{r^2}u_\theta \\
+(2A_{2121}\sin\theta + A_{2211}\sin\theta - A_{2212}\cos\theta + A_{2221}\cos\theta - A_{2222}\sin\theta)\frac{\partial\varphi_z}{\partial r} \\
+\frac{(2A_{2121}\cos\theta + A_{2211}\cos\theta + A_{2212}\sin\theta - A_{2221}\sin\theta - A_{2222}\cos\theta)}{r}\frac{\partial\varphi_z}{\partial\theta} = 0, \\
\\
(-A_{2122}\cos\theta + A_{2222}\sin\theta)\frac{\partial^2 u_r}{\partial r^2} + \frac{(A_{2121}\sin\theta + A_{2221}\cos\theta)}{r^2}\frac{\partial^2 u_r}{\partial\theta^2} \\
+\frac{(-A_{2121}\cos\theta + A_{2122}\sin\theta + A_{2221}\sin\theta + A_{2222}\cos\theta)}{r}\frac{\partial^2 u_r}{\partial r\partial\theta} \\
+\frac{(-A_{2122}\cos\theta + A_{2222}\sin\theta)}{r}\frac{\partial u_r}{\partial r} + \frac{(A_{2121}\cos\theta + A_{2122}\sin\theta - A_{2221}\sin\theta + A_{2222}\cos\theta)}{r^2}\frac{\partial u_r}{\partial\theta} \\
+\frac{(A_{2122}\cos\theta - A_{2222}\sin\theta)}{r^2}u_r + \frac{(A_{2122}\sin\theta + A_{2222}\cos\theta)}{r^2}\frac{\partial^2 u_\theta}{\partial\theta^2} + (A_{2121}\cos\theta - A_{2221}\sin\theta)\frac{\partial^2 u_\theta}{\partial r^2} \\
+\frac{(-A_{2121}\sin\theta - A_{2122}\cos\theta - A_{2221}\cos\theta + A_{2222}\sin\theta)}{r}\frac{\partial^2 u_\theta}{\partial r\partial\theta} \\
+\frac{(A_{2121}\cos\theta - A_{2221}\sin\theta)}{r}\frac{\partial u_\theta}{\partial r} + \frac{(-A_{2121}\sin\theta + A_{2122}\cos\theta - A_{2221}\cos\theta - A_{2222}\sin\theta)}{r^2}\frac{\partial u_\theta}{\partial\theta} \\
+\frac{(-A_{2121}\cos\theta + A_{2221}\sin\theta)}{r^2}u_\theta \\
+(-2A_{2121}\cos\theta - A_{2211}\cos\theta - A_{2212}\sin\theta + A_{2221}\sin\theta + A_{2222}\cos\theta)\frac{\partial\varphi_z}{\partial r} \\
+\frac{(2A_{2121}\sin\theta + A_{2211}\sin\theta - A_{2212}\cos\theta + A_{2221}\cos\theta - A_{2222}\sin\theta)}{r}\frac{\partial\varphi_z}{\partial\theta} = 0, \\
\\
C_{2323}\frac{\partial^2\varphi_z}{\partial r^2} + \frac{C_{2323}}{r^2}\frac{\partial^2\varphi_z}{\partial\theta^2} + \frac{C_{2323}}{r}\frac{\partial\varphi_z}{\partial r} + 2(-2A_{2121} - A_{2211} + A_{2222})\varphi_z \\
+(-2A_{2122} - A_{2212} - A_{2221})\frac{\partial u_r}{\partial r} + \frac{(-2A_{2121} - A_{2211} + A_{2222})}{r}\frac{\partial u_r}{\partial\theta} \\
+\frac{(-2A_{2122} - A_{2212} - A_{2221})}{r}u_r + (2A_{2121} + A_{2211} - A_{2222})\frac{\partial u_\theta}{\partial r} \\
+\frac{(-2A_{2122} - A_{2212} - A_{2221})}{r}\frac{\partial u_\theta}{\partial\theta} + \frac{(2A_{2121} + A_{2211} - A_{2222})}{r}u_\theta = 0
\end{cases}
\tag{3.4.7}
$$

Considering the system of partial differential equations, as well as the developed boundary conditions, one can proceed with a discussion on the solvability of the system.

To proceed with existence and uniqueness theorems, as discussed in Chapter 2, one must begin by showing that the system of partial differential equations is uniformly elliptic. Then, positivity of the strain energy density must follow to establish the solution as a minimizer of the energy functional. To establish the ellipticity of the system, the differential operator, containing only higher order derivatives, must be invertible, or have non-zero determinant.

Since the governing system is invariant to coordinate transformations, the invertibility of the higher order differential operator will be checked in Cartesian coordinates. In Cartesian coordinates, the matrix of higher order derivatives is written in the form

$$\underline{\boldsymbol{L}}(\xi_\alpha) = \begin{bmatrix} a_{11} & a_{12} & a_{13} \\ a_{21} & a_{22} & a_{23} \\ a_{31} & a_{32} & a_{33} \end{bmatrix} \tag{3.4.8}$$

where

$$a_{11} = A_{2222}\xi_1^2 + A_{2121}\xi_2^2 + (A_{2122} + A_{2221})\xi_1\xi_2,$$
$$a_{12} = -A_{2221}\xi_1^2 + A_{2122}\xi_2^2 + (-A_{2121} + A_{2222})\xi_1\xi_2,$$
$$a_{13} = (-A_{2212} + A_{2221})\xi_1 + (2A_{2121} + A_{2211} - A_{2222})\xi_2,$$
$$a_{21} = A_{2122}\xi_1^2 + A_{2221}\xi_2^2 + (-A_{2121} + A_{2222})\xi_1\xi_2,$$
$$a_{22} = A_{2121}\xi_1^2 + A_{2222}\xi_2^2 + (-A_{2122} - A_{2221})\xi_1\xi_2,$$
$$a_{23} = (-2A_{2121} - A_{2211} + A_{2222})\xi_1 + (-A_{2212} + A_{2221})\xi_2,$$
$$a_{31} = (-2A_{2122} - A_{2212} - A_{2221})\xi_1 + (-2A_{2121} - A_{2211} + A_{2222})\xi_2,$$
$$a_{32} = (2A_{2121} + A_{2211} - A_{2222})\xi_1 + (-2A_{2122} - A_{2212} - A_{2221})\xi_2,$$
$$a_{33} = C_{2323}\xi_1^2 + C_{2323}\xi_2^2 + 2(-2A_{2121} - A_{2211} + A_{2222})\xi_1\xi_2$$

and the derivatives, ξ_α, have been defined as

$$\xi_1 = \frac{\partial}{\partial x_1}$$
$$\xi_2 = \frac{\partial}{\partial x_2}$$

Computing the determinant of the matrix, the condition for uniform ellipticity is such that

$$
\begin{aligned}
&(\xi_1^2+\xi_2^2)\{(\xi_1^2+\xi_2^2)(A_{2121}A_{2222}C_{2323}-A_{2122}A_{2221}C_{2323})\\
&+2A_{2121}A_{2211}A_{2222}-A_{2121}A_{2212}^2-2A_{2121}A_{2212}A_{2221}-A_{2121}A_{2221}^2\\
&-2A_{2121}A_{2222}^2+A_{2122}A_{2211}A_{2212}-A_{2122}A_{2211}A_{2221}-A_{2122}A_{2212}A_{2222}\\
&+2A_{2122}A_{2221}A_{2222}+A_{2211}^2A_{2222}-A_{2211}A_{2212}A_{2221}-A_{2211}A_{2221}^2\\
&-2A_{2211}A_{2222}^2+A_{2212}A_{2221}A_{2222}+A_{2221}^2A_{2222}+A_{2222}^3\}\neq 0
\end{aligned}
\tag{3.4.9}
$$

Additional constraints on the elasticity constants can be imposed by the condition that the strain energy density of the system is positive definite (establishing the solution as a minimizer of the energy functional). The strain energy density of the system is given by

$$U_0=\frac{1}{2}\mu_{ji}\varkappa_{ji}+\frac{1}{2}\sigma_{ji}\epsilon_{ji}$$

Substituting the plane strain constitutive relations for σ and μ and expanding the tensors, the strain energy density becomes

$$
\begin{aligned}
U_0=&\frac{1}{2}A_{2222}\epsilon_{11}^2+\frac{1}{2}(-A_{2221}-A_{2122})\epsilon_{11}\epsilon_{12}+\frac{1}{2}(A_{2122}+A_{2221})\epsilon_{11}\epsilon_{21}+\frac{1}{2}A_{2121}\epsilon_{12}^2\\
&+(-A_{2121}-A_{2211}+A_{2222})\epsilon_{12}\epsilon_{21}+\frac{1}{2}(-A_{2122}-A_{2221})\epsilon_{12}\epsilon_{22}+\frac{1}{2}A_{2121}\epsilon_{21}^2\\
&+\frac{1}{2}(A_{2122}+A_{2221})\epsilon_{21}\epsilon_{22}+\frac{1}{2}A_{2222}\epsilon_{22}^2+\frac{1}{2}C_{2323}\varkappa_{13}^2+\frac{1}{2}C_{2323}\varkappa_{23}^2
\end{aligned}
$$

To show the positive definiteness of the strain energy density, the symmetric matrix corresponding to the quadratic form is obtained. The corresponding matrix, hereby

referred to as U_m is

$$U_m = \begin{bmatrix} \frac{1}{2}A_{2222} & \frac{1}{4}(-A_{2221} - A_{2122}) & \frac{1}{4}(A_{2122} + A_{2221}) & \frac{1}{2}A_{2211} & 0 & 0 \\ \frac{1}{4}(-A_{2221} - A_{2122}) & \frac{1}{2}A_{2121} & \frac{1}{2}(-A_{2121} - A_{2211} + A_{2222}) & \frac{1}{4}(-A_{2122} - A_{2221}) & 0 & 0 \\ \frac{1}{4}(A_{2122} + A_{2221}) & \frac{1}{2}(-A_{2121} - A_{2211} + A_{2222}) & \frac{1}{2}A_{2121} & \frac{1}{4}(A_{2122} + A_{2221}) & 0 & 0 \\ \frac{1}{2}A_{2211} & \frac{1}{4}(-A_{2122} - A_{2221}) & \frac{1}{4}(A_{2122} + A_{2221}) & \frac{1}{2}A_{2222} & 0 & 0 \\ 0 & 0 & 0 & 0 & \frac{1}{2}C_{2323} & 0 \\ 0 & 0 & 0 & 0 & 0 & \frac{1}{2}C_{2323} \end{bmatrix} \tag{3.4.10}$$

The matrix U_m is said to be positive definite if its eigenvalues are real and positive. Computing the eignevalues yields the conditions

$$\begin{aligned} &C_{2323} > 0 \\ &A_{2222} - A_{2221} > 0 \\ &A_{2222} - A_{2211} > 0 \\ &A_{2121} + \frac{1}{2}A_{2211} + \frac{1}{2}A_{2221} \pm \frac{1}{2}\sqrt{\begin{array}{l} 4A_{2121}^2 - 4A_{2121}A_{2211} + 4A_{2121}A_{2221} - 8A_{2121}A_{2222} \\ + 4A_{2122}^2 + 8A_{2122}A_{2221} + A_{2211}^2 - 2A_{2211}A_{2221} \\ + 4A_{2222}A_{2211} + 5A_{2221}^2 - 4A_{2221}A_{2222} + 4A_{2222}^2 \end{array}} > 0 \end{aligned} \tag{3.4.11}$$

where the resulting equations are defined in terms of the unknown material constants A_{2121}, A_{2122}, A_{2211}, A_{2212}, A_{2221}, A_{2222}, C_{2313}, C_{2323}. Without known bounds on these constants, the positive definiteness of the operator cannot be shown. Therefore, it is essential to the solution of the boundary value problem that values/bounds on these constants are obtained.

Due to the microscopic nature of the Cosserat degrees of freedom (microrotations), measurements of the gradient of these quantities must occur at a length scale on the order of the grain size of the constituents. That is, the gradient of the rotation of a material point which is the size of the monomers that form the polymer resin must be measured. The size of a typical polyethylene monomer is on the order of 1Å. Measuring these quantities in three dimensions is quite difficult and requires very sophisticated equipment, and is beyond the scope of this work. Until such a test can be suitably performed, the ellipticity of the system cannot be guaranteed. As such, this chapter attempts only to derive the conditions upon which a solution to the system exists, with the solution being obtained in future works.

Chapter 4

Exponentially Graded Composites with Microstructure

4.1 Formulating the Problem

Starting with the constitutive law for a linear elastic, isotropic, Cosserat continuum (equations (2.5.30) and (2.5.31)), discussed in section 2.5, the formulation for the governing equations of an exponentially graded, linear elastic, isotropic Cosserat material is now developed. While exponential grading is considered in this work, the procedures used can be applied to any chosen grading type.

In a functionally graded material, the elastic constants, and consequently, the associated

engineering constants, are functions of position, written as

$$\mu = \mu(\vec{\boldsymbol{x}}) \tag{4.1.1}$$

$$\lambda = \lambda(\vec{\boldsymbol{x}}) \tag{4.1.2}$$

$$\alpha = \alpha(\vec{\boldsymbol{x}}) \tag{4.1.3}$$

$$\beta = \beta(\vec{\boldsymbol{x}}) \tag{4.1.4}$$

$$\gamma = \gamma(\vec{\boldsymbol{x}}) \tag{4.1.5}$$

$$\varepsilon = \varepsilon(\vec{\boldsymbol{x}}) \tag{4.1.6}$$

where $\vec{\boldsymbol{x}}$ is the global position vector.
Considering the functionally graded material properties, in conjunction with the equations of equilibrium, a set of coupled partial differential equations describing the homogenized system can be obtained.

4.1.1 Strain Energy Considerations

Section 2.4 discussed the conditions necessary to properly formulate the governing equations of elasticity. To reflect adequately reflect the physical properties of a linear elastic material, restrictions on the elastic constants must be imposed. Considerations for strain energy will be developed, which will yield restrictions on the constants and ultimately set up a framework for proving elliptic regularity of the governing system of differential equations. Starting with the expression for the internal energy density of an isotropic, Cosserat material [44],

$$U_0 = \frac{\mu+\alpha}{2}\gamma_{ij}\gamma_{ij} + \frac{\mu-\alpha}{2}\gamma_{ij}\gamma_{ji} + \frac{1}{2}\lambda\gamma_{kk}\gamma_{nn} + \frac{\gamma+\gamma}{2}\varkappa_{ij}\varkappa_{ij} + \frac{\gamma-\gamma}{2}\varkappa_{ij}\varkappa_{ji} + \frac{1}{2}\beta\varkappa_{kk}\varkappa_{nn}, \tag{4.1.7}$$

and re-labelling

$$\begin{aligned}
&\gamma_{11} = y_1 \quad \gamma_{22} = y_2 \quad \gamma_{33} = y_3 \quad \varkappa_{11} = y_4 \quad \varkappa_{22} = y_5 \quad \varkappa_{33} = y_6 \\
&\gamma_{31} = y_7 \quad \gamma_{13} = y_8 \quad \varkappa_{13} = y_9 \quad \varkappa_{31} = y_{10} \quad \gamma_{21} = y_{11} \quad \varkappa_{12} = y_{12} \\
&\gamma_{12} = y_{13} \quad \varkappa_{21} = y_{14} \quad \gamma_{23} = y_{15} \quad \varkappa_{23} = y_{16} \quad \gamma_{32} = y_{17} \quad \varkappa_{32} = y_{18}
\end{aligned} \tag{4.1.8}$$

the internal energy can be re-written as

$$2U_0 = a_{\alpha\beta}y_\alpha y_\beta \tag{4.1.9}$$

with the coefficient matrix re-written in the form

$$\left|a_{\alpha\beta}\right| = \begin{bmatrix} I & & & & \\ & II & & & \\ & & III & & \\ & & & IV & \\ & & & & V \end{bmatrix}$$

with its determinant Δ being represented as the product of 5 determinants

$$\Delta = \Delta_I \cdot \Delta_{II} \cdot \Delta_{III} \cdot \Delta_{IV} \cdot \Delta_V$$

where

$$\Delta_I = \begin{vmatrix} \lambda+2\mu & \lambda & \lambda \\ \lambda & \lambda+2\mu & \lambda \\ \lambda & \lambda & \lambda+2\mu \end{vmatrix}, \Delta_{II} = \begin{vmatrix} \beta+2\gamma & \beta & \beta \\ \beta & \beta+2\gamma & \beta \\ \beta & \beta & \beta+2\gamma \end{vmatrix} \tag{4.1.10}$$

$$\Delta_{III} = \begin{vmatrix} \mu+\alpha & \mu-\alpha & 0 & 0 \\ \mu-\alpha & \mu+\alpha & 0 & 0 \\ 0 & 0 & \gamma+\varepsilon & \gamma-\varepsilon \\ 0 & 0 & \gamma-\varepsilon & \gamma+\varepsilon \end{vmatrix},$$

$$\Delta_{IV} = \Delta_V = \begin{vmatrix} \mu+\alpha & 0 & \mu-\alpha & 0 \\ 0 & \gamma+\varepsilon & 0 & \gamma-\varepsilon \\ \mu-\alpha & 0 & \mu+\alpha & 0 \\ 0 & \gamma-\varepsilon & 0 & \gamma+\varepsilon \end{vmatrix}$$

From Sylvester's criterion (theorem 2.3.1), for a quadratic form A with entries a_{ij} to be positive definite, the requirement is such that

$$M_1 = a_{11} > 0, M_l = \begin{vmatrix} a_{11} & \cdots & a_{1l} \\ \vdots & \ddots & \vdots \\ a_{l1} & \cdots & a_{ll} \end{vmatrix} > 0, \quad l = 1...dim(A)$$

where l represents the dimensionality of the matrix M_l.

For an exponentially graded, linear elastic, isotropic material, the adiabatic constants are

given by

$$\mu\left(\vec{\boldsymbol{x}}\right) = \mu_0 e^{\vec{\boldsymbol{G}}\cdot\vec{\boldsymbol{x}}} \tag{4.1.11}$$

$$\lambda\left(\vec{\boldsymbol{x}}\right) = \lambda_0 e^{\vec{\boldsymbol{G}}\cdot\vec{\boldsymbol{x}}} \tag{4.1.12}$$

$$\alpha\left(\vec{\boldsymbol{x}}\right) = \alpha_0 e^{\vec{\boldsymbol{G}}\cdot\vec{\boldsymbol{x}}} \tag{4.1.13}$$

$$\beta\left(\vec{\boldsymbol{x}}\right) = \beta_0 e^{\vec{\boldsymbol{G}}\cdot\vec{\boldsymbol{x}}} \tag{4.1.14}$$

$$\gamma\left(\vec{\boldsymbol{x}}\right) = \gamma_0 e^{\vec{\boldsymbol{G}}\cdot\vec{\boldsymbol{x}}} \tag{4.1.15}$$

$$\varepsilon\left(\vec{\boldsymbol{x}}\right) = \varepsilon_0 e^{\vec{\boldsymbol{G}}\cdot\vec{\boldsymbol{x}}} \tag{4.1.16}$$

where $\vec{\boldsymbol{G}} = (G_1, G_2, G_3)$ is the selected isotropic grading vector (G_i= constant).
The required determinants for the strain energy of the exponentially graded system, starting with Δ_I, are:

$$M_1{}^{(1)} = e^{\vec{\boldsymbol{G}}\cdot\vec{\boldsymbol{x}}}\left(\lambda_0 + 2\mu_0\right) > 0 \Rightarrow \lambda_0 + 2\mu_0 > 0 \tag{4.1.17}$$

$$M_2{}^{(1)} = \begin{vmatrix} e^{\vec{\boldsymbol{G}}\cdot\vec{\boldsymbol{x}}}\left(\lambda_0 + 2\mu_0\right) & \lambda_0 e^{\vec{\boldsymbol{G}}\cdot\vec{\boldsymbol{x}}} \\ \lambda_0 e^{\vec{\boldsymbol{G}}\cdot\vec{\boldsymbol{x}}} & e^{\vec{\boldsymbol{G}}\cdot\vec{\boldsymbol{x}}}\left(\lambda_0 + 2\mu_0\right) \end{vmatrix} = e^{2\vec{\boldsymbol{G}}\cdot\vec{\boldsymbol{x}}}\left[4\mu_0\left(\lambda_0 + \mu_0\right)\right] > 0 \tag{4.1.18}$$

$$M_3{}^{(1)} = \begin{vmatrix} e^{\vec{\boldsymbol{G}}\cdot\vec{\boldsymbol{x}}}\left(\lambda_0 + 2\mu_0\right) & \lambda_0 e^{\vec{\boldsymbol{G}}\cdot\vec{\boldsymbol{x}}} & \lambda_0 e^{\vec{\boldsymbol{G}}\cdot\vec{\boldsymbol{x}}} \\ \lambda_0 e^{\vec{\boldsymbol{G}}\cdot\vec{\boldsymbol{x}}} & e^{\vec{\boldsymbol{G}}\cdot\vec{\boldsymbol{x}}}\left(\lambda_0 + 2\mu_0\right) & \lambda_0 e^{\vec{\boldsymbol{G}}\cdot\vec{\boldsymbol{x}}} \\ \lambda_0 e^{\vec{\boldsymbol{G}}\cdot\vec{\boldsymbol{x}}} & \lambda_0 e^{\vec{\boldsymbol{G}}\cdot\vec{\boldsymbol{x}}} & e^{\vec{\boldsymbol{G}}\cdot\vec{\boldsymbol{x}}}\left(\lambda_0 + 2\mu_0\right) \end{vmatrix} = e^{3\vec{\boldsymbol{G}}\cdot\vec{\boldsymbol{x}}}\left[4\mu_0^2\left(3\lambda_0 + 2\mu_0\right)\right] > 0 \tag{4.1.19}$$

Since $e^{\vec{\boldsymbol{G}}\cdot\vec{\boldsymbol{x}}} > 0$,

$$\lambda_0 + 2\mu_0 > 0 \tag{4.1.20}$$

$$4\mu_0\left(\lambda_0 + \mu_0\right) > 0 \tag{4.1.21}$$

$$4\mu_0^2\left(3\lambda_0 + 2\mu_0\right) > 0 \tag{4.1.22}$$

Combining the inequalities yields the most restrictive case

$$3\lambda_0 + 2\mu_0 > 0 \tag{4.1.23}$$

$$\mu_0 > 0 \tag{4.1.24}$$

Similarly, from Δ_{II},

$$\beta_0 + 2\gamma_0 > 0 \tag{4.1.25}$$

$$4\gamma_0\left(\beta_0 + \gamma_0\right) > 0 \tag{4.1.26}$$

$$4\gamma_0^2\left(3\beta_0 + 2\gamma_0\right) > 0 \tag{4.1.27}$$

Combining the inequalities yields the most restrictive case

$$3\beta_0 + 2\gamma_0 > 0 \tag{4.1.28}$$

$$\gamma_0 > 0 \tag{4.1.29}$$

Lastly, from $\Delta_{III}, \Delta_{IV}, \Delta_V$, the following restrictions can be obtained

$$\alpha_0, \varepsilon_0 > 0 \tag{4.1.30}$$

$$\mu_0 + \alpha_0 > 0 \tag{4.1.31}$$

$$\gamma_0 + \varepsilon_0 > 0 \tag{4.1.32}$$

Combining the conditions to obtain the most restrictive cases, the final conditions required for positive strain energy of the exponentially graded system are

$$\mu_0, \alpha_0, \gamma_0, \varepsilon_0 > 0 \tag{4.1.33}$$

$$3\lambda_0 + 2\mu_0 > 0 \tag{4.1.34}$$

$$3\beta_0 + 2\gamma_0 > 0 \tag{4.1.35}$$

4.1.2 Governing Equations

To obtain the system of partial differential equations required to describe the exponentially graded material, the constitutive equations are, along with the deformation-degree of freedom relations, substituted into the force and moment equilibrium equations (equations (2.5.34) and (2.5.35)), where body forces are once again neglected. The resulting coupled system of partial differential equations is expressed in matrix form such that

$$\begin{bmatrix} \underline{\boldsymbol{A}} & \underline{\boldsymbol{B}} \\ \underline{\boldsymbol{0}} & \underline{\boldsymbol{C}} \end{bmatrix} \begin{bmatrix} \vec{\boldsymbol{u}} \\ \vec{\boldsymbol{\varphi}} \end{bmatrix} = \begin{bmatrix} \vec{\boldsymbol{0}} \\ \vec{\boldsymbol{0}} \end{bmatrix} \tag{4.1.36}$$

where $\underline{\mathbf{0}}$ is a 3×3 null matrix, $\vec{\mathbf{0}}$ is a 3×1 null vector, and the matrix entries for $\underline{\boldsymbol{A}}, \underline{\boldsymbol{B}}$, and $\underline{\boldsymbol{C}}$ are given by

$$a_{ii} = (2\mu_0 + \lambda_0)\,\delta_{ij}\left(G_i\xi_j + \xi_i^2\right) + (\mu_0 + \alpha_0)\left(1 - \delta_{ij}\right)\left(G_j\xi_j + \xi_j\xi_j\right), \tag{4.1.37}$$

$$a_{ij,i\neq j} = \lambda_0\left(G_i\xi_j + \xi_i\xi_j\right) + (\mu_0 - \alpha_0)\left(1 - \delta_{ij}\right)\left(G_j\xi_i + \xi_i\xi_j\right), \tag{4.1.38}$$

$$b_{ij} = 2\alpha_0\epsilon_{ijk}\left(\delta_{ij} - 1\right)\left(G_k + \xi_k\right), \tag{4.1.39}$$

$$c_{ii} = (2\gamma_0 + \beta_0)\,\delta_{ij}\left(G_i\xi_j + \xi_i^2\right) + (\gamma_0 + \varepsilon_0)\left(1 - \delta_{ij}\right)\left(G_j\xi_j + \xi_j\xi_j\right), \tag{4.1.40}$$

$$c_{ij,i\neq j} = \beta_0\left(G_i\xi_j + \xi_i\xi_j\right) + (\gamma_0 - \varepsilon_0)\left(1 - \delta_{ij}\right)\left(G_j\xi_i + \xi_i\xi_j\right) \tag{4.1.41}$$

with only repeated indices not present in the component labels representing summation, and the partial differential operator characterising the system of differential equations is given by

$$\underline{\boldsymbol{L}}\left(\vec{\boldsymbol{\xi}}\right) = \begin{bmatrix} \underline{\boldsymbol{A}} & \underline{\boldsymbol{B}} \\ \underline{\mathbf{0}} & \underline{\boldsymbol{C}} \end{bmatrix} \tag{4.1.42}$$

such that

$$\underline{\boldsymbol{L}}\left(\vec{\boldsymbol{\xi}}\right)\vec{\boldsymbol{U}}(\vec{\boldsymbol{x}}) = \underline{\mathbf{0}} \tag{4.1.43}$$

in the absence of body forces, where ξ_i correspond to the derivatives $\frac{\partial}{\partial x_i}$.
The differential stress operator mapping the degrees of freedom to stresses and couple stresses acting on a surface element with normal vector $\vec{n}$ is given by

$$\underline{\boldsymbol{T}}\left(\vec{\boldsymbol{\xi}}\right) = \begin{bmatrix} \underline{\boldsymbol{D}} & \underline{\boldsymbol{E}} \\ \underline{\mathbf{0}} & \underline{\boldsymbol{F}} \end{bmatrix} \tag{4.1.44}$$

where $\underline{\mathbf{0}}$ is a 3×3 null matrix, and the matrix entries for $\underline{\boldsymbol{D}}, \underline{\boldsymbol{E}}$, and $\underline{\boldsymbol{F}}$ are given by

$$d_{ii} = (2\mu_0 + \lambda_0)\,\delta_{ij} n_j \xi_j + (\mu_0 + \alpha_0)\left(1 - \delta_{ij}\right) n_j \xi_j, \tag{4.1.45}$$

$$d_{ij,i\neq j} = \lambda_0 n_i \xi_j + (\mu_0 - \alpha_0)\, n_j \xi_i, \tag{4.1.46}$$

$$e_{ij} = 2\alpha_0 \epsilon_{ijk}\left(\delta_{ij} - 1\right) n_k, \tag{4.1.47}$$

$$f_{ii} = (2\gamma_0 + \beta_0)\,\delta_{ij} n_j \xi_j + (\gamma_0 + \varepsilon_0)\left(1 - \delta_{ij}\right) n_j \xi_j, \tag{4.1.48}$$

$$f_{ij,i\neq j} = \beta_0 n_i \xi_j + (\gamma_0 - \varepsilon_0)\, n_j \xi_i \tag{4.1.49}$$

4.2 Existence and Uniqueness of the Solution

As discussed in section 2.4, the existence and uniqueness of the solution to the mixed boundary value problem in elastostatics can be obtained through the Lax Milgram theorem (theorem 2.3.3). To satisfy the requirements of the theorem, Korn's inequality (theorem 2.3.2) is required. To satisfy this requirement, the governing system of partial differential equations must be shown to be uniformly elliptic. In section 2.4, this requirement amounted to the matrix $\underline{\boldsymbol{L_0}}\left(\vec{\boldsymbol{\xi}}\right)$ corresponding to the second order derivatives in the system of partial differential equations defined by operator $\underline{\boldsymbol{L}}\left(\vec{\boldsymbol{\xi}}\right)$ being invertible. The matrix $\underline{\boldsymbol{L_0}}\left(\vec{\boldsymbol{\xi}}\right)$, with entries

$$a_{ii} = (2\mu_0 + \lambda_0)\,\delta_{ij}\xi_i^2 + (\mu_0 + \alpha_0)\left(1 - \delta_{ij}\right)\xi_j\xi_j, \tag{4.2.1}$$

$$a_{ij,i\neq j} = \left((2\mu_0 + \lambda_0) - (\mu_0 + \alpha_0)\right)\xi_i\xi_j, \tag{4.2.2}$$

$$b_{ij} = 0, \tag{4.2.3}$$

$$c_{ii} = (2\gamma_0 + \beta_0)\,\delta_{ij}\xi_i^2 + (\gamma_0 + \varepsilon_0)\left(1 - \delta_{ij}\right)\xi_j\xi_j, \tag{4.2.4}$$

$$c_{ij,i\neq j} = \left((2\gamma_0 + \beta_0) - (\gamma_0 + \varepsilon_0)\right)\xi_i\xi_j \tag{4.2.5}$$

$$\tag{4.2.6}$$

is invertible for all $\xi \neq 0$, since

$$det\underline{\boldsymbol{L_0}}\left(\vec{\boldsymbol{\xi}}\right) = (2\mu_0 + \lambda_0)\,(2\gamma_0 + \beta_0)\,(\mu_0 + \alpha_0)\,(\gamma_0 + \varepsilon_0)\left(\xi_1^2 + \xi_2^2 + \xi_3^2\right)^6, \tag{4.2.7}$$

and the expressions involving the adiabatic constants are nonnegative (equations (4.1.20), (4.1.25), (4.1.31), (4.1.32)). The above condition, in conjunction with the conditions for positive strain energy, show that (4.1.36) represents a uniformly elliptic system. Following from uniform ellipticity, the requirements for theorems 2.3.2 and 2.3.3 are satisfied, and show that the variational formulation of the governing system has a unique solution.

Due to the complex nature of system (4.1.36), linear terms in the system of partial differential equations arising from the exponential grading prevent factoring the system into a suitable form for obtaining an analytical solution. As such, integral equation methods and potential theories [90, 91, 92] cannot be used to obtain an analytical solution to (4.1.36), and numerical approximation techniques are recommended. As such, the finite element method will be used to solve the equivalent variational problem.

4.3 Finite Element Implementation of the Solution

In what follows, the mixed boundary value problem below (Figure 4.1) will be considered.

Find $\vec{\boldsymbol{U}} = \left(u_x, u_y, u_z, \varphi_x, \varphi_y, \varphi_z\right)^T \in H^1(\Omega)$ such that

$$\begin{aligned} \underline{\boldsymbol{L}}\vec{\boldsymbol{U}} &= \underline{\mathbf{0}} \quad \text{in } \Omega, \\ \vec{\boldsymbol{U}} &= \vec{\tilde{\boldsymbol{U}}} \quad \text{on } \partial\Omega_1, \\ \vec{\boldsymbol{t}} &= \vec{\tilde{\boldsymbol{t}}} \quad \text{on } \partial\Omega_2, \end{aligned} \tag{4.3.1}$$

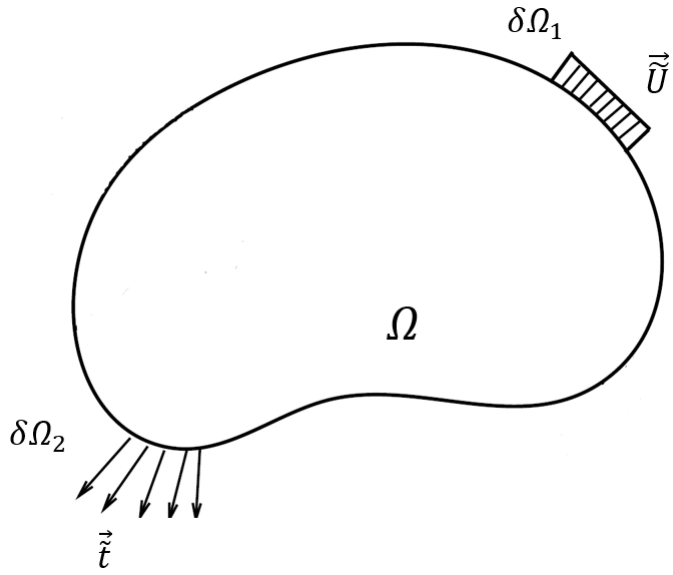

Figure 4.1: Geometrical representation of mixed boundary value problem

where $\vec{\tilde{\boldsymbol{U}}}$ is the generalized displacement vector, prescribed on the Dirichlet part of the boundary $\partial\Omega_1$, and $\vec{\tilde{\boldsymbol{t}}}$ is the generalized traction vector prescribed on the Neumann part of the boundary $\partial\Omega_2$, with $\partial\Omega = \Gamma = \partial\Omega_1 \cup \partial\Omega_2$.

The first step in developing the finite element formulation is to consider the variational

principle relating the internal and external work done. Specifically, the variational principle is obtained by allowing the difference between the internal work done and external work done to vanish, and it is given by

$$W\left(\vec{\boldsymbol{u}},\vec{\boldsymbol{\varphi}},\vec{\bar{\boldsymbol{u}}},\vec{\bar{\boldsymbol{\varphi}}}\right)=W^{int}\left(\vec{\boldsymbol{u}},\vec{\boldsymbol{\varphi}},\vec{\bar{\boldsymbol{u}}},\vec{\bar{\boldsymbol{\varphi}}}\right)-W^{ext}\left(\vec{\bar{\boldsymbol{u}}},\vec{\bar{\boldsymbol{\varphi}}}\right)=\vec{\mathbf{0}} \tag{4.3.2}$$

where $\vec{\bar{\boldsymbol{u}}},\vec{\bar{\boldsymbol{\varphi}}}$ are the vectors of virtual displacements and microrotations. Re-writing the variational principle in terms of quantities of interest, on the defined domains, we have

$$\int_{\Omega}\left(\bar{\boldsymbol{\gamma}}^{T}\boldsymbol{\sigma}+\bar{\boldsymbol{\varkappa}}^{T}\boldsymbol{\mu}\right)d\Omega-\int_{\Omega}\left(\vec{\bar{\boldsymbol{u}}}^{T}\vec{\boldsymbol{p}}_{v}+\vec{\bar{\boldsymbol{\varphi}}}^{T}\vec{\boldsymbol{m}}_{v}\right)d\Omega+\int_{\Gamma}\left(\vec{\bar{\boldsymbol{u}}}^{T}\vec{\boldsymbol{p}}_{s}+\vec{\bar{\boldsymbol{\varphi}}}^{T}\vec{\boldsymbol{m}}_{s}\right)d\Gamma=\vec{\mathbf{0}} \tag{4.3.3}$$

where $\vec{\boldsymbol{p}}_{s}$ and $\vec{\boldsymbol{m}}_{s}$ are prescribed stresses and couple stresses defined on the surface Γ, and $\vec{\boldsymbol{p}}_{v}$ and $\vec{\boldsymbol{m}}_{v}$ are body stresses and couple stresses defined in the interior domain Ω. The first term in equation (4.3.3) represents the internal energy of the continuum, with the second term representing the work done due to body forces, and the last representing the work done due to external forces. To simplify the expressions for use in the finite element method, some grouping of vectors is introduced.

First, the degrees of freedom are grouped such that $\vec{\boldsymbol{U}}=\left(u_x,u_y,u_z,\varphi_x,\varphi_y,\varphi_z\right)^{T}$. Next,

the strains are grouped such that

$$\boldsymbol{\mathcal{E}} = \begin{bmatrix} \boldsymbol{\gamma} \\ \boldsymbol{\varkappa} \end{bmatrix} = \begin{bmatrix} \gamma_{11} \\ \gamma_{22} \\ \gamma_{33} \\ \gamma_{12} \\ \gamma_{13} \\ \gamma_{23} \\ \gamma_{21} \\ \gamma_{31} \\ \gamma_{32} \\ \varkappa_{11} \\ \varkappa_{22} \\ \varkappa_{33} \\ \varkappa_{12} \\ \varkappa_{13} \\ \varkappa_{23} \\ \varkappa_{21} \\ \varkappa_{31} \\ \varkappa_{32} \end{bmatrix}, \tag{4.3.4}$$

Following the grouping of the strains, the corresponding stresses are grouped such that

$$\boldsymbol{\Sigma} = \begin{bmatrix} \boldsymbol{\sigma} \\ \boldsymbol{\mu} \end{bmatrix} = \begin{bmatrix} \sigma_{11} \\ \sigma_{22} \\ \sigma_{33} \\ \sigma_{12} \\ \sigma_{13} \\ \sigma_{23} \\ \sigma_{21} \\ \sigma_{31} \\ \sigma_{32} \\ \mu_{11} \\ \mu_{22} \\ \mu_{33} \\ \mu_{12} \\ \mu_{13} \\ \mu_{23} \\ \mu_{21} \\ \mu_{31} \\ \mu_{32} \end{bmatrix}, \tag{4.3.5}$$

Considering the constitutive laws for a linear elastic Cosserat material with central

symmetry, defined in equations (2.5.23) and (2.5.24), the expressions

$$\begin{aligned} \sigma_{ji} &= a_{jikl}\gamma_{kl} \\ \Rightarrow \boldsymbol{\sigma} &= \underline{\boldsymbol{A}}\boldsymbol{\gamma}, \end{aligned} \tag{4.3.6}$$

$$\begin{aligned} \mu_{ji} &= b_{jikl}\varkappa_{kl} \\ \Rightarrow \boldsymbol{\mu} &= \underline{\boldsymbol{B}}\boldsymbol{\varkappa}, \end{aligned} \tag{4.3.7}$$

can be grouped such that

$$\boldsymbol{\Sigma} = \begin{bmatrix} \underline{\boldsymbol{A}} & \underline{\boldsymbol{0}} \\ \underline{\boldsymbol{0}} & \underline{\boldsymbol{B}} \end{bmatrix} \boldsymbol{\mathcal{E}} = \underline{\boldsymbol{C}}\boldsymbol{\mathcal{E}}, \tag{4.3.8}$$

where

$$\underline{\boldsymbol{A}} = e^{\vec{\boldsymbol{G}}\cdot\vec{\boldsymbol{x}}} \begin{bmatrix} 2\mu_0+\lambda_0 & \lambda_0 & \lambda_0 & 0 & 0 & 0 & 0 & 0 & 0 \\ \lambda_0 & 2\mu_0+\lambda_0 & \lambda_0 & 0 & 0 & 0 & 0 & 0 & 0 \\ \lambda_0 & \lambda_0 & 2\mu_0+\lambda_0 & 0 & 0 & 0 & 0 & 0 & 0 \\ 0 & 0 & 0 & \mu_0+\alpha_0 & 0 & 0 & \mu_0-\alpha_0 & 0 & 0 \\ 0 & 0 & 0 & 0 & \mu_0+\alpha_0 & 0 & 0 & \mu_0-\alpha_0 & 0 \\ 0 & 0 & 0 & 0 & 0 & \mu_0+\alpha_0 & 0 & 0 & \mu_0-\alpha_0 \\ 0 & 0 & 0 & \mu_0-\alpha_0 & 0 & 0 & \mu_0+\alpha_0 & 0 & 0 \\ 0 & 0 & 0 & 0 & \mu_0-\alpha_0 & 0 & 0 & \mu_0+\alpha_0 & 0 \\ 0 & 0 & 0 & 0 & 0 & \mu_0-\alpha_0 & 0 & 0 & \mu_0+\alpha_0 \end{bmatrix}, \tag{4.3.9}$$

and

$$\underline{\boldsymbol{B}} = e^{\vec{\boldsymbol{G}}\cdot\vec{\boldsymbol{x}}} \begin{bmatrix} 2\gamma_0+\beta_0 & \beta_0 & \beta_0 & 0 & 0 & 0 & 0 & 0 & 0 \\ \beta_0 & 2\gamma_0+\beta_0 & \beta_0 & 0 & 0 & 0 & 0 & 0 & 0 \\ \beta_0 & \beta_0 & 2\gamma_0+\beta_0 & 0 & 0 & 0 & 0 & 0 & 0 \\ 0 & 0 & 0 & \gamma_0+\varepsilon_0 & 0 & 0 & \gamma_0-\varepsilon_0 & 0 & 0 \\ 0 & 0 & 0 & 0 & \gamma_0+\varepsilon_0 & 0 & 0 & \gamma_0-\varepsilon_0 & 0 \\ 0 & 0 & 0 & 0 & 0 & \gamma_0+\varepsilon_0 & 0 & 0 & \gamma_0-\varepsilon_0 \\ 0 & 0 & 0 & \gamma_0-\varepsilon_0 & 0 & 0 & \gamma_0+\varepsilon_0 & 0 & 0 \\ 0 & 0 & 0 & 0 & \gamma_0-\varepsilon_0 & 0 & 0 & \gamma_0+\varepsilon_0 & 0 \\ 0 & 0 & 0 & 0 & 0 & \gamma_0-\varepsilon_0 & 0 & 0 & \gamma_0+\varepsilon_0 \end{bmatrix}. \tag{4.3.10}$$

Lastly, the body and surface stresses and couple stresses are grouped such that $\vec{\boldsymbol{T}}_{\boldsymbol{v}} = (\vec{\boldsymbol{p}}_v, \vec{\boldsymbol{m}}_v)^T$, and $\vec{\boldsymbol{T}}_{\boldsymbol{s}} = (\vec{\boldsymbol{p}}_s, \vec{\boldsymbol{m}}_s)^T$ respectively. With these groupings, the variational formulation from equation (4.3.3) reduces to

$$\int_\Omega \bar{\boldsymbol{\mathcal{E}}}^T \boldsymbol{\Sigma} d\Omega - \int_\Omega \bar{\boldsymbol{U}}^T \vec{\boldsymbol{T}}_v d\Omega + \int_\Gamma \vec{\bar{\boldsymbol{U}}}^T \vec{\boldsymbol{T}}_s d\Gamma = \vec{\boldsymbol{0}}, \tag{4.3.11}$$

a convenient form for the application of the finite element method.

Due to the varying material properties within a functionally graded continuum, careful consideration is required in selecting the appropriate elements. Martínez-Pañeda's [93] work on functionally graded finite elements suggests a need for quadratic elements to avoid introducing error related to non-linearly varying elastic properties. As such, quadratic, isoparameteric elements will be considered. To properly discretize both simple and complex geometries, two elements will be constructed: A quadratic, 20-noded isoparametric quadrilateral, and a quadratic, 15-noded isoparametric wedge. In what follows, the standard isoparametric approximations for the nodal degrees of freedom are

used, such that

$$\vec{\boldsymbol{U}} = \underline{\boldsymbol{N}}^T \vec{\boldsymbol{d}}^e \tag{4.3.12}$$

$$\vec{\vec{\boldsymbol{U}}} = \underline{\boldsymbol{N}}^T \vec{\vec{\boldsymbol{d}}}^e \tag{4.3.13}$$

where $\underline{\boldsymbol{N}}$ has dimensions $6n \times 6$, with n corresponding to the number of nodes in the element, matrices of shape functions, and
$\vec{\boldsymbol{d}}^e = \left[u_{x_1}, u_{y_1}, u_{z_1}, \varphi_{x_1}, \varphi_{y_1}, \varphi_{z_1}, \cdots, u_{x_n}, u_{y_n}, u_{z_n}, \varphi_{x_n}, \varphi_{y_n}, \varphi_{z_n}\right]^T$ is a $6n \times 1$ vector containing the element's nodal degrees of freedom. The matrix $\underline{\boldsymbol{N}}$ can be represented in block form, such that

$$\underline{\boldsymbol{N}} = \begin{bmatrix} \underline{\boldsymbol{N_1}} & \underline{\boldsymbol{0}} & \underline{\boldsymbol{N_2}} & \underline{\boldsymbol{0}} & \cdots & \underline{\boldsymbol{N_n}} & \underline{\boldsymbol{0}} \\ \underline{\boldsymbol{0}} & \underline{\boldsymbol{N_1}} & \underline{\boldsymbol{0}} & \underline{\boldsymbol{N_2}} & \cdots & \underline{\boldsymbol{0}} & \underline{\boldsymbol{N_n}} \end{bmatrix}^T \tag{4.3.14}$$

and

$$\underline{\boldsymbol{N_i}} = \begin{bmatrix} N_i & 0 & 0 \\ 0 & N_i & 0 \\ 0 & 0 & N_i \end{bmatrix} \tag{4.3.15}$$

represent matrices containing the element shape function N_i at node i. Next, the deformation-degree of freedom relations (equations (2.5.32) and (2.5.33)) are used to construct the deformation matrix $\underline{\boldsymbol{D}}$ $(18 \times 6n)$, mapping the vector $\vec{\boldsymbol{d}}^e$ to the deformations $\vec{\boldsymbol{\mathcal{E}}}$. The deformation matrix $\underline{\boldsymbol{D}}$ can be represented in block form, such that

$$\underline{\boldsymbol{D}} = \begin{bmatrix} \underline{\boldsymbol{D_1}} & \underline{\boldsymbol{D_2}} & \cdots & \underline{\boldsymbol{D_n}} \end{bmatrix} \tag{4.3.16}$$

and

$$\underline{\boldsymbol{D_i}} = \begin{bmatrix} \frac{\partial N_i}{\partial x} & 0 & 0 & 0 & 0 & 0 \\ 0 & \frac{\partial N_i}{\partial y} & 0 & 0 & 0 & 0 \\ 0 & 0 & \frac{\partial N_i}{\partial z} & 0 & 0 & 0 \\ 0 & \frac{\partial N_i}{\partial x} & 0 & 0 & 0 & -N_i \\ 0 & 0 & \frac{\partial N_i}{\partial x} & 0 & N_i & 0 \\ 0 & 0 & \frac{\partial N_i}{\partial y} & -N_i & 0 & 0 \\ \frac{\partial N_i}{\partial y} & 0 & 0 & 0 & 0 & N_i \\ \frac{\partial N_i}{\partial z} & 0 & 0 & 0 & -N_i & 0 \\ 0 & \frac{\partial N_i}{\partial z} & 0 & N_i & 0 & 0 \\ 0 & 0 & 0 & \frac{\partial N_i}{\partial x} & 0 & 0 \\ 0 & 0 & 0 & 0 & \frac{\partial N_i}{\partial y} & 0 \\ 0 & 0 & 0 & 0 & 0 & \frac{\partial N_i}{\partial z} \\ 0 & 0 & 0 & 0 & \frac{\partial N_i}{\partial x} & 0 \\ 0 & 0 & 0 & 0 & 0 & \frac{\partial N_i}{\partial x} \\ 0 & 0 & 0 & 0 & 0 & \frac{\partial N_i}{\partial y} \\ 0 & 0 & 0 & \frac{\partial N_i}{\partial y} & 0 & 0 \\ 0 & 0 & 0 & \frac{\partial N_i}{\partial z} & 0 & 0 \\ 0 & 0 & 0 & 0 & \frac{\partial N_i}{\partial z} & 0 \end{bmatrix}. \tag{4.3.17}$$

Furthermore, the chain rule used to relate differentiation in the global system to

differentiation in the local system is given by

$$\begin{bmatrix} \frac{\partial N_i}{\partial x} \\ \frac{\partial N_i}{\partial y} \\ \frac{\partial N_i}{\partial z} \end{bmatrix} = \begin{bmatrix} \frac{\partial \xi}{\partial x} & \frac{\partial \eta}{\partial x} & \frac{\partial \zeta}{\partial x} \\ \frac{\partial \xi}{\partial y} & \frac{\partial \eta}{\partial y} & \frac{\partial \zeta}{\partial y} \\ \frac{\partial \xi}{\partial z} & \frac{\partial \eta}{\partial z} & \frac{\partial \zeta}{\partial z} \end{bmatrix} \begin{bmatrix} \frac{\partial N_i}{\partial \xi} \\ \frac{\partial N_i}{\partial \eta} \\ \frac{\partial N_i}{\partial \zeta} \end{bmatrix} = \underline{\boldsymbol{J}}^{-1} \begin{bmatrix} \frac{\partial N_i}{\partial \xi} \\ \frac{\partial N_i}{\partial \eta} \\ \frac{\partial N_i}{\partial \zeta} \end{bmatrix} \tag{4.3.18}$$

where the Jacobian matrix of transformation $\underline{\boldsymbol{J}}$ is defined as

$$\underline{\boldsymbol{J}} = \begin{bmatrix} \frac{\partial x}{\partial \xi} & \frac{\partial y}{\partial \xi} & \frac{\partial z}{\partial \xi} \\ \frac{\partial x}{\partial \eta} & \frac{\partial y}{\partial \eta} & \frac{\partial z}{\partial \eta} \\ \frac{\partial x}{\partial \zeta} & \frac{\partial y}{\partial \zeta} & \frac{\partial z}{\partial \zeta} \end{bmatrix}. \tag{4.3.19}$$

Substituting the definitions into the variational formulation,

$$\begin{aligned}
&\int_\Omega \bar{\boldsymbol{\varepsilon}}^T \boldsymbol{\Sigma} d\Omega - \int_\Omega \vec{\bar{\boldsymbol{U}}}^T \vec{\boldsymbol{T}}_v d\Omega + \int_\Gamma \vec{\bar{\boldsymbol{U}}}^T \vec{\boldsymbol{T}}_s d\Gamma = \vec{\boldsymbol{0}} \\
\Rightarrow &\int_\Omega \left(\underline{\boldsymbol{D}} \vec{\bar{\boldsymbol{d}}}^e\right)^T (\underline{\boldsymbol{C}} \boldsymbol{\mathcal{E}}) \, d\Omega - \int_\Omega \left(\underline{\boldsymbol{N}}^T \vec{\bar{\boldsymbol{d}}}^e\right)^T \vec{\boldsymbol{T}}_v d\Omega + \int_\Gamma \left(\underline{\boldsymbol{N}}^T \vec{\bar{\boldsymbol{d}}}^e\right)^T \vec{\boldsymbol{T}}_s d\Gamma = \vec{\boldsymbol{0}} \\
\Rightarrow &\int_\Omega \left(\underline{\boldsymbol{D}} \vec{\bar{\boldsymbol{d}}}^e\right)^T \left(\underline{\boldsymbol{C}} \underline{\boldsymbol{D}} \vec{\boldsymbol{d}}^e\right) d\Omega - \int_\Omega \vec{\bar{\boldsymbol{d}}}^{e\,T} \underline{\boldsymbol{N}} \vec{\boldsymbol{T}}_v d\Omega + \int_\Gamma \vec{\bar{\boldsymbol{d}}}^{e\,T} \underline{\boldsymbol{N}} \vec{\boldsymbol{T}}_s d\Gamma = \vec{\boldsymbol{0}} \\
\Rightarrow &\int_\Omega \vec{\bar{\boldsymbol{d}}}^{e\,T} \underline{\boldsymbol{D}}^T \underline{\boldsymbol{C}} \underline{\boldsymbol{D}} \vec{\boldsymbol{d}}^e d\Omega - \int_\Omega \vec{\bar{\boldsymbol{d}}}^{e\,T} \underline{\boldsymbol{N}} \vec{\boldsymbol{T}}_v d\Omega + \int_\Gamma \vec{\bar{\boldsymbol{d}}}^{e\,T} \underline{\boldsymbol{N}} \vec{\boldsymbol{T}}_s d\Gamma = \vec{\boldsymbol{0}} \\
\Rightarrow &\vec{\bar{\boldsymbol{d}}}^{e\,T} \left[\int_\Omega \underline{\boldsymbol{D}}^T \underline{\boldsymbol{C}} \underline{\boldsymbol{D}} d\Omega\right] \vec{\boldsymbol{d}}^e - \vec{\bar{\boldsymbol{d}}}^{e\,T} \left[\int_\Omega \underline{\boldsymbol{N}} \vec{\boldsymbol{T}}_v d\Omega\right] + \vec{\bar{\boldsymbol{d}}}^{e\,T} \left[\int_\Gamma \underline{\boldsymbol{N}} \vec{\boldsymbol{T}}_s d\Gamma\right] = \vec{\boldsymbol{0}} \\
&\Rightarrow \left[\int_\Omega \underline{\boldsymbol{D}}^T \underline{\boldsymbol{C}} \underline{\boldsymbol{D}} d\Omega\right] \vec{\boldsymbol{d}}^e = \left[\int_\Omega \underline{\boldsymbol{N}} \vec{\boldsymbol{T}}_v d\Omega\right] - \left[\int_\Gamma \underline{\boldsymbol{N}} \vec{\boldsymbol{T}}_s d\Gamma\right] \qquad (4.3.20) \\
&\Rightarrow \underline{\boldsymbol{K}}^e \vec{\boldsymbol{d}}^e = \underline{\boldsymbol{F}}^{e,\Omega} - \underline{\boldsymbol{F}}^{e,\Gamma} = \underline{\boldsymbol{F}}^e \qquad (4.3.21)
\end{aligned}$$

one obtains the familiar form for the finite element method, where $\underline{\boldsymbol{K}}^e$ is the element stiffness matrix, $\underline{\boldsymbol{F}}^{e,\Omega}$ represents the body force vector, and $\underline{\boldsymbol{F}}^{e,\Gamma}$ represents the external

force vector.

4.3.1 Implementation into Commercial Software (Abaqus)

Typically, user defined material behaviour is implemented in Abaqus [12] in the form of a user defined material subroutine (UMAT). The material behaviour is then applied to an element selected from the Abaqus element library. The elements are not suitable for the analysis presented in this work, as the three additional kinematically independent degrees of freedom (microrotations) are not accounted for in the available elements.

Several approaches [57, 94, 95] to make use of the available elements, replacing definitions for some variables with the required microrotations have been implemented, but are convoluted in nature. To establish a dedicated Cosserat element as a foundation for future works involving plasticity and other effects, this work will instead construct a user element using the UEL subroutine.

The UEL subroutine defines all the relevant quantities for element computations, and can include a constitutive update to avoid having to define a user material. In its basic form, the UEL subroutine offers the current solution at each calculation step, among other useful quantities, and requires at minimum definitions for the element stiffness matrix, and the residual force vector $\underline{\boldsymbol{F}}^e$. The subroutine also provides a storage vector to house any solution dependent state variable that can be printed to the output database. Visualization of the results is an area of concern with user defined elements, as Abaqus is incapable of natively displaying contour plots for quantities of interest, other than the 3 classical nodal displacements. Furthermore, Abaqus employs Voigt notation to define stresses, and as such, the native output database structure is not suitable to store the

results of elements with asymmetric stress states. Approaches in the literature have attempted to overcome some of these issues using ingenious techniques.

The issue of contour plot visualization was circumvented by [96] through the use of a ghost mesh approach, where the results from the user material simulation were overlaid onto the results form another simulation in which the material had negligible properties. While this approach allows for native visualization of user elements that hold the same degrees of freedom as the available elements in the Abaqus library, it does not solve the issue for elements with additional degrees of freedom. Another approach by [57] overcomes the issue of asymmetric stress storage by generating three output databases, storing 6 of 18 stress/couple stress components in each, and keeping track of the variables manually. While effective, this approach can present some confusion to the user, and will not be used in this work. Instead, this work aims to bypass the Abaqus output database altogether, electing to write the desired output to a series of comma separated value (CSV) files for post-processing.

A post processing code is developed in Python, which reads the input file used for simulation, as well as the generated CSV output, and leverages object oriented programming to replicate the output database hierarchical structure that Abaqus employs. Following the post processing of the results, the issue of visualization remains.

To address this issue, the processed data stored in the replicated output database structure is written to a series of files in the Virtual Toolkit (VTK) format, which is an open source format used by many scientific visualization softwares. Once processed into VTK format, the results can be viewed on open source visualization software such as Paraview. In this work, the portion of the post processing code pertaining to the conversion to VTK format is based on the approach by [97].

To summarize, the contributions to the finite element implementation for an exponentially graded Cosserat material is as follows

- Write the UEL subroutine in FORTRAN and output nodal displacements, reactions, deformations, and stresses at each increment, for each element, in the form of 4 CSV files
- Write the post-processing Python code that takes as input the Abaqus input file, and 4 CSV output files, and generates a VTK file for each increment (a series of VTK files representing increments in an analysis are stored as VTU)

The UEL script contains the main UEL subroutine, which assembles the element stiffness matrix, and residual force vector, as well as writing the desired output to the CSV files. Within this subroutine, both element formulations (quadrilateral and wedge) are defined. Based on the selection in the input file, the appropriate formulation in the UEL will be used. The main subroutine performs the numerical integration (Gauss Quadrature), yielding the required stiffness matrix and force vector. In addition, deformations and stresses are computed at the nodes (through extrapolation from the integration points), and written to the CSV files.

To perform the above computations, several utility subroutines are written within the UEL script (not subroutine). The developed subroutines

- Compute the element shape functions at a given point in the local coordinate system
- Compute the element shape function derivatives at a given point in the local coordinate system

- Compute the global coordinates at a given local coordinate point (to compute effects of functional grading)
- Compute the Jacobian matrix, its inverse, and determinant at a given point in the local coordinate system
- Compute the deformation-degree of freedom matrix at a given point in the local coordinate system
- Compute the contributions to the stiffness matrix, and residual force vector at a given point in the local coordinate system (quadrature point). This process involves the contribution from the exponential grading

The main subroutine loops over the quadrature points, computing the overall contributions to the element stiffness matrix and residual force vector.

The post-processing code performs the following operations

- Define the appropriate structures and dictionaries needed to replicate the Abaqus output database hierarchy.
- Define input file reader function to parse input file and re-construct the mesh
- Define functions to read the CSV files and store the data into the appropriate structures
- Loop over analysis frames and steps to generate top-level Step and Frame objects and dictionaries to finalize the data hierarchy
- Loop over generated data structure to write one VTU file per analysis increment, using the procedure outlined by [97]

The resulting VTU files can be opened easily in Paraview, with the visualization offering a similar experience to that provided by Abaqus. From the user's perspective, running an analysis is rather simple. The user would generate an analysis input file, in which the select the the element type to correspond to the user element of their choice. They would then provide the material properties (adiabatic constants, grading vector), and run the analysis as usual, with the associated UEL attached. Once the analysis is complete, the user would simply run the post-processing code, with the only input being the location of the files. Once complete, the user would then proceed to open the generated VTU files in Paraview for a similar visualization experience to Abaqus.

The details pertaining to the quadrilateral and wedge elements, the quadrature rules used, and numerical examples are presented in the following sections.

4.3.2 20-noded Quadrilateral

Following from the construction of the finite element formulation in Section 4.3, a 20-noded isoparametric quadratic quadrilateral element can be designed with the nodal coordinates and numbering shown in Figure 4.2. The chosen node numbering follows the convention employed by Abaqus to facilitate integration into the software.

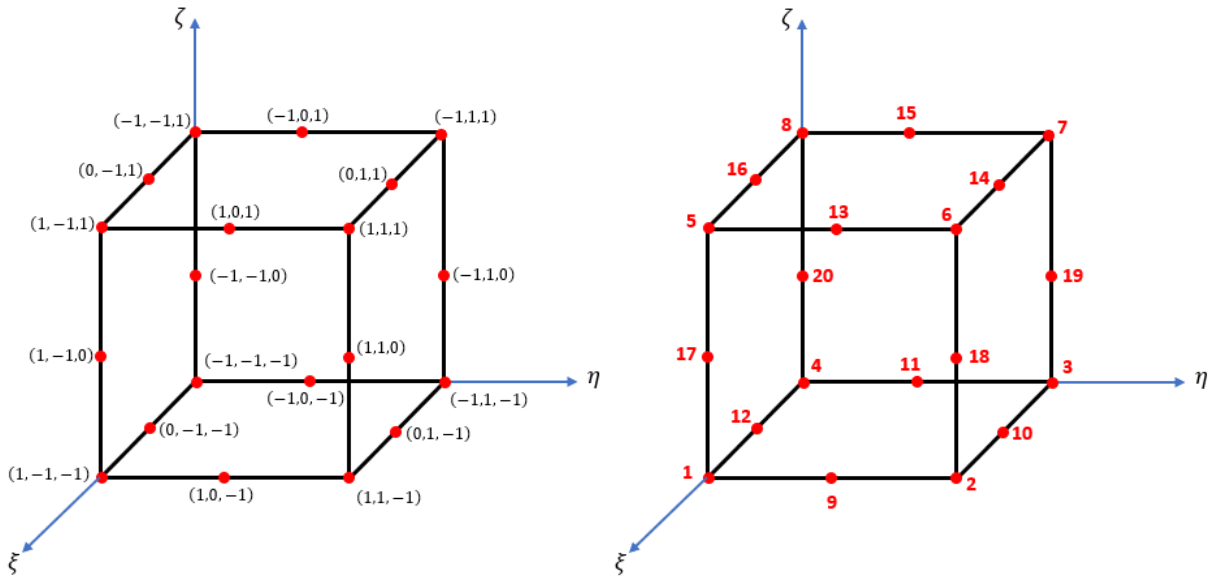

(a) (b)

Figure 4.2: (a) Nodal locations in local coordinate system (b) Nodal numbering convention used for quadrilateral element

The associated shape functions take the form

$$N_i = \frac{1}{8}\left(1+\xi_i\xi\right)\left(1+\eta_i\eta\right)\left(1+\zeta_i\zeta\right)\left(\xi_i\xi+\eta_i\eta+\zeta_i\zeta-2\right), \qquad i=1,\ldots,8 \tag{4.3.22}$$

$$N_i = \frac{1}{4}\left(1-\xi^2\right)\left(1+\eta_i\eta\right)\left(1+\zeta_i\zeta\right), \qquad i=10,12,14,16 \tag{4.3.23}$$

$$N_i = \frac{1}{4}\left(1+\xi_i\xi\right)\left(1-\eta^2\right)\left(1+\zeta_i\zeta\right), \qquad i=9,11,13,15 \tag{4.3.24}$$

$$N_i = \frac{1}{4}\left(1+\xi_i\xi\right)\left(1+\eta_i\eta\right)\left(1-\zeta^2\right), \qquad i=17,18,19,20 \tag{4.3.25}$$

in the natural coordinate system,where (ξ_i, η_i, ζ_i) represents the local coordinates of node i.

Given the definition of the shape functions, all the remains is to devise an adequate quadrature scheme in the local coordinate system to numerically compute the required integrals. Considering the integrals for the stiffness and force matrices in equation (4.3.20), one can see that the greatest complexity in the integrands is present in the integral for the stiffness matrix.

The deformation-displacement matrices each contribute terms of linear order in the local coordinate system, while the matrix of elastic constants contribute an exponential term, raised to the power of a linear order term in the global coordinate system. As such, one can consider the argument of the exponential term to be of quadratic order in the local coodinate system, resulting from the quadratic nature of the interpolation functions. Given the order of the individual terms, the integrand of the stiffness matrix will include terms of the form $a^2e^{a^2}$, where a represents the integrated variable.

In the absence of an appropriate quadrature rule for the integrated composite function, the number of quadrature points in each principal direction was selected based on

achieving Single Precision accuracy using typical Gauss-Legendre quadrature. Abaqus provides two scales of accuracy, with results being calculated using Single Precision (default), or Double Precision.

Within the realm of practical calculation, Single Precision is sufficient in capturing the desired accuracy of computations. The differences between Single Precision and Double Precision can be mainly attributed to the solver being used. In an Implicit, static analysis, the time step is much larger than in Explicit analyses, with round-off errors not accumulating given that the solver must satisfy a convergence tolerance [98]. In an Explicit analysis, the convergence criteria differs, with a smaller time step allowing for more round-off errors. Since the elements used in this study are designed for a static, Implicit time step, Single Precision will suffice to avoid round-off errors.

To achieve Single Precision accuracy for the aforementioned function, 8 quadrature points are necessary in each principal direction, resulting in an $8 \times 8 \times 8$ quadrature scheme. The Gauss points and weights are calculated by considering the roots of the 8^{th} order Legendre polynomial, defined below,

$$P_0(x) = 1$$

$$P_1(x) = x$$

$$(n+1)\,P_{n+1}(x) = (2n+1)\,xP_n(x) - nP_{n-1}(x) \tag{4.3.26}$$

$$\Rightarrow P_8(x) = \frac{1}{896}\left(45045x^8 - 84084x^6 + 48510x^4 - 8820x^2 + 245\right) \tag{4.3.27}$$

$$w_i = \frac{2}{\left(1 - x_i^2\right)\left[P_n'\left(x_i\right)\right]^2} \tag{4.3.28}$$

where x_i are the roots of the polynomial, and w_i are the associated weights. The roots and weights of the 8^{th} order polynomial are presented in Table 4.1.

Table 4.1: 8 point Gauss-Legendre quadrature scheme roots and associated weights

Gauss Point Location (x_i)	**Associated Weight** (w_i)
$\pm$0.18343464250	0.36268378338
$\pm$0.52553240992	0.31370664588
$\pm$0.79666647741	0.22238103445
$\pm$0.96028985650	0.10122853629

4.3.3 15-noded Wedge

To construct a 15-noded isoparametric quadratic wedge element, in a similar manner to the quadrilateral element, the node numbering convention used by Abaqus is followed, and can be seen in Figure 4.3.

The associated shape functions take the form

$$N_1 = \frac{1}{2}(1-\xi-\eta)(\zeta-1)(2\xi+2\eta+\zeta) \tag{4.3.29}$$

$$N_2 = \frac{1}{2}\xi(1-\zeta)(2\xi-\zeta-2) \tag{4.3.30}$$

$$N_3 = \frac{1}{2}\eta(1-\zeta)(2\eta-\zeta-2) \tag{4.3.31}$$

$$N_4 = \frac{1}{2}(1-\xi-\eta)(1+\zeta)(-2\xi-2\eta+\zeta) \tag{4.3.32}$$

$$N_5 = \frac{1}{2}\xi(1+\zeta)(2\xi+\zeta-2) \tag{4.3.33}$$

$$N_6 = \frac{1}{2}\eta(1+\zeta)(2\eta+\zeta-2) \tag{4.3.34}$$

$$N_7 = 2\xi(1-\xi-\eta)(1-\zeta) \tag{4.3.35}$$

$$N_8 = 2\xi\eta(1-\zeta) \tag{4.3.36}$$

$$N_9 = 2\eta(1-\xi-\eta)(1-\zeta) \tag{4.3.37}$$

$$N_{10} = 2\xi(1-\xi-\eta)(1+\zeta) \tag{4.3.38}$$

$$N_{11} = 2\xi\eta(1+\zeta) \tag{4.3.39}$$

$$N_{12} = 2\eta(1-\xi-\eta)(1+\zeta) \tag{4.3.40}$$

$$N_{13} = (1-\xi-\eta)\left(1-\zeta^2\right) \tag{4.3.41}$$

$$N_{14} = \xi\left(1-\zeta^2\right) \tag{4.3.42}$$

$$N_{15} = \eta\left(1-\zeta^2\right) \tag{4.3.43}$$

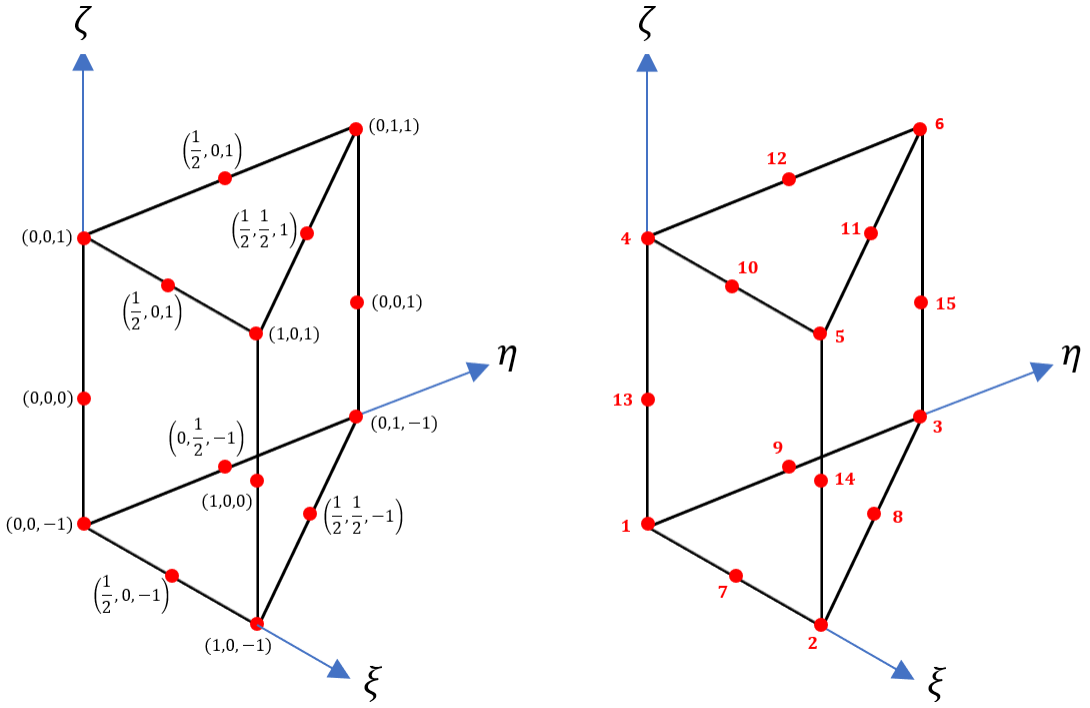

Figure 4.3: (a) Nodal locations in local coordinate system (b) Nodal numbering convention used for wedge element

Once again, all the remains is to devise an adequate quadrature scheme in the local coordinate system to numerically compute the required integrals. Following the same procedure used for the quadrilateral element to obtain the desired accuracy, a 9 point formula for integration over triangular domains is used, and extended to three dimensions using the 8 point rule for the quadrilateral. The approach for quadrature over triangles is outlined in [99], where the integration of an n^{th} degree polynomial is computed analytically and equated to the quadrature rule, obtaining a system of non-linear equations in terms of the quadrature points and weights. The procedure can be reduced

to solving

$$\iint f dA = A \sum_{i=1}^{N} w_i f\left(\xi_i, \eta_i\right), \tag{4.3.44}$$

where A represents the area of the triangle, ξ_i and η_i are the coordinates of the i^{th} sampling point, w_i is the associated weight, and f is the function to be integrated. Since the quadrature formulas must be exact for all polynomials of a complete set, one can write out the above equation for each such polynomial, generating a system of non-linear equations that must be solved. The results for each degree of accuracy are widely available in the literature, with the results for the selected 9 point scheme presented in Table 4.2.

Table 4.2: 9 point Gauss-Legendre quadrature scheme points and associated weights for 2D triangular domains

Gauss Point Location (ξ_i)	**Gauss Point Location** (η_i)	**Associated Weight** (w_i)
0.124949503233232	0.437525248383384	0.205950504760887
0.437525248383384	0.124949503233232	0.205950504760887
0.437525248383384	0.437525248383384	0.205950504760887
0.797112651860071	0.165409927389841	0.063691414286223
0.797112651860071	0.037477420750088	0.063691414286223
0.165409927389841	0.797112651860071	0.063691414286223
0.165409927389841	0.037477420750088	0.063691414286223
0.037477420750088	0.797112651860071	0.063691414286223
0.037477420750088	0.165409927389841	0.063691414286223

4.3.4 Numerical Examples - Classical Limit

Typically, verification of solutions to finite element analyses would require comparison with experimental tests. While measurement tools are becoming more refined as the field of nano fabrication expands, and preliminary measurements have been made, testing and measurement of microrotations is currently difficult due to the size at which measurements must take place.

Until such a time where these measurements become more accessible and commonplace, verification of the designed user elements, and by extension the solution to the formulated boundary value problems, will involve recovery of the classical limit. Such a verification only provides a foundational step to establishing the model as an analysis tool, as a full verification can only be done once the aforementioned measurements can take place. Nevertheless, recovery of the classical limit is an important first step.

To adequately verify the recovery of the classical limit, the Cosserat adiabatic elastic constants $(\alpha, \beta, \gamma, \varepsilon)$ are set to 0, which recovers the classical equilibrium equations. With regards to finite element modelling, three test cases are considered for the two individual elements, as well as an assembly of elements. The elements are tested and compared to Abaqus equivalents under uniaxial compression, shear, and torsion loading to ensure recovery of the classical limit.

The designed quadrilateral and wedge elements can be compared to their classical counterparts in Abaqus, labelled C3D20, C3D15, a 20 noded quadrilateral element and 15 noded wedge element, respectively. The material analysed represents a typical polymer with a Young's modulus of $1250MPa$ and Poisson's ratio of 0.25. These properties translate to values of $\lambda = \nu = 500\ MPa$.

In all comparisons, the individual displacement components, as well as stress components, are compared to ensure the classical limit is recovered. To ensure an adequate comparison, the same boundary conditions are employed in both models, with the addition of setting the three rotational degrees of freedom to 0 in the user element.

For the sake of conciseness, this chapter displays the comparisons for uniaxial compression, with the remaining two load cases appearing in Appendix A. Throughout what follows, the Dirichlet problem stated below is solved, with prescribed displacements imposing the required loading scenario. All displayed units are measured in N, mm, and MPa.

The boundary value problem considered (Dirichlet) is formulated as

$$\begin{aligned} &\underline{\boldsymbol{L}}\vec{\boldsymbol{U}} = \underline{\mathbf{0}} \quad \text{in } \Omega, \\ &\vec{\boldsymbol{U}} = \vec{\tilde{\boldsymbol{U}}} \quad \text{on } \partial\Omega_1, \\ &\vec{\boldsymbol{t}} = \vec{\mathbf{0}} \quad \text{on } \partial\Omega_2, \end{aligned} \tag{4.3.45}$$

where $\vec{\tilde{\boldsymbol{U}}}$ is the generalized displacement vector, prescribed on the Dirichlet part of the boundary $\partial\Omega_1$, and $\vec{\tilde{\boldsymbol{t}}}$ is the generalized traction vector prescribed on the Neumann part of the boundary $\partial\Omega_2$, where $\partial\Omega = \partial\Omega_1 \cup \partial\Omega_2$.

Single Quadrilateral Element - Uniaxial Compression

The solution to the Dirichlet problem for a single quadrilateral element (Figure 4.4) under uniaxial compression is solved and presented below, with the compression loading taking the form of a prescribed downward displacement of $0.1mm$ on all nodes on the top surface of the quadrilateral, and fixed conditions (all displacements and rotations set to 0) prescribed on the bottom surface.

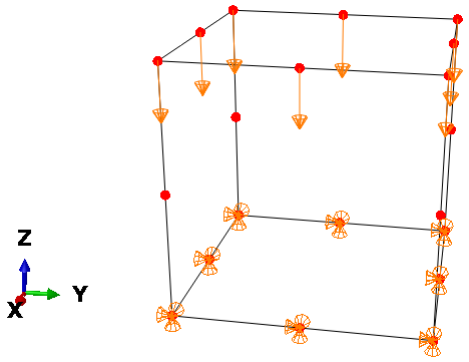

Figure 4.4: Boundary conditions and loading for single quadrilateral element (user/C3D20)

Figures 4.5-4.7 compare the displacement components, normal stresses, and shear stresses of the user element to Abaqus' C3D20 element at the final analysis increment.

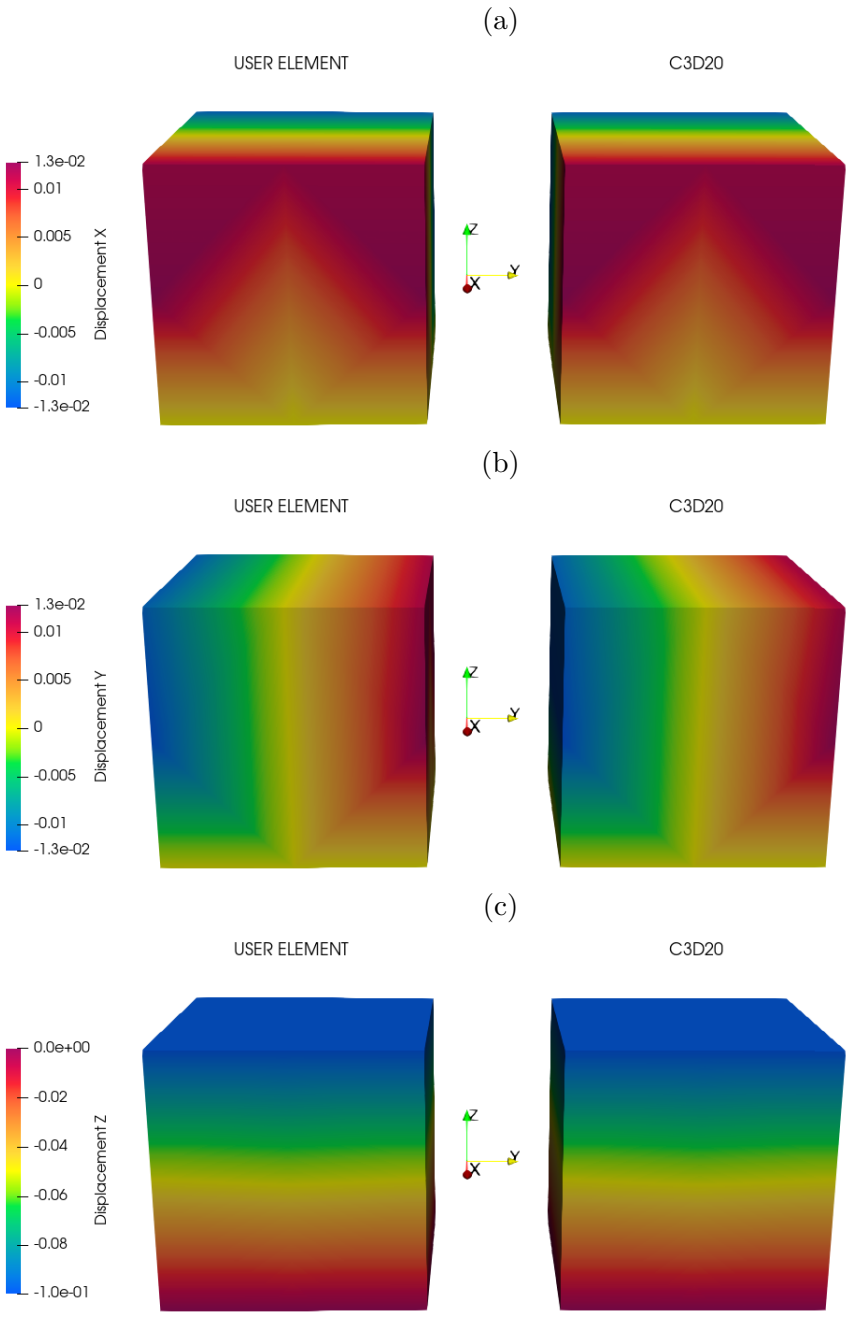

Figure 4.5: Comparison of nodal displacements between user element and Abaqus in the (a) x, (b) y, and (c) z directions for quadrilateral element under uniaxial compression

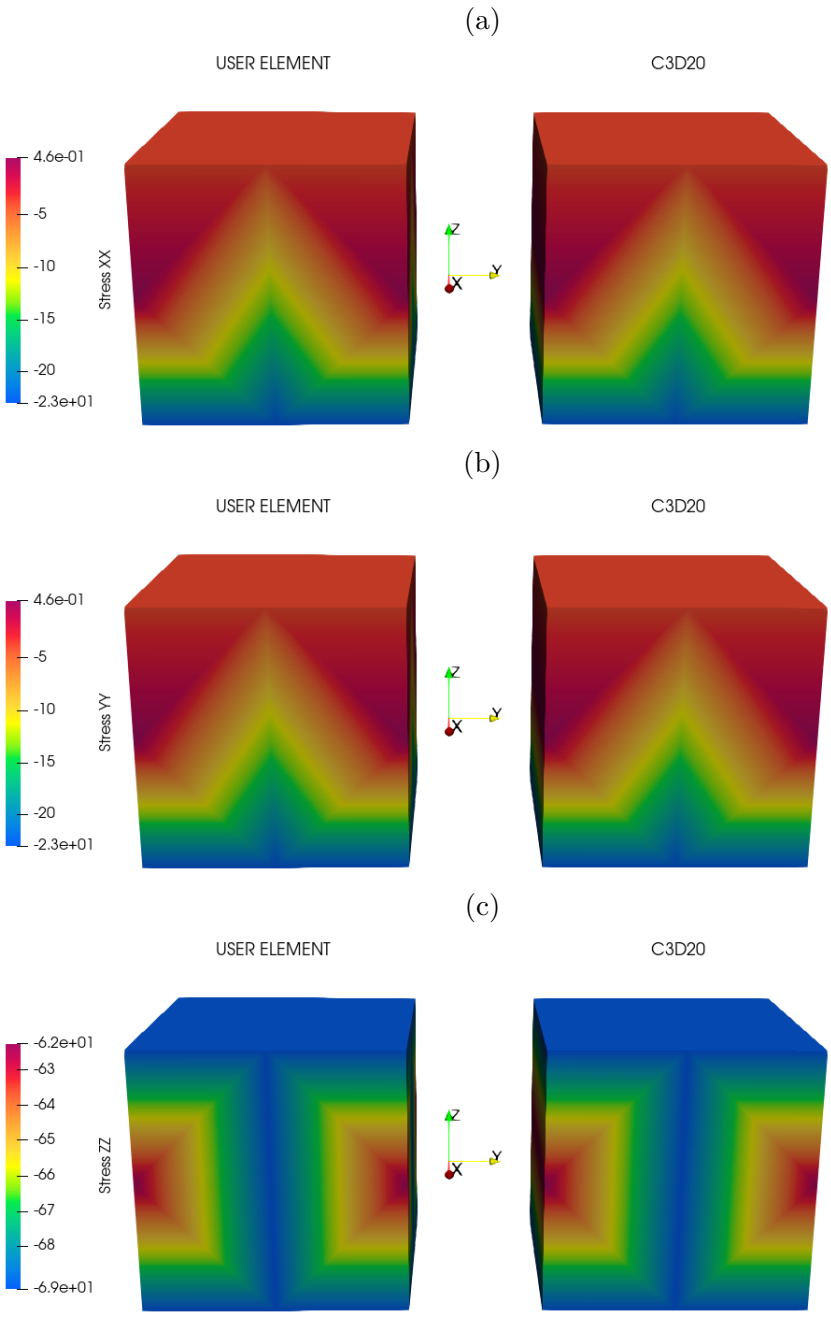

Figure 4.6: Comparison of nodal normal stress components (a) XX, (b) YY, and (c) ZZ between user element and Abaqus for quadrilateral element under uniaxial compression

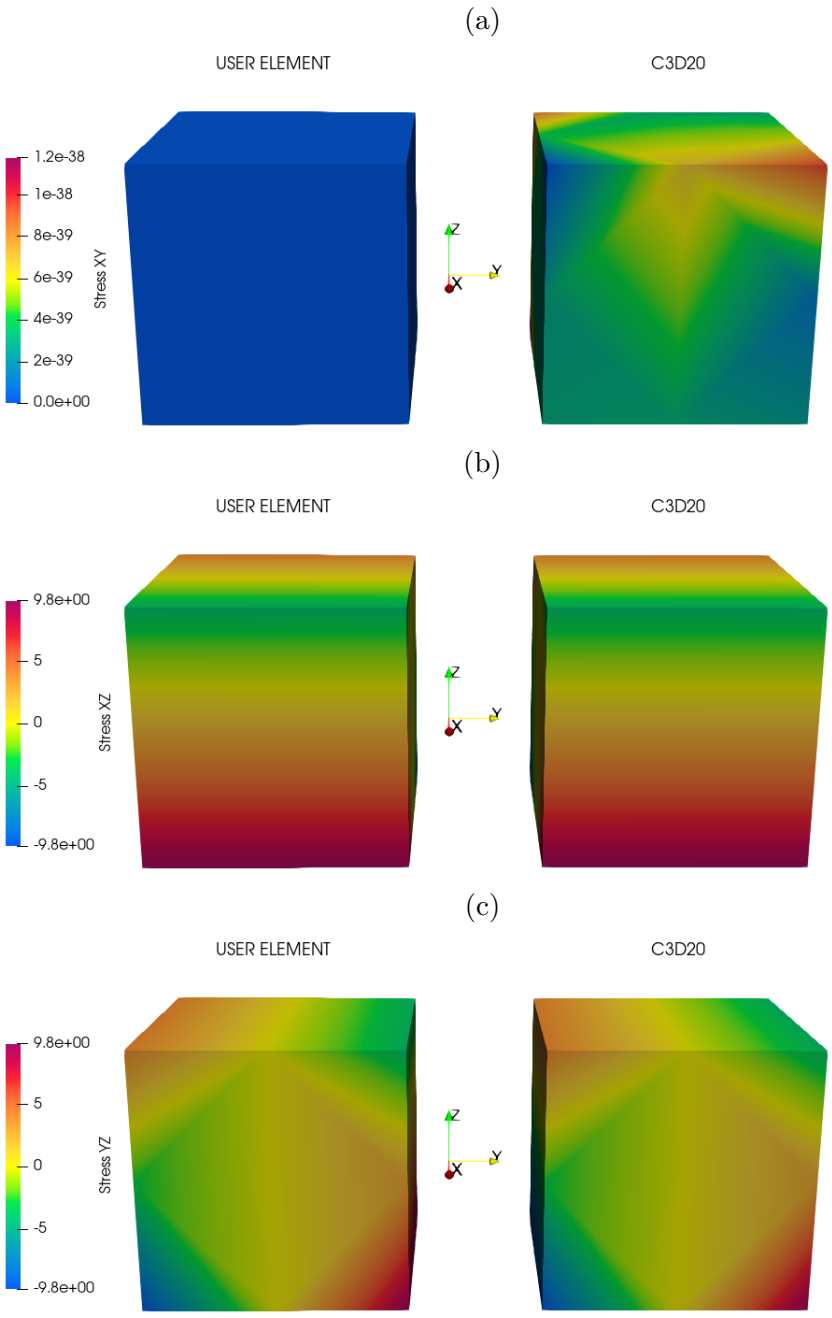

Figure 4.7: Comparison of nodal shear stress components (a) XY, (b) XZ, and (c) YZ between user element and Abaqus for quadrilateral element under uniaxial compression

The numerical values corresponding to the compared solutions displayed in Figures 4.5-4.7 are identical up to Single Precision order, with the shear stress component σ_{xy} in the user element differing from its classical counterpart by an order of $10^{-38}MPa$. This difference can be considered negligible, with the non-zero value in the classical element likely being attributed to fewer quadrature points ($3 \times 3 \times 3$) being considered.

Quadrilateral Element Assembly - Uniaxial Compression

The solution to the Dirichlet problem for a quadrilateral element assembly (Figure 4.8), comprising of 27 quadrilateral elements, under uniaxial compression is solved and presented below, with the compression loading taking the form of a prescribed downward displacement of $0.1mm$ on all nodes on the top surface of the quadrilateral, and fixed conditions (all displacements and rotations set to 0) prescribed on the bottom surface.

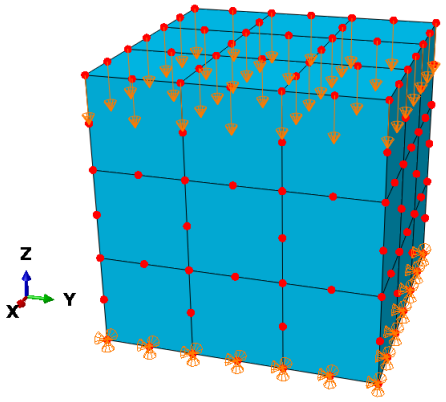

Figure 4.8: Boundary conditions and loading for 27 element quadrilateral element assembly (user/C3D20)

Figures 4.9-4.11 compare the displacement components, normal stresses, and shear stresses of the user element assembly to an equivalent C3D20 element assembly at the final analysis increment.

(a)

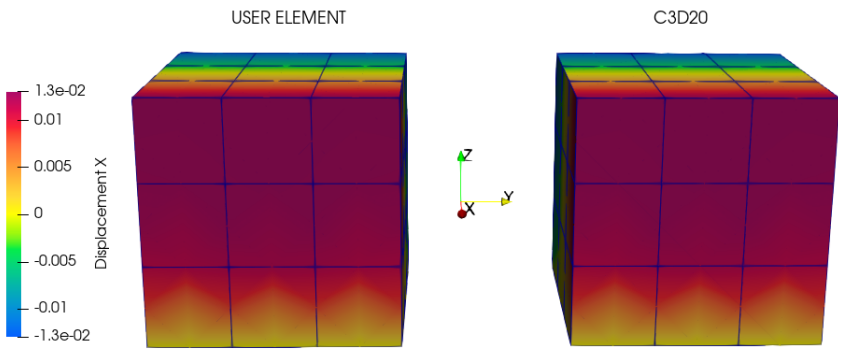

(b)

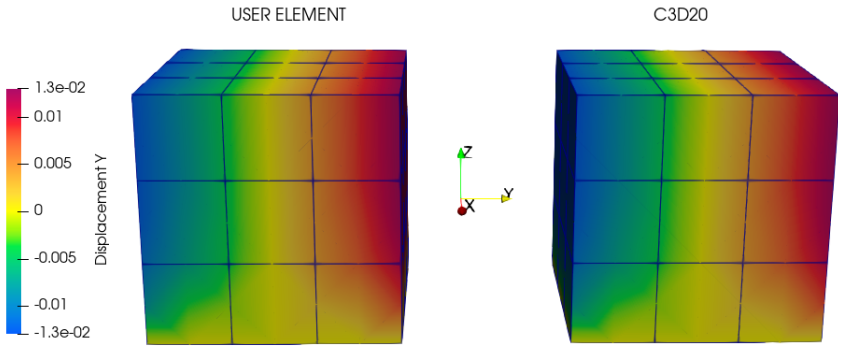

(c)

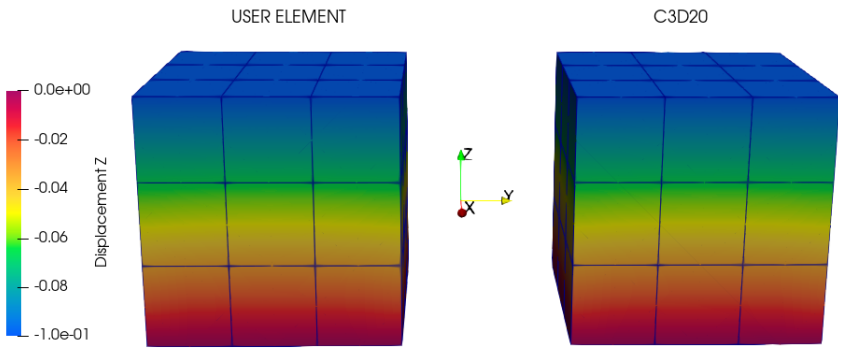

Figure 4.9: Comparison of nodal displacements between user element and Abaqus assemblies in the (a) x, (b) y, and (c) z directions for quadrilateral assembly under uniaxial compression

(a)

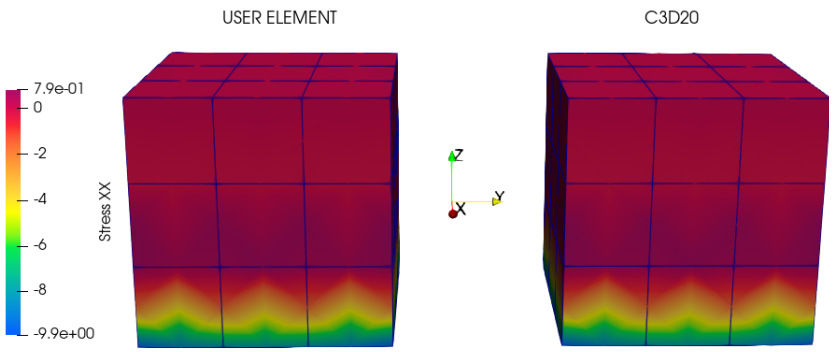

(b)

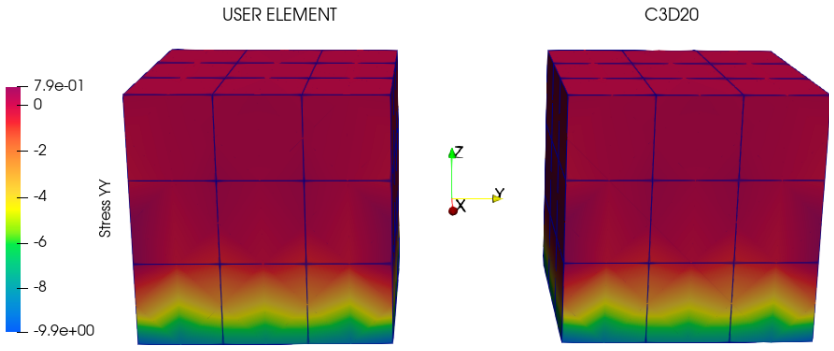

(c)

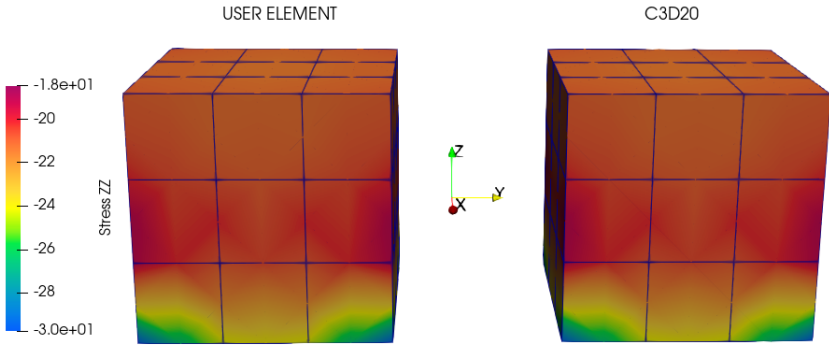

Figure 4.10: Comparison of nodal normal stress components (a) XX, (b) YY, and (c) ZZ between user element and Abaqus assemblies for quadrilateral assembly under uniaxial compression

(a)

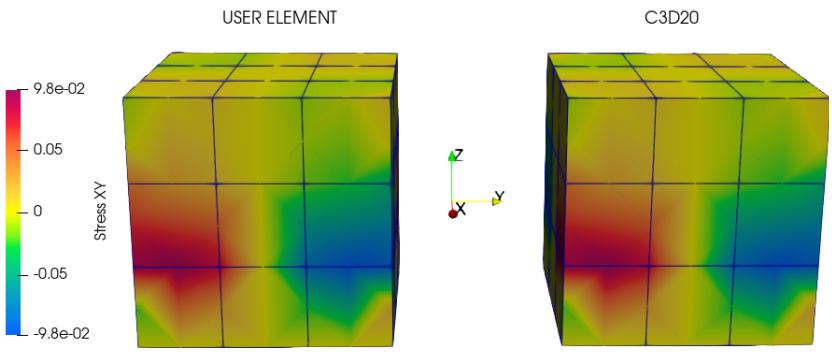

(b)

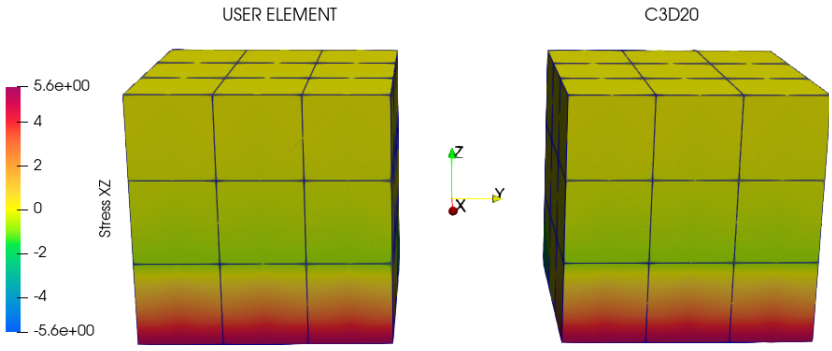

(c)

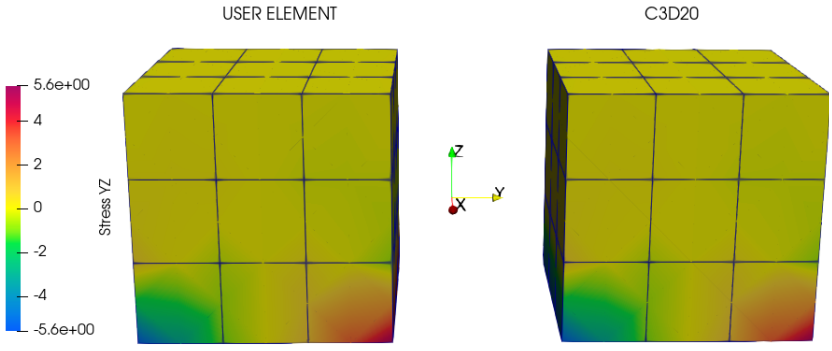

Figure 4.11: Comparison of nodal shear stress components (a) XY, (b) XZ, and (c) YZ between user element and Abaqus assemblies for quadrilateral assembly under uniaxial compression

The numerical values corresponding to the compared solutions displayed in Figures 4.9-4.11 are identical up to Single Precision order, with the shear stress component σ_{xy} difference observed for the single element no longer being present. The absence of this difference is simply attributed to the magnitude of the shear stress component being of order $10^{-2}MPa$, which is several times larger than the order of the difference observed in the single element. This suggests that the difference observed in the single element test does not propagate into a noticeable difference as the size of the assembly increases.

Single Wedge Element - Uniaxial Compression

The solution to the Dirichlet problem for a single wedge element (Figure 4.12) under uniaxial compression is solved and presented below, with the compression loading taking the form of a prescribed downward displacement of $0.1mm$ on all nodes on the top surface of the quadrilateral, and fixed conditions (all displacements and rotations set to 0) prescribed on the bottom surface.

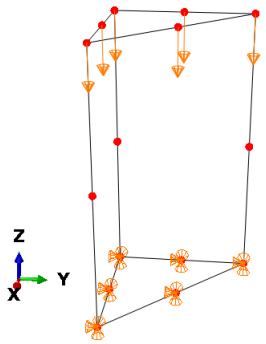

Figure 4.12: Boundary conditions and loading for single wedge element (user/C3D15)

Figures 4.13-4.15 compare the displacement components, normal stresses, and shear stresses of the user element to Abaqus' C3D15 element at the final analysis increment.

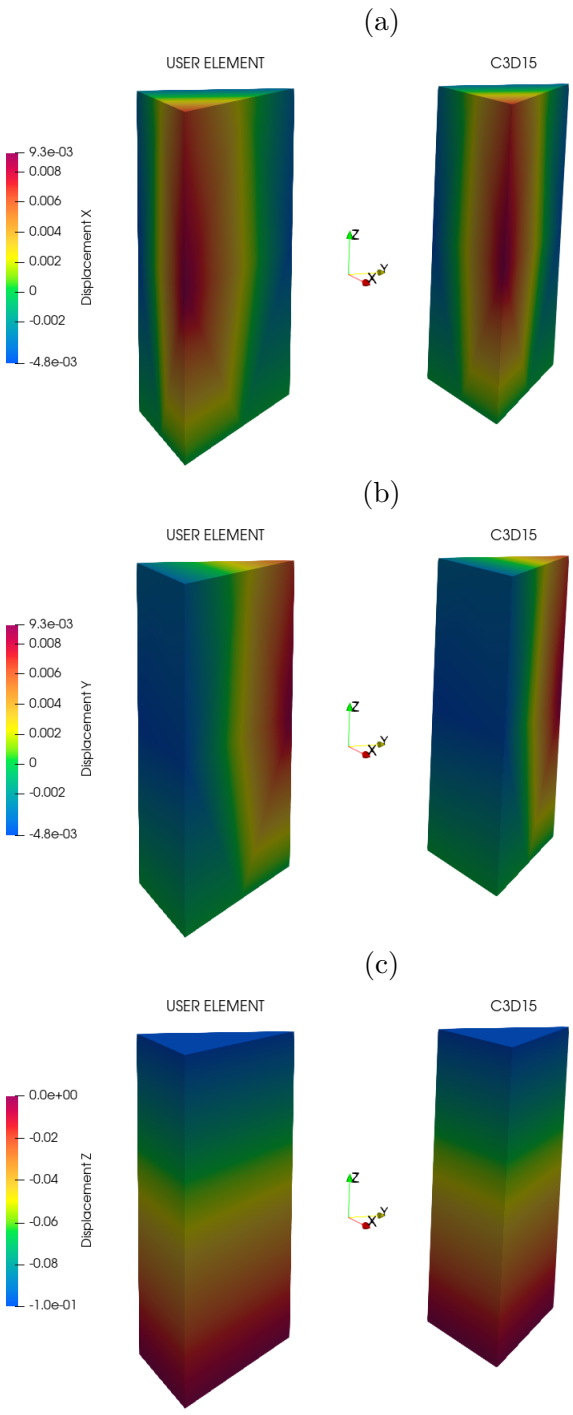

Figure 4.13: Comparison of nodal displacements between user element and Abaqus in the (a) x, (b) y, and (c) z directions for wedge element under uniaxial compression

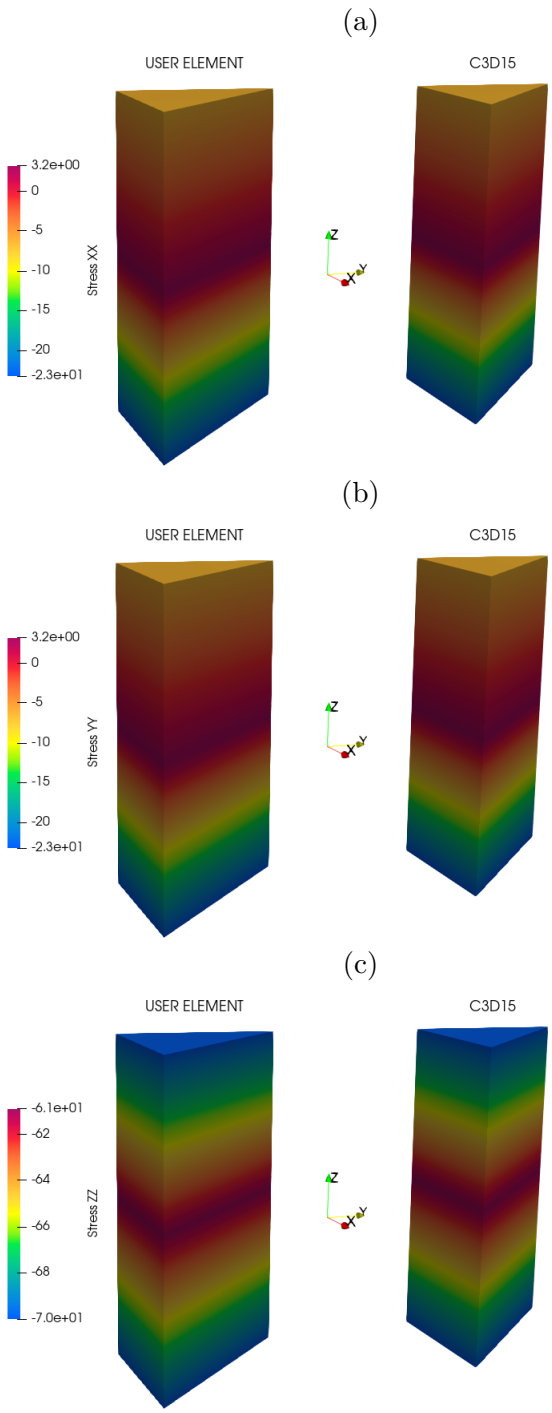

Figure 4.14: Comparison of nodal normal stress components (a) XX, (b) YY, and (c) ZZ between user element and Abaqus for wedge element under uniaxial compression

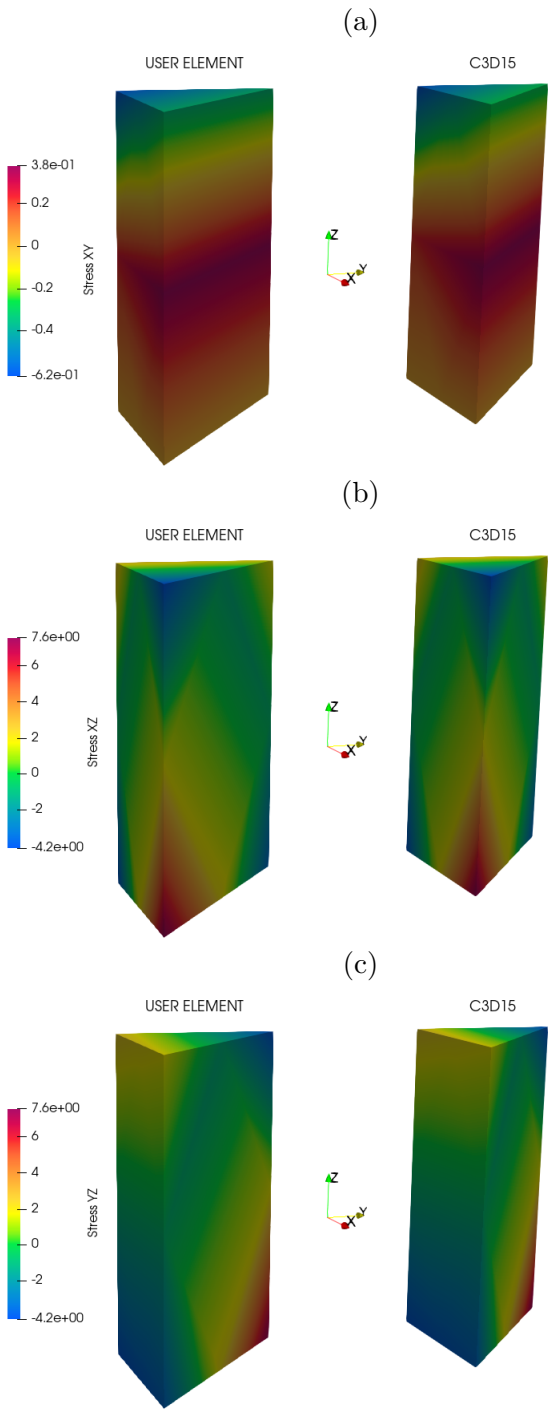

Figure 4.15: Comparison of nodal shear stress components (a) XY, (b) XZ, and (c) YZ between user element and Abaqus for wedge element under uniaxial compression

The numerical values corresponding to the compared solutions displayed in Figures 4.13-4.15 are identical up to Single Precision order, with the shear stress component σ_{xy} difference observed for the single quadrilateral element not present.

Wedge Element Assembly (Cylinder) - Uniaxial Compression

The solution to the Dirichlet problem for a cylindrical wedge element assembly (Figure 4.16), comprising of 36 wedge elements, under uniaxial compression is solved and presented below, with the compression loading taking the form of a prescribed downward displacement of $0.1mm$ on all nodes on the top surface of the quadrilateral, and fixed conditions (all displacements and rotations set to 0) prescribed on the bottom surface.

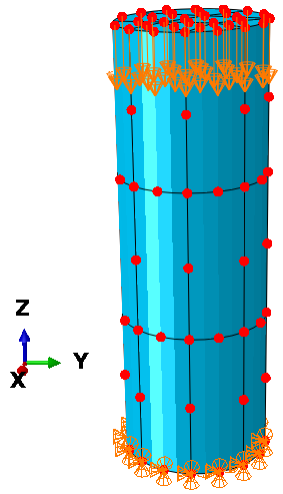

Figure 4.16: Boundary conditions and loading for 36 element cylindrical wedge element assembly (user/C3D15)

Figures 4.17-4.19 compare the displacement components, normal stresses, and shear stresses of the user element assembly to an equivalent C3D15 element assembly at the final analysis increment.

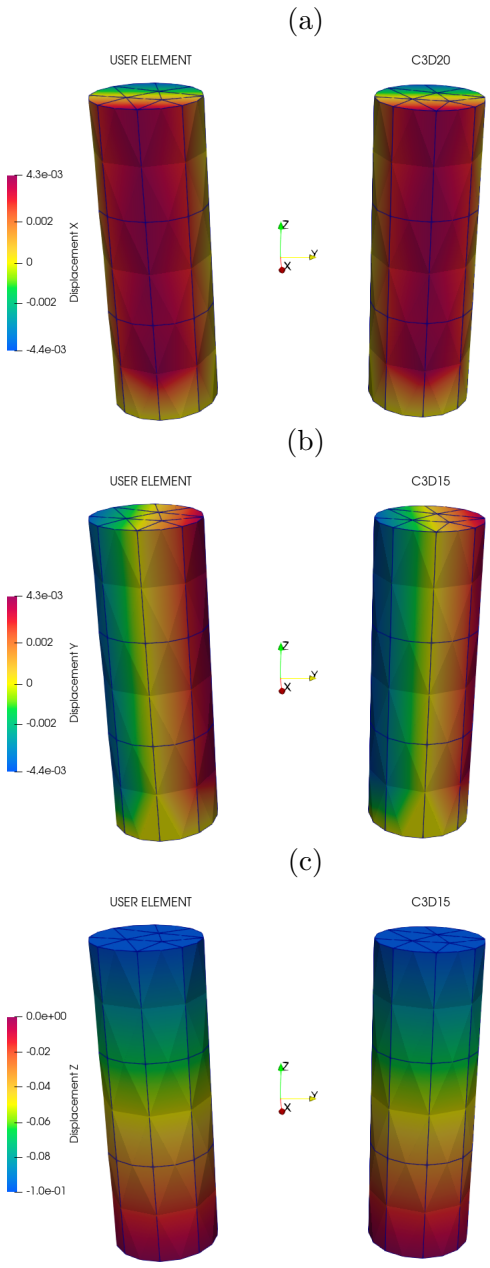

Figure 4.17: Comparison of nodal displacements between user element and Abaqus assemblies in the (a) x, (b) y, and (c) z directions for wedge assembly under uniaxial compression

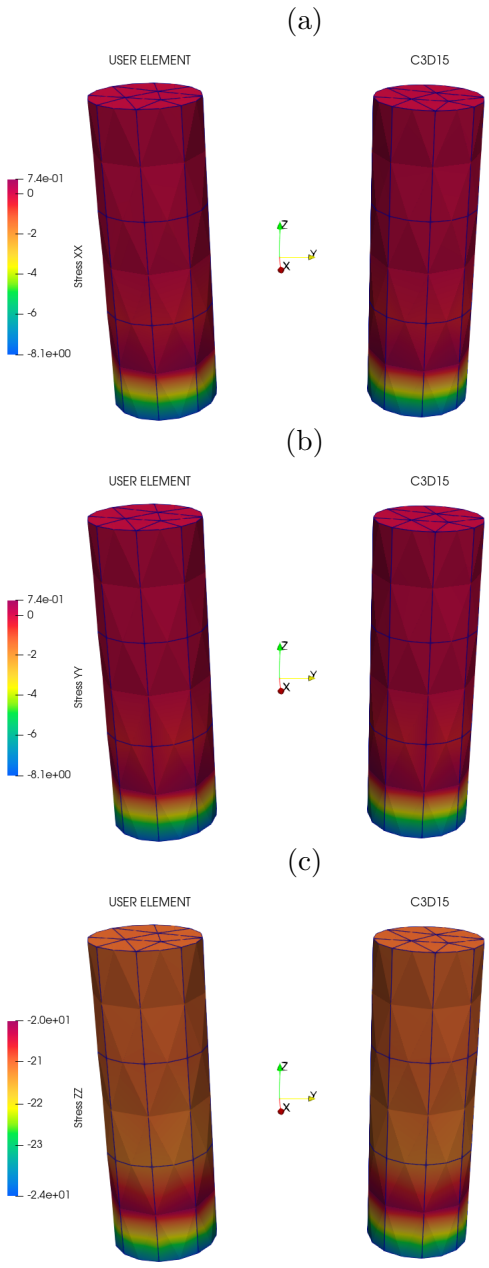

Figure 4.18: Comparison of nodal normal stress components (a) XX, (b) YY, and (c) ZZ between user element and Abaqus assemblies for wedge assembly under uniaxial compression

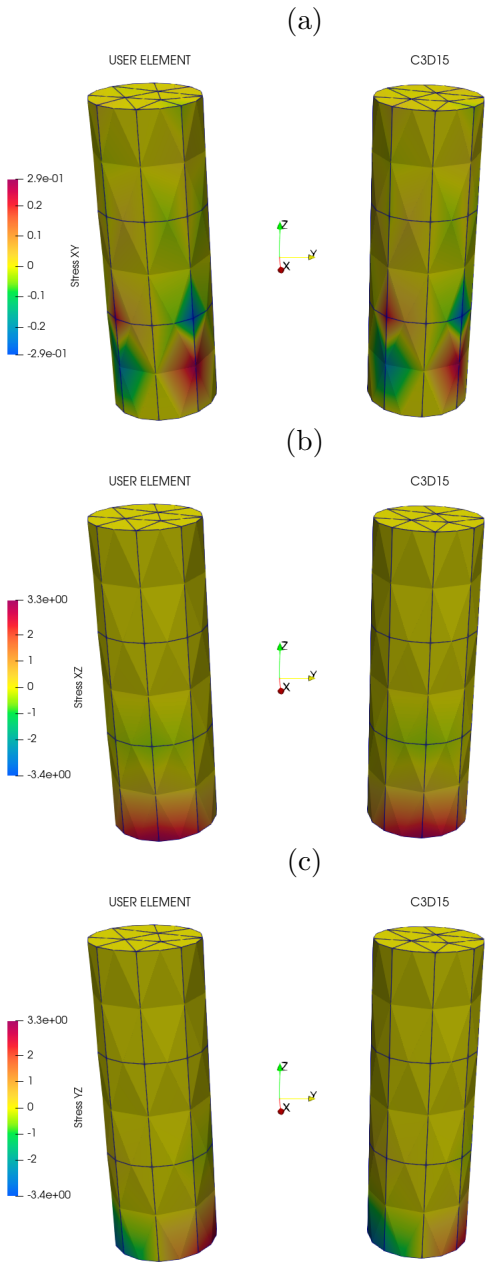

Figure 4.19: Comparison of nodal shear stress components (a) XY, (b) XZ, and (c) YZ between user element and Abaqus assemblies for wedge assembly under uniaxial compression

The numerical values corresponding to the compared solutions displayed in Figures 4.17-4.19 are identical up to Single Precision order, completing the recovery of the classical limit in the case of uniaxial compression for the designed elements as well as assemblies of the elements.

Appendix A contains the remaining loading scenarios, with the comparisons to the C3D20 and C3D15 elements and their assemblies displaying the same trends for the cases of shear and torsion. In all cases, the results are identical up to Single precision order, validating recovery of the classical limit.

4.3.5 Numerical Examples - Conceptual Cases on Elements

While the proposed model cannot be fully validated until proper experimental measurements can be made, this work aims to demonstrate the model's future applicability by considering conceptual cases in which the classical solution is compared to solutions in which only Cosserat effects are considered, only exponential grading is considered, and a case in which both effects are considered.

The cases of uniaxial compression, shear, and torsion loading will once again be considered in the context of the Dirichlet problem for the quadrilateral and wedge single element, and assembly configurations analysed in Section 4.3.4. These conceptual analyses aim to provide a proof of concept for the developed analysis tool, and help future users understand the influence of the model parameters on the solution.

The following analyses will display the results for the load case in which the most significant differences arise (torsion), with the remaining cases being displayed in

Appendix B. In all analyses presented in this section and Appendix B, the material elastic constants considered are $\lambda = \mu = 500\ MPa$ in all cases, $\alpha = 500\ MPa$, $\beta = \gamma = \varepsilon = 500\ N$ in all cases with Cosserat effects, and a chosen grading vector of $\vec{\boldsymbol{G}} = (1, 1, 1)$ in all cases where exponential grading is considered. These values are chosen arbitrarily as no robust measurements of the parameters have been made experimentally, and only serve to display a proof of concept.

To present the results in a concise manner and avoid displaying the individual components of displacement, microrotation, stress, and couple stress for each case, only the relevant quantities are displayed in the main body of the thesis. For the complete set of results, the reader is directed to Appendix B.

Single Quadrilateral Element - Torsion

The solution to the Dirichlet problem for a single quadrilateral element under torsion loading is solved and presented below, with the torsion loading taking the form of prescribed displacements of $0.1mm$ in opposing directions on the top surface nodes to simulate a force couple. The bottom nodes of the quadrilateral are fixed (all displacements and rotations set to 0). Figure 4.20 illustrates the loading and boundary conditions.

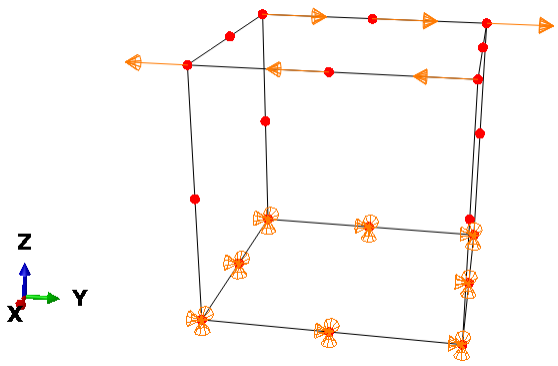

Figure 4.20: Boundary conditions and loading for single quadrilateral element in torsion

Table 4.3: Ranges for magnitudes of tensors of interest for quadrilateral element under torsion

Tensor Magnitude	**Classical**	**Cosserat**	**Exponential Grading**	**Exponential Grading with Cosserat**
$\|\vec{\boldsymbol{u}}\|_{min}\,(mm)$	0	0	0	0
$\|\vec{\boldsymbol{u}}\|_{max}\,(mm)$	0.1173	0.1042	0.1	0.1062
$\|\vec{\boldsymbol{\varphi}}\|_{min}\,(rad)$	0	0	0	0
$\|\vec{\boldsymbol{\varphi}}\|_{max}\,(rad)$	0	0.04040	0	0.0436
$\|\vec{\boldsymbol{\sigma}}\|_{min}\,(MPa)$	20.9006	5.6464	4.8047	3.0801
$\|\vec{\boldsymbol{\sigma}}\|_{max}\,(MPa)$	52.1183	101.8299	850.3520	543.0272
$\|\vec{\boldsymbol{\mu}}\|_{min}\,(MPa \cdot mm)$	0	21.7250	0	3.6057
$\|\vec{\boldsymbol{\mu}}\|_{max}\,(MPa \cdot mm)$	0	40.5563	0	286.2751

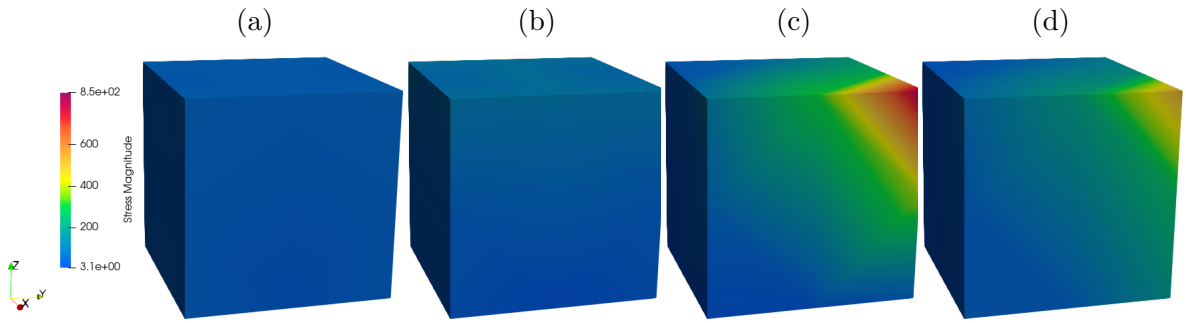

Figure 4.21: Comparison of nodal stresses vector magnitude for (a) classical, (b) Cosserat, (c) functionally graded, and (d) functionally graded with Cosserat effects cases for a quadrilateral element under torsion

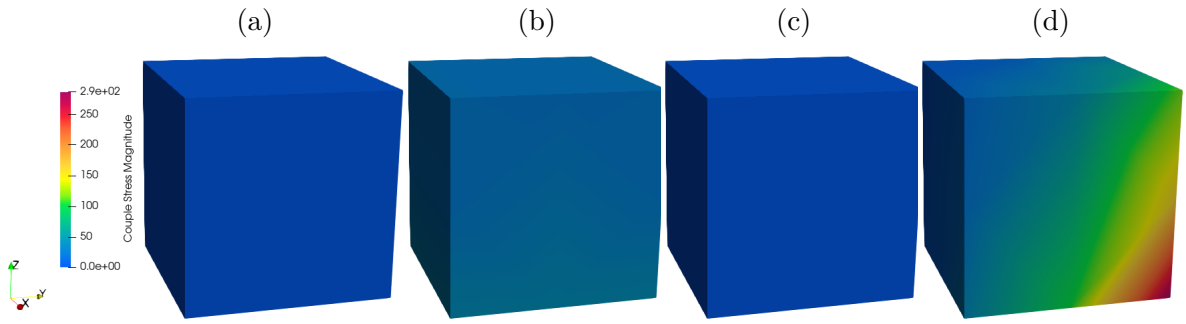

Figure 4.22: Comparison of nodal couple stresses vector magnitude for (a) classical, (b) Cosserat, (c) functionally graded, and (d) functionally graded with Cosserat effects cases for a quadrilateral element under torsion

Figure 4.21 displays the stress response of the torqued quadrilateral element. While the classical (a), and Cosserat without grading (b) cases appear to display no stresses in comparison to the graded cases, they do exhibit a stress tensor magnitude in the vicinity of $20 - 100MPa$. The reason for the difference in observed magnitude with the graded cases is due to the influence of the grading vector. The grading vector significantly stiffens the material as it tends towards the point $(1, 1, 1)$, resulting in a localization of stresses two orders of magnitude larger than the non graded cases. This suggests a

significant sensitivity of the stress response to the chosen grading vector. To avoid obtaining undesirable stress concentrations, careful consideration of the grading parameters must be taken into account.

Figure 4.22 displays the couple stress response of the compressed quadrilateral element. The classical (a), and exponential grading (c) cases display no couple stresses due a lack of Cosserat parameters. The Cosserat (b) and Cosserat with exponential grading (d) cases exhibit a similar redistribution of couple stresses, with the highest localization occurring at the fixed nodes opposing the stiffest portion of the material.

Considering the ranges for the stress magnitudes in Table 4.3, one can consider the influence of the Cosserat parameters to be in the form of a stress redistribution. To further investigate these effects, the percentage change in stress magnitude of the different cases relative to classical case are considered in Figure 4.23.

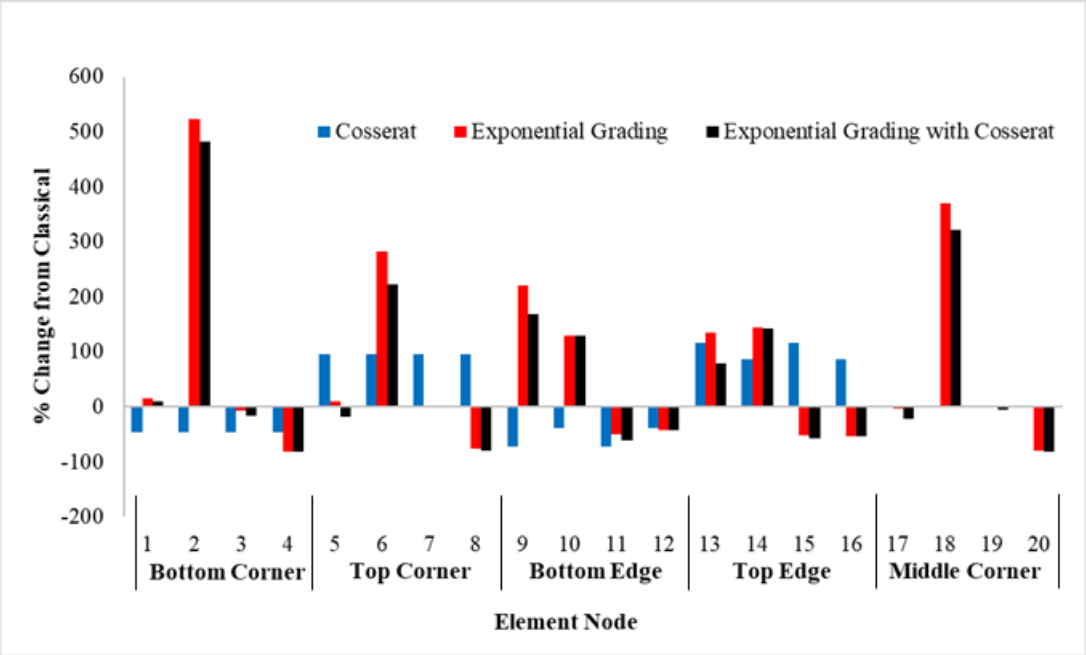

Figure 4.23: Percentage change in stress magnitude relative to classical case for single quadrilateral element in torsion

Comparing the response for the classical element to the element with Cosserat effects only in Figure 4.23, the stresses at the fixed nodes appear to decrease, while the stresses at the loaded nodes appear to increase. One possible explanation for this redistribution is the dependence on the Cosserat strain measure on the nodal microrotations. In addition to the linear deformation, the applied loading acts to warp the nodes on the loading surface, altering the magnitude of the strain measure. The nature of the alteration depends on the loading, as the induced warping can act to increase, or decrease, the strain at a given point.

The cases of uniaxial compression and shear (Appendix B) display less prominent microstructural effects, with a slight redistribution being present in the case of shear

loading, and negligible microstructural effects being present in the case of uniaxial compression. These results are in accordance with the experiments discussed in Chapter 2.2, in which uniaxial compression did not display significant Cosserat effects.

Quadrilateral Element Assembly- Torsion

The solution to the Dirichlet problem for a quadrilateral element assembly under torsion loading is solved and presented below, with the torsion loading taking the form of prescribed displacements of $0.1mm$ in opposing directions on the top surface nodes to simulate a force couple. The bottom nodes of the quadrilateral are fixed (all displacements and rotations set to 0). Figure 4.24 illustrates the loading and boundary conditions.

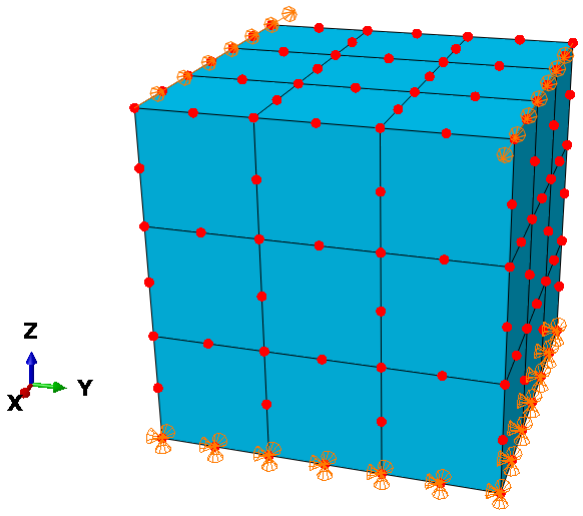

Figure 4.24: Boundary conditions and loading for quadrilateral element assembly in torsion

Table 4.4: Ranges for magnitudes of tensors of interest for quadrilateral element assembly under torsion

Tensor Magnitude	**Classical**	**Cosserat**	**Exponential Grading**	**Exponential Grading with Cosserat**
$\|\vec{\boldsymbol{u}}\|_{min}\,(mm)$	0	0	0	0
$\|\vec{\boldsymbol{u}}\|_{max}\,(mm)$	0.1210	0.1137	0.1376	0.1277
$\|\vec{\boldsymbol{\varphi}}\|_{min}\,(rad)$	0	0	0	0
$\|\vec{\boldsymbol{\varphi}}\|_{max}\,(rad)$	0	0.0284	0	0.04360
$\|\vec{\boldsymbol{\sigma}}\|_{min}\,(MPa)$	2.1259	2.1327	0.0185	0.0271
$\|\vec{\boldsymbol{\sigma}}\|_{max}\,(MPa)$	39.7725	40.9494	3843.9182	3773.5657
$\|\vec{\boldsymbol{\mu}}\|_{min}\,(MPa \cdot mm)$	0	3.6908	0	0.0081
$\|\vec{\boldsymbol{\mu}}\|_{max}\,(MPa \cdot mm)$	0	9.0501	0	3051.8681

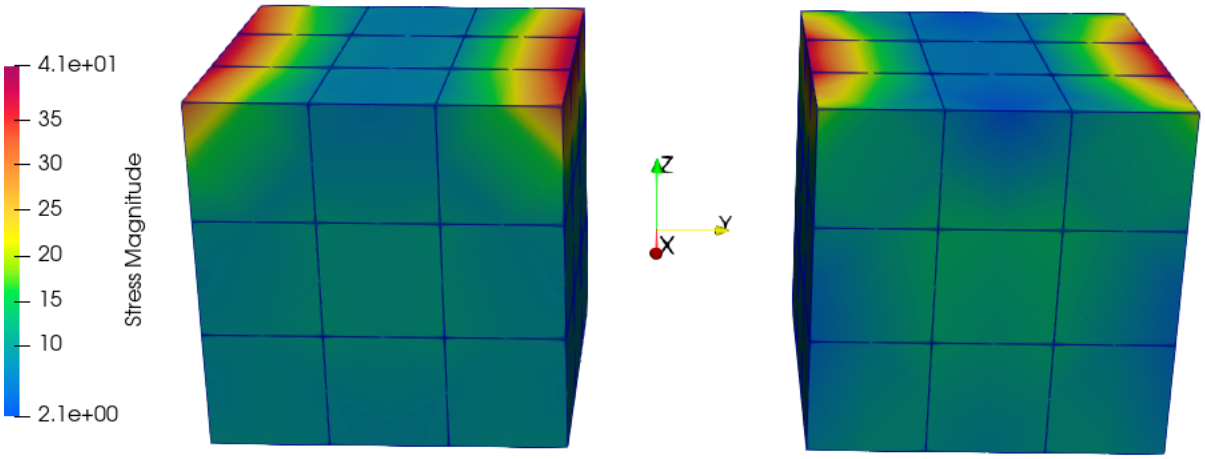

Figure 4.25: Comparison of stress tensor magnitude for quadrilateral element assembly in torsion for classical (right) and Cosserat (left) cases

Comparing the values for the stresses and couple stresses shown in Table 4.4 in the exponentially graded and ungraded cases, the same pattern observed in the single quadrilateral test emerges. The magnitude of the stresses increases significantly, once again due to the exponential grading redistributing the stresses to the stiffest portions of the material. This behaviour is constant throughout all element tests and is consistent with the expected behaviour.

With regards to the stresses in the Cosserat and classical cases, the difference in the magnitude of the stress tensors is minimal. This behaviour differs from the single quadrilateral element and suggests the presence of a size effect. The comparison is further explored by comparing the stress magnitudes in Figure 4.25. The results show a localization of stresses at the load application points, similar in magnitude. Figure 4.25 illustrates the presence of stress redistribution, with the localization of stresses shifting from the edges where the loads are applied towards the associated edge nodes. This redistribution is noticeably smaller than that observed in the single element test.

The difference in the observed stress redistribution compared to the single element tests suggests a relationship between the inherent microstructural length scale present in the Cosserat elasticity model and the size of the specimen. As discussed in Chapter 2.2, several studies indicated a trend in which microstructural effects were more prominent the closer the size of the specimen was to the microstructural length scale.

Single Wedge Element- Torsion

The solution to the Dirichlet problem for a wedge element under torsion loading is solved and presented below, with the torsion loading taking the form of prescribed displacements of $0.1mm$ in opposing directions on the top surface nodes to simulate a force couple. The bottom nodes of the quadrilateral are fixed (all displacements and rotations set to 0). Figure 4.26 illustrates the loading and boundary conditions.

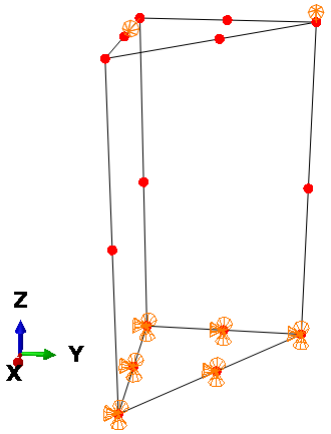

Figure 4.26: Boundary conditions and loading for single wedge element in torsion

Table 4.5: Ranges for magnitudes of tensors of interest for single wedge element in torsion

Tensor Magnitude	**Classical**	**Cosserat**	**Exponential Grading**	**Exponential Grading with Cosserat**
$\|\vec{\boldsymbol{u}}\|_{min}\,(mm)$	0	0	0	0
$\|\vec{\boldsymbol{u}}\|_{max}\,(mm)$	0.1553	0.1016	0.1527	0.1021
$\|\vec{\boldsymbol{\varphi}}\|_{min}\,(rad)$	0	0	0	0
$\|\vec{\boldsymbol{\varphi}}\|_{max}\,(rad)$	0	0.0526	0	0.0506
$\|\vec{\boldsymbol{\sigma}}\|_{min}\,(MPa)$	13.9622	8.5089	28.8933	9.9589
$\|\vec{\boldsymbol{\sigma}}\|_{max}\,(MPa)$	64.7636	224.3267	121.8205	551.1409
$\|\vec{\boldsymbol{\mu}}\|_{min}\,(MPa \cdot mm)$	0	24.6688	0	28.9863
$\|\vec{\boldsymbol{\mu}}\|_{max}\,(MPa \cdot mm)$	0	46.296	0	121.6067

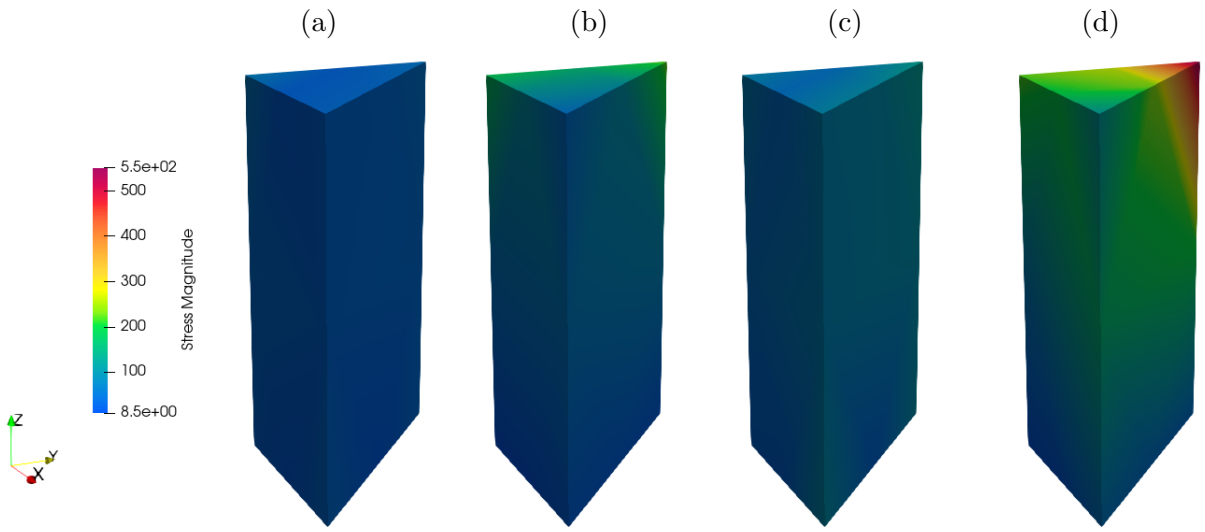

Figure 4.27: Comparison of nodal stresses vector magnitude for (a) classical, (b) Cosserat, (c) functionally graded, and (d) functionally graded with Cosserat effects cases for a wedge element under torsion

Comparing the magnitudes of the stresses in the Cosserat and classical cases, the difference in very significant is comparison to the other element tests. Both Table 4.5 and Figure 4.27 display a noticeable difference in the stresses between the classical and Cosserat cases, with the redistribution being prominent enough to compare with the functionally graded cases. The increase in stresses at the load application point can be attributed to the load application itself, as the couple is applied to two out of the 3 top corner nodes. Due to the nature of the wedge element, a centrally symmetric couple is difficult to apply. As a result, excessive warping is induced along the edge joining the two nodes, resulting in a significantly larger, localized stress magnitude. The findings suggest that careful consideration is required in how loads are applied to individual wedge elements.

With regards to the influence of exponential grading, Figure 4.27 reinforces the notion that grading effects dominate the stress redistribution in the direction of the grading vector. To ensure a smooth transition in material properties and avoid significant localization, the magnitude of the grading vector must remain quite small; a parametric study is recommended.

Wedge Element Assembly- Torsion

The solution to the Dirichlet problem for a cylindrical wedge element assembly under torsion loading is solved and presented below, with the torsion loading taking the form of prescribed displacements of $0.1mm$ in opposing directions on the top surface nodes to simulate a force couple. The bottom nodes of the quadrilateral are fixed (all displacements and rotations set to 0). Figure 4.28 illustrates the loading and boundary conditions.

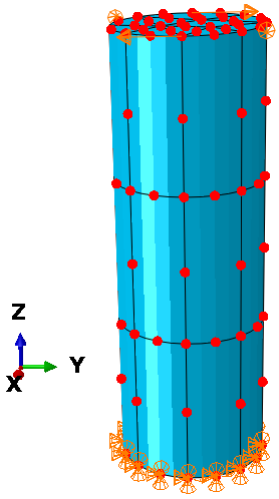

Figure 4.28: Boundary conditions and loading for cylindrical wedge element assembly in torsion

Table 4.6: Ranges for magnitudes of tensors of interest for cylindrical wedge element assembly in torsion

Tensor Magnitude	**Classical**	**Cosserat**	**Exponential Grading**	**Exponential Grading with Cosserat**
$\|\vec{\boldsymbol{u}}\|_{min}\,(mm)$	0	0	0	0
$\|\vec{\boldsymbol{u}}\|_{max}\,(mm)$	0.1046	0.1	0.1008	0.1044
$\|\vec{\boldsymbol{\varphi}}\|_{min}\,(rad)$	0	0	0	0
$\|\vec{\boldsymbol{\varphi}}\|_{max}\,(rad)$	0	0.0678	0	0.0635
$\|\vec{\boldsymbol{\sigma}}\|_{min}\,(MPa)$	0.9384	1.0787	0.6026	1.3333
$\|\vec{\boldsymbol{\sigma}}\|_{max}\,(MPa)$	24.3715	90.4330	35.3645	110.3864
$\|\vec{\boldsymbol{\mu}}\|_{min}\,(MPa \cdot mm)$	0	8.5542	0	2.8222
$\|\vec{\boldsymbol{\mu}}\|_{max}\,(MPa \cdot mm)$	0	17.5964	0	64.5506

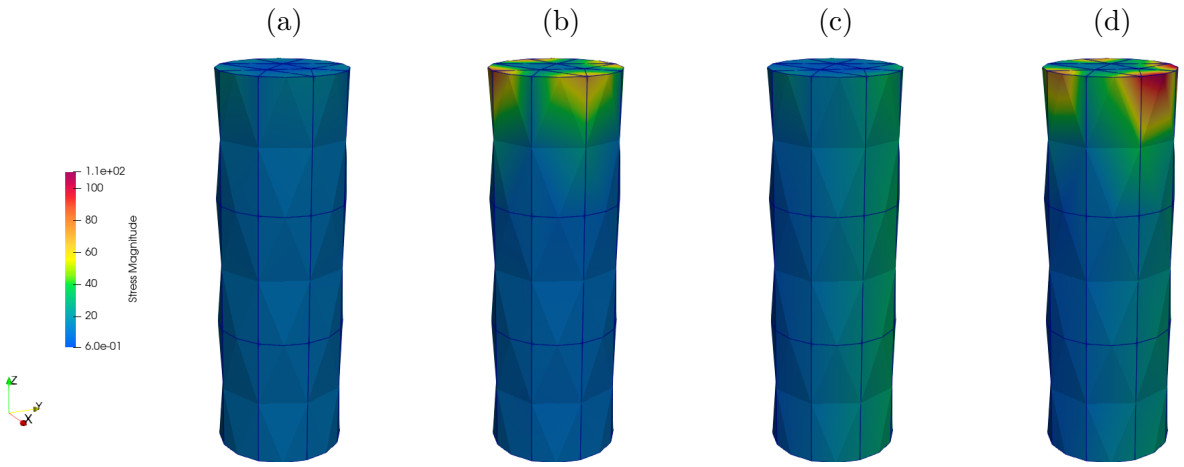

Figure 4.29: Comparison of nodal stresses vector magnitude for (a) classical, (b) Cosserat, (c) functionally graded, and (d) functionally graded with Cosserat effects cases for a wedge element assembly under torsion

Comparing the magnitudes of the stresses in the Cosserat and classical cases, the difference is still significant in comparison to the other element tests, but less pronounced than in the individual element test. Both Table 4.6 and Figure 4.29 display, once again, a noticeable difference in the stresses between the classical and Cosserat cases. These localized stresses appear exactly at the load application nodes, indicating a sensitivity to the load application method for wedge elements in torsion. Once again, the microstructural effects are less pronounced in the assembly models, suggesting the presence of size effects.

Once again, the sensitivity to the grading vector can be observed in Figure 4.29, where the stresses are more localized at the stiffest material points. Appendix B further illustrates the influence of load type on the response, as torsion loading prompts a significant microstructural response, with shear loading prompting a less significant response, and compression loading yielding the least sensitive response.

4.3.6 Numerical Examples - Parametric Study on Torsional Characteristic Length

To further exemplify the applicability of the proposed model, a parametric study on the influence of the torsional characteristic length defined in Section 2.5 is conducted on cylindrical specimens under torsional loading. The aim of the study is to replicate the size effect trends observed by Rueger and Lakes [14], to investigate the influence of the torsional characteristic length on the response of exponentially graded cylinders, and ascertain whether grading the cylinder along its axis will affect the torsional properties.

To conduct the investigation, a cylinder with a length of 10 mm is torqued about its axis through a rigid attachment. Since the Dirichlet problem is solved, the torque is applied through a displacement couple acting on a rigid attachment at the top of the cylinder, shown in Figure 4.30. In all cases, the ends of the rigid attachment are displaced 0.4 mm to generate a clockwise moment about the z-axis (axis of cylinder).

The rigid attachment is treated as a classical material, with a Young's modulus of 8000 MPa (and Poisson's ratio of 0.25), approximately eight times stiffer than the stiffest portion of the cylinder. The assembly is modelled a single part, with the mesh consisting entirely of the designed quadratic wedge elements. The cylinder is fixed at its base, with the boundary conditions shown in Figure 4.30.

The obtained results are presented in terms of the shear stresses σ_{xz}, representing the torsional shear stresses, couple stresses for cases with Cosserat material properties, and applied moment versus curvature responses to provide context to the torsional properties of the cylinder.

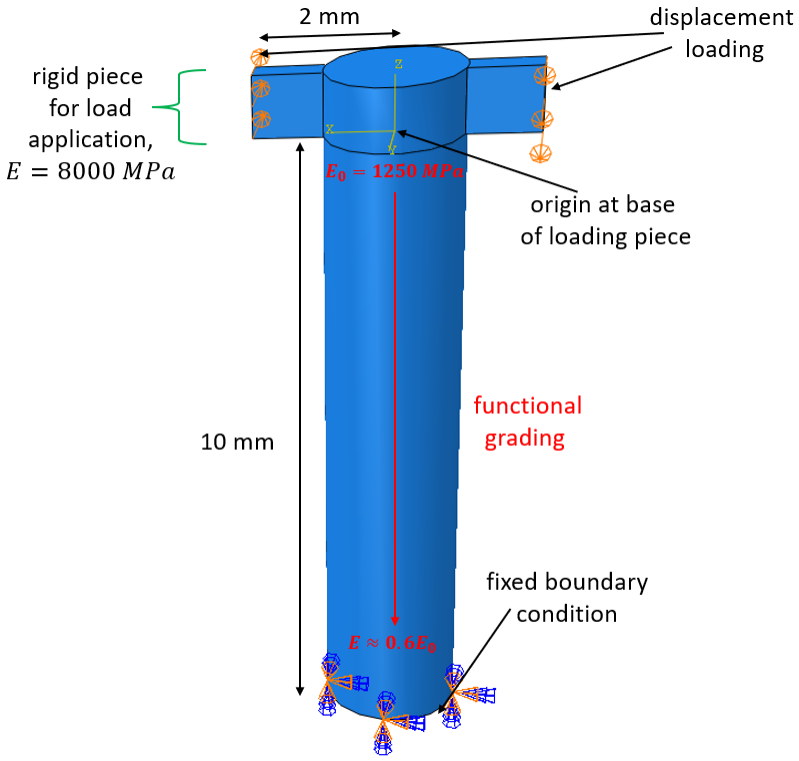

Figure 4.30: Finite element model assembly with boundary conditions

To investigate the influence of the torsional characteristic length on the response of the specimen, the other engineering properties (equations 2.5.36-2.5.41) must be held constant, or set in terms of the torsional characteristic length. A constant polar ratio of $\Psi = 1.5$, and coupling number of $N = 0.5$ are chosen, with the characteristic bending length set to twice the torsional characteristic length. The restrictions allow the elastic constants to be re-written, using equations 2.5.36-2.5.41, in terms of the torsional characteristic length such that

$$\lambda_0 = 500MPa, \tag{4.3.46}$$

$$\mu_0 = 500MPa, \tag{4.3.47}$$

$$\alpha_0 = \frac{500}{3}MPa, \tag{4.3.48}$$

$$\gamma_0 = 500l_t^2N, \tag{4.3.49}$$

$$\varepsilon_0 = 7500l_t^2N, \tag{4.3.50}$$

$$\beta_0 = -\frac{1000}{3}l_t^2N, \tag{4.3.51}$$

with the selected grading running along the cylinder's axis such that the stiffness at the support is approximately 60% of the stiffness at the top of the cylinder (1250 MPa). This corresponds to a grading vector of $\vec{\boldsymbol{G}} = (0, 0, 0.05)$.

First, the study aims to demonstrate that the proposed model is mesh insensitive, as the Cosserat model natively introduces an inherent length scale. Next, the study aims to demonstrate the model's invariance to axial, exponential grading under torsional loading. Finally, the study aims to replicate the size effect observed by [14], in which the torsional rigidity exhibits a size effect in the case of Cosserat elasticity.

Three different mesh sizes are considered in this work - 0.1 mm, 0.5 mm, and 1 mm. The model assemblies for each of the mesh sizes can be seen in Figure 4.31.

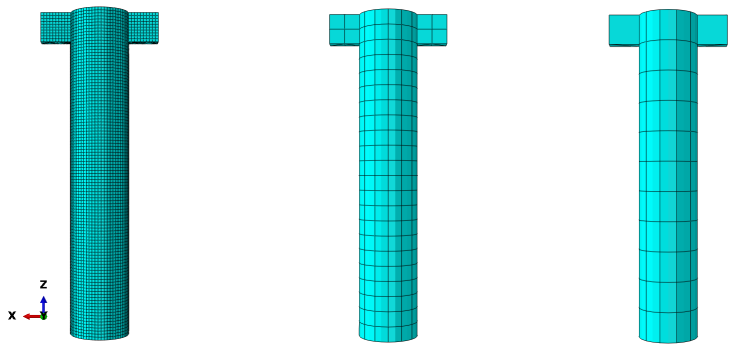

(a) (b) (c)

Figure 4.31: Cylindrical assembly for mesh sizes of (a) 0.1 mm, (b) 0.5 mm, and (c) 1 mm

To capture a wide range of torsional characteristic lengths, values of $l_t = 0, 0.1, 0.5, 1, 5$ mm are considered for the investigations, where a characteristic length of 0 mm represents a classical specimen, with no Cosserat parameters. Table 4.7 highlights the associated Cosserat elastic constants associated with the selected torsional characteristic length. All results are presented in units of N, mm, and MPa.

Table 4.7: Torsional characteristic lengths used and associated elastic constants

l_t (mm)	λ_0 (MPa)	μ_0 (MPa)	α_0 (MPa)	γ_0 (N)	ε_0 (N)	β_0 (N)
0 (Classical)	500	500	0	0	0	0
0.1	500	500	$\frac{500}{3}$	5	75	$-\frac{10}{3}$
0.5	500	500	$\frac{500}{3}$	125	1875	$-\frac{250}{3}$
1	500	500	$\frac{500}{3}$	500	7500	$-\frac{1000}{3}$
5	500	500	$\frac{500}{3}$	12500	187500	$-\frac{25000}{3}$

Influence of Grading

In this study, three specimens with a diameter of 2 mm are considered to investigate whether the axial grading influences the response under torsional loading. A classical specimen (no Cosserat effects) is compared to a specimen with a torsional characteristic length of 0.1 mm (minimal Cosserat effects), and a specimen with a torsional characteristic length of 5 mm (significant Cosserat effects).

The three specimens are tested in the case where the cylinder is exponentially graded along the axis of moment application ($\vec{\boldsymbol{G}} = (0, 0, 0.05)$), and the case without functional grading. The corresponding material properties are listed in Table 4.7.

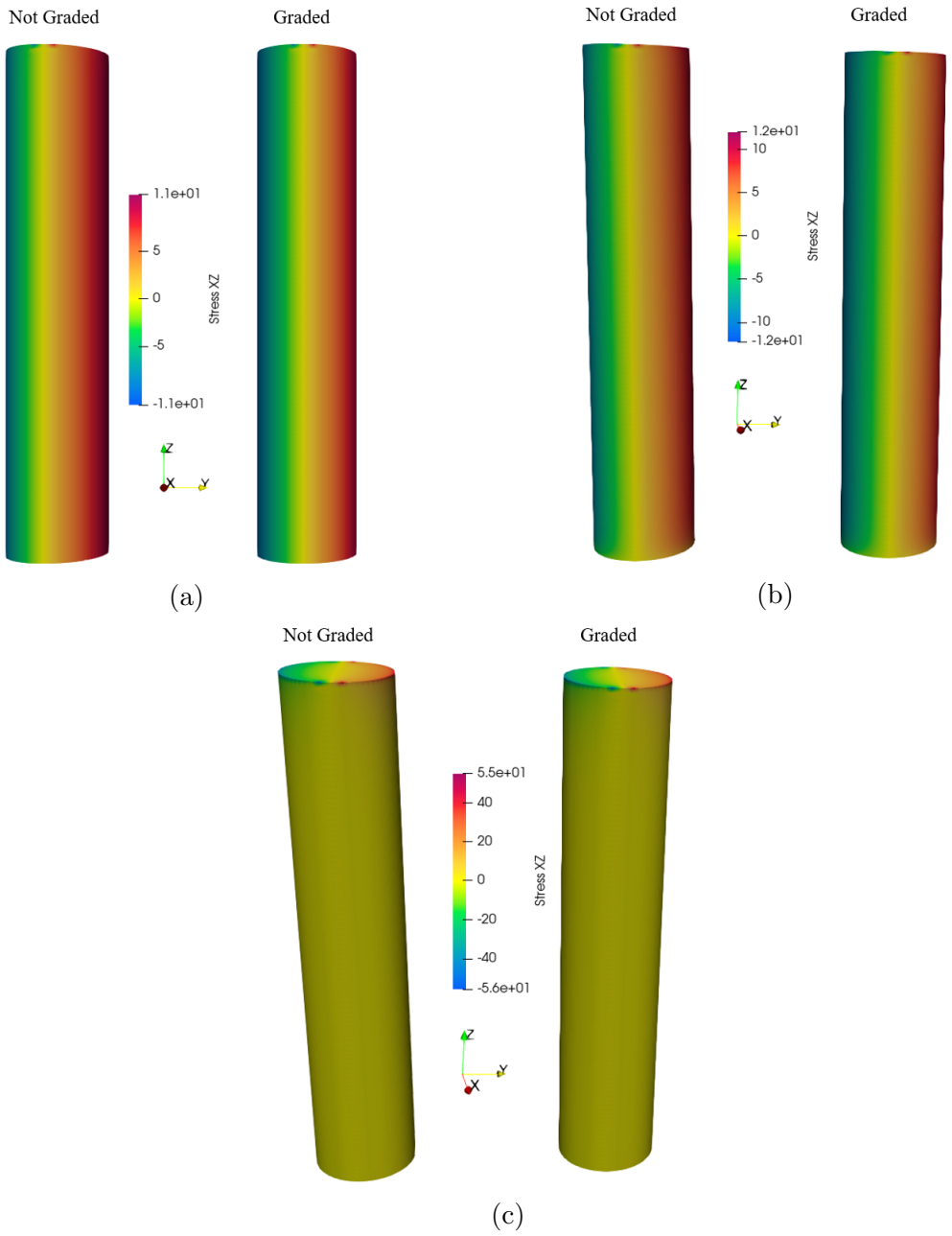

Figure 4.32: Torsional shear stress σ_{xz} comparison for torsional characteristic lengths of (a) 0 mm (classical), (b) 0.1 mm, and (c) 5 mm for graded and non-graded cases

Figure 4.32 compares the torsional shear stress σ_{xz} for the specimens with $l_t = 0, 0.1, 5$ mm, respectively. In all cases, the response for the exponentially graded, and non-graded specimens are identical, suggesting an invariance of the response to the grading along the rotation axis. The invariance is further exemplified in Figure 4.33,

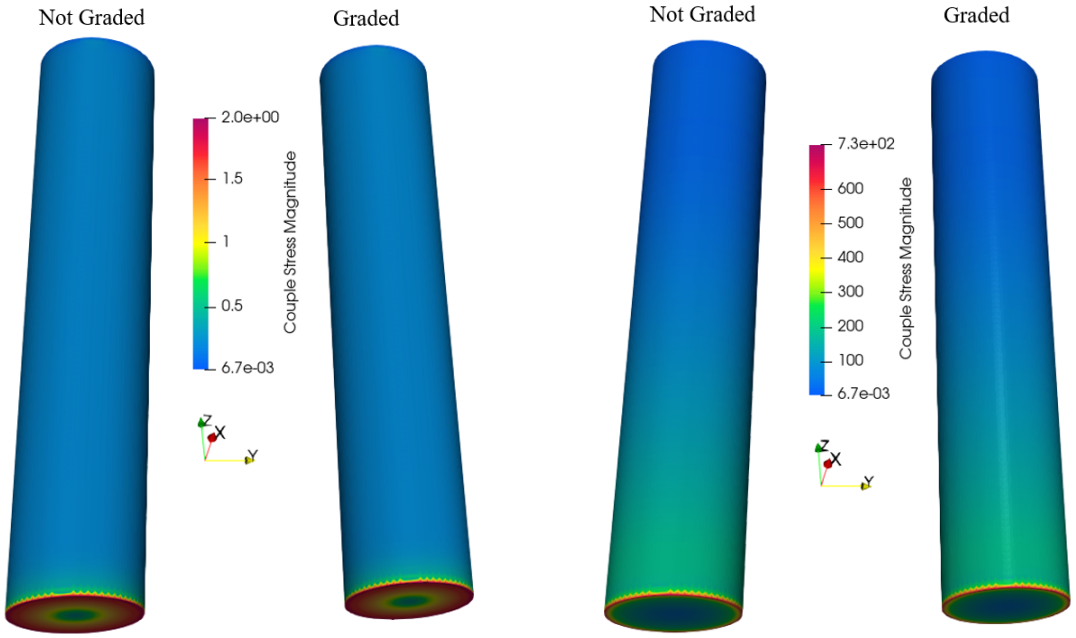

Figure 4.33: Couple stress tensor magnitude comparison for torsional characteristic lengths of (a) 0.1 mm, and (b) 5 mm for graded and non-graded cases

where the magnitude of the couple stress tensor in the two non-classical cases are compared, and shown to be identical in the graded, and non-graded, cases. The results suggest that exponential grading can be applied along the axis of a cylinder, without affecting the torsional properties of the cylinder.

Influence of Mesh

Next, a study in which the three aforementioned mesh sizes are used to evaluate the model's invariance to mesh size is conducted. The three specimens from Figure 4.31 are analysed for each characteristic length displayed in Table 4.7. However, only the contour plots for the classical, $l_t = 0.1\ mm$, and $l_t = 5\ mm$ cases are shown for conciseness, as they display the notable trends.

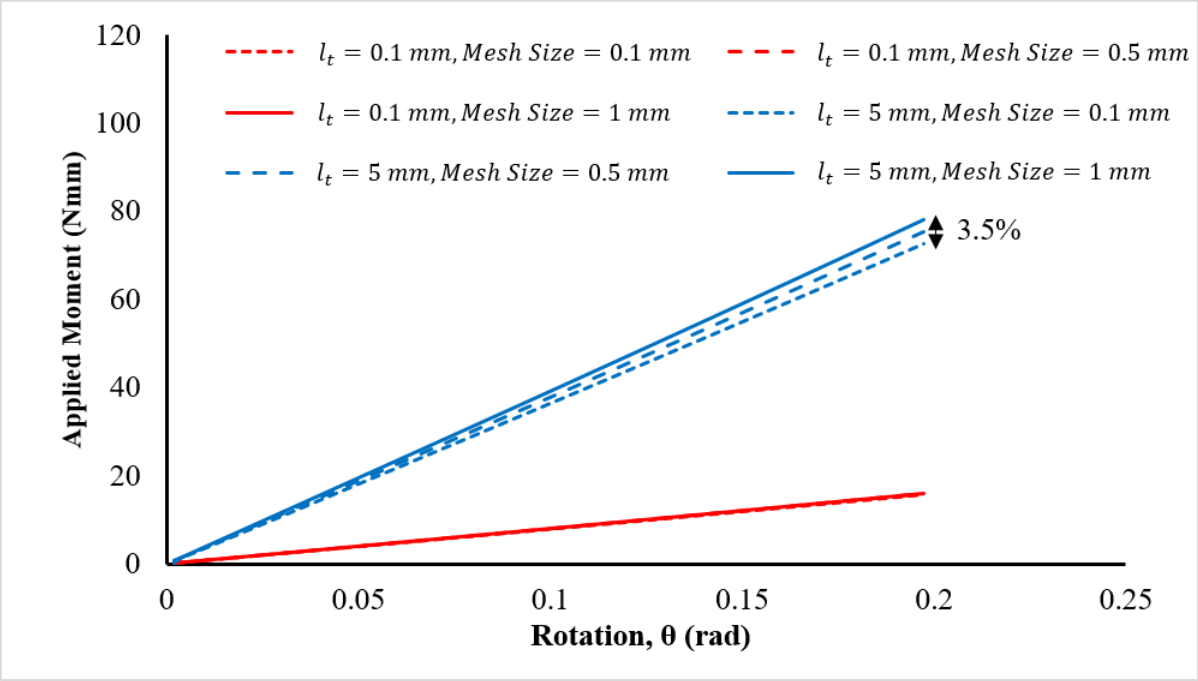

Figure 4.34: Influence of mesh size for specimens with small and large torsional characteristic lengths

Figure 4.34 illustrates compares the moment-curvature results for the specimens with the smallest and largest torsional characteristic lengths, for each mesh size considered. The specimens with the smallest Cosserat parameters display identical results for all mesh

sizes, while the specimens with the largest Cosserat parameters, corresponding to $l_t = 5$ mm display minor mesh sensitivity as peak load is approached. Given the large torsional characteristic length in these specimens, some divergence in the response around peak load is to be expected.

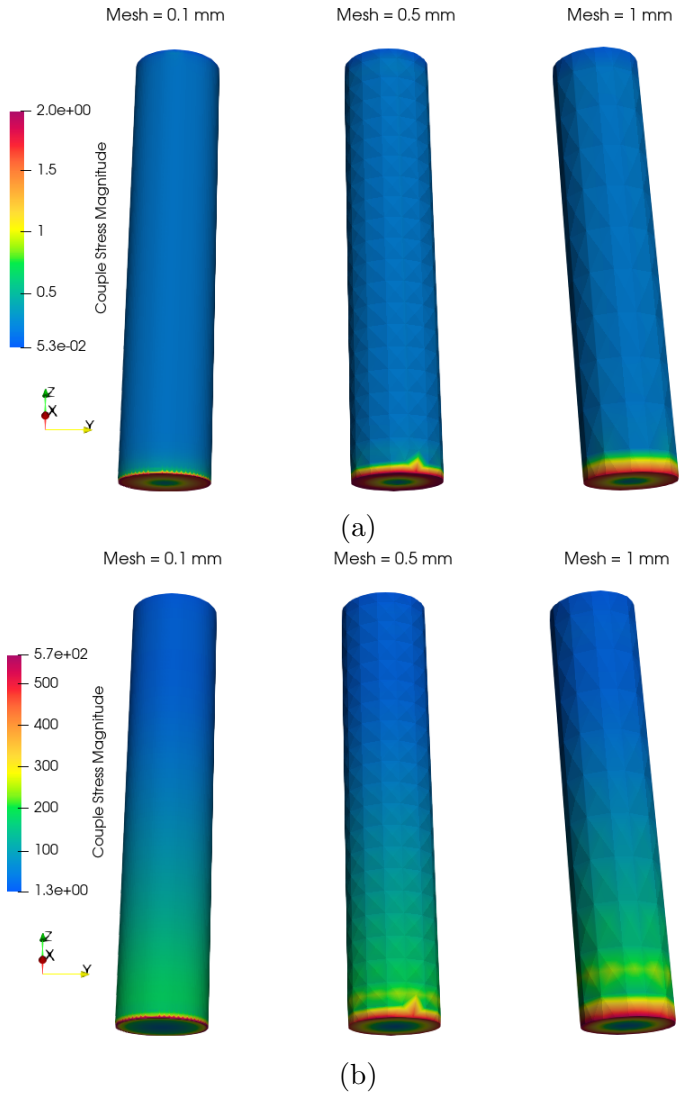

Figure 4.35: Couple stress tensor magnitude comparison for torsional characteristic lengths of (a) 0.1 mm, and (b) 5 mm

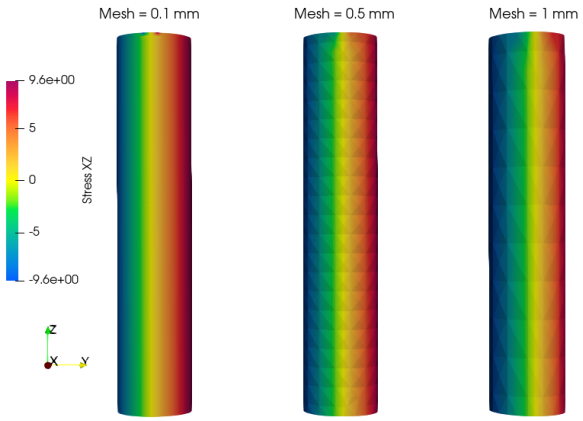

(a)

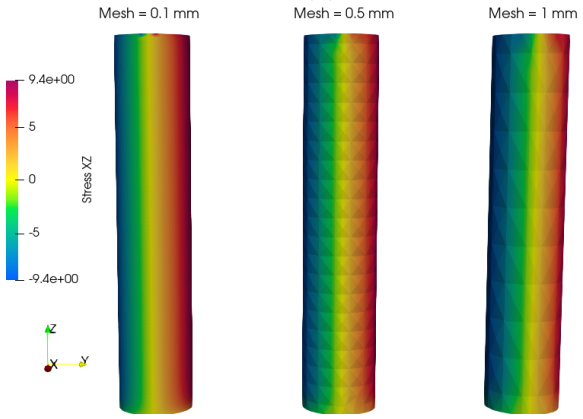

(b)

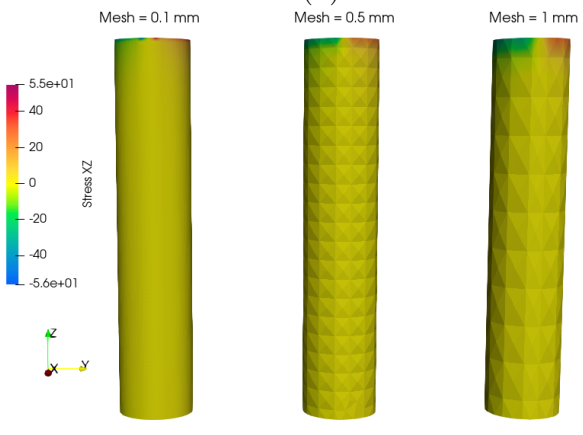

(c)

Figure 4.36: Torsional shear stress σ_{xz} comparison for torsional characteristic lengths of (a) 0 mm (classical), (b) 0.1 mm, and (c) 5 mm

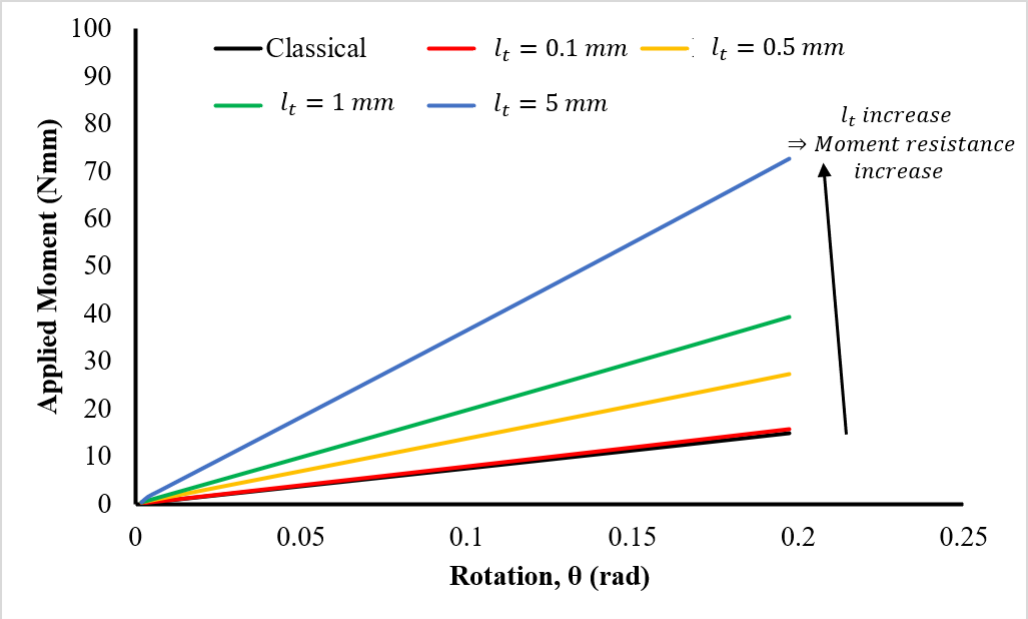

Figure 4.37: Influence of torsional characteristic length on moment resistance for specimen with fine mesh

Both the torsional shear stresses in Figure 4.36, and couple stresses in Figure 4.35 further exemplify the invariance of the model to mesh size, as the stresses and couple stresses shown are near identical for each of the mesh sizes considered, with the slight visual variability arising from the smoothing of the nodal values over the size of the elements. The nodal data is however within 1% between each of the specimens.

Lastly, the moment-curvature responses for the finest mesh (0.1 mm) are compared for each characteristic length considered in the study, to highlight the influence of the characteristic length on the torsional properties of the specimens. Figure 4.37 denotes increasing moment resistance with increasing characteristic length for specimens with identical geometry, suggesting that the torsional characteristic length of a specimen is proportional to its torsional rigidity.

Size Effect Study and Influence of Torsional Characteristic Length

In addition to investigating the influence of mesh size on the proposed model, an investigation into the effects of structural size (cylinder diameter) on the torsional properties of the specimens is conducted. The aim of the study is to demonstrate that for an axially (exponentially) graded cylinder, the trends experimentally observed by Rueger and Lakes [14] hold.

In this study, specimens with 3 diameter sizes are considered - 0.5 mm, 1 mm, and 2 mm, respectively. All specimens are modelled using the procedures outlined in Figure 4.30, with a mesh size of 0.1 mm. The torsional characteristic lengths considered are $l_t = 0, 0.1, 0.5, 1$ mm, with $l_t = 0$ mm, once again

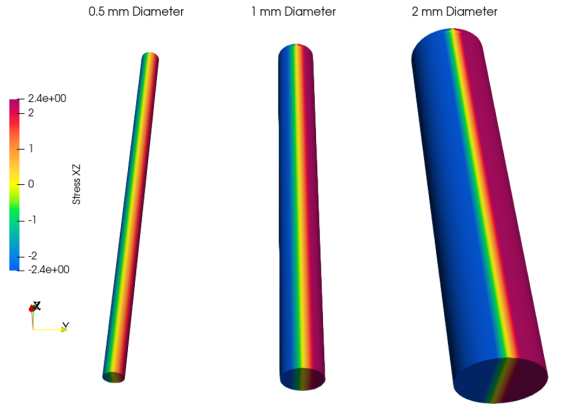

(a)

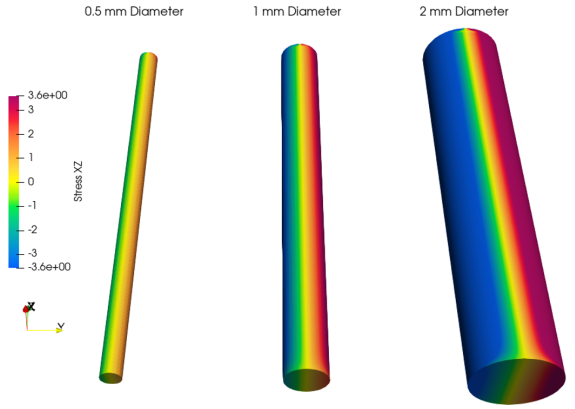

(b)

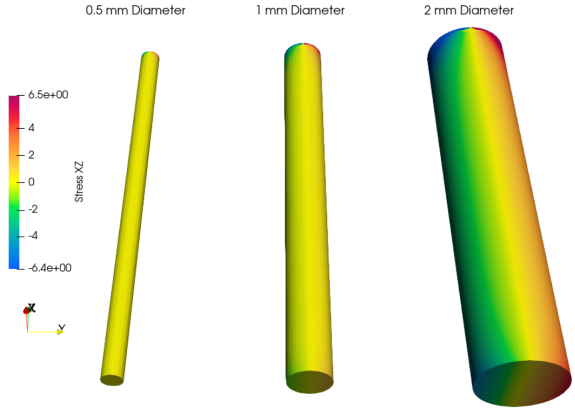

(c)

Figure 4.38: Torsional shear stress σ_{xz} comparison for torsional characteristic lengths of (a) 0 mm (classical), (b) 0.1 mm, and (c) 1 mm for cylinder diameters of 0.5 mm, 1 mm, and 2 mm

representing the classical case. The corresponding elastic constants used can be found in Table 4.7. The specimen responses are once again presented in the form of torsional shear stresses σ_{xz}, and magnitudes of the couple stress tensors.

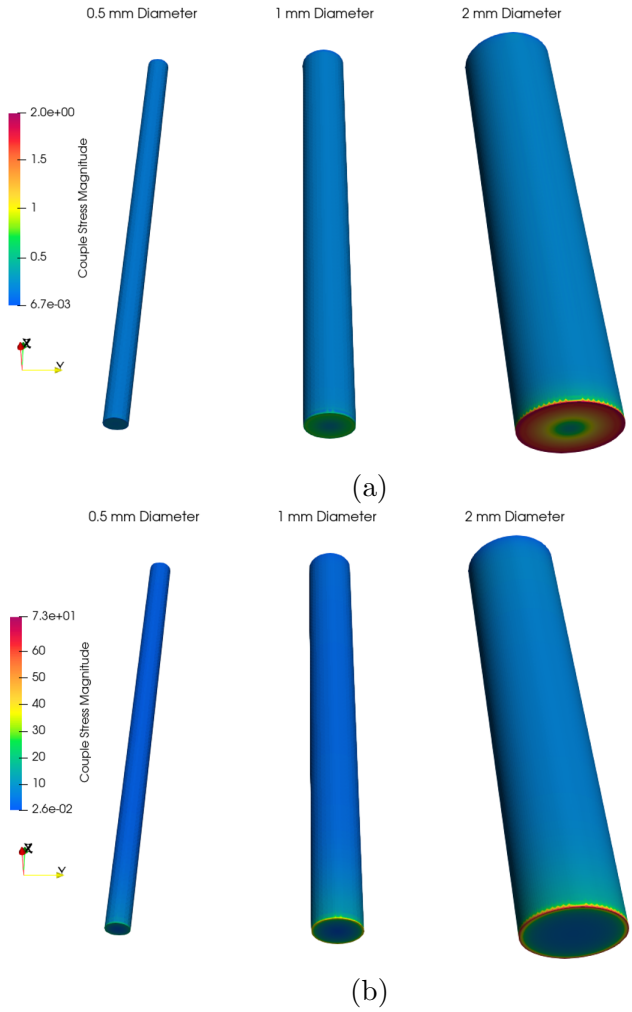

Figure 4.39: Couple stress tensor magnitude comparison for torsional characteristic lengths of (a) 0.1 mm, and (b) 1 mm for cylinder diameters of 0.5 mm, 1 mm, and 2 mm

Figure 4.38 highlights the physical influence of specimen size and Cosserat parameters on the torsional response of the cylinders. In the classical case, there appears to be no

significant difference between the torsional shear stresses experienced by the 3 cylinders, with a slightly less negligible difference in the specimens with a small characteristic length. Figure 4.38 (b) demonstrates the influence of the Cosserat parameters on the response, with a minor difference appearing between the thinnest and thickest cylinders in the form of a stress redistribution. The stresses appear to be localising at the circumferential edge along the y-axis, most prominently in the case of the thinnest cylinder. This redistribution/localization of stress is more significant in Figure 4.38 (c), where the ratio of torsional characteristic length to specimen diameter is largest, capturing the so-called size effect.

Figure 4.39 elucidates the reasoning for the phenomenon through the magnitude of the couple stress tensor. As the ratio of torsional characteristic length to specimen diameter increases, the couple stress localize at the circumference of the cylinders, at the supports, most notably in the smallest specimen. The localization of the couple stresses induces a localization of torsional shear stresses, re-affirming the presence of a size effect inherent to Cosserat theory.

Since an analytical solution is not available for exponentially graded Cosserat elastic bodies, an analytical expression for the torsional rigidity of the specimens is unavailable, and as a result, the relative stiffness as well. In lieu of a direct comparison tot he experiment carried out by by Rueger and Lakes [14], an equivalent comparison is drawn through a normalized torsional rigidity. Figure 4.40 compares the normalized torsional rigidity relative to specimen diameter for the analysed specimens, with the torsional rigidity $\frac{M}{\theta}$ divided by specimen radius, and normalized through division by the classical torsional rigidity. The normalized rigidity is therefore computed by the expression

$$\Omega = \frac{\frac{M}{\theta}}{\{\frac{M}{\theta}\}_{classical}}. \tag{4.3.52}$$

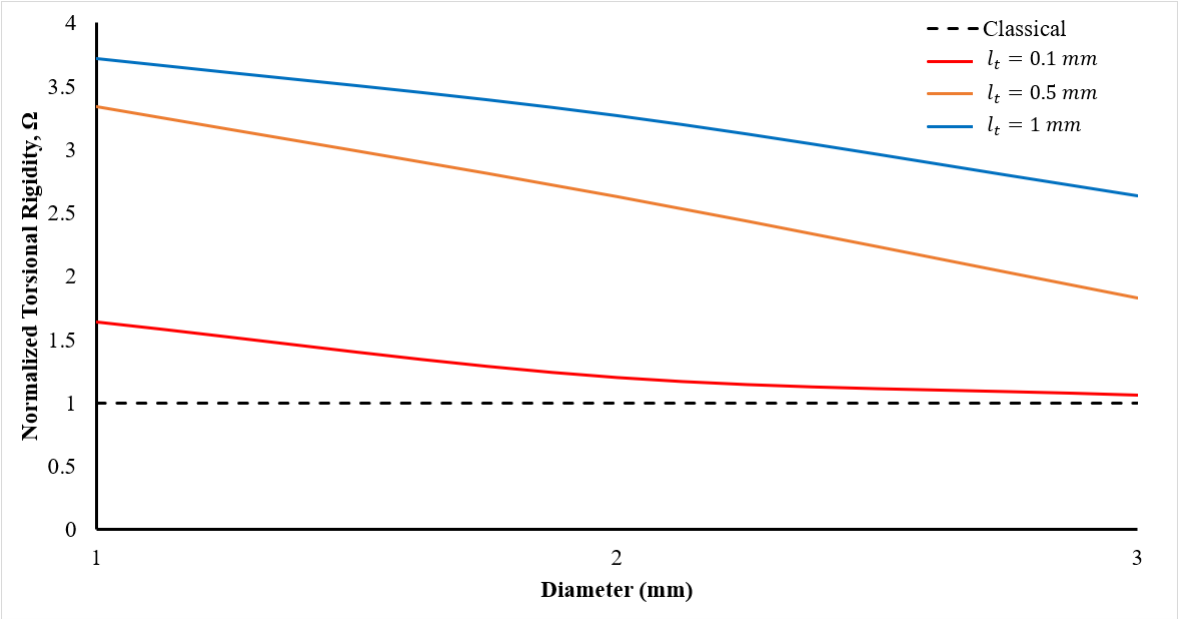

Figure 4.40: Influence of structural diameter on normalized torsional rigidity (size effect)

The plotted expressions in Figure 4.40 denote the expected trends, with the normalized torsional rigidity converging to the classical case as the diameter of the specimens increases, and the normalized rigidity increasing as the characteristic length in torsion increases.

Chapter 5

Conclusions and Recommendations for Future Work

The main objective of this thesis was to devise mathematical models to describe the behaviour of bimaterial composites, with the inclusion of microstructural effects using Cosserat elasticity. The research was divided into two sections: modelling transversely isotropic composites, and modelling functionally graded isotropic composites.

5.1 Modelling Fiber Reinforced Polymers with Unidirectional Fibers

The modelling of transversely isotropic composites focused on developing the constitutive equations for fiber reinforced polymers with unidirectional fibers, and obtaining the

associated equilibrium equations. The governing equations were developed, along with a boundary condition linking the microscale to the macroscale.

The associated conditions to prove the existence and uniqueness of their solution were also developed. The work was however limited by the unavailability of the elastic material constants, as testing within the Cosserat regime is still a developing field.

Once the experimental procedures for the measurement of the elastic constants become more developed, future endeavours into obtaining an analytical solution to the governing equations can take place.

5.2 Modelling Isotropic, Exponentially Graded Composites

The modelling of isotropic, exponentially graded composites focused on developing and solving the governing equations of equilibrium. Specifically, the three-dimensional equations of equilibrium (6 coupled partial differential equations) were formulated, and were shown to be uniformly elliptic.

The Lax-Milgram theorem was then used to show the existence and uniqueness of the solution to the equivalent energetic formulation, enabling the use of the finite element method to solve associated boundary problems. While measurement of the elastic constants still pose a problem, the research aimed to develop a useful analysis tool that can be used to analyse structures with the developed model. To accomplish this, the finite element method was used to design two elements capable of modelling the behaviour of an exponentially graded material with microstructural considerations.

A 20-noded quadratic, isoparametric quadrilateral element, and a 15-noded quadratic, isoparametric wedge element were designed and implemented into the commercial software Abaqus through a user element subroutine (UEL). Due to the difficulties in visualizing the response of models containing user defined elements, a post processing package was written to generate visualization files that can be viewed in open source scientific visualization software such as Paraview. The aim of this work was to set up a foundation for an analysis tool capable of modelling the behaviour of these materials, as the industry is shifting towards the use of tailor-made materials.

Once the model was developed and implemented, the two elements would ideally need to be validated against experimental data to ensure their accuracy. As experimental measurements are as yet unavailable due to the difficulty in measuring microrotations, the steps taken to validate the model comprised of recovering the classical limit in the absence of microstructural effects - a common procedure employed in such models.

To ensure recovery of the classical limit, the two elements were tested under common loading cases (compression, shear, and torsion), with the response compared to equivalent classical elements in Abaqus (C3D20 and C3D15). In all tests, the Dirichlet problem was solved, with loads applied in the form of prescribed displacements. The results agreed with the classical elements, showing recovery of the classical limit.

While a more complete analysis was unavailable due to the lack of measured elastic constants, this work still aimed to provide a proof of concept with assumed parameters to display the use of the developed model as an analysis tool. The elements, and an assembly of the elements, were tested in compression, shear, and torsion in the classical case, the case with Cosserat elasticity only, the case with exponential grading only, and

the case where both effects were present. A parametric analysis was also conducted to demonstrate the applicability of the model in verifying experimentally observed trends. The observations summarized are subject to the validity of the model, which must still be experimentally verified. The key observations from the analyses conducted are summarized as follows:

- The response of the material is very sensitive to the exponential grading vector. To achieve a smooth transition in elastic properties, a grading vector with a very small magnitude must be used. If the grading vector has a large magnitude, the response is completely governed by the functional grading, resulting in highly localized stresses

- The significance of microstructural effects on the global response depends on the loading case. Little to no effects are observed in the case of compression loading for all elements and their assemblies. Shear loading produces some global effects that diminish as the size of the specimen increases. Torsion loading results in the most significant effects, and also begin to diminish as specimen size increases

- Material with microstructure exhibit a size effect, with the influence of microstructure becoming less prominent as the size of the specimen becomes large compared to the inherent microstructural length

- With regards to stresses in the material, Cosserat effects can be viewed as a redistribution of stresses due to warping induced by microrotations

5.3 Recommendations for Future Work

Based on the insights gained from this work, the following recommendations for future works can be offered:

- Testing of specimens with microstructure to determine the Cosserat elastic constants
- Further parametric studies on the Cosserat elastic constants to determine their influence on the response under various loading conditions. This facilitates the identification of material constants (analogous to modulus of elasticity)
- Parametric studies on the grading vector under various loading conditions to offer recommendations for the design of exponentially graded materials
- Extensions to different types of grading. This process is facilitated with the codes developed in this work. To change the type of grading, existence and uniqueness of the system must once again be shown. Once done, all that must change in the developed code is the term in the constitutive update containing the grading, and the quadrature rule used; the rest is unchanged
- Size effect studies to determine the range of influence of microstructure on the global response of the material. This allows one to determine when Cosserat elasticity must be used, or whether a simpler elastic model is sufficient
- Extensions into plasticity modelling to provide a complete analysis tool for materials with microstructural effects

References

[1] Hashin, Z. (1983). Analysis of composite materials-a survey. *Journal of Applied Mechanics, 50*(3), 481-505.

[2] Momber, A. (2011). Corrosion and corrosion protection of support structures for offshore wind energy devices (OWEA). *Materials and Corrosion, 62*(5), 391-404.

[3] Pindera, M. J., Arnold, S. M., Aboudi, J., & Hui, D. (1994). Use of composites in functionally graded materials-invited papers-functionally graded, Advanced Composites Materials Symposium University-of-Virginia, Charlottesville, USA-6-9 June 1993-Foreword. *Composites Engineering, 4*(1), R7-R9.

[4] Mahamood, R. M., Akinlabi, E. T., Shukla, M., & Pityana, S. L. (2012). Functionally graded material: an overview.

[5] Wang, S. S. (1983). Fracture mechanics for delamination problems in composite materials. *Journal of composite materials, 17*(3), 210-223.

[6] Asghari, M., Ahmadian, M. T., Kahrobaiyan, M. H., & Rahaeifard, M. (2010). On the size-dependent behavior of functionally graded micro-beams. *Materials & Design (1980-2015), 31*(5), 2324-2329.

[7] Niino, M. (1987). Functionally gradient materials as thermal barrier for space plane. *J. Jpn. Composite Mater., 13,* 257-264.

[8] Udupa, G., Rao, S. S., & Gangadharan, K. V. (2014). Functionally graded composite materials: an overview. *Procedia Materials Science, 5,* 1291-1299.

[9] Tsui, Y. C., Howard, S. J., & Clyne, T. W. (1994). The effect of residual stresses on the debonding of coatings—II. An experimental study of a thermally sprayed system. *Acta metallurgica et materialia, 42*(8), 2837-2844.

[10] Koizumi, M. F. G. M. (1997). FGM activities in Japan. *Composites Part B: Engineering, 28*(1-2), 1-4.

[11] Knoppers, G. E., Gunnink, J. W., Van Den Hout, J., & Van Vliet, W. (2005, December). The reality of functionally graded material products. In *Intelligent Production Machines and Systems: First I* PROMS Virtual Conference, Elsevier, Amsterdam* (pp. 467-474).

[12] Dassault Systems Simulia Corp (DSS) (2012). "ABAQUS Analysis User's Manual 6.12". Providence, RI, USA.

[13] Tang, H. X., & Hu, Z. L. (2017). Application of the Cosserat continua to numerical studies on the properties of the materials. *Mechanics of Advanced Materials and Structures, 24*(10), 797-808.

[14] Rueger, Z., & Lakes, R. S. (2017). Strong Cosserat elastic effects in a unidirectional composite. *Zeitschrift für angewandte Mathematik und Physik, 68*(3), 1-9.

[15] Yoon, H. S., & Katz, J. L. (1983). Is bone a Cosserat solid?. *Journal of Materials Science, 18*(5), 1297-1305.

[16] Anderson, W. B., & Lakes, R. S. (1994). Size effects due to Cosserat elasticity and surface damage in closed-cell polymethacrylimide foam. *Journal of Materials Science, 29*(24), 6413-6419.

[17] Calvetti, F., Combe, G., & Lanier, J. (1997). Experimental micromechanical analysis of a 2D granular material: relation between structure evolution and loading path. *Mechanics of Cohesive-frictional Materials: An International Journal on Experiments, Modelling and Computation of Materials and Structures, 2*(2), 121-163.

[18] Sakhaei, A. H., Erland, S., & Dodwell, T. J. (2020). A finite deformation Cosserat continuum model for uncured carbon fibre composites. *Mechanics of Materials, 151*, 103611.

[19] Münch, I., Neff, P., & Wagner, W. (2011). Transversely isotropic material: nonlinear Cosserat versus classical approach. *Continuum Mechanics and Thermodynamics, 23*(1), 27-34.

[20] Lakes, R., & Drugan, W. J. (2015). Bending of a Cosserat elastic bar of square cross section: Theory and experiment. *Journal of Applied Mechanics, 82*(9).

[21] Fleck, N. A., Muller, G. M., Ashby, M. F., & Hutchinson, J. W. (1994). Strain gradient plasticity: theory and experiment. *Acta Metallurgica et materialia, 42*(2), 475-487.

[22] Xu, Y., Li, M., & Huo, X. (2018). Size Effect of Bending Properties of Zirconia Ceramics Based on Cosserat Theory. In *Proceedings of the International Workshop on Materials, Chemistry and Engineering-Volume 1* (pp. 371-377).

[23] Huang, W., & Xu, K. (2015). Characteristic lengths in Cosserat continuum modeling of granular materials. *Engineering computations*.

[24] Lakes, R. S., & Benedict, R. L. (1982). Noncentrosymmetry in micropolar elasticity. *International Journal of Engineering Science, 20*(10), 1161-1167.

[25] Diepolder, W., Mannl, V., & Lippman, H. (1991). The Cosserat continuum, a model for grain rotations in metals?. *International journal of plasticity, 7*(4), 313-328.

[26] Cosserat, E., & Cosserat, F. (1909). *Théorie des corps déformables*. Herman et Fils, Paris.

[27] Mora, R., & Waas, A. M. (2000). Measurement of the Cosserat constant of circular-cell polycarbonate honeycomb. *Philosophical Magazine A, 80*(7), 1699-1713.

[28] Reddy, G. K., & Venkatasubramanian, N. K. (1979). On the flexural rigidity of a micropolar elastic circular cylindrical tube. *International Journal of Engineering Science, 17*(9), 1015-1021.

[29] Papamichos, E. (2010). Continua with microstructure: Cosserat theory. *European journal of environmental and civil engineering, 14*(8-9), 1011-1029.

[30] Park, H. C., & Lakes, R. S. (1986). Cosserat micromechanics of human bone: strain redistribution by a hydration sensitive constituent. *Journal of biomechanics, 19*(5), 385-397.

[31] Yang, J. F. C., & Lakes, R. S. (1982). Experimental study of micropolar and couple stress elasticity in compact bone in bending. *Journal of biomechanics, 15*(2), 91-98.

[32] Lakes, R. S. (2016). Reduced warp in torsion of reticulated foam due to Cosserat elasticity: experiment. *Zeitschrift für angewandte Mathematik und Physik ZAMP, 67*(3), 1-6.

[33] Kapiturova, M., Gracie, R., & Potapenko, S. (2016). Simulation of cracks in a Cosserat medium using the extended finite element method. *Mathematics and Mechanics of Solids, 21*(5), 621-635.

[34] Meyer, C. D. (2000). *Matrix analysis and applied linear algebra* (Vol. 71). Siam.

[35] Kantorovich, L. V., & Akilov, G. P. (2016). *Functional analysis*. Elsevier.

[36] Hunter, J. (2014). *Notes on Partial Differential Equations*. Personal Collection of John K. Hunter, Department of Mathematics, University of Califoria at Davis, California, USA.

[37] Stewart, D. J. (1998). *Finite element schemes for elliptic boundary value problems with rough coefficients* (Doctoral dissertation, Brunel University, School of Information Systems, Computing and Mathematics).

[38] Hadamard, J. (1952). *Lectures on Cauchy's problem in linear partial differential equations*. New York: Dover Publications V, 316 p. (1952).

[39] Payne, R. K. L., & Knops, R. J. (1971). *Uniqueness theorems in linear elasticity*. Springer Tracts in Natural Phylosophy, 19.

[40] Miranda, C. (1970). Partial Differential Equations of Elliptic Type. Springer, *Berlin*.

[41] Marin, L., & Lesnic, D. (2007). The method of fundamental solutions for nonlinear functionally graded materials. *International journal of solids and structures, 44*(21), 6878-6890.

[42] Eringen, A. C. (2012). *Microcontinuum field theories: I. Foundations and solids*. Springer Science & Business Media.

[43] Eringen, A. C. (1999). Theory of micropolar elasticity. In *Microcontinuum field theories* (pp. 101-248). Springer, New York, NY.

[44] Nowacki, W. (1986). Theory of asymmetric elasticity. *Pergamon Press, Headington Hill Hall, Oxford OX 3 0 BW, UK, 1986.*

[45] Lakes, R. (2016). Physical meaning of elastic constants in Cosserat, void, and microstretch elasticity. *Journal of Mechanics of Materials and Structures, 11*(3), 217-229.

[46] Arczewska P. (2017). Practical performance criteria and durability prediction modeling of glass Fiber reinforced polymer (GFRP) bars. Doctoral Thesis, University of Waterloo.

[47] Gross, S. P., Yost, J. R., Dinehart, D. W., Svensen, E., & Liu, N. (2003). Shear strength of normal and high strength concrete beams reinforced with GFRP bars. In *High performance materials in bridges* (pp. 426-437).

[48] Stoner, J. G., & Polak, M. A. (2020). Finite element modelling of GFRP reinforced concrete beams. *Computers and Concrete, An International Journal, 25*(4), 369-382.

[49] Krall, M., & Polak, M. A. (2019). Concrete beams with different arrangements of GFRP flexural and shear reinforcement. *Engineering Structures*, 198, 109333.

[50] Mahmoud, K., & El-Salakawy, E. (2016). Effect of transverse reinforcement ratio on the shear strength of GFRP-RC continuous beams. *Journal of Composites for Construction, 20*(1), 04015023.

[51] Habeeb, M. N., & Ashour, A. F. (2008). Flexural behavior of continuous GFRP reinforced concrete beams. *Journal of composites for construction, 12*(2), 115-124.

[52] Razaqpur, A. G., & Spadea, S. (2015). Shear strength of FRP reinforced concrete members with stirrups. *Journal of Composites for Construction, 19*(1), 04014025.

[53] Tran, T. H., Monchiet, V., & Bonnet, G. (2012). A micromechanics-based approach for the derivation of constitutive elastic coefficients of strain-gradient media. *International Journal of Solids and Structures, 49*(5), 783-792.

[54] Rahali, Y., Giorgio, I., Ganghoffer, J. F., & dell'Isola, F. (2015). Homogenization à la Piola produces second gradient continuum models for linear pantographic lattices. *International Journal of Engineering Science, 97,* 148-172.

[55] Boutin, C., Giorgio, I., & Placidi, L. (2017). Linear pantographic sheets: asymptotic micro-macro models identification. *Mathematics and Mechanics of Complex Systems, 5*(2), 127-162.

[56] Giorgio, I., & Della Corte, A. (2017). Dynamics of 1D nonlinear pantographic continua. *Nonlinear Dynamics, 88*(1), 21-31.

[57] Eremeyev, V. A., & Pietraszkiewicz, W. (2012). Material symmetry group of the non-linear polar-elastic continuum. *International Journal of Solids and Structures, 49*(14), 1993-2005.

[58] Wang, G., & Pindera, M. J. (2016). Locally-exact homogenization theory for transversely isotropic unidirectional composites. *Mechanics Research Communications, 78,* 2-14.

[59] Wang, G., & Pindera, M. J. (2016). Locally-exact homogenization of unidirectional composites with coated or hollow reinforcement. *Materials & Design, 93,* 514-528.

[60] Drago, A. S., & Pindera, M. J. (2008). A locally exact homogenization theory for periodic microstructures with isotropic phases. *Journal of applied mechanics, 75*(5).

[61] Eremeyev, V. A., & Lebedev, L. P. (2013). Existence of weak solutions in elasticity. *Mathematics and Mechanics of Solids, 18*(2), 204-217.

[62] Altenbach, H., Eremeyev, V. A., & Lebedev, L. P. (2010). On the existence of solution in the linear elasticity with surface stresses. *ZAMM-Journal of Applied Mathematics and Mechanics/Zeitschrift für Angewandte Mathematik und Mechanik: Applied Mathematics and Mechanics, 90*(3), 231-240.

[63] Berdichevsky, V. L. (2009). Variational principles. In *Variational Principles of Continuum Mechanics* (pp. 3-44). Springer, Berlin, Heidelberg.

[64] Olver, P. J. (2012). *The calculus of variations*. Applied Mathematics Lecture Notes. Sec, 21, 4.

[65] Suiker, A. S. J., De Borst, R., & Chang, C. S. (2001). Micro-mechanical modelling of granular material. Part 1: Derivation of a second-gradient micro-polar constitutive theory. *Acta Mechanica, 149*(1), 161-180.

[66] Zervos, A., Vardoulakis, I., Jean, M., & Lerat, P. (2000). Numerical investigation of granular interfaces kinematics. *Mechanics of Cohesive-frictional Materials: An International Journal on Experiments, Modelling and Computation of Materials and Structures, 5*(4), 305-324.

[67] Kuhn, M. R. (1999). Structured deformation in granular materials. *Mechanics of materials, 31*(6), 407-429.

[68] Kuhn, M. R., & Bagi, K. (2002). Particle rotations in granular materials. In: *15th ASCE Engineering Mechanics Conference*, Columbia University, New York.

[69] Radjai, F., & Roux, S. (2002). Turbulentlike fluctuations in quasistatic flow of granular media. *Physical review letters, 89*(6), 064302.

[70] Didwania, A. K., Ledniczky, K., & Goddard, J. D. (2001). Kinematic Diffusion in Quasi-Static Granular Deformation. *The Quarterly Journal of Mechanics and Applied Mathematics, 54*(3), 413-429.

[71] Walsh, S. D. C., & Tordesillas, A. (2004). A thermomechanical approach to the development of micropolar constitutive models of granular media. *Acta mechanica, 167*(3), 145-169.

[72] Vardoulakis, I., & Unterreiner, P. (1995). Interfacial localisation in simple shear tests on a granular medium modelled as a Cosserat continuum. In *Studies in Applied Mechanics* (Vol. 42, pp. 487-512). Elsevier.

[73] Weitsman, Y. (1965). Couple-stress effects on stress concentration around a cylindrical inclusion in a field of uniaxial tension. *Journal of Applied Mechanics, 32*(2), 424-428.

[74] Mindlin, R. D. (1962). Influence of couple-stresses on stress concentrations. *Experimental mechanics, 3*(1), 1-7.

[75] Hollister, S. J., & Kikuchi, N. (1992). A comparison of homogenization and standard mechanics analyses for periodic porous composites. *Computational mechanics, 10*(2), 73-95.

[76] Hassani, B., & Hinton, E. (1998). A review of homogenization and topology optimization I—homogenization theory for media with periodic structure. *Computers & Structures, 69*(6), 707-717.

[77] Guedes, J., & Kikuchi, N. (1990). Preprocessing and postprocessing for materials based on the homogenization method with adaptive finite element methods. *Computer methods in applied mechanics and engineering, 83*(2), 143-198.

[78] Hill, R. (1963). Elastic properties of reinforced solids: some theoretical principles. *Journal of the Mechanics and Physics of Solids, 11*(5), 357-372.

[79] Perdahcıoğlu, E. S., & Geijselaers, H. J. (2011). Constitutive modeling of two phase materials using the mean field method for homogenization. *International journal of material forming, 4*(2), 93-102.

[80] Fish, J., & Shek, K. (2000). Multiscale analysis of composite materials and structures. *Composites Science and Technology, 60*(12-13), 2547-2556.

[81] Bensoussan, A., Lions, J. L., & Papanicolaou, G. (2011). *Asymptotic analysis for periodic structures* (Vol. 374). American Mathematical Soc..

[82] Wang, G., Chen, Q., He, Z., & Pindera, M. J. (2018). Homogenized moduli and local stress fields of unidirectional nano-composites. *Composites Part B: Engineering, 138,* 265-277.

[83] Shmoylova, E., Potapenko, S., & Rothenburg, L. (2007). Boundary element analysis of stress distribution around a crack in plane micropolar elasticity. *International journal of engineering science, 45*(2-8), 199-209.

[84] Voigt, W. (1887). Theoretische Studien über die Elasticitätsverhältnisse der Krystalle. Abh. Kgl. Ges. Wiss. Göttingen. *Math. Kl, 34*, 3-51.

[85] McFarland, A. W., & Colton, J. S. (2005). Role of material microstructure in plate stiffness with relevance to microcantilever sensors. *Journal of Micromechanics and Microengineering, 15*(5), 1060.

[86] Gupta, A., & Talha, M. (2015). Recent development in modeling and analysis of functionally graded materials and structures. *Progress in Aerospace Sciences, 79,* 1-14.

[87] Erdogan, F. (1995). Fracture mechanics of functionally graded materials. *Composites Engineering, 5*(7), 753-770.

[88] Shaw, L. L. (1998). The crack driving force of functionally graded materials. *Journal of materials science letters, 17*(1), 65-67.

[89] Watanabe, Y., Inaguma, Y., Sato, H., & Miura-Fujiwara, E. (2009). A novel fabrication method for functionally graded materials under centrifugal force: The centrifugal mixed-powder method. *Materials, 2*(4), 2510-2525.

[90] Potapenko, S. (2005). A generalized Fourier approximation in anti-plane Cosserat elasticity. *Journal of Elasticity, 81*(2), 159-177.

[91] Potapenko, S., Schiavone, P., & Mioduchowski, A. (2005). Antiplane shear deformations in a linear theory of elasticity with microstructure. *Zeitschrift für angewandte Mathematik und Physik ZAMP, 56*(3), 516-528.

[92] Potapenko, S. (2005). Fundamental sequences of functions in the approximation of the solution to the mixed boundary-value problem in anti-plane Cosserat elasticity. *Acta mechanica, 177*(1), 61-69.

[93] Martínez-Pañeda, E. (2019). On the finite element implementation of functionally graded materials. *Materials, 12*(2), 287.

[94] Peng, C. W., Dong, L. B., & Wu, Q. (2011). Numerical implementation of elasto-plastic Cosserat continuum model in ABAQUS. *Journal of Wuhan Institute of Technology*.

[95] Berthold, R., Bartholdt, M. N., Wiese, M., Kahms, S., Spindeldreier, S., & Raatz, A. (2021, November). A Preliminary Study of Soft Material Robotic Modelling: Finite Element Method and Cosserat Rod Model. In *2021 9th International Conference on Control, Mechatronics and Automation (ICCMA)* (pp. 7-13). IEEE.

[96] Shi, J., Chopp, D., Lua, J., Sukumar, N., & Belytschko, T. (2010). Abaqus implementation of extended finite element method using a level set representation for three-dimensional fatigue crack growth and life predictions. *Engineering Fracture Mechanics, 77*(14), 2840-2863.

[97] Liu, Q., Li, J., & Liu, J. (2017). ParaView visualization of Abaqus output on the mechanical deformation of complex microstructures. *Computers & geosciences, 99,* 135-144.

[98] Cravero, J., Elkady, A., & Lignos, D. G. (2021). Closure to "Experimental Evaluation and Numerical Modeling of Wide-Flange Steel Columns Subjected to Constant and Variable Axial Load Coupled with Lateral Drift Demands" by Julien

Cravero, Ahmed Elkady, and Dimitrios G. Lignos. *Journal of Structural Engineering, 147*(3), 07020020.

[99] Cowper, G. R. (1973). Gaussian quadrature formulas for triangles. *International Journal for Numerical Methods in Engineering, 7*(3), 405-408.

Appendices

Appendix A

Classical Comparisons

A.1 Single Quadrilateral

A.1.1 Shear

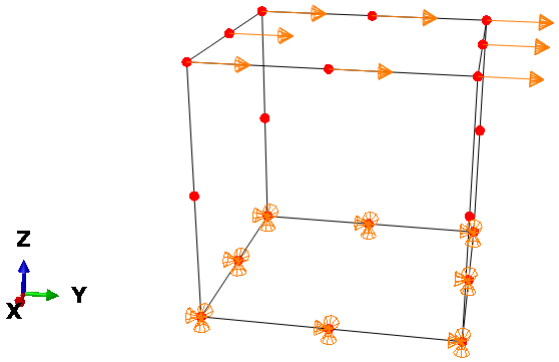

Figure A.1: Boundary conditions and loading for single quadrilateral element in shear

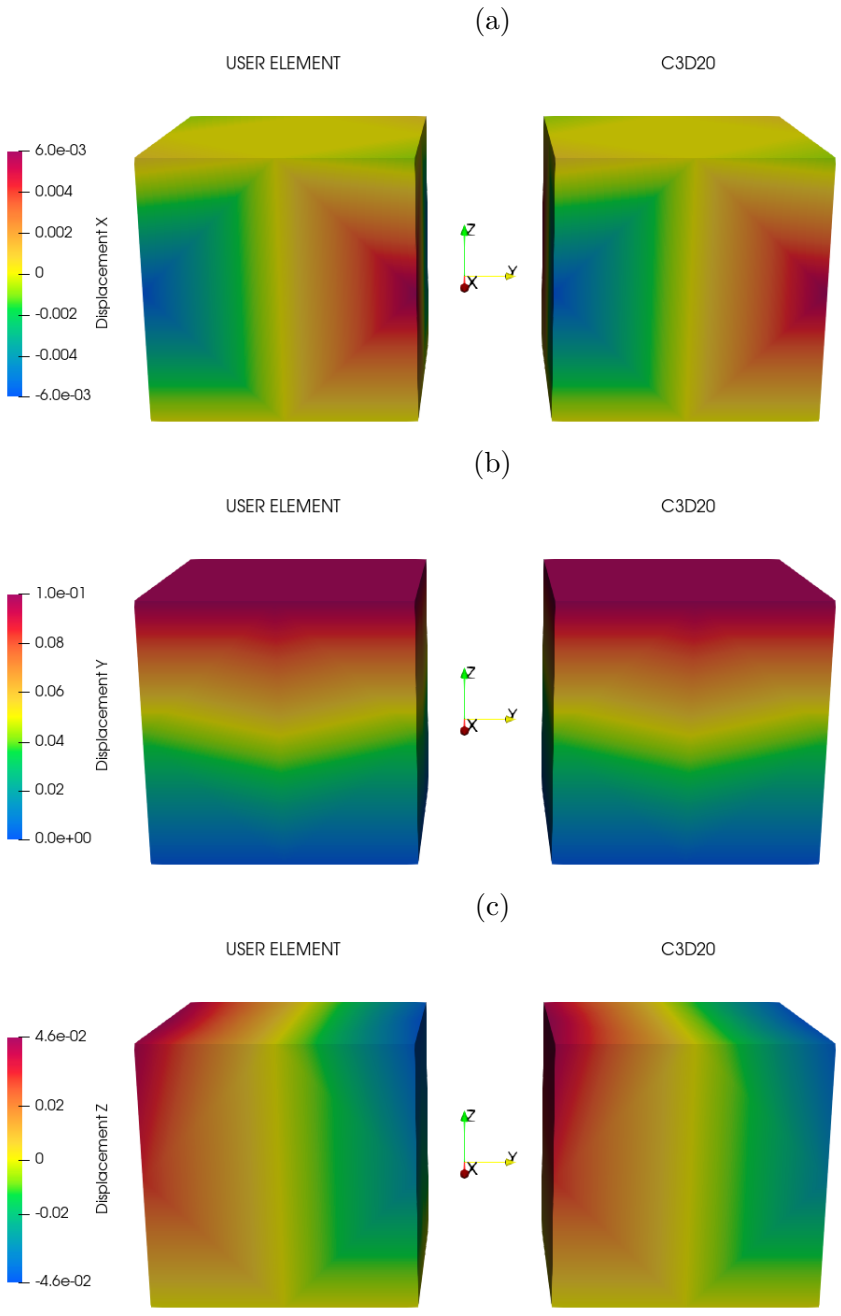

Figure A.2: Comparison of nodal displacements between user element and Abaqus in the (a) x, (b) y, and (c) z directions for quadrilateral element under shear

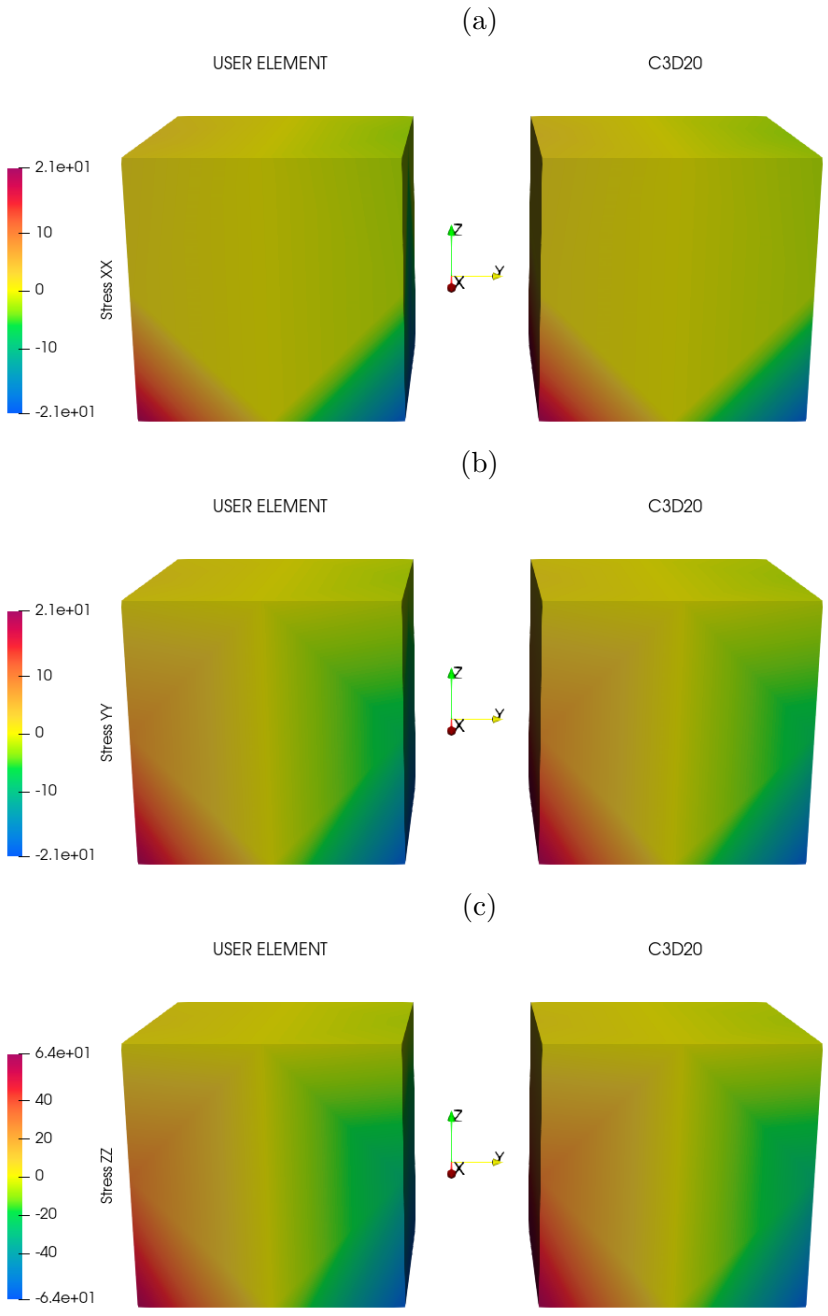

Figure A.3: Comparison of nodal normal stress components (a) XX, (b) YY, and (c) ZZ between user element and Abaqus for quadrilateral element under shear

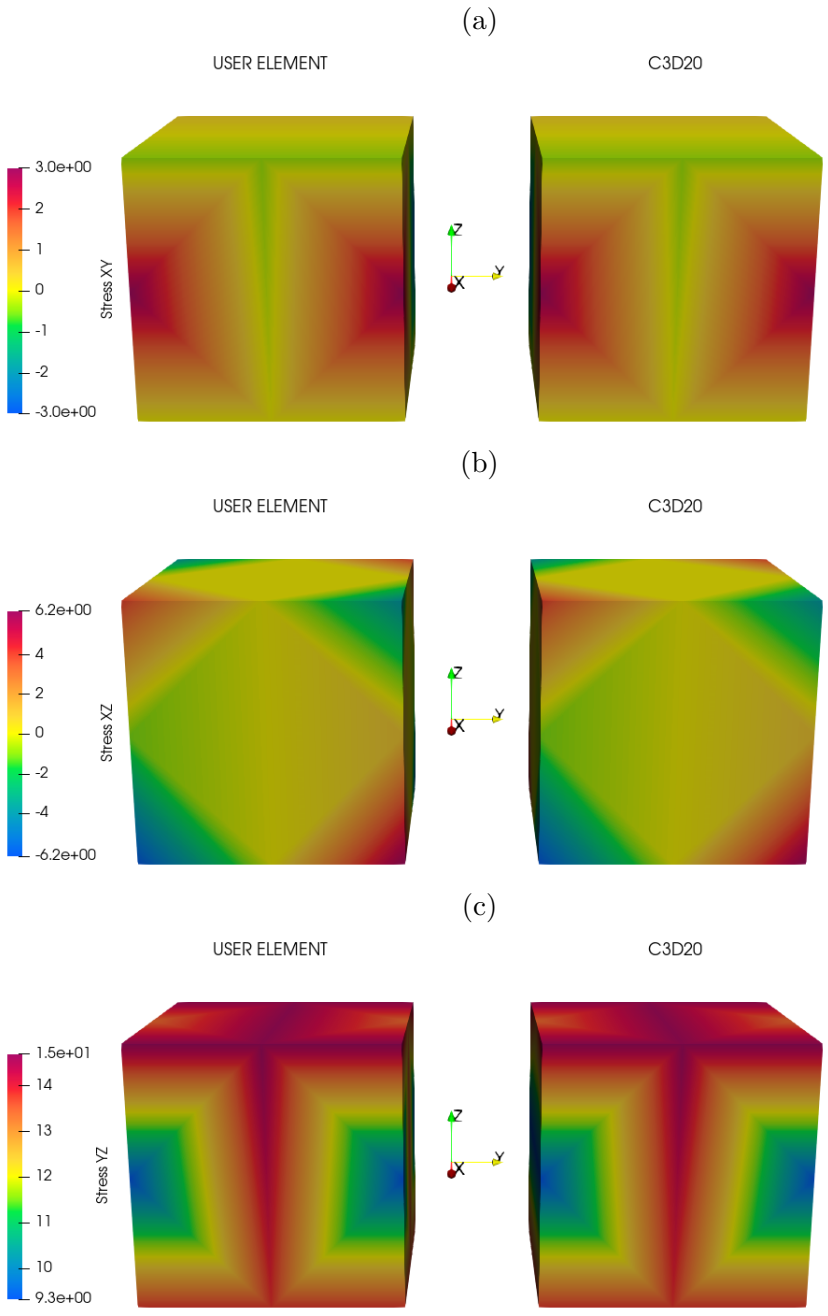

Figure A.4: Comparison of nodal shear stress components (a) XY, (b) XZ, and (c) YZ between user element and Abaqus for quadrilateral element under shear

A.1.2 Torsion

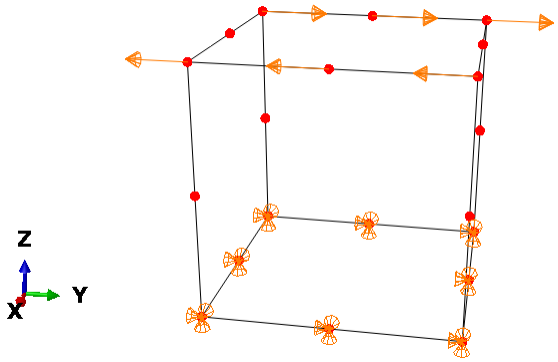

Figure A.5: Boundary conditions and loading for single quadrilateral element in torsion

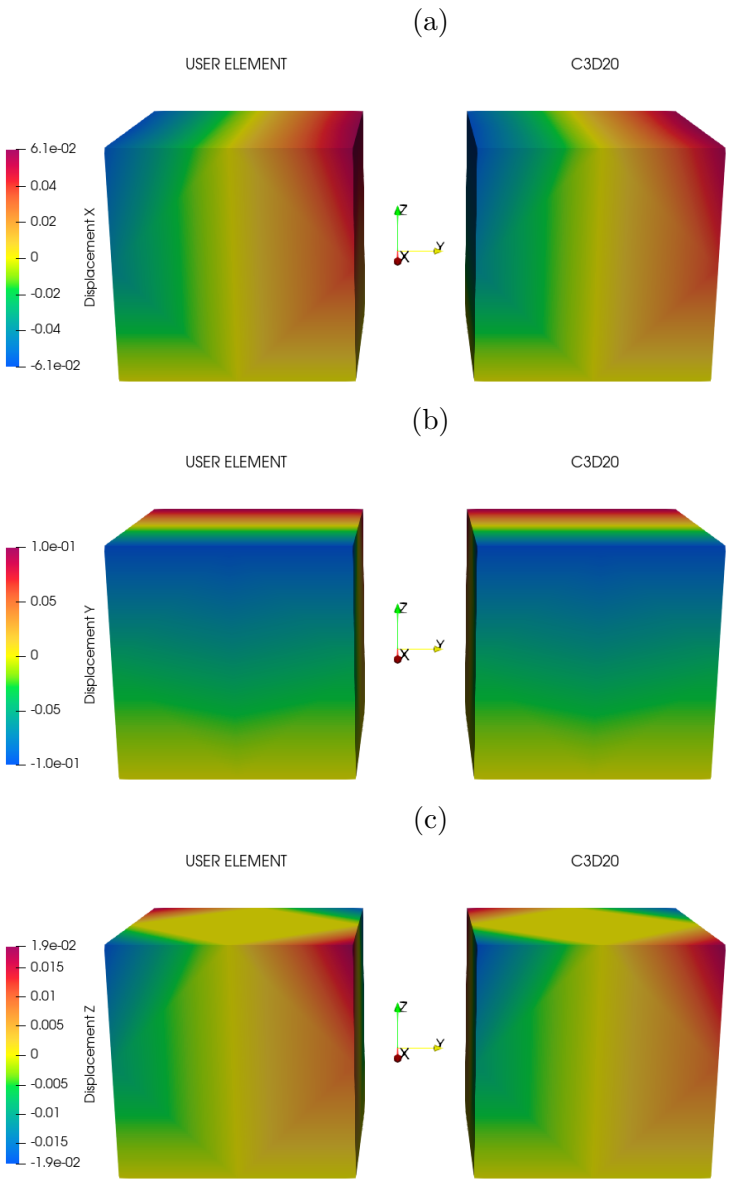

Figure A.6: Comparison of nodal displacements between user element and Abaqus in the (a) x, (b) y, and (c) z directions for quadrilateral element under torsion

(a)

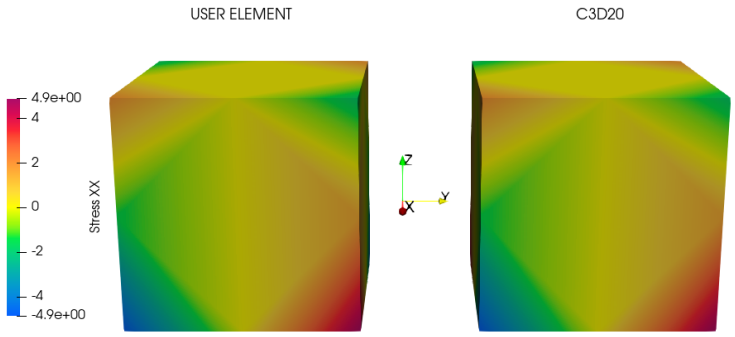

(b)

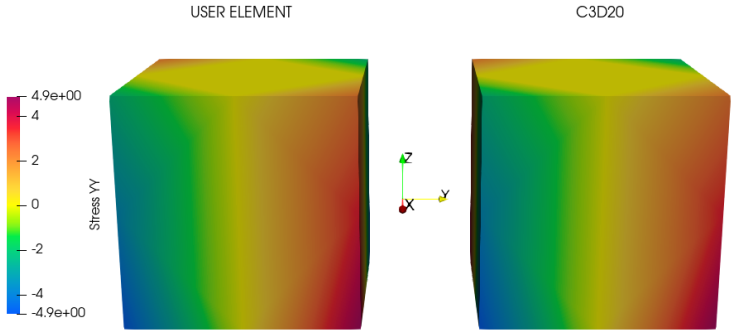

(c)

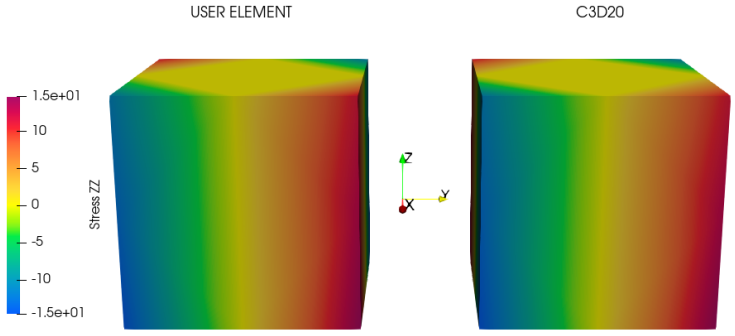

Figure A.7: Comparison of nodal normal stress components (a) XX, (b) YY, and (c) ZZ between user element and Abaqus for quadrilateral element under torsion

(a)

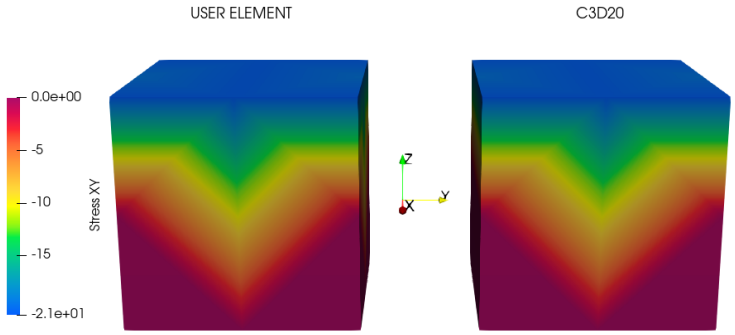

(b)

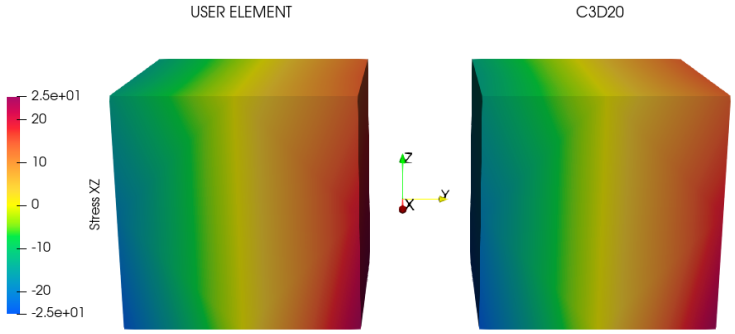

(c)

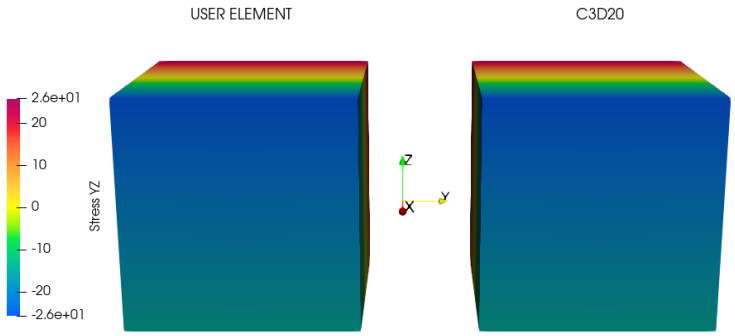

Figure A.8: Comparison of nodal shear stress components (a) XY, (b) XZ, and (c) YZ between user element and Abaqus for quadrilateral element under torsion

A.2 Single Wedge

A.2.1 Shear

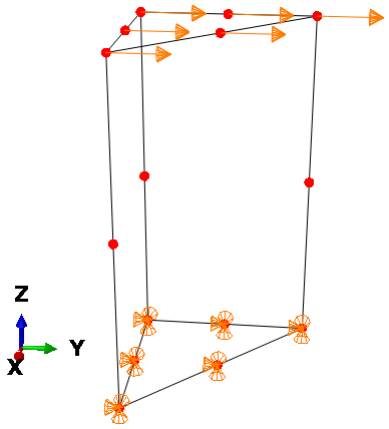

Figure A.9: Boundary conditions and loading for single wedge element in shear

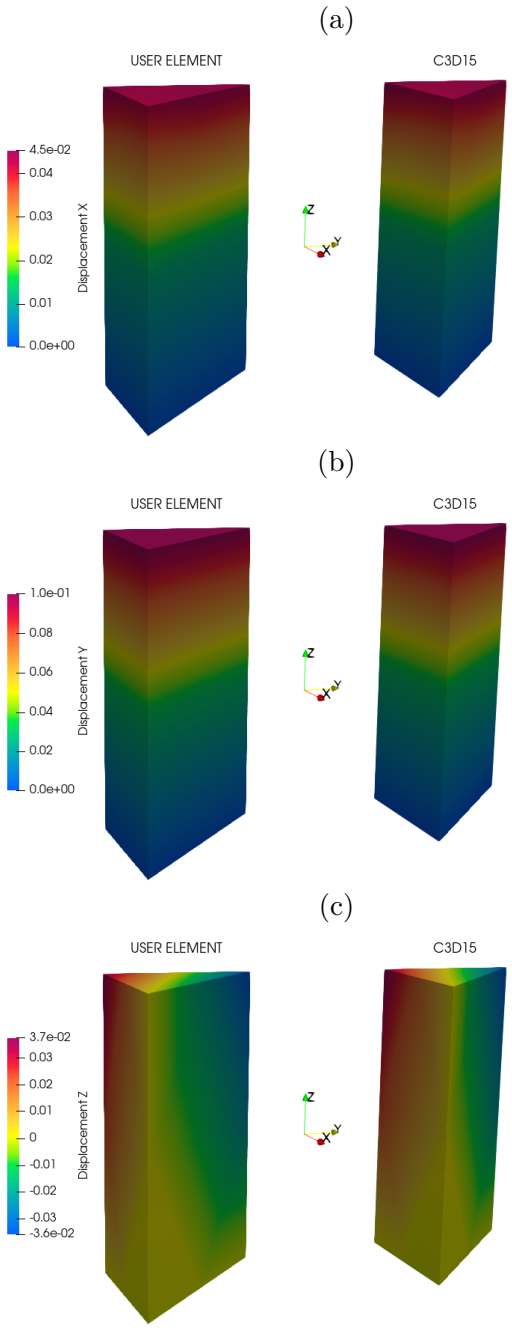

Figure A.10: Comparison of nodal displacements between user element and Abaqus in the (a) x, (b) y, and (c) z directions for wedge element under shear

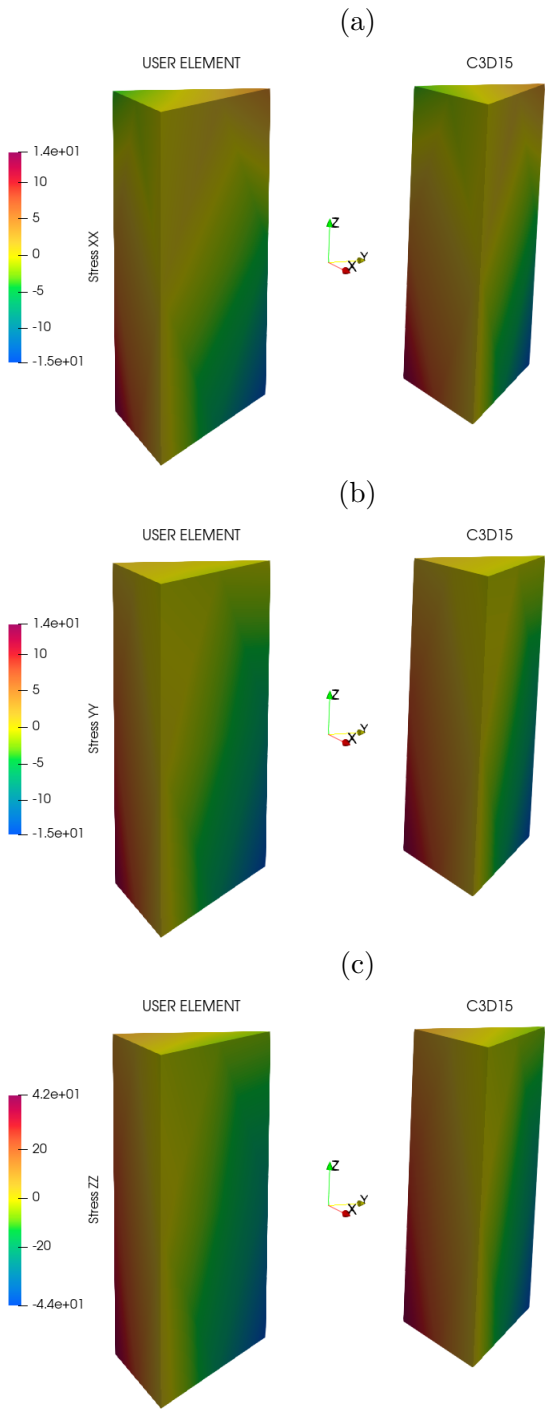

Figure A.11: Comparison of nodal normal stress components (a) XX, (b) YY, and (c) ZZ between user element and Abaqus for wedge element under shear

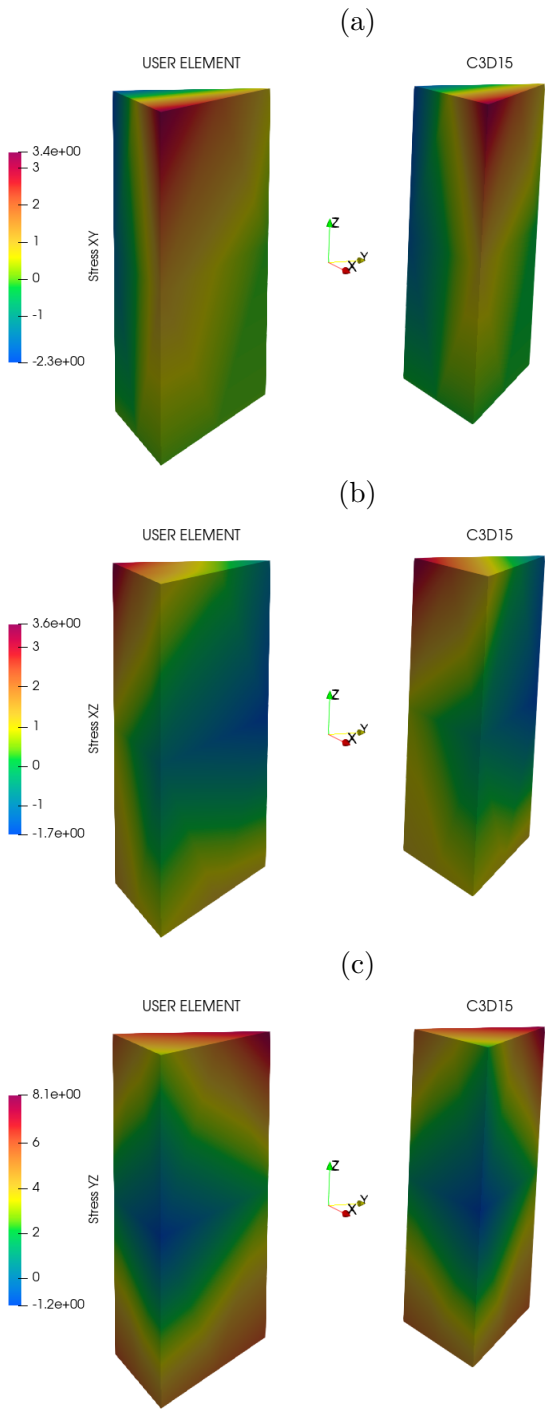

Figure A.12: Comparison of nodal shear stress components (a) XY, (b) XZ, and (c) YZ between user element and Abaqus for wedge element under shear

A.2.2 Torsion

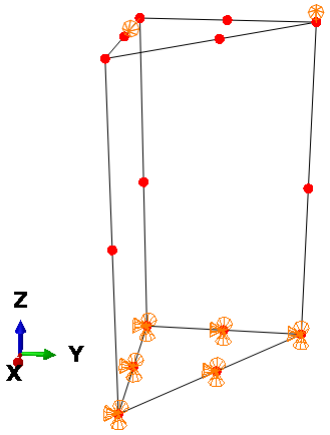

Figure A.13: Boundary conditions and loading for single wedge element in torsion

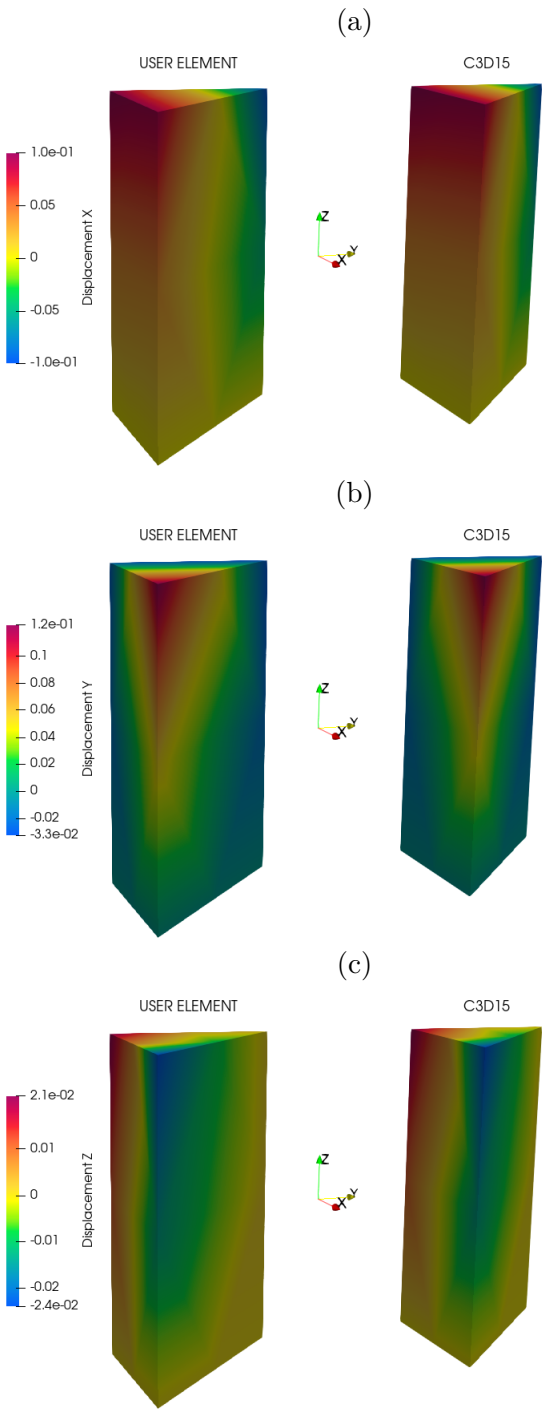

Figure A.14: Comparison of nodal displacements between user element and Abaqus in the (a) x, (b) y, and (c) z directions for wedge element under torsion

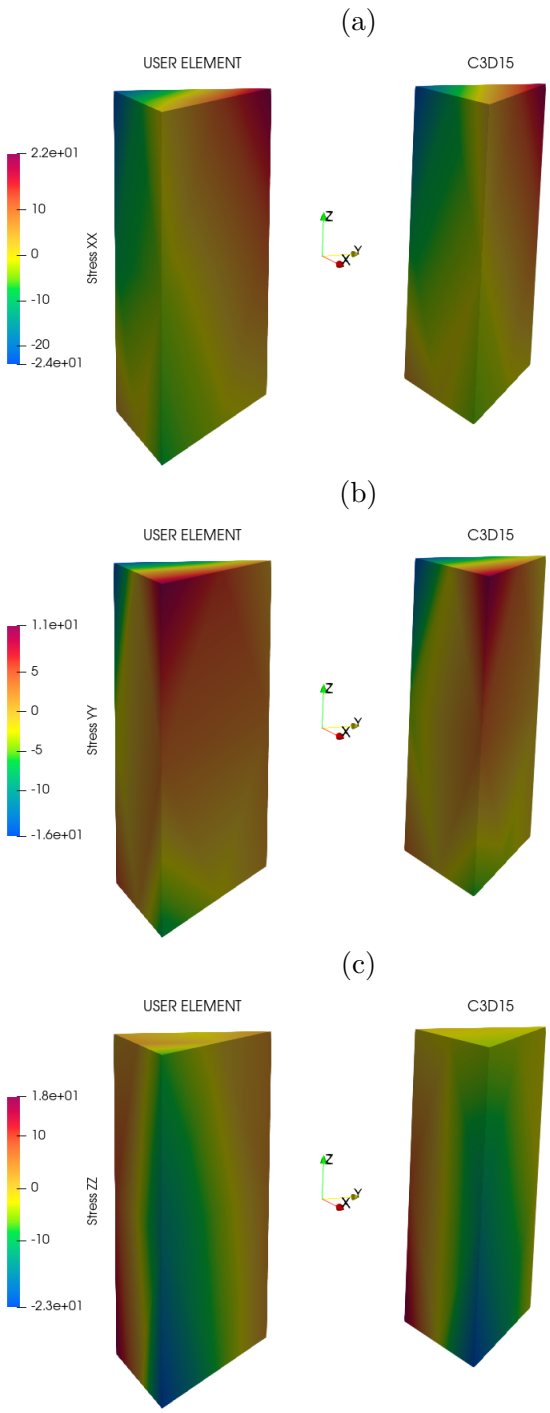

Figure A.15: Comparison of nodal normal stress components (a) XX, (b) YY, and (c) ZZ between user element and Abaqus for wedge element under torsion

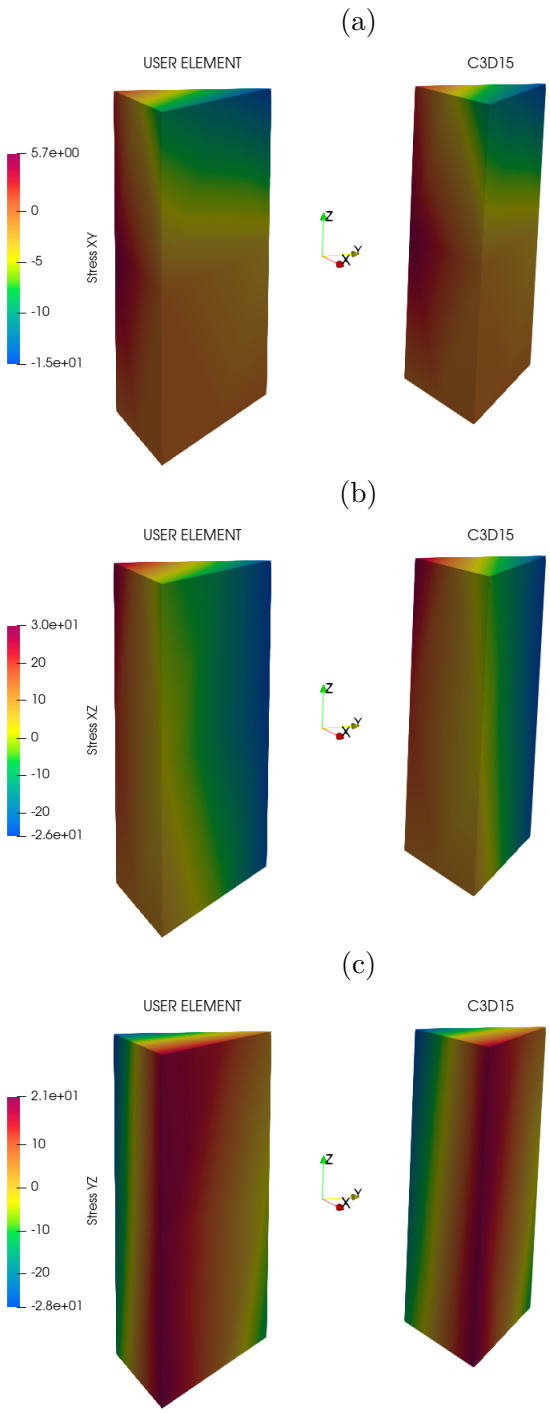

Figure A.16: Comparison of nodal shear stress components (a) XY, (b) XZ, and (c) YZ between user element and Abaqus for wedge element under torsion

A.3 Quadrilateral Assembly

A.3.1 Shear

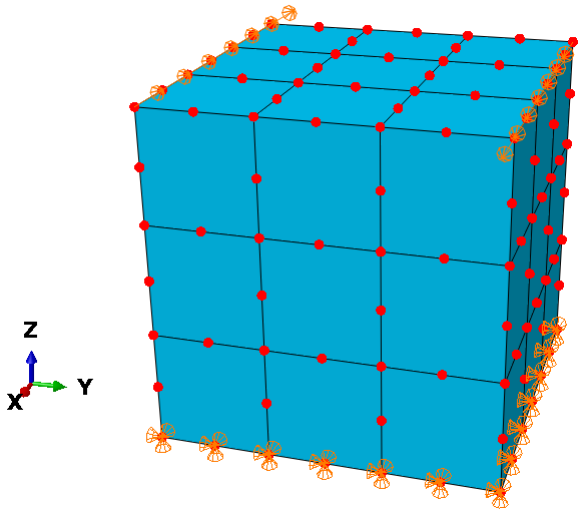

Figure A.17: Boundary conditions and loading for quadrilateral element assembly in shear

(a)

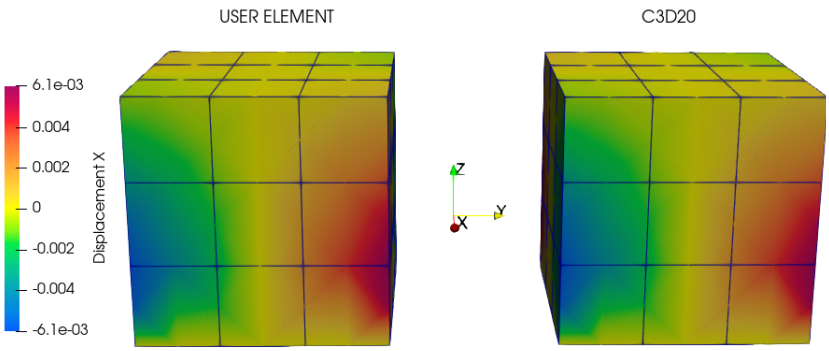

(b)

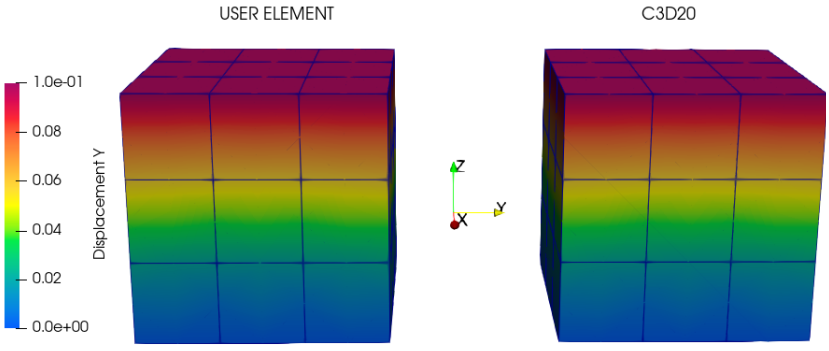

(c)

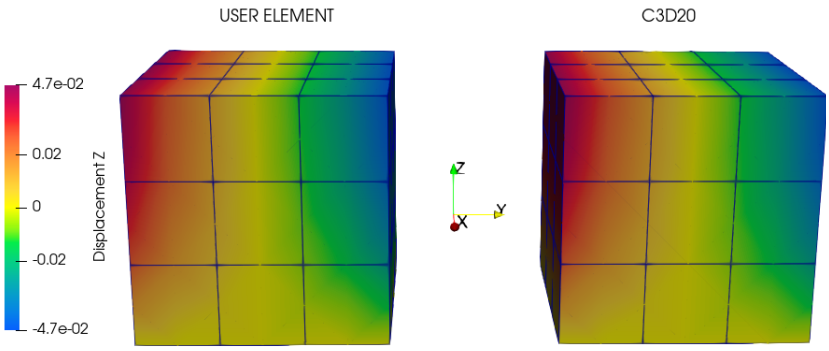

Figure A.18: Comparison of nodal displacements between user element and Abaqus assemblies in the (a) x, (b) y, and (c) z directions for quadrilateral assembly under shear

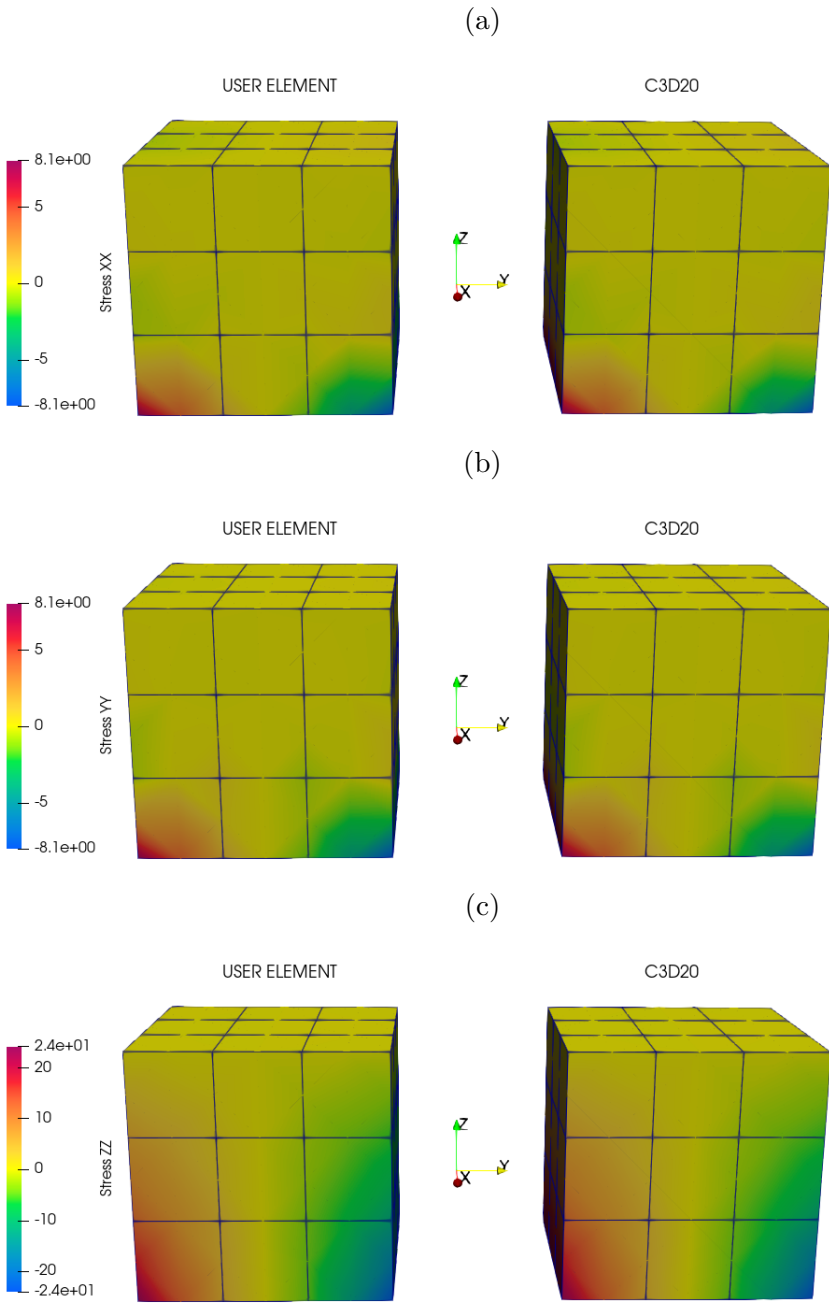

Figure A.19: Comparison of nodal normal stress components (a) XX, (b) YY, and (c) ZZ between user element and Abaqus assemblies for quadrilateral assembly under shear

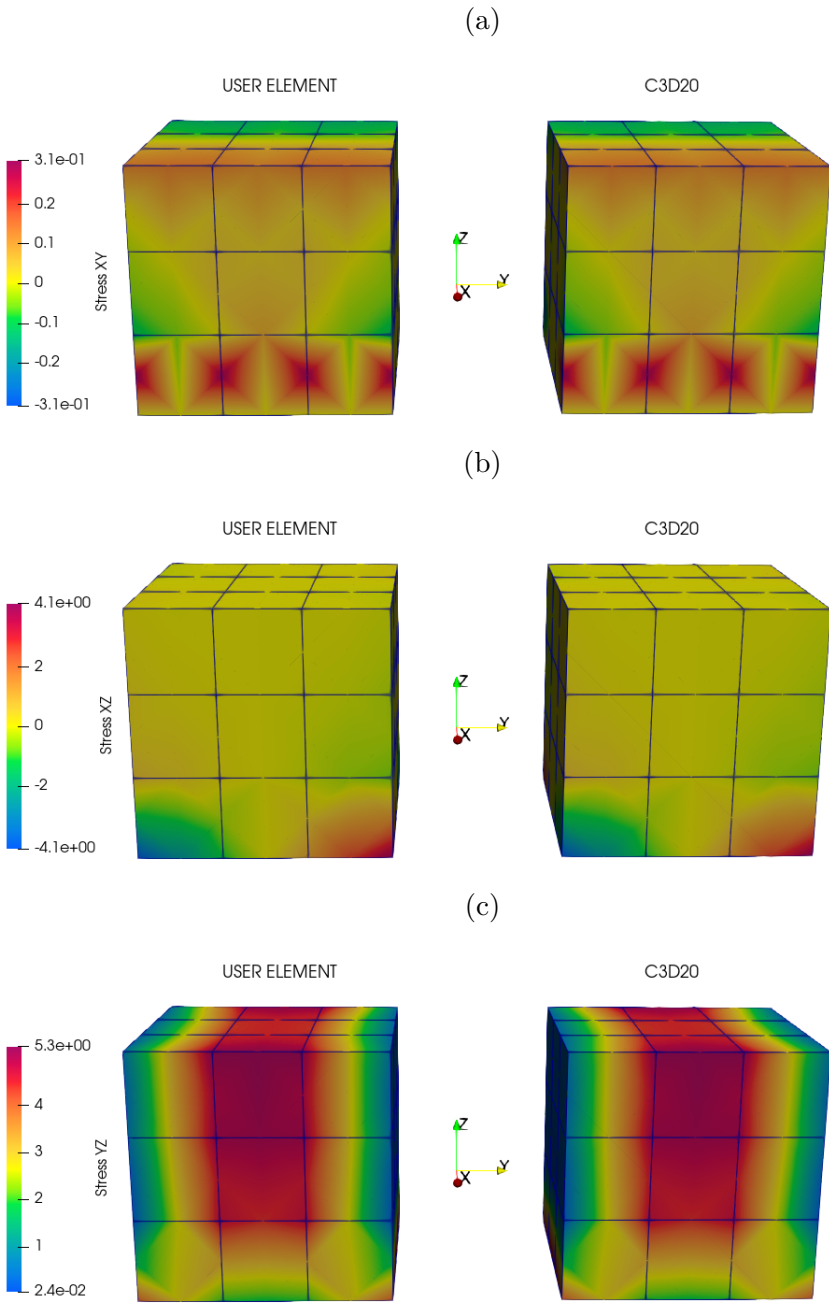

Figure A.20: Comparison of nodal shear stress components (a) XY, (b) XZ, and (c) YZ between user element and Abaqus assemblies for quadrilateral assembly under shear

A.3.2 Torsion

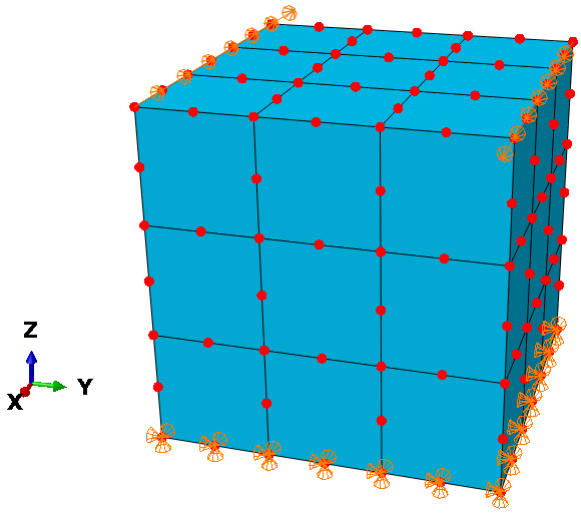

Figure A.21: Boundary conditions and loading for quadrilateral element assembly in torsion

(a)

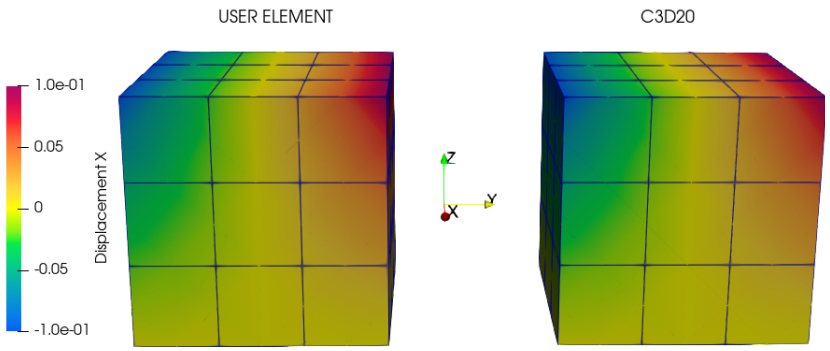

(b)

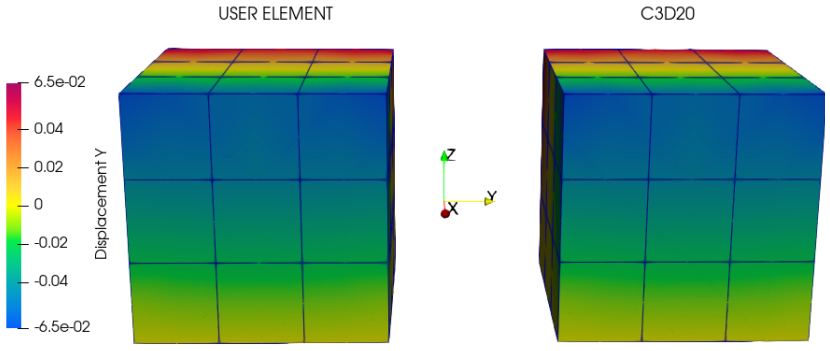

(c)

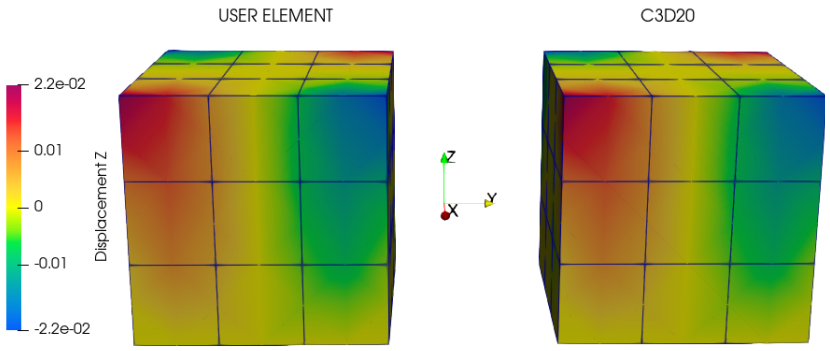

Figure A.22: Comparison of nodal displacements between user element and Abaqus assemblies in the (a) x, (b) y, and (c) z directions for quadrilateral assembly under torsion

(a)

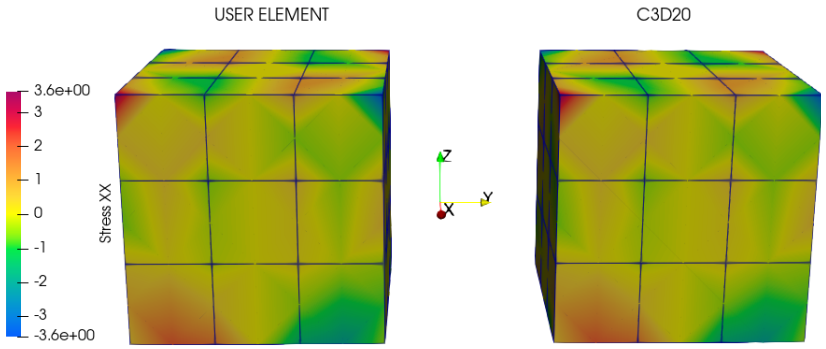

(b)

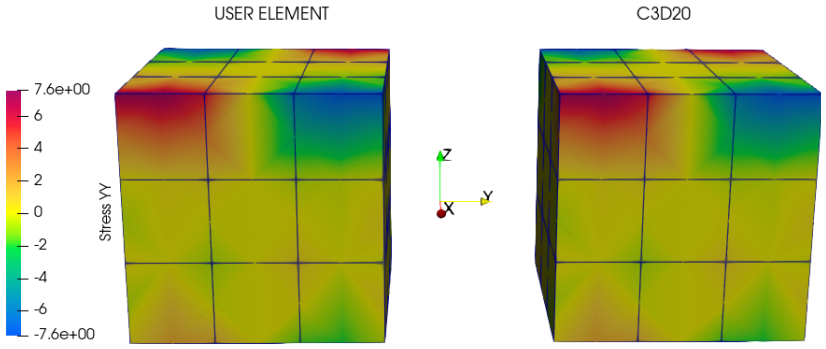

(c)

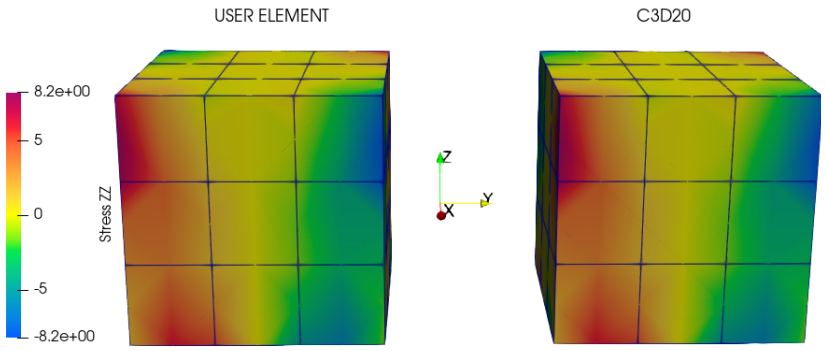

Figure A.23: Comparison of nodal normal stress components (a) XX, (b) YY, and (c) ZZ between user element and Abaqus assemblies for quadrilateral assembly under torsion

(a)

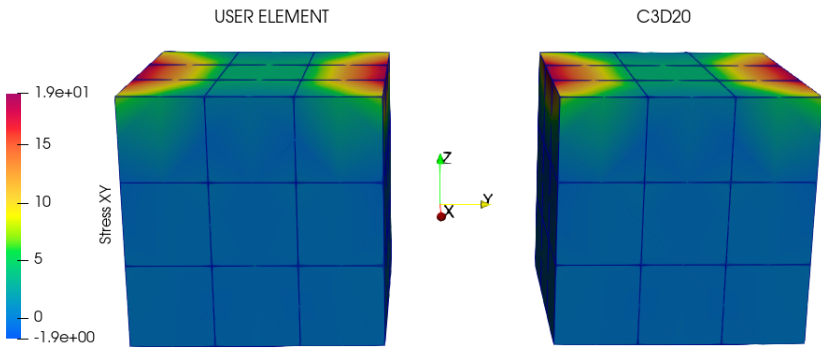

(b)

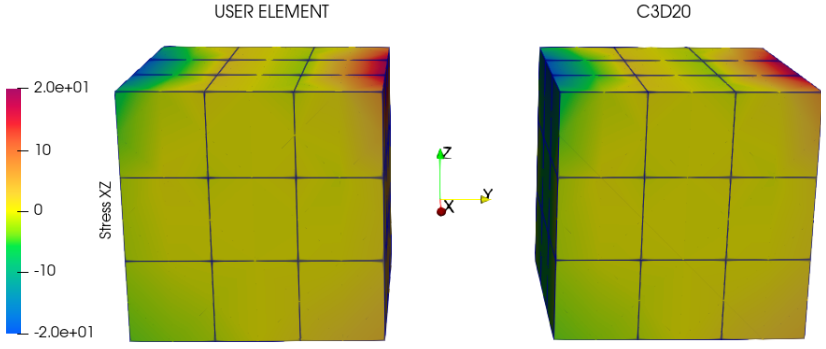

(c)

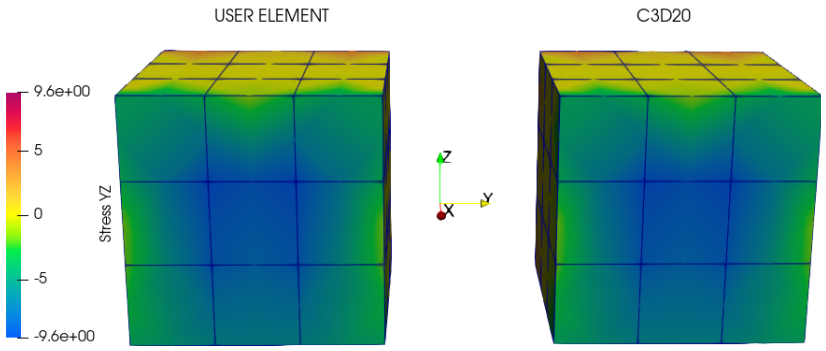

Figure A.24: Comparison of nodal shear stress components (a) XY, (b) XZ, and (c) YZ between user element and Abaqus assemblies for quadrilateral assembly under torsion

A.4 Wedge Assembly

A.4.1 Shear

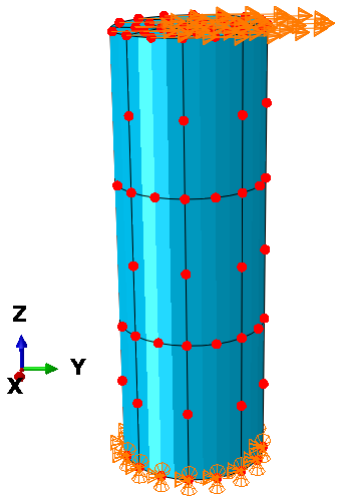

Figure A.25: Boundary conditions and loading for cylindrical wedge element assembly in shear

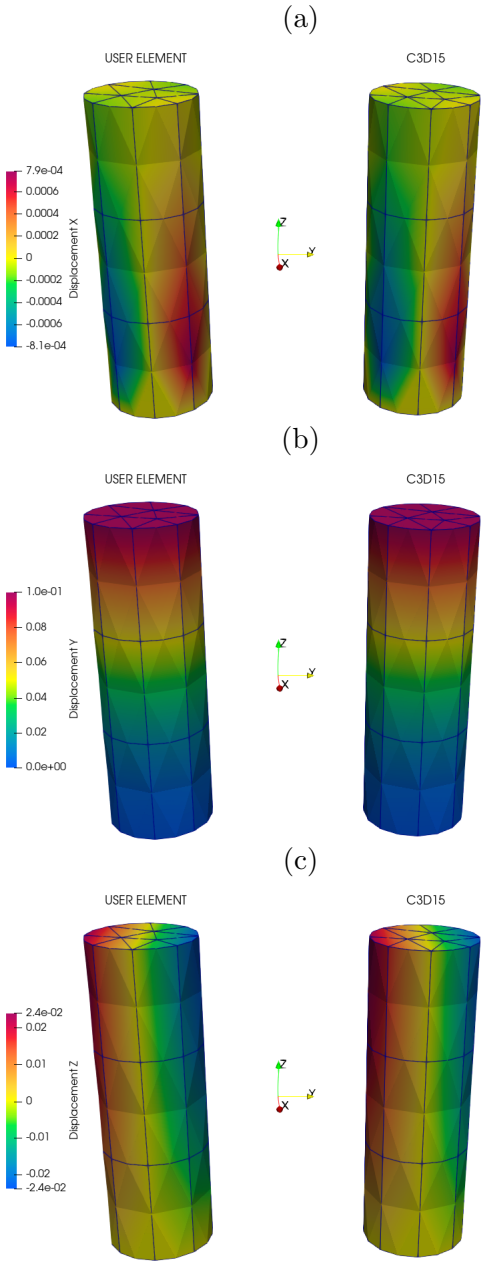

Figure A.26: Comparison of nodal displacements between user element and Abaqus assemblies in the (a) x, (b) y, and (c) z directions for wedge assembly under shear

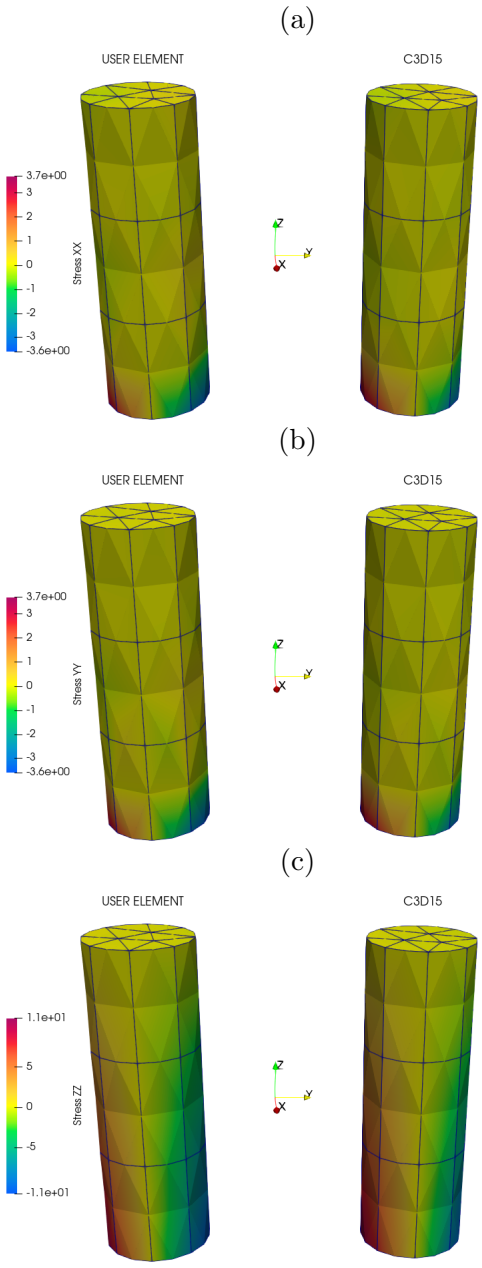

Figure A.27: Comparison of nodal normal stress components (a) XX, (b) YY, and (c) ZZ between user element and Abaqus assemblies for wedge assembly under shear

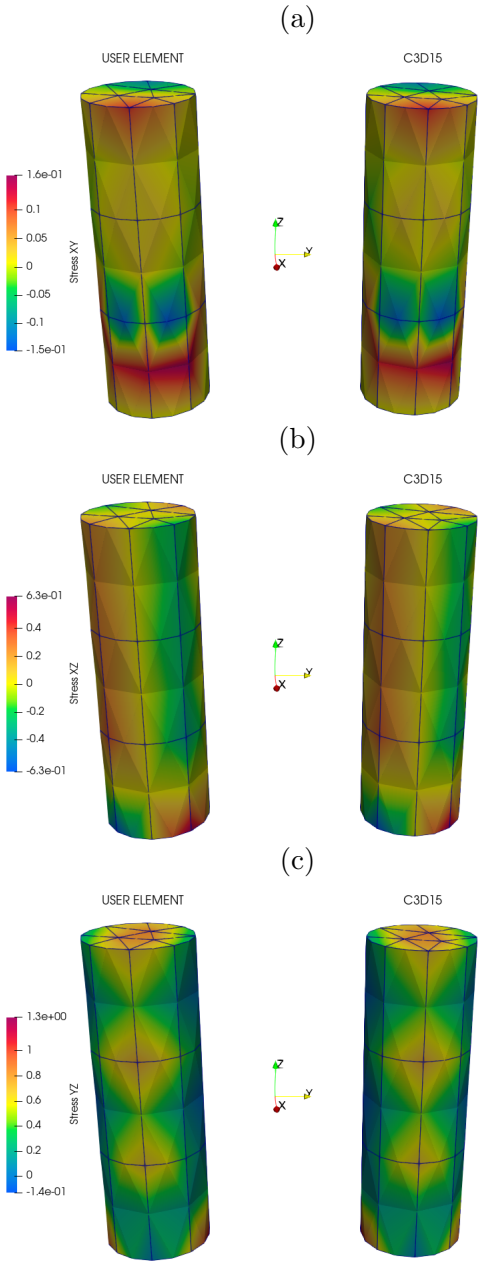

Figure A.28: Comparison of nodal shear stress components (a) XY, (b) XZ, and (c) YZ between user element and Abaqus assemblies for wedge assembly under shear

A.4.2 Torsion

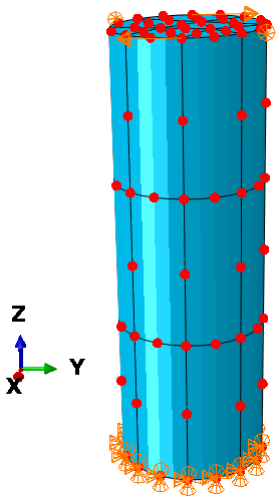

Figure A.29: Boundary conditions and loading for cylindrical wedge element assembly in torsion

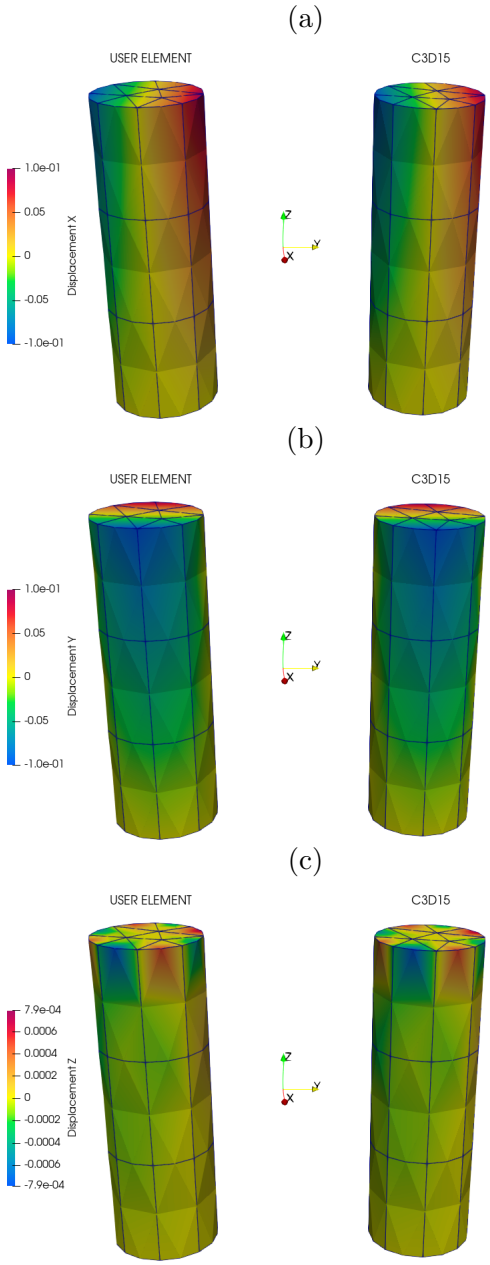

Figure A.30: Comparison of nodal displacements between user element and Abaqus assemblies in the (a) x, (b) y, and (c) z directions for wedge assembly under torsion

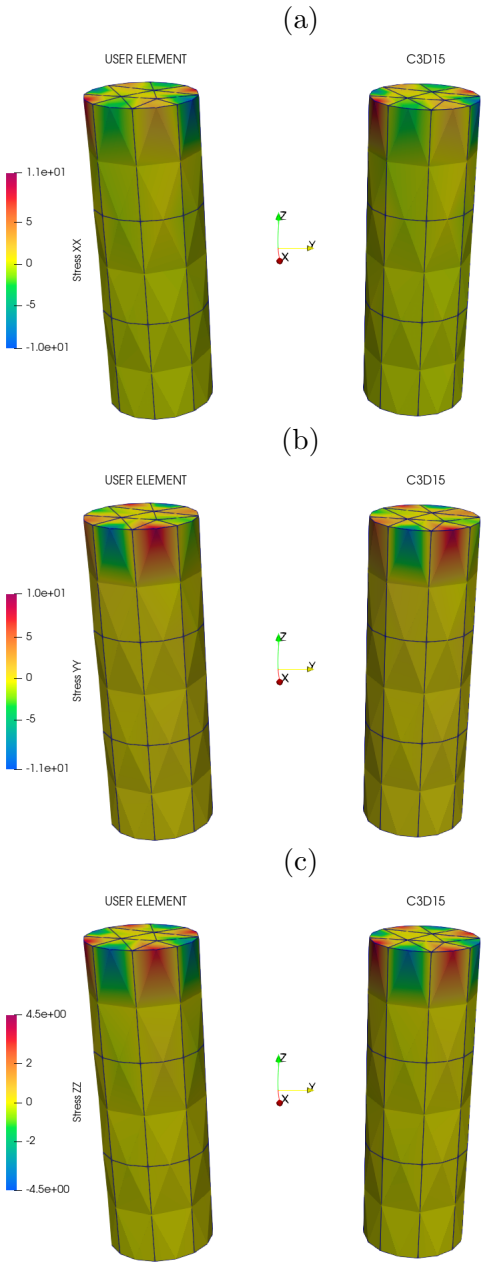

Figure A.31: Comparison of nodal normal stress components (a) XX, (b) YY, and (c) ZZ between user element and Abaqus assemblies for wedge assembly under torsion

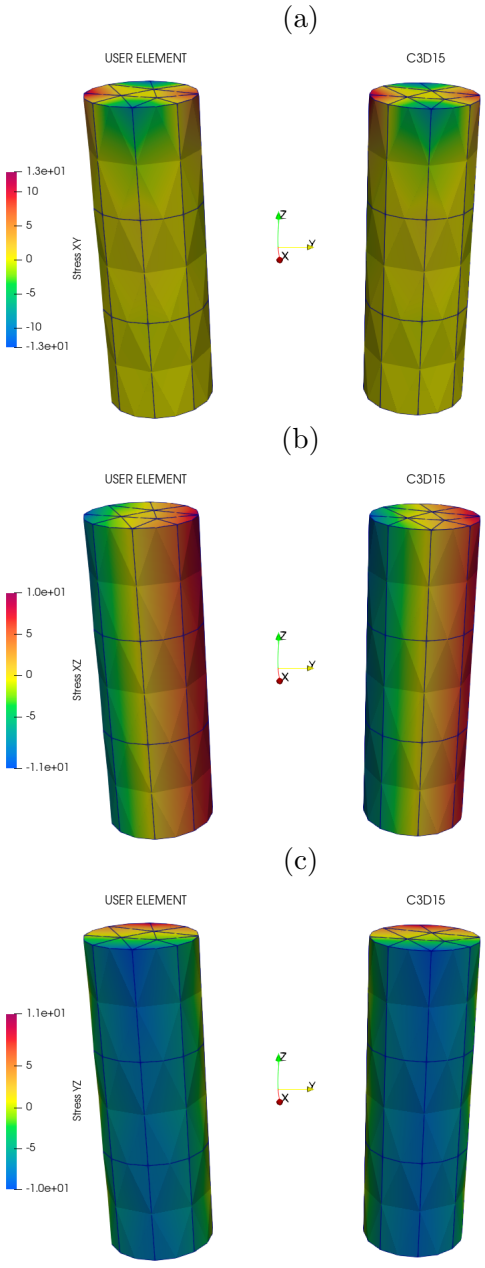

Figure A.32: Comparison of nodal shear stress components (a) XY, (b) XZ, and (c) YZ between user element and Abaqus assemblies for wedge assembly under torsion

Appendix B

Conceptual Cases

B.1 Single Quadrilateral

B.1.1 Compression

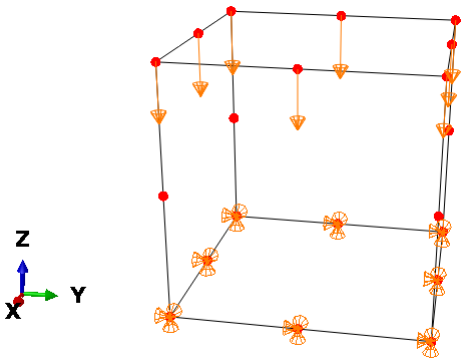

Figure B.1: Boundary conditions and loading for single quadrilateral element in uniaxial compression

Table B.1: Ranges for magnitudes of tensors of interest for quadrilateral element in uniaxial compression

Tensor Magnitude	**Classical**	**Cosserat**	**Exponential Grading**	**Exponential Grading with Cosserat**
$\|\vec{\boldsymbol{u}}\|_{min}\,(mm)$	0	0	0	0
$\|\vec{\boldsymbol{u}}\|_{max}\,(mm)$	0.1013	0.1015	0.1021	0.1024
$\|\vec{\boldsymbol{\varphi}}\|_{min}\,(rad)$	0	0	0	0
$\|\vec{\boldsymbol{\varphi}}\|_{max}\,(rad)$	0	0.0014	0	0.0018
$\|\vec{\boldsymbol{\sigma}}\|_{min}\,(MPa)$	62.5391	63.6816	8.4902	8.6884
$\|\vec{\boldsymbol{\sigma}}\|_{max}\,(MPa)$	79.0199	80.0747	574.2159	576.5704
$\|\vec{\boldsymbol{\mu}}\|_{min}\,(MPa \cdot mm)$	0	1.4202	0	0.2104
$\|\vec{\boldsymbol{\mu}}\|_{max}\,(MPa \cdot mm)$	0	3.7572	0	20.5358

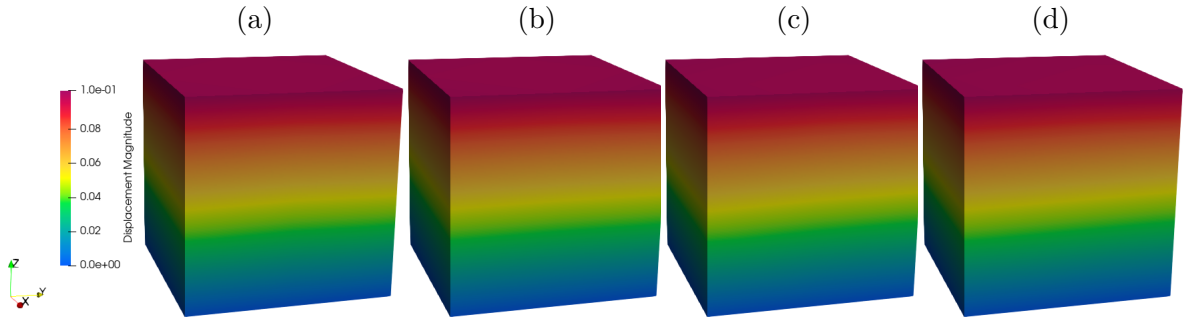

Figure B.2: Comparison of nodal displacements vector magnitude for (a) classical, (b) Cosserat, (c) functionally graded, and (d) functionally graded with Cosserat effects cases for a quadrilateral element in uniaxial compression

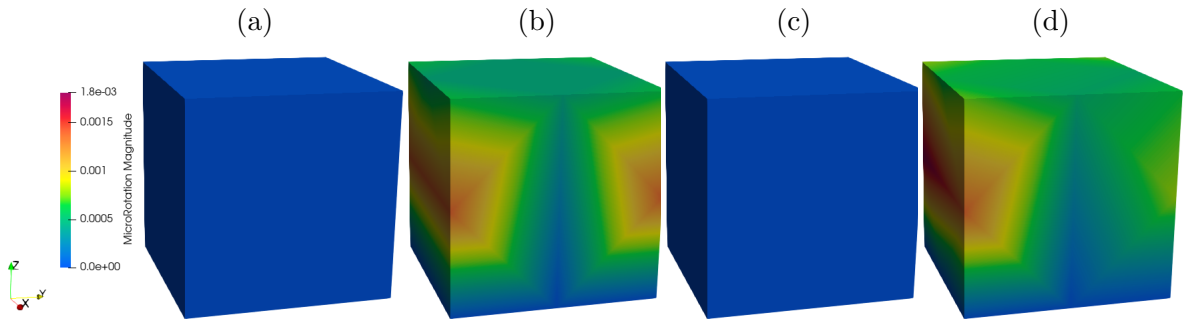

Figure B.3: Comparison of nodal rotations vector magnitude for (a) classical, (b) Cosserat, (c) functionally graded, and (d) functionally graded with Cosserat effects cases for a quadrilateral element in uniaxial compression

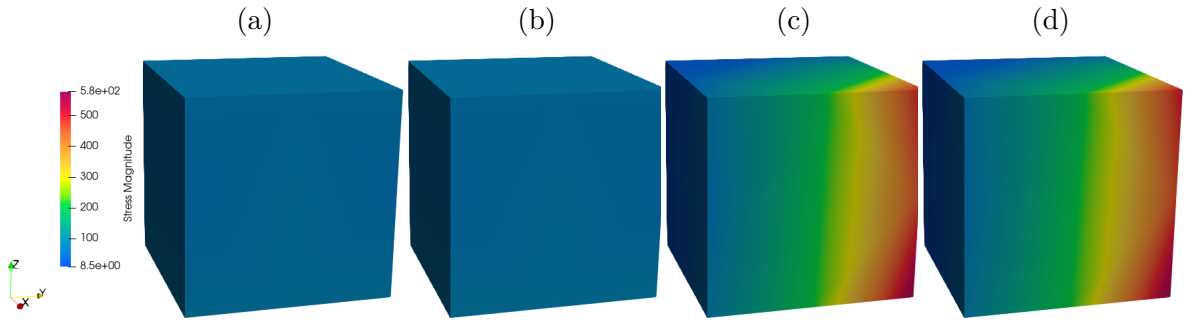

Figure B.4: Comparison of nodal stresses vector magnitude for (a) classical, (b) Cosserat, (c) functionally graded, and (d) functionally graded with Cosserat effects cases for a quadrilateral element in uniaxial compression

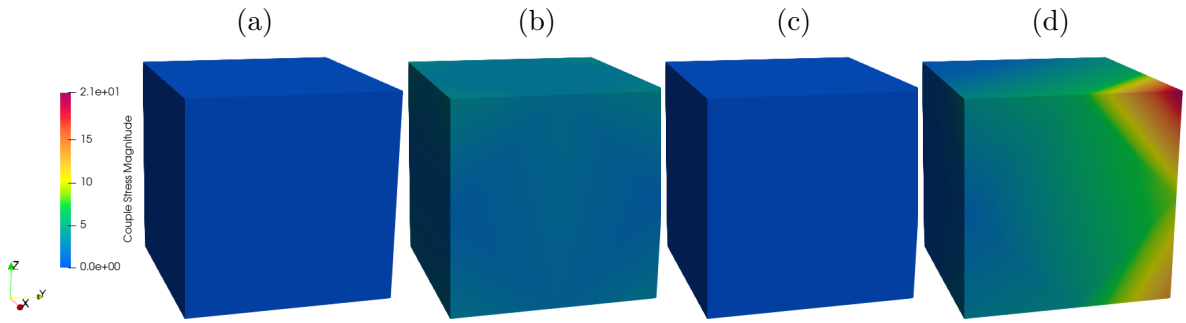

Figure B.5: Comparison of nodal couple stresses vector magnitude for (a) classical, (b) Cosserat, (c) functionally graded, and (d) functionally graded with Cosserat effects cases for a quadrilateral element in uniaxial compression

B.1.2 Shear

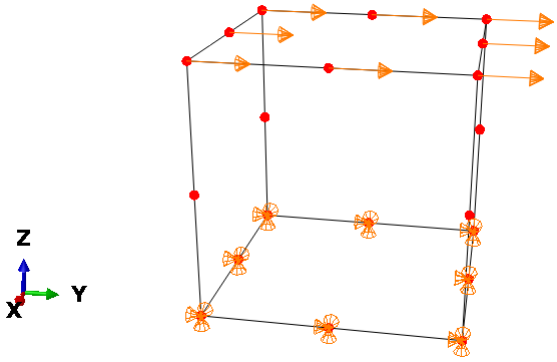

Figure B.6: Boundary conditions and loading for single quadrilateral element in shear

Table B.2: Ranges for magnitudes of tensors of interest for quadrilateral element in shear

Tensor Magnitude	**Classical**	**Cosserat**	**Exponential Grading**	**Exponential Grading with Cosserat**
$\|\vec{\boldsymbol{u}}\|_{min}\,(mm)$	0	0	0	0
$\|\vec{\boldsymbol{u}}\|_{max}\,(mm)$	0.1099	0.1042	0.1	0.1066
$\|\vec{\boldsymbol{\varphi}}\|_{min}\,(rad)$	0	0	0	0
$\|\vec{\boldsymbol{\varphi}}\|_{max}\,(rad)$	0	0.0370	0	0.0384
$\|\vec{\boldsymbol{\sigma}}\|_{min}\,(MPa)$	19.5603	31.5239	6.7668	4.8977
$\|\vec{\boldsymbol{\sigma}}\|_{max}\,(MPa)$	73.3376	54.8330	369.4528	334.9027
$\|\vec{\boldsymbol{\mu}}\|_{min}\,(MPa \cdot mm)$	0	0.6994	0	0.3707
$\|\vec{\boldsymbol{\mu}}\|_{max}\,(MPa \cdot mm)$	0	36.6073	0	278.6727

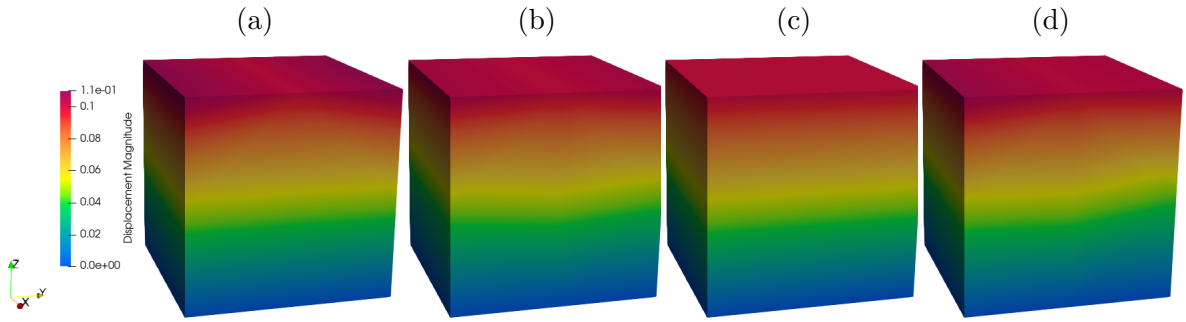

Figure B.7: Comparison of nodal displacements vector magnitude for (a) classical, (b) Cosserat, (c) functionally graded, and (d) functionally graded with Cosserat effects cases for a quadrilateral element in shear

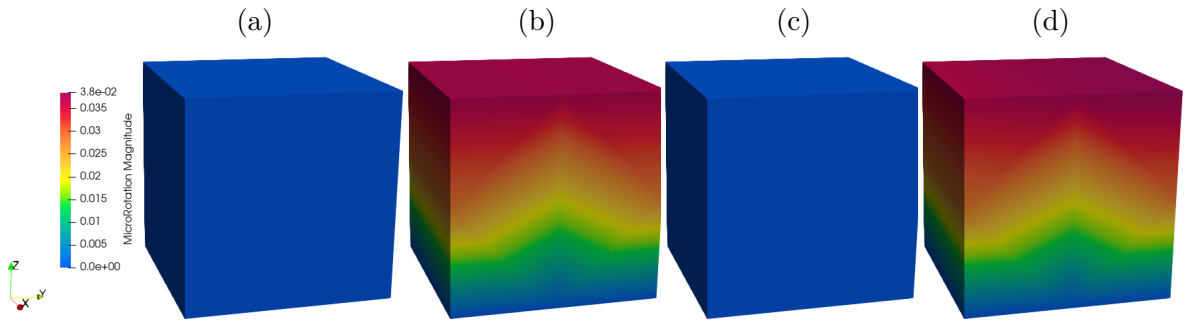

Figure B.8: Comparison of nodal rotations vector magnitude for (a) classical, (b) Cosserat, (c) functionally graded, and (d) functionally graded with Cosserat effects cases for a quadrilateral element in shear

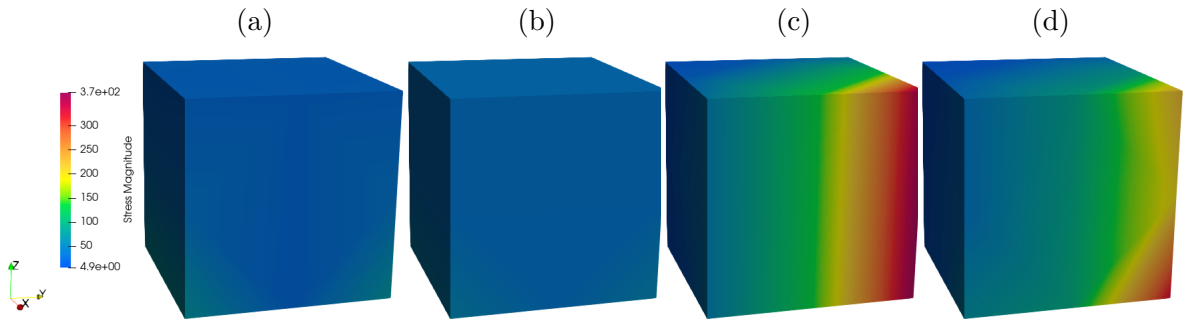

Figure B.9: Comparison of nodal stresses vector magnitude for (a) classical, (b) Cosserat, (c) functionally graded, and (d) functionally graded with Cosserat effects cases for a quadrilateral element in shear

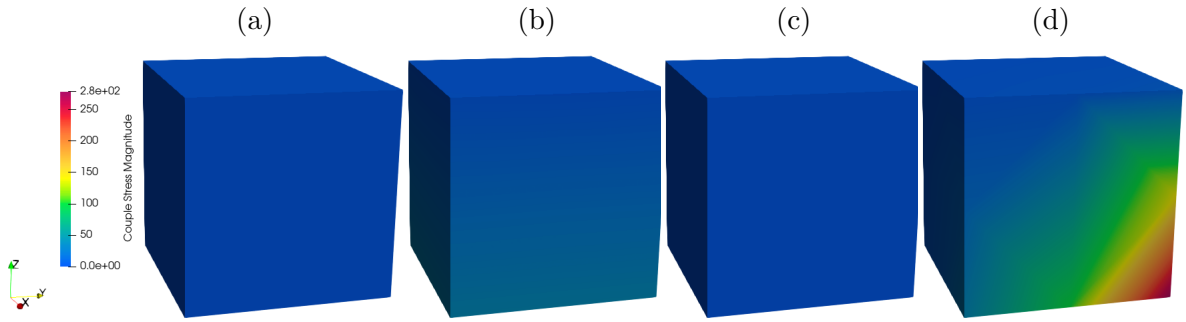

Figure B.10: Comparison of nodal couple stresses vector magnitude for (a) classical, (b) Cosserat, (c) functionally graded, and (d) functionally graded with Cosserat effects cases for a quadrilateral element in shear

B.1.3 Torsion

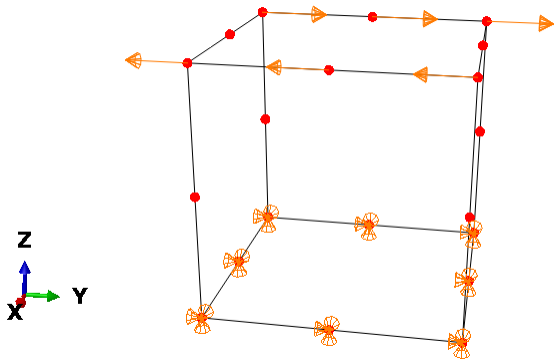

Figure B.11: Boundary conditions and loading for single quadrilateral element in torsion

Table B.3: Ranges for magnitudes of tensors of interest for quadrilateral element in torsion

Tensor Magnitude	**Classical**	**Cosserat**	**Exponential Grading**	**Exponential Grading with Cosserat**
$\|\vec{\boldsymbol{u}}\|_{min}\,(mm)$	0	0	0	0
$\|\vec{\boldsymbol{u}}\|_{max}\,(mm)$	0.1173	0.1042	0.1	0.1062
$\|\vec{\boldsymbol{\varphi}}\|_{min}\,(rad)$	0	0	0	0
$\|\vec{\boldsymbol{\varphi}}\|_{max}\,(rad)$	0	0.04040	0	0.0436
$\|\vec{\boldsymbol{\sigma}}\|_{min}\,(MPa)$	20.9006	5.6464	4.8047	3.0801
$\|\vec{\boldsymbol{\sigma}}\|_{max}\,(MPa)$	52.1183	101.8299	850.3520	543.0272
$\|\vec{\boldsymbol{\mu}}\|_{min}\,(MPa \cdot mm)$	0	21.7250	0	3.6057
$\|\vec{\boldsymbol{\mu}}\|_{max}\,(MPa \cdot mm)$	0	40.5563	0	286.2751

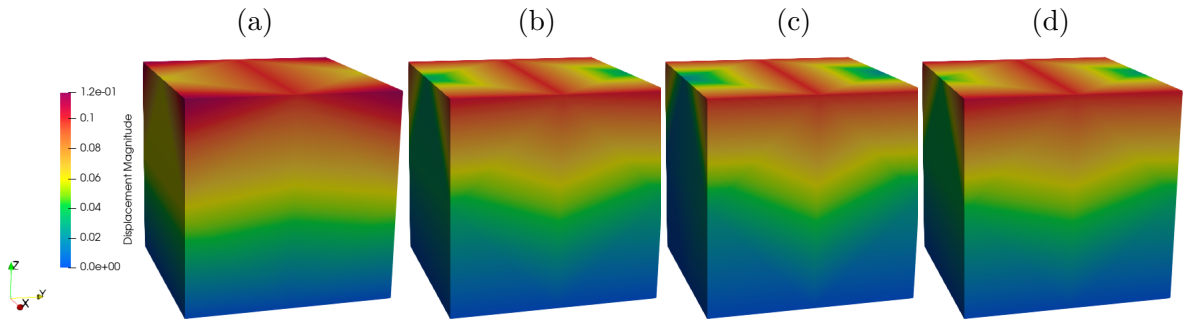

Figure B.12: Comparison of nodal displacements vector magnitude for (a) classical, (b) Cosserat, (c) functionally graded, and (d) functionally graded with Cosserat effects cases for a quadrilateral element in torsion

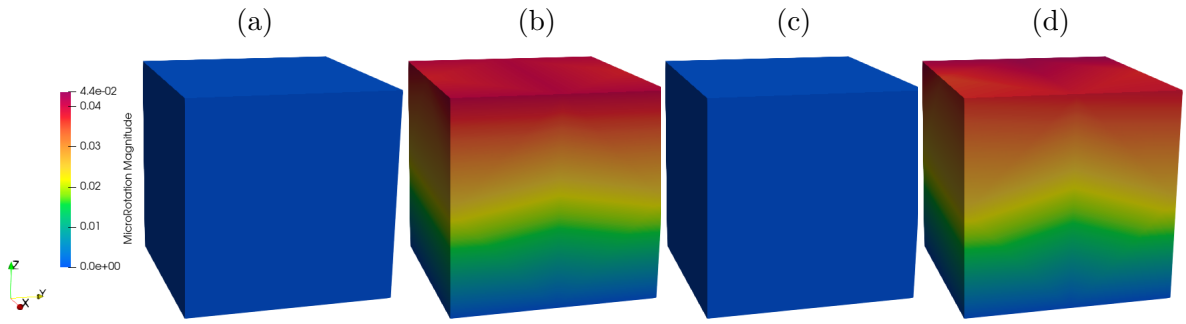

Figure B.13: Comparison of nodal rotations vector magnitude for (a) classical, (b) Cosserat, (c) functionally graded, and (d) functionally graded with Cosserat effects cases for a quadrilateral element in torsion

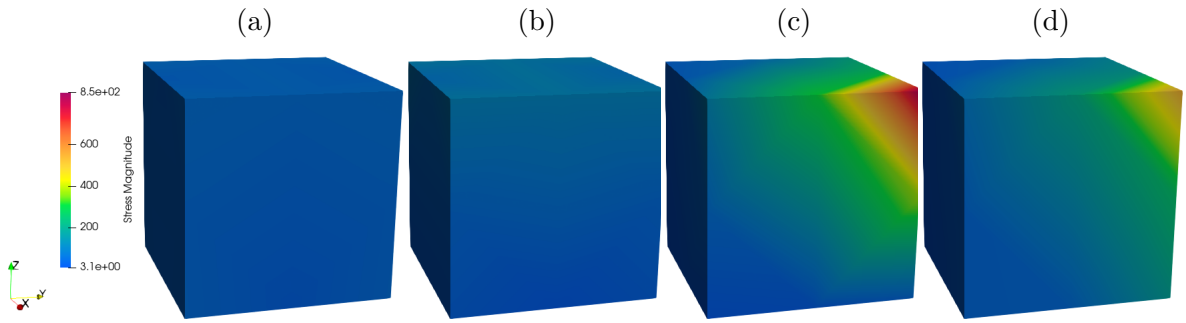

Figure B.14: Comparison of nodal stresses vector magnitude for (a) classical, (b) Cosserat, (c) functionally graded, and (d) functionally graded with Cosserat effects cases for a quadrilateral element in torsion

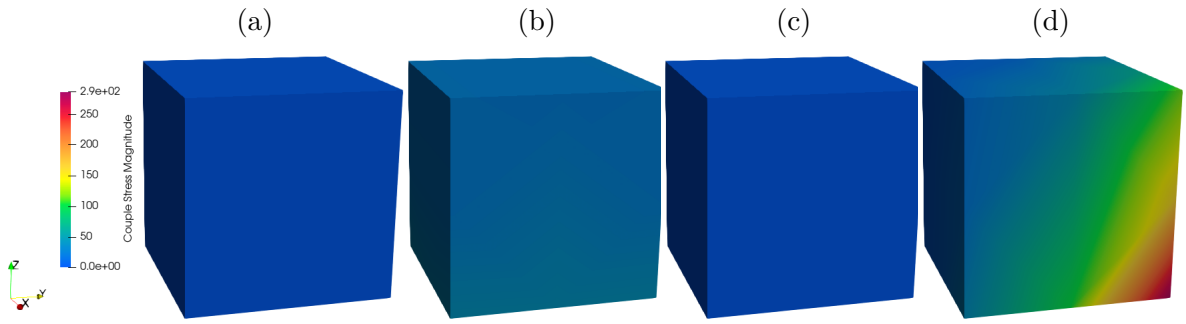

Figure B.15: Comparison of nodal couple stresses vector magnitude for (a) classical, (b) Cosserat, (c) functionally graded, and (d) functionally graded with Cosserat effects cases for a quadrilateral element in torsion

B.2 Single Wedge

B.2.1 Compression

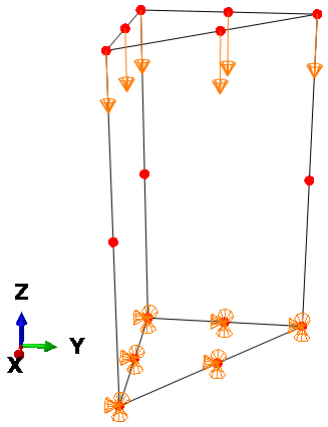

Figure B.16: Boundary conditions and loading for single wedge element in uniaxial compression

Table B.4: Ranges for magnitudes of tensors of interest for wedge element in uniaxial compression

Tensor Magnitude	**Classical**	**Cosserat**	**Exponential Grading**	**Exponential Grading with Cosserat**
$\|\vec{\boldsymbol{u}}\|_{min}\,(mm)$	0	0	0	0
$\|\vec{\boldsymbol{u}}\|_{max}\,(mm)$	0.1003	0.1003	0.1003	0.1003
$\|\vec{\boldsymbol{\varphi}}\|_{min}\,(rad)$	0	0	0	0
$\|\vec{\boldsymbol{\varphi}}\|_{max}\,(rad)$	0	0.0005	0	0.0005
$\|\vec{\boldsymbol{\sigma}}\|_{min}\,(MPa)$	61.0916	61.3622	61.1052	61.3943
$\|\vec{\boldsymbol{\sigma}}\|_{max}\,(MPa)$	78.3058	78.7716	212.7073	213.8461
$\|\vec{\boldsymbol{\mu}}\|_{min}\,(MPa \cdot mm)$	0	0.1488	0	0.2715
$\|\vec{\boldsymbol{\mu}}\|_{max}\,(MPa \cdot mm)$	0	1.6501	0	4.5660

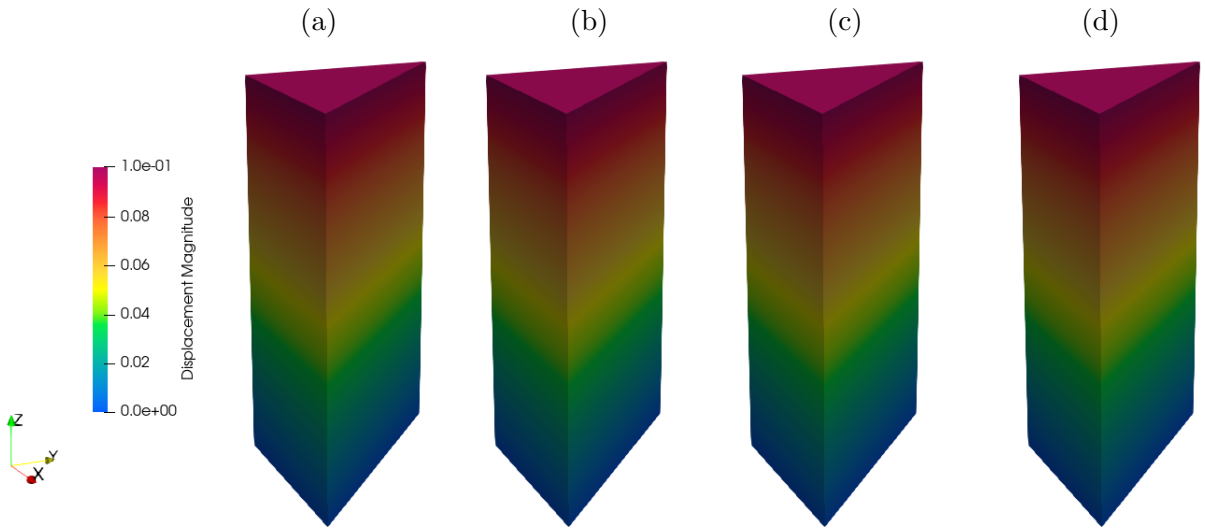

Figure B.17: Comparison of nodal displacements vector magnitude for (a) classical, (b) Cosserat, (c) functionally graded, and (d) functionally graded with Cosserat effects cases for a wedge element in uniaxial compression

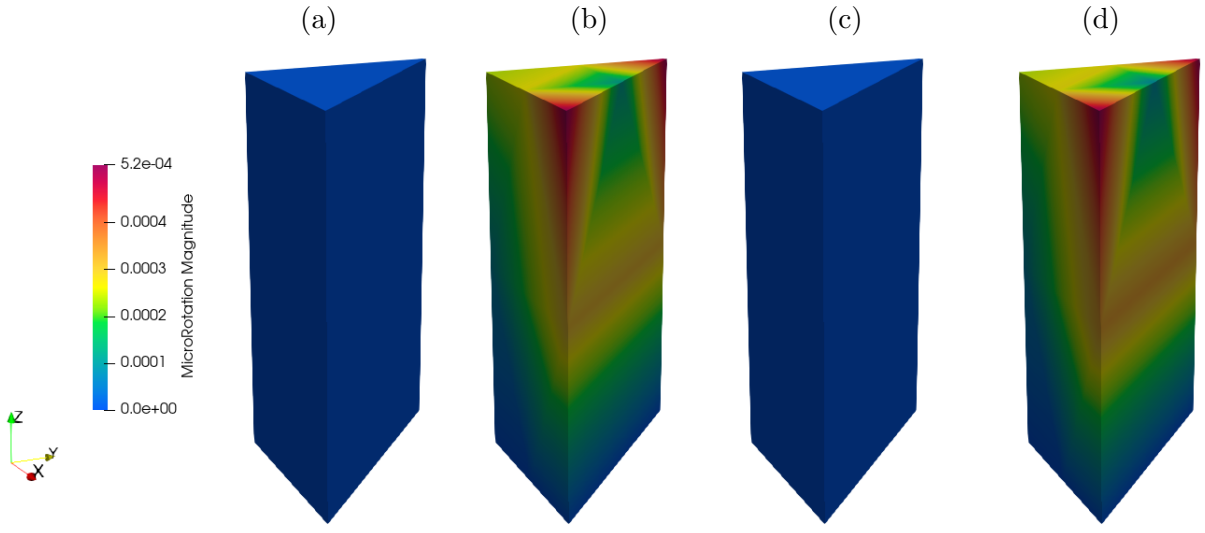

Figure B.18: Comparison of nodal rotations vector magnitude for (a) classical, (b) Cosserat, (c) functionally graded, and (d) functionally graded with Cosserat effects cases for a wedge element in uniaxial compression

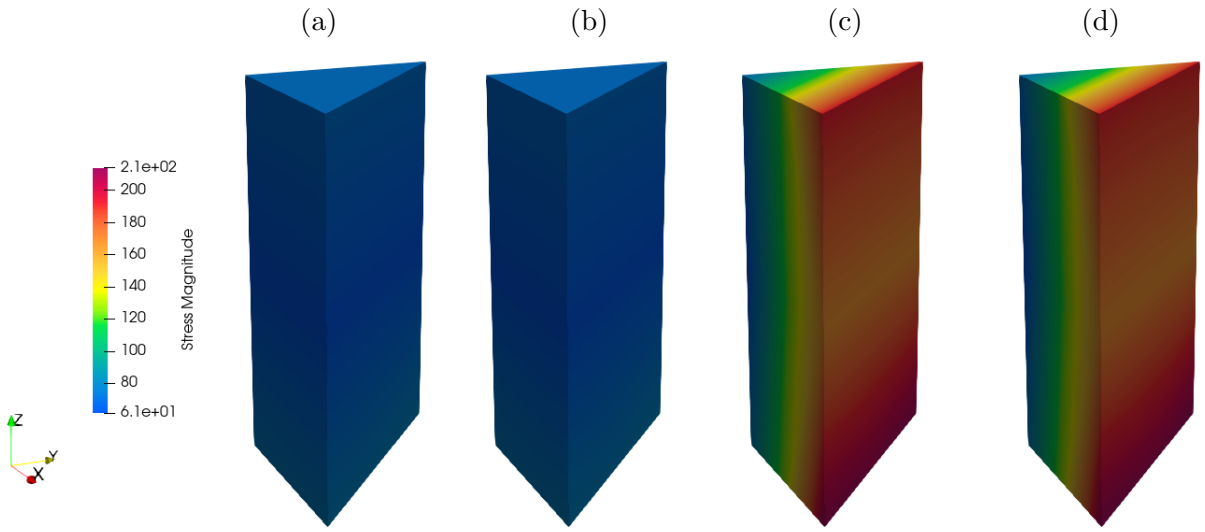

Figure B.19: Comparison of nodal stresses vector magnitude for (a) classical, (b) Cosserat, (c) functionally graded, and (d) functionally graded with Cosserat effects cases for a wedge element in uniaxial compression

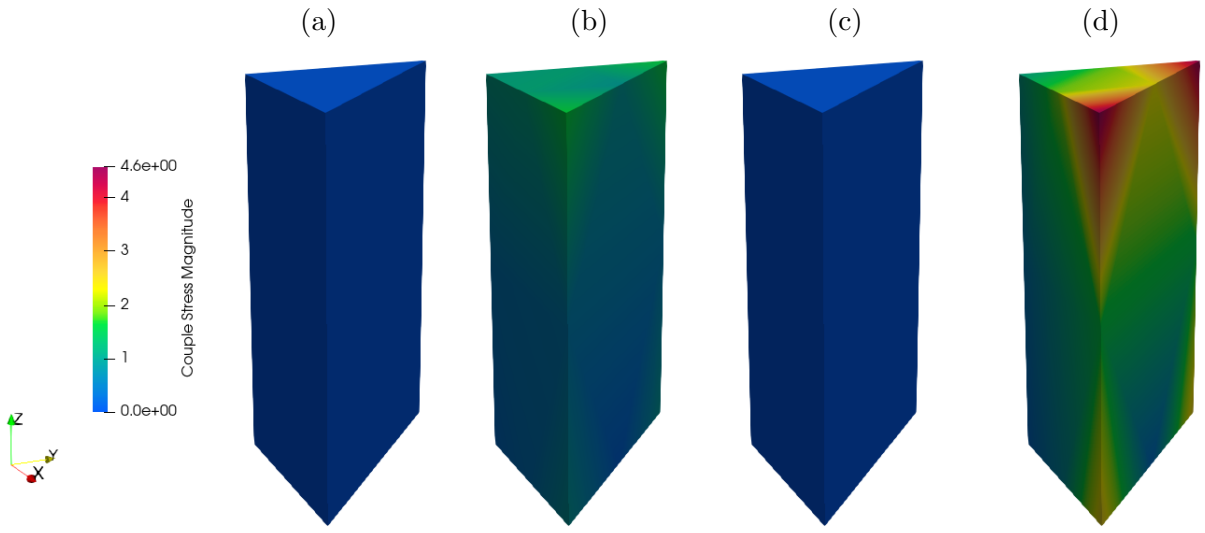

Figure B.20: Comparison of nodal couple stresses vector magnitude for (a) classical, (b) Cosserat, (c) functionally graded, and (d) functionally graded with Cosserat effects cases for a wedge element in uniaxial compression

B.2.2 Shear

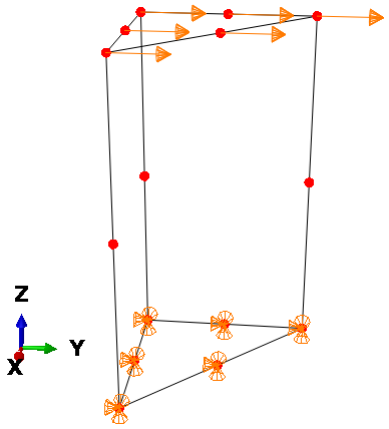

Figure B.21: Boundary conditions and loading for single wedge element in shear

Table B.5: Ranges for magnitudes of tensors of interest for wedge element in shear

Tensor Magnitude	Classical	Cosserat	Exponential Grading	Exponential Grading with Cosserat
$\|\vec{\boldsymbol{u}}\|_{min}\,(mm)$	0	0	0	0
$\|\vec{\boldsymbol{u}}\|_{max}\,(mm)$	0.1160	0.1033	0.1221	0.1030
$\|\vec{\boldsymbol{\varphi}}\|_{min}\,(rad)$	0	0	0	0
$\|\vec{\boldsymbol{\varphi}}\|_{max}\,(rad)$	0	0.0420	0	0.0420
$\|\vec{\boldsymbol{\sigma}}\|_{min}\,(MPa)$	2.8622	21.2401	7.0488	22.7937
$\|\vec{\boldsymbol{\sigma}}\|_{max}\,(MPa)$	49.7601	49.4535	116.9044	129.9243
$\|\vec{\boldsymbol{\mu}}\|_{min}\,(MPa \cdot mm)$	0	1.1978	0	1.2486
$\|\vec{\boldsymbol{\mu}}\|_{max}\,(MPa \cdot mm)$	0	40.728	0	110.6026

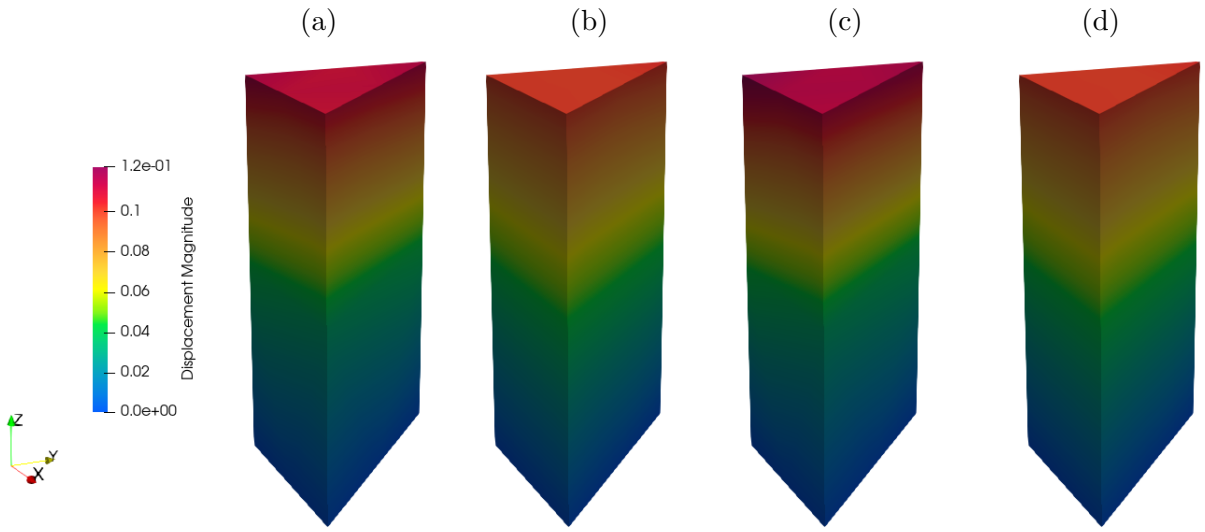

Figure B.22: Comparison of nodal displacements vector magnitude for (a) classical, (b) Cosserat, (c) functionally graded, and (d) functionally graded with Cosserat effects cases for a wedge element in shear

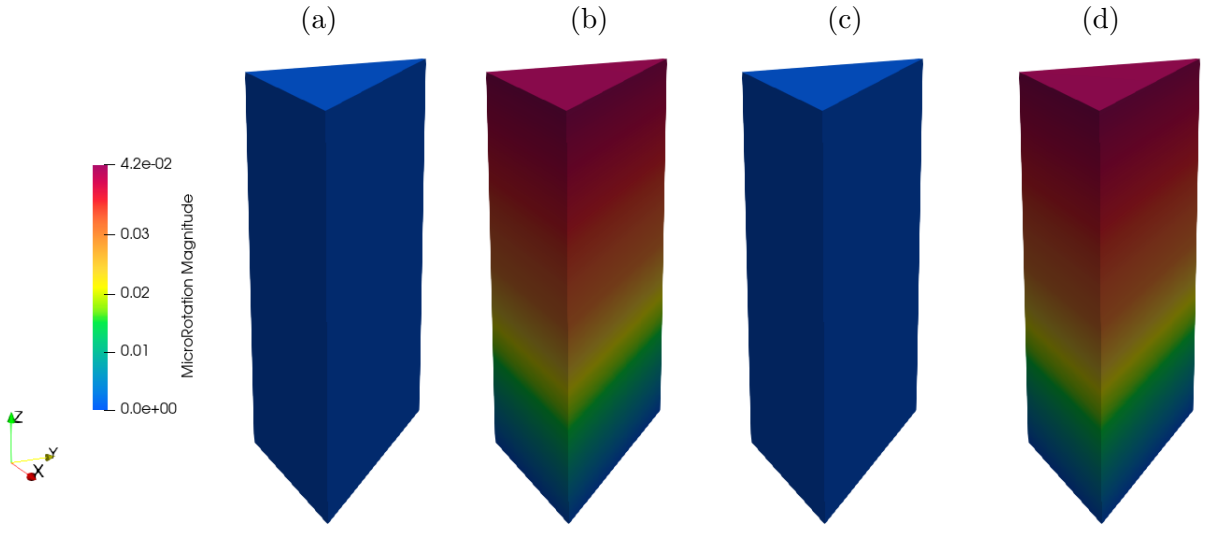

Figure B.23: Comparison of nodal rotations vector magnitude for (a) classical, (b) Cosserat, (c) functionally graded, and (d) functionally graded with Cosserat effects cases for a wedge element in shear

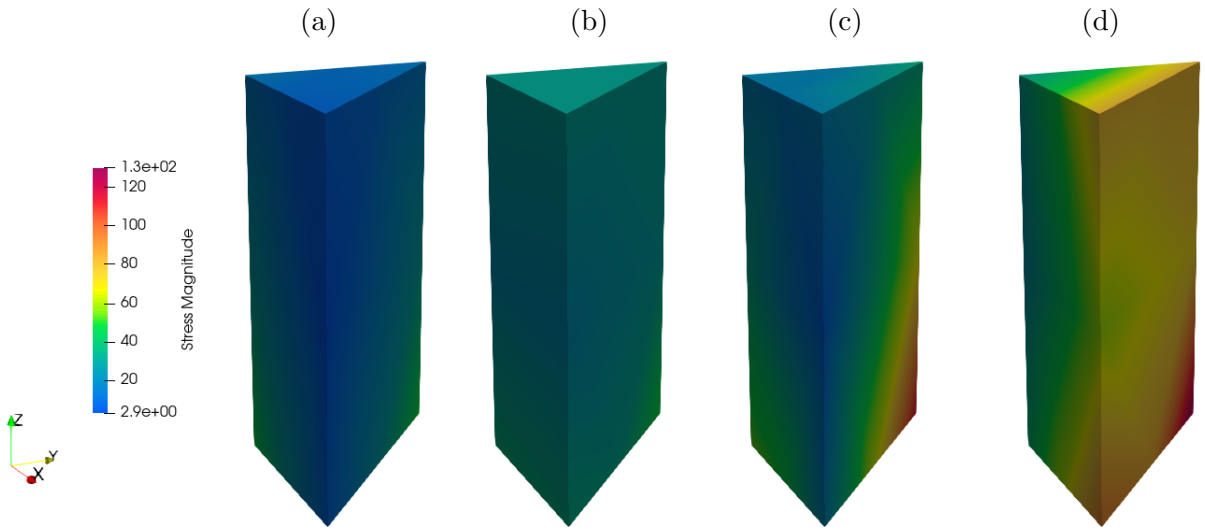

Figure B.24: Comparison of nodal stresses vector magnitude for (a) classical, (b) Cosserat, (c) functionally graded, and (d) functionally graded with Cosserat effects cases for a wedge element in shear

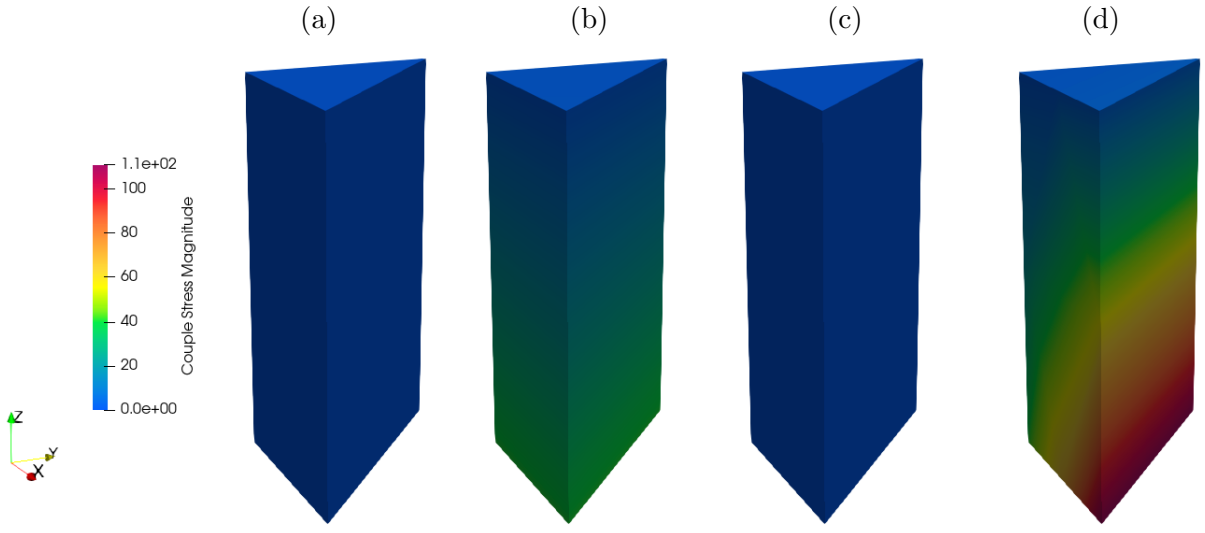

Figure B.25: Comparison of nodal couple stresses vector magnitude for (a) classical, (b) Cosserat, (c) functionally graded, and (d) functionally graded with Cosserat effects cases for a wedge element in shear

B.2.3 Torsion

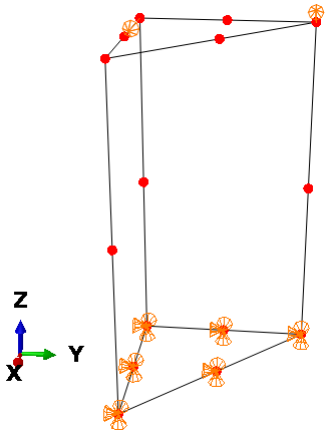

Figure B.26: Boundary conditions and loading for single wedge element in torsion

Table B.6: Ranges for magnitudes of tensors of interest for wedge element in torsion

Tensor Magnitude	**Classical**	**Cosserat**	**Exponential Grading**	**Exponential Grading with Cosserat**
$\|\vec{\boldsymbol{u}}\|_{min}\,(mm)$	0	0	0	0
$\|\vec{\boldsymbol{u}}\|_{max}\,(mm)$	0.1553	0.1016	0.1527	0.1021
$\|\vec{\boldsymbol{\varphi}}\|_{min}\,(rad)$	0	0	0	0
$\|\vec{\boldsymbol{\varphi}}\|_{max}\,(rad)$	0	0.0526	0	0.0506
$\|\vec{\boldsymbol{\sigma}}\|_{min}\,(MPa)$	13.9622	8.5089	28.8933	9.9589
$\|\vec{\boldsymbol{\sigma}}\|_{max}\,(MPa)$	64.7636	224.3267	121.8205	551.1409
$\|\vec{\boldsymbol{\mu}}\|_{min}\,(MPa \cdot mm)$	0	24.6688	0	28.9863
$\|\vec{\boldsymbol{\mu}}\|_{max}\,(MPa \cdot mm)$	0	46.2963	0	121.6067

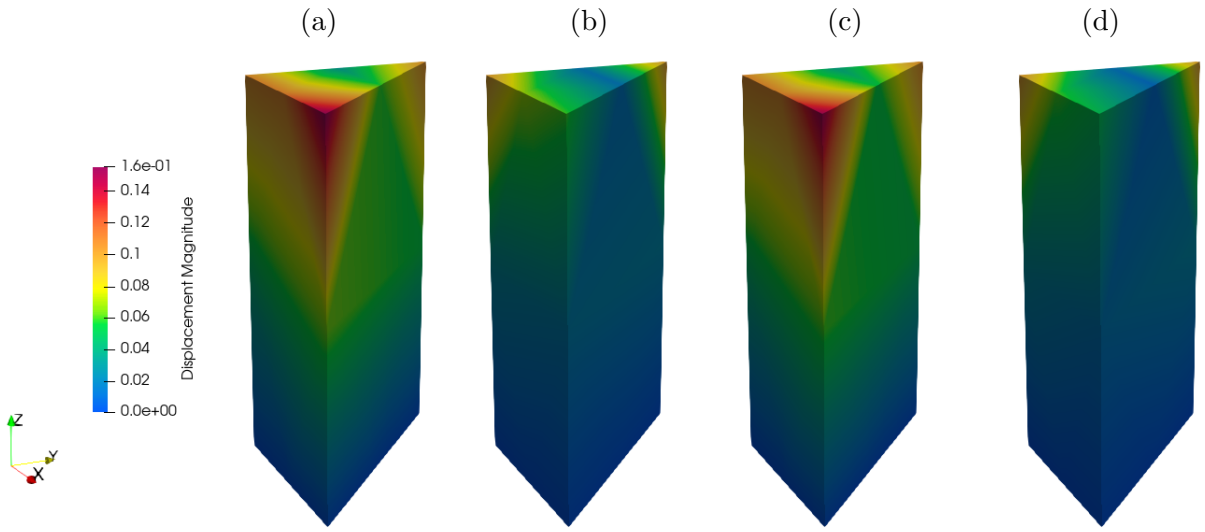

Figure B.27: Comparison of nodal displacements vector magnitude for (a) classical, (b) Cosserat, (c) functionally graded, and (d) functionally graded with Cosserat effects cases for a wedge element in torsion

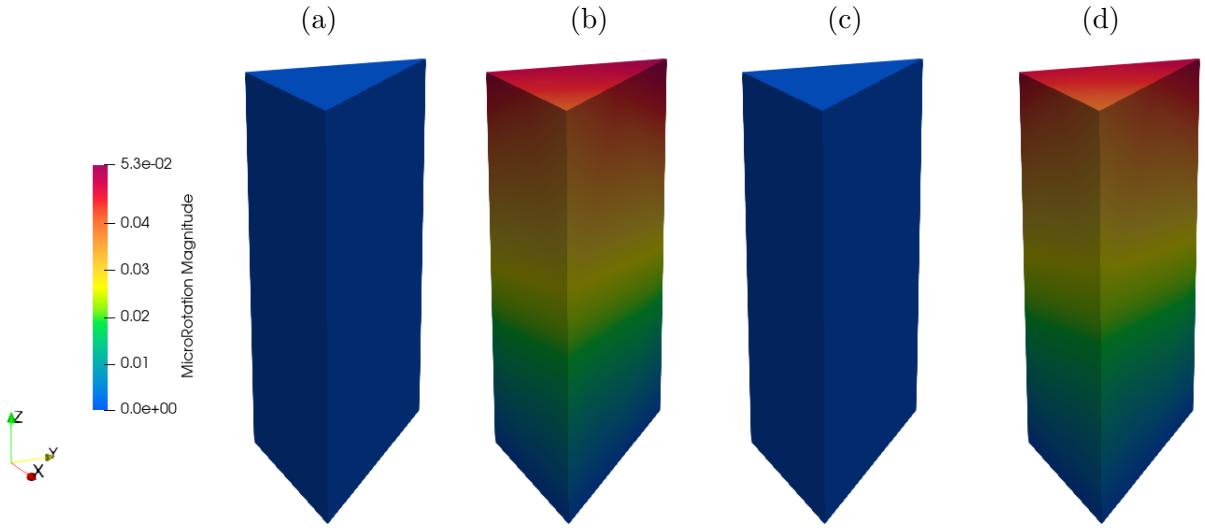

Figure B.28: Comparison of nodal rotations vector magnitude for (a) classical, (b) Cosserat, (c) functionally graded, and (d) functionally graded with Cosserat effects cases for a wedge element in torsion

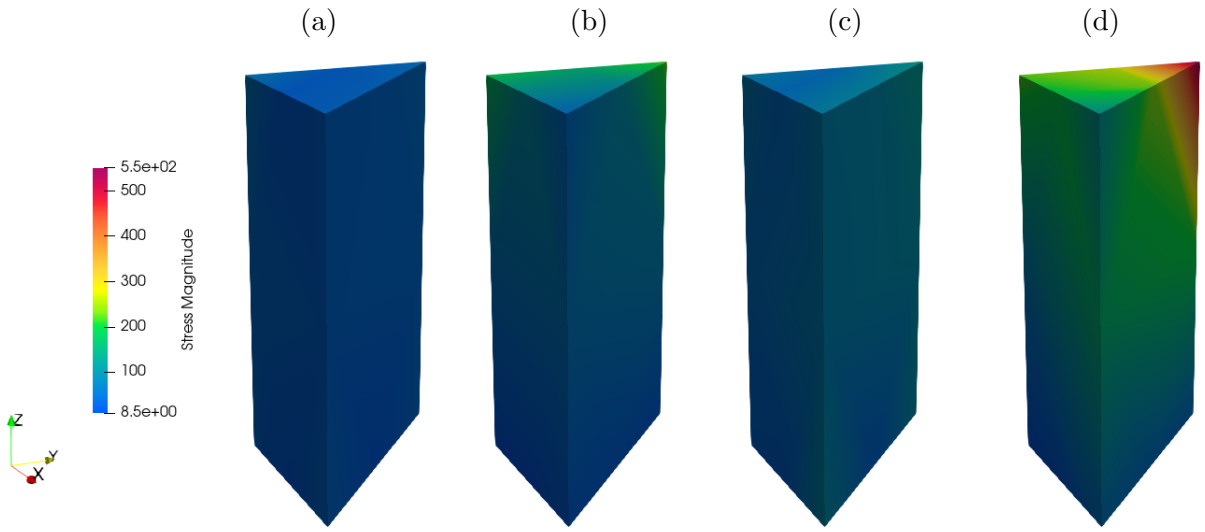

Figure B.29: Comparison of nodal stresses vector magnitude for (a) classical, (b) Cosserat, (c) functionally graded, and (d) functionally graded with Cosserat effects cases for a wedge element in torsion

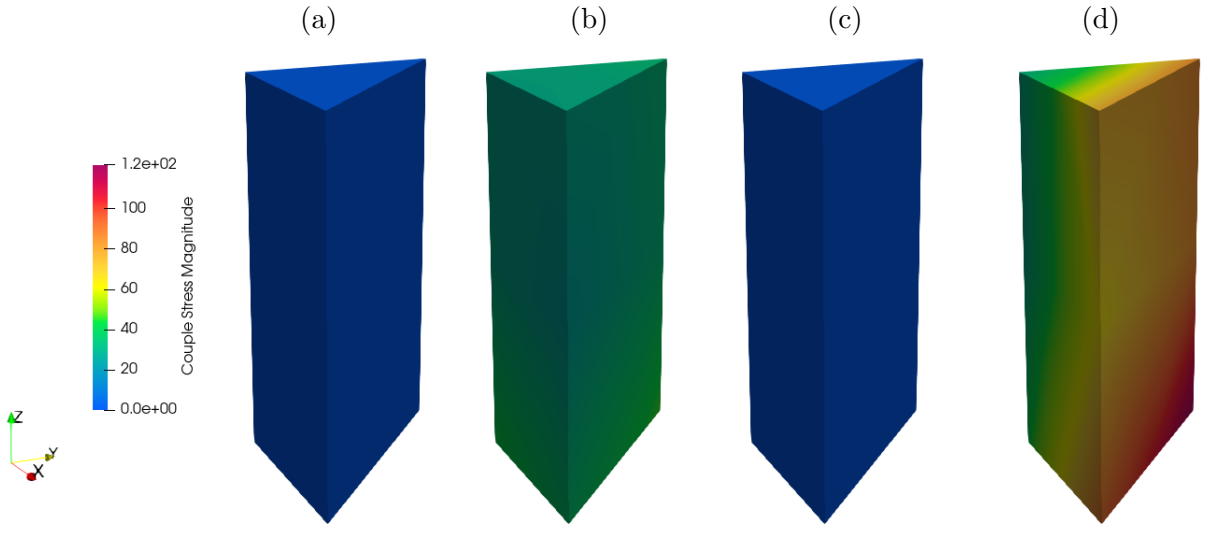

Figure B.30: Comparison of nodal couple stresses vector magnitude for (a) classical, (b) Cosserat, (c) functionally graded, and (d) functionally graded with Cosserat effects cases for a wedge element in torsion

B.3 Quadrilateral Assembly

B.3.1 Compression

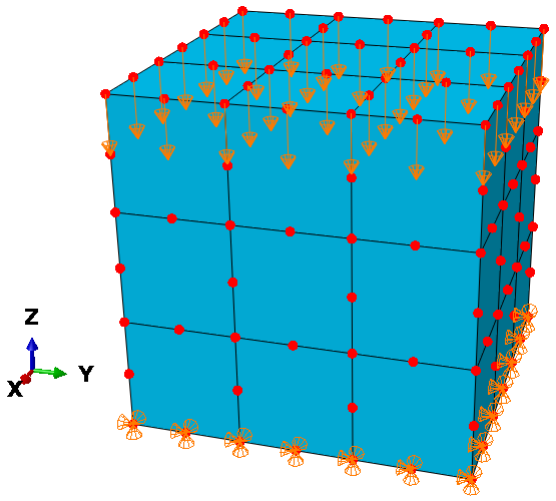

Figure B.31: Boundary conditions and loading for quadrilateral element assembly in uniaxial compression

Table B.7: Ranges for magnitudes of tensors of interest for quadrilateral element assembly in uniaxial compression

Tensor Magnitude	Classical	Cosserat	Exponential Grading	Exponential Grading with Cosserat
$\|\vec{\boldsymbol{u}}\|_{min}\,(mm)$	0	0	0	0
$\|\vec{\boldsymbol{u}}\|_{max}\,(mm)$	0.1017	0.1017	0.1039	0.1042
$\|\vec{\boldsymbol{\varphi}}\|_{min}\,(rad)$	0	0	0	0
$\|\vec{\boldsymbol{\varphi}}\|_{max}\,(rad)$	0	0.0024	0	0.0041
$\|\vec{\boldsymbol{\sigma}}\|_{min}\,(MPa)$	19.1076	20.0620	0.0403	0.0463
$\|\vec{\boldsymbol{\sigma}}\|_{max}\,(MPa)$	34.7683	30.8085	10981.2121	10397.3750
$\|\vec{\boldsymbol{\mu}}\|_{min}\,(MPa \cdot mm)$	0	0.0545	0	0.0003
$\|\vec{\boldsymbol{\mu}}\|_{max}\,(MPa \cdot mm)$	0	3.8994	0	503.0924

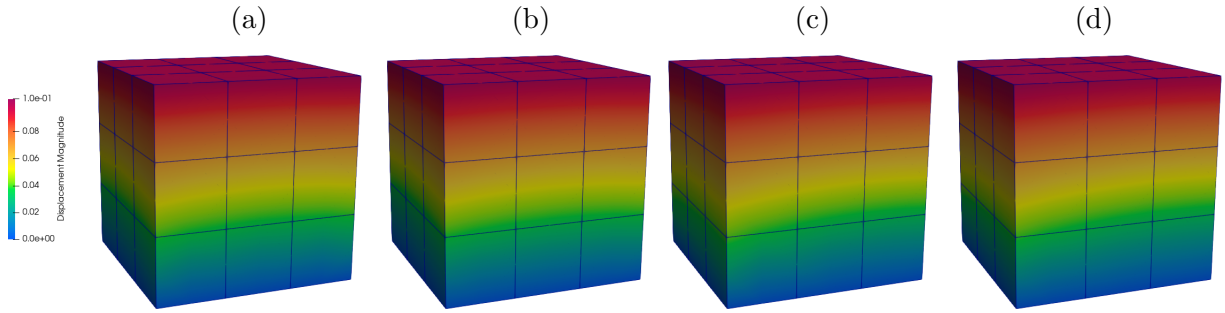

Figure B.32: Comparison of nodal displacements vector magnitude for (a) classical, (b) Cosserat, (c) functionally graded, and (d) functionally graded with Cosserat effects cases for a quadrilateral element assembly in uniaxial compression

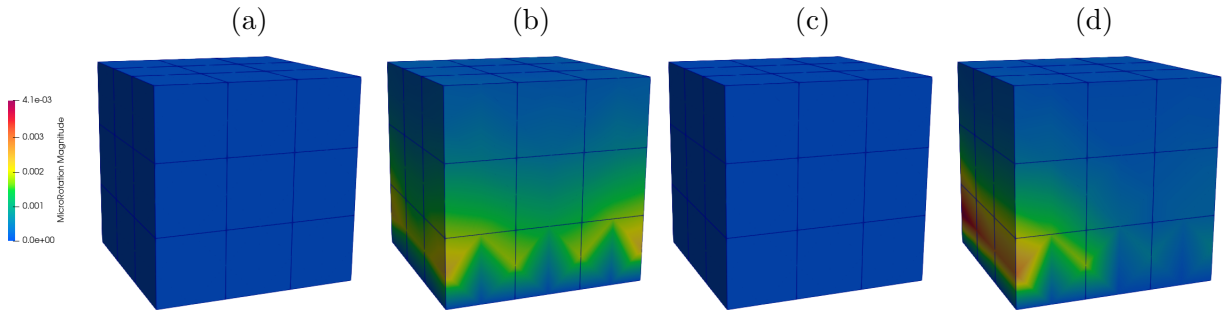

Figure B.33: Comparison of nodal rotations vector magnitude for (a) classical, (b) Cosserat, (c) functionally graded, and (d) functionally graded with Cosserat effects cases for a quadrilateral element assembly in uniaxial compression

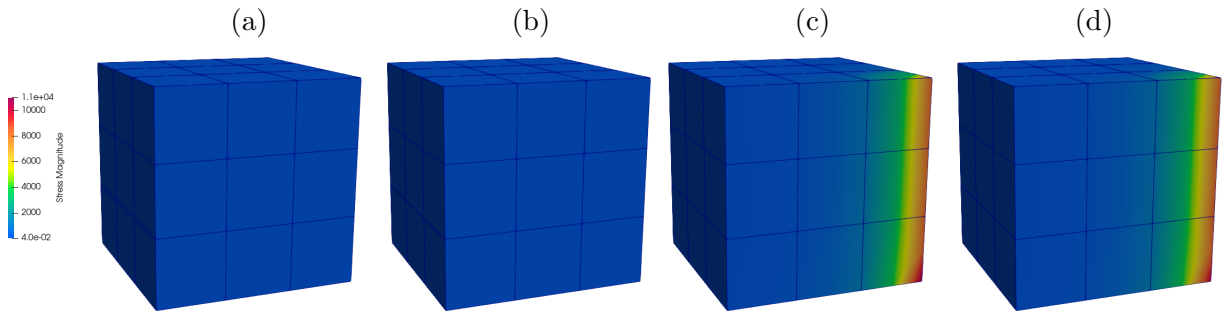

Figure B.34: Comparison of nodal stresses vector magnitude for (a) classical, (b) Cosserat, (c) functionally graded, and (d) functionally graded with Cosserat effects cases for a quadrilateral element assembly in uniaxial compression

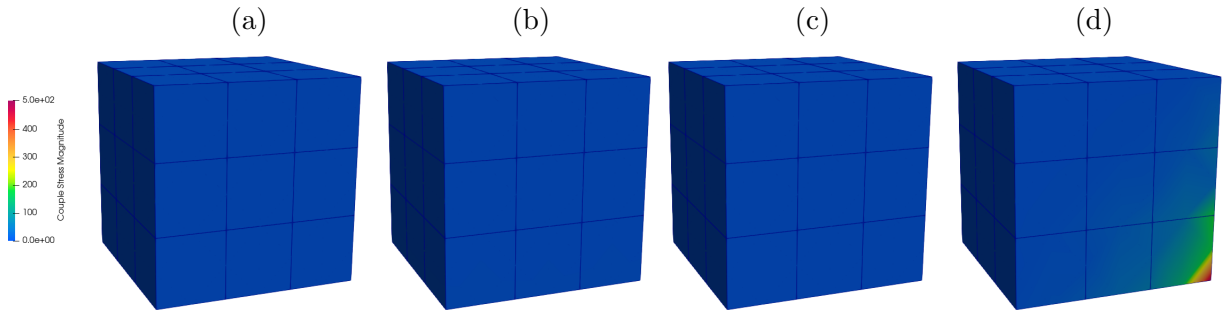

Figure B.35: Comparison of nodal couple stresses vector magnitude for (a) classical, (b) Cosserat, (c) functionally graded, and (d) functionally graded with Cosserat effects cases for a quadrilateral element assembly in uniaxial compression

B.3.2 Shear

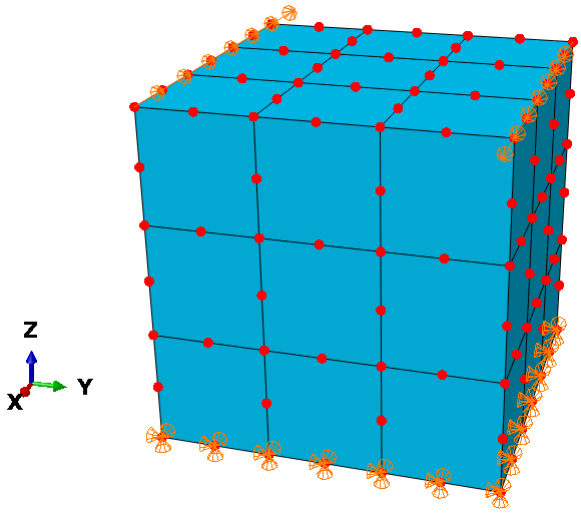

Figure B.36: Boundary conditions and loading for quadrilateral element assembly in shear

Table B.8: Ranges for magnitudes of tensors of interest for quadrilateral element assembly in shear

Tensor Magnitude	Classical	Cosserat	Exponential Grading	Exponential Grading with Cosserat
$\|\vec{\boldsymbol{u}}\|_{min}\,(mm)$	0	0	0	0
$\|\vec{\boldsymbol{u}}\|_{max}\,(mm)$	0.1103	0.1096	0.1303	0.1291
$\|\vec{\boldsymbol{\varphi}}\|_{min}\,(rad)$	0	0	0	0
$\|\vec{\boldsymbol{\varphi}}\|_{max}\,(rad)$	0	0.0191	0	0.0221
$\|\vec{\boldsymbol{\sigma}}\|_{min}\,(MPa)$	0.7251	2.8734	0.0100	0.0116
$\|\vec{\boldsymbol{\sigma}}\|_{max}\,(MPa)$	28.0315	23.7692	4568.2118	4125.8641
$\|\vec{\boldsymbol{\mu}}\|_{min}\,(MPa \cdot mm)$	0	0.1888	0	0.0012
$\|\vec{\boldsymbol{\mu}}\|_{max}\,(MPa \cdot mm)$	0	8.4489	0	3038.3940

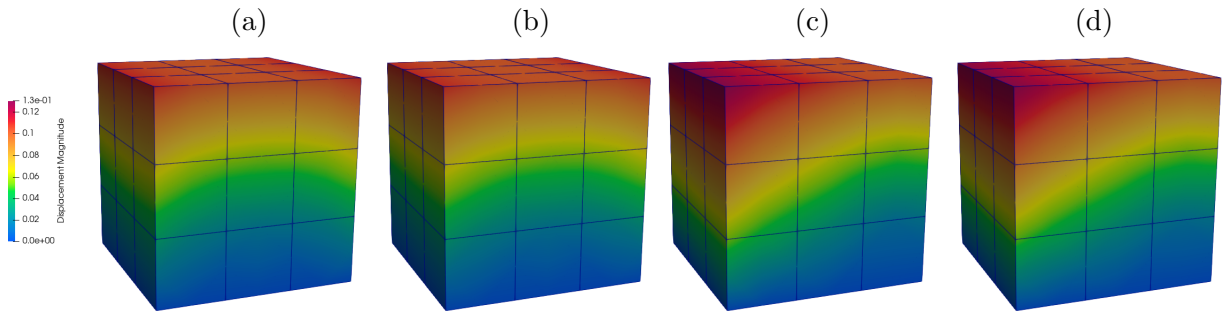

Figure B.37: Comparison of nodal displacements vector magnitude for (a) classical, (b) Cosserat, (c) functionally graded, and (d) functionally graded with Cosserat effects cases for a quadrilateral element assembly in shear

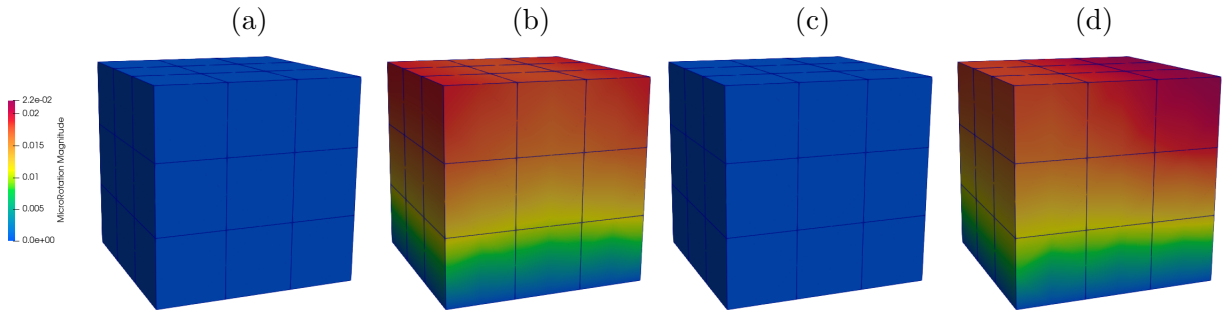

Figure B.38: Comparison of nodal rotations vector magnitude for (a) classical, (b) Cosserat, (c) functionally graded, and (d) functionally graded with Cosserat effects cases for a quadrilateral element assembly in shear

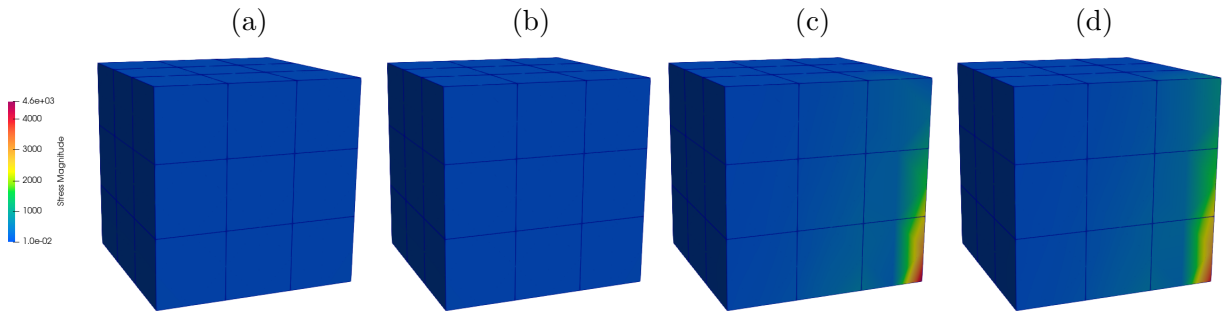

Figure B.39: Comparison of nodal stresses vector magnitude for (a) classical, (b) Cosserat, (c) functionally graded, and (d) functionally graded with Cosserat effects cases for a quadrilateral element assembly in shear

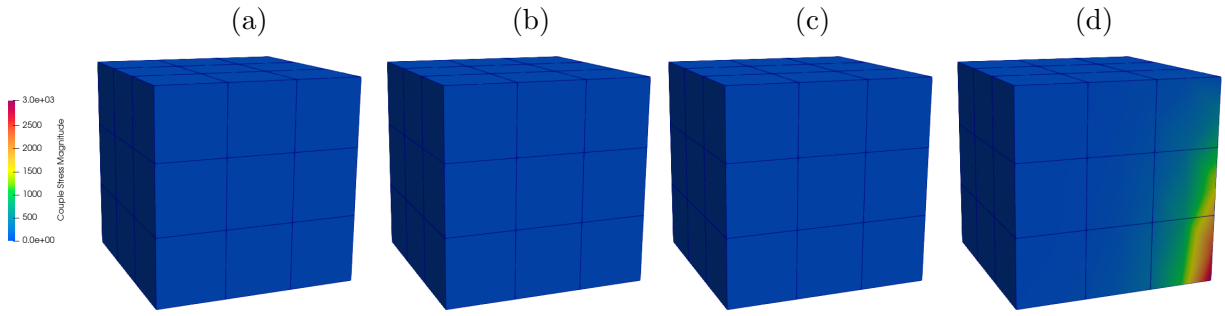

Figure B.40: Comparison of nodal couple stresses vector magnitude for (a) classical, (b) Cosserat, (c) functionally graded, and (d) functionally graded with Cosserat effects cases for a quadrilateral element assembly in shear

B.3.3 Torsion

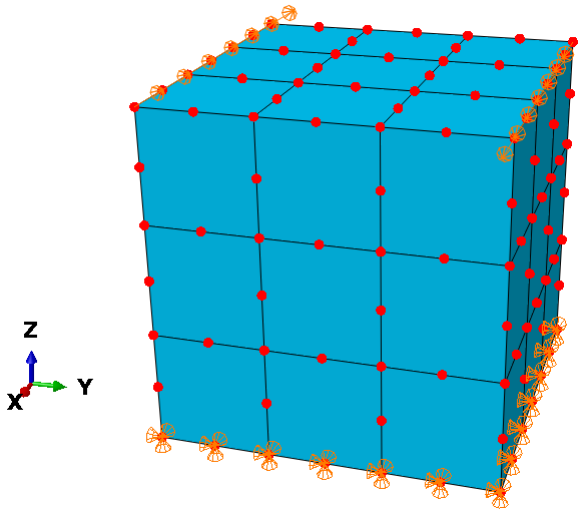

Figure B.41: Boundary conditions and loading for quadrilateral element assembly in torsion

Table B.9: Ranges for magnitudes of tensors of interest for quadrilateral element assembly in torsion

Tensor Magnitude	**Classical**	**Cosserat**	**Exponential Grading**	**Exponential Grading with Cosserat**
$\|\vec{\boldsymbol{u}}\|_{min}\,(mm)$	0	0	0	0
$\|\vec{\boldsymbol{u}}\|_{max}\,(mm)$	0.1210	0.1137	0.1376	0.1277
$\|\vec{\boldsymbol{\varphi}}\|_{min}\,(rad)$	0	0	0	0
$\|\vec{\boldsymbol{\varphi}}\|_{max}\,(rad)$	0	0.0284	0	0.04360
$\|\vec{\boldsymbol{\sigma}}\|_{min}\,(MPa)$	2.1259	2.1327	0.0185	0.0271
$\|\vec{\boldsymbol{\sigma}}\|_{max}\,(MPa)$	39.7725	40.9494	3843.9182	3773.5657
$\|\vec{\boldsymbol{\mu}}\|_{min}\,(MPa \cdot mm)$	0	3.6908	0	0.0081
$\|\vec{\boldsymbol{\mu}}\|_{max}\,(MPa \cdot mm)$	0	9.0501	0	3051.8681

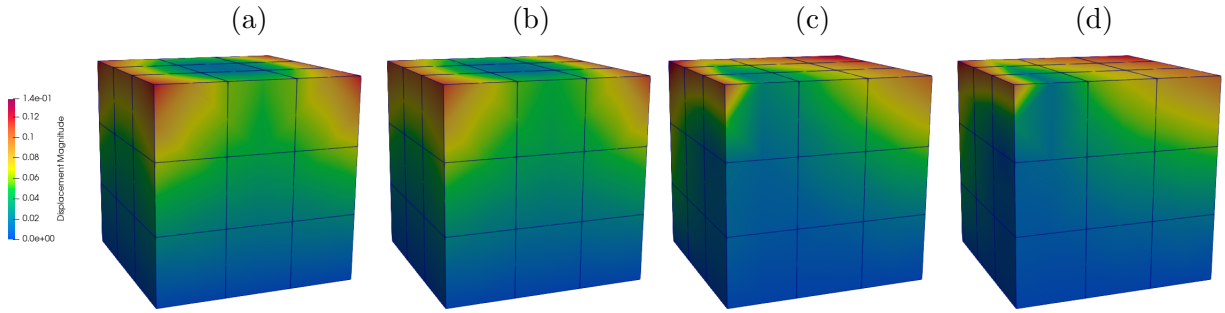

Figure B.42: Comparison of nodal displacements vector magnitude for (a) classical, (b) Cosserat, (c) functionally graded, and (d) functionally graded with Cosserat effects cases for a quadrilateral element assembly in torsion

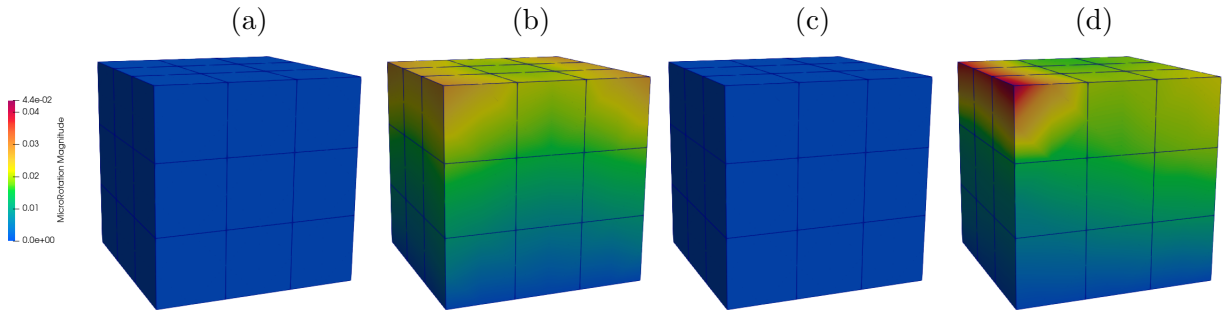

Figure B.43: Comparison of nodal rotations vector magnitude for (a) classical, (b) Cosserat, (c) functionally graded, and (d) functionally graded with Cosserat effects cases for a quadrilateral element assembly in torsion

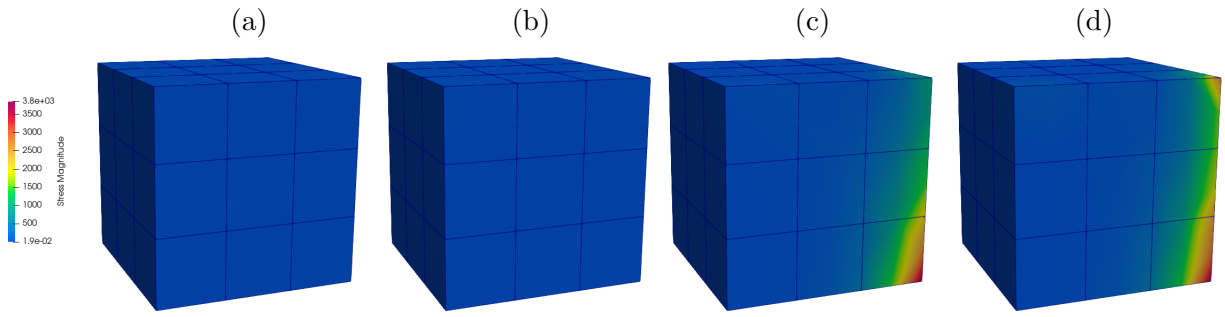

Figure B.44: Comparison of nodal stresses vector magnitude for (a) classical, (b) Cosserat, (c) functionally graded, and (d) functionally graded with Cosserat effects cases for a quadrilateral element assembly in torsion

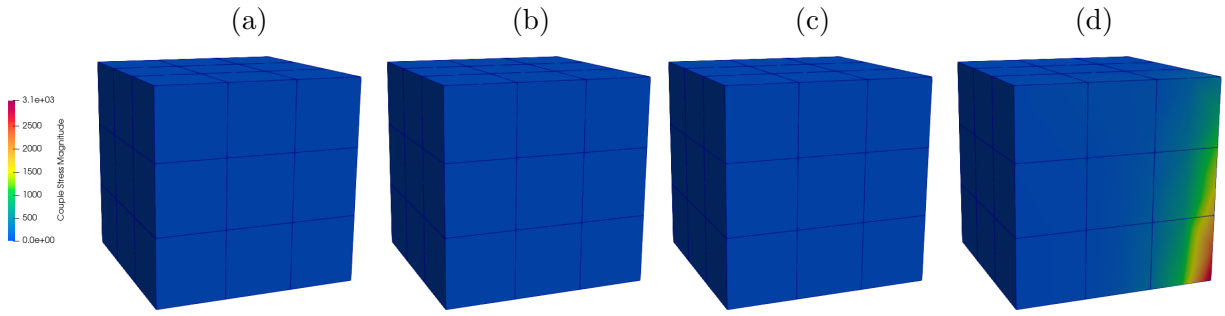

Figure B.45: Comparison of nodal couple stresses vector magnitude for (a) classical, (b) Cosserat, (c) functionally graded, and (d) functionally graded with Cosserat effects cases for a quadrilateral element assembly in torsion

B.4 Wedge Assembly

B.4.1 Compression

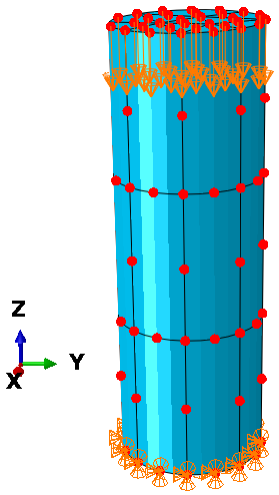

Figure B.46: Boundary conditions and loading for cylindrical wedge element assembly in uniaxial compression

Table B.10: Ranges for magnitudes of tensors of interest for cylindrical wedge element assembly in uniaxial compression

Tensor Magnitude	**Classical**	**Cosserat**	**Exponential Grading**	**Exponential Grading with Cosserat**
$\|\vec{\boldsymbol{u}}\|_{min}\,(mm)$	0	0	0	0
$\|\vec{\boldsymbol{u}}\|_{max}\,(mm)$	0.1001	0.1001	0.1002	0.1002
$\|\vec{\boldsymbol{\varphi}}\|_{min}\,(rad)$	0	0	0	0
$\|\vec{\boldsymbol{\varphi}}\|_{max}\,(rad)$	0	0.0004	0	0.0004
$\|\vec{\boldsymbol{\sigma}}\|_{min}\,(MPa)$	20.0502	20.3662	4.9660	5.0573
$\|\vec{\boldsymbol{\sigma}}\|_{max}\,(MPa)$	27.2069	25.8658	108.9635	104.5149
$\|\vec{\boldsymbol{\mu}}\|_{min}\,(MPa \cdot mm)$	0	0.0063	0	0.00216
$\|\vec{\boldsymbol{\mu}}\|_{max}\,(MPa \cdot mm)$	0	1.1147	0	2.2672

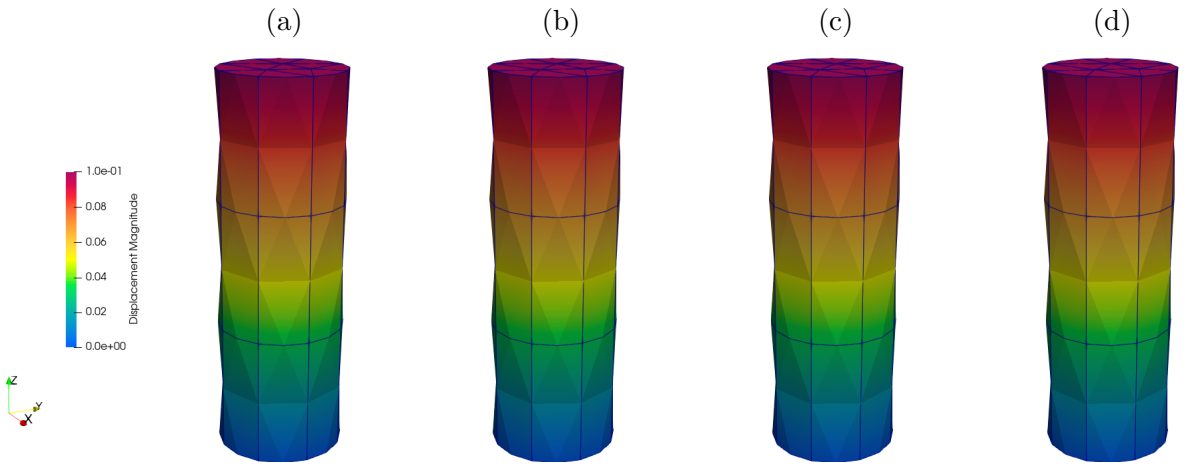

Figure B.47: Comparison of nodal displacements vector magnitude for (a) classical, (b) Cosserat, (c) functionally graded, and (d) functionally graded with Cosserat effects cases for a wedge element assembly in uniaxial compression

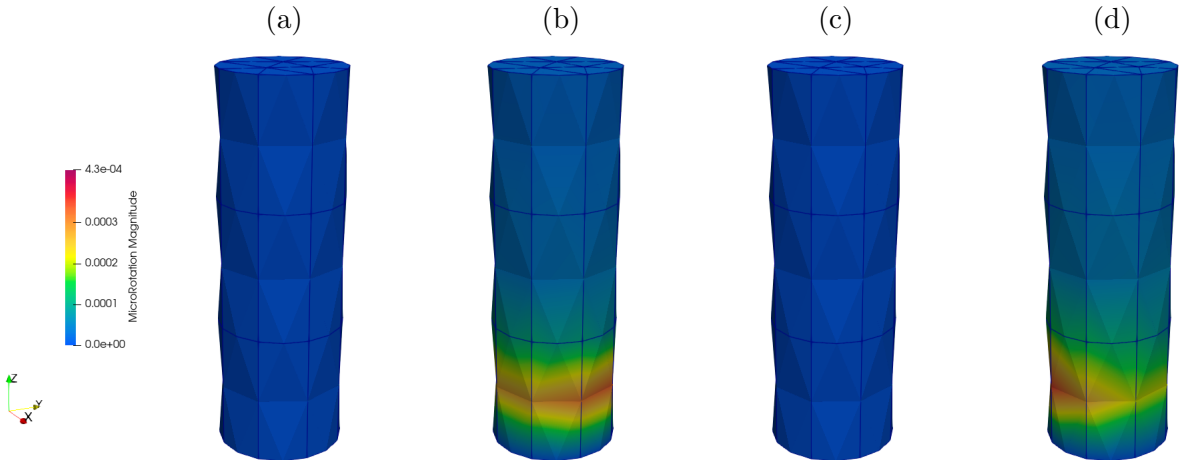

Figure B.48: Comparison of nodal rotations vector magnitude for (a) classical, (b) Cosserat, (c) functionally graded, and (d) functionally graded with Cosserat effects cases for a wedge element assembly in uniaxial compression

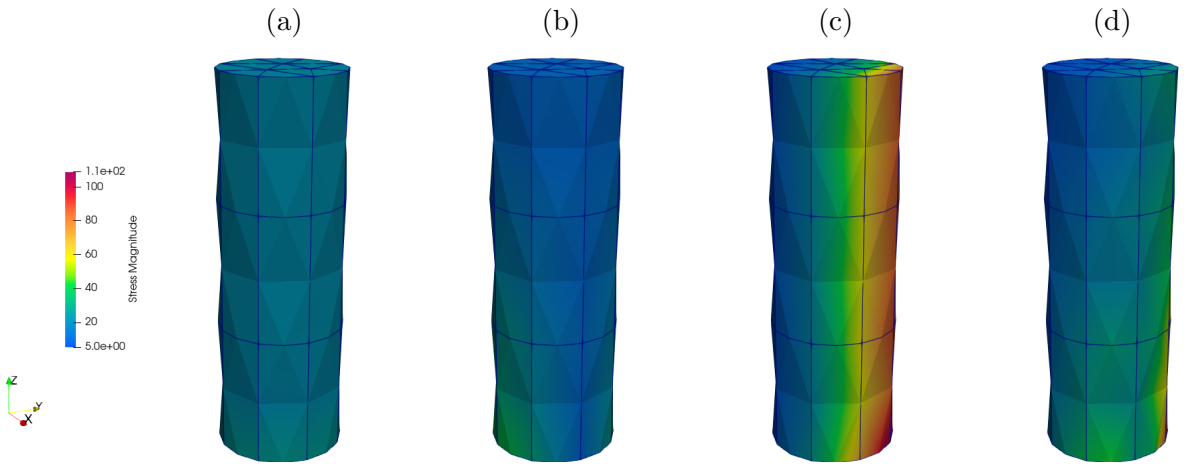

Figure B.49: Comparison of nodal stresses vector magnitude for (a) classical, (b) Cosserat, (c) functionally graded, and (d) functionally graded with Cosserat effects cases for a wedge element assembly in uniaxial compression

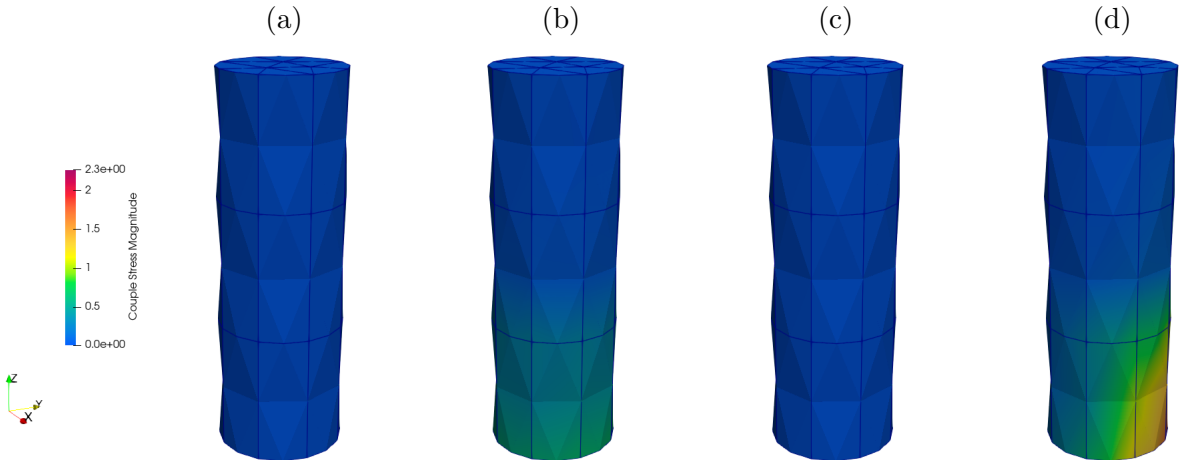

Figure B.50: Comparison of nodal couple stresses vector magnitude for (a) classical, (b) Cosserat, (c) functionally graded, and (d) functionally graded with Cosserat effects cases for a wedge element assembly in uniaxial compression

B.4.2 Shear

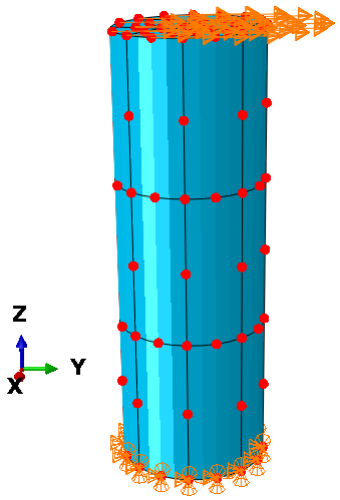

Figure B.51: Boundary conditions and loading for cylindrical wedge element assembly in shear

Table B.11: Ranges for magnitudes of tensors of interest for cylindrical wedge element assembly in shear

Tensor Magnitude	**Classical**	**Cosserat**	**Exponential Grading**	**Exponential Grading with Cosserat**
$\|\vec{\boldsymbol{u}}\|_{min}\,(mm)$	0	0	0	0
$\|\vec{\boldsymbol{u}}\|_{max}\,(mm)$	0.1028	0.1024	0.1046	0.1037
$\|\vec{\boldsymbol{\varphi}}\|_{min}\,(rad)$	0	0	0	0
$\|\vec{\boldsymbol{\varphi}}\|_{max}\,(rad)$	0	0.0226	0	0.0227
$\|\vec{\boldsymbol{\sigma}}\|_{min}\,(MPa)$	0.0424	1.5769	0.1434	0.4770
$\|\vec{\boldsymbol{\sigma}}\|_{max}\,(MPa)$	12.3537	11.7619	32.3391	30.7875
$\|\vec{\boldsymbol{\mu}}\|_{min}\,(MPa \cdot mm)$	0	0.0656	0	0.0199
$\|\vec{\boldsymbol{\mu}}\|_{max}\,(MPa \cdot mm)$	0	7.6520	0	30.8197

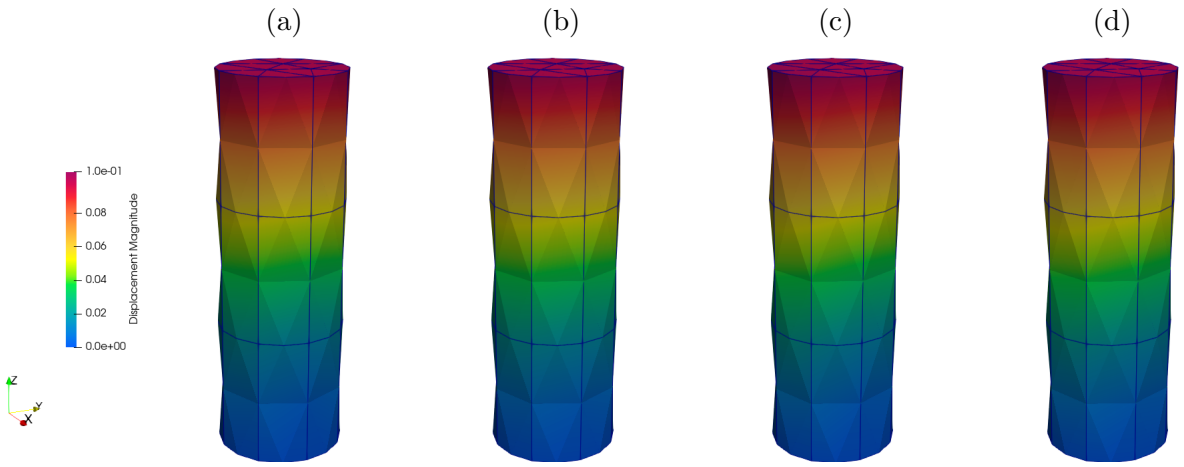

Figure B.52: Comparison of nodal displacements vector magnitude for (a) classical, (b) Cosserat, (c) functionally graded, and (d) functionally graded with Cosserat effects cases for a wedge element assembly in shear

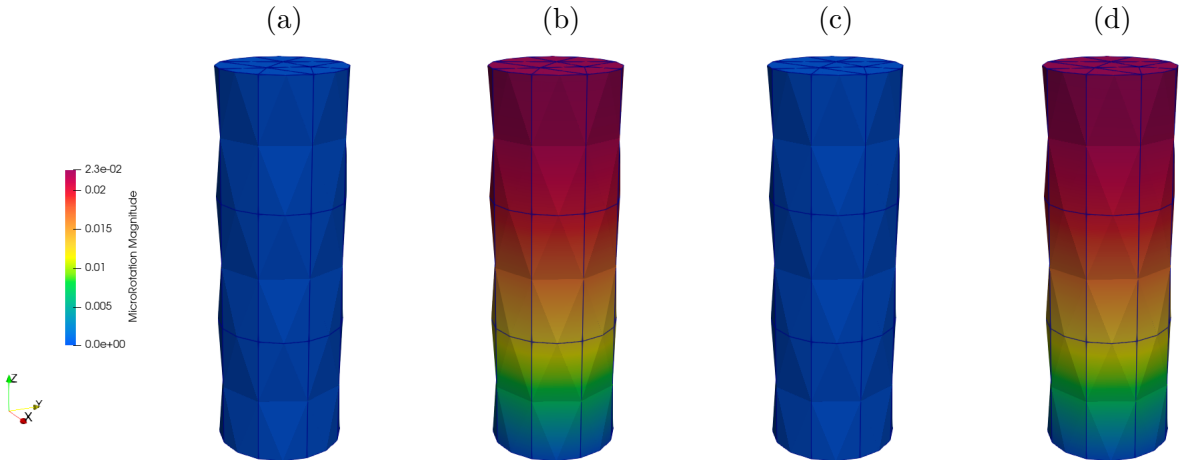

Figure B.53: Comparison of nodal rotations vector magnitude for (a) classical, (b) Cosserat, (c) functionally graded, and (d) functionally graded with Cosserat effects cases for a wedge element assembly in shear

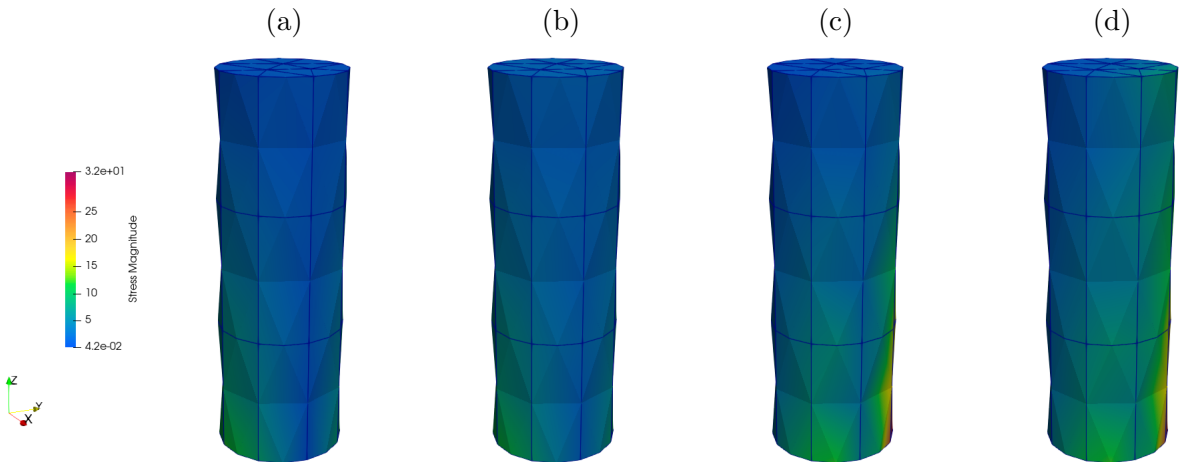

Figure B.54: Comparison of nodal stresses vector magnitude for (a) classical, (b) Cosserat, (c) functionally graded, and (d) functionally graded with Cosserat effects cases for a wedge element assembly in shear

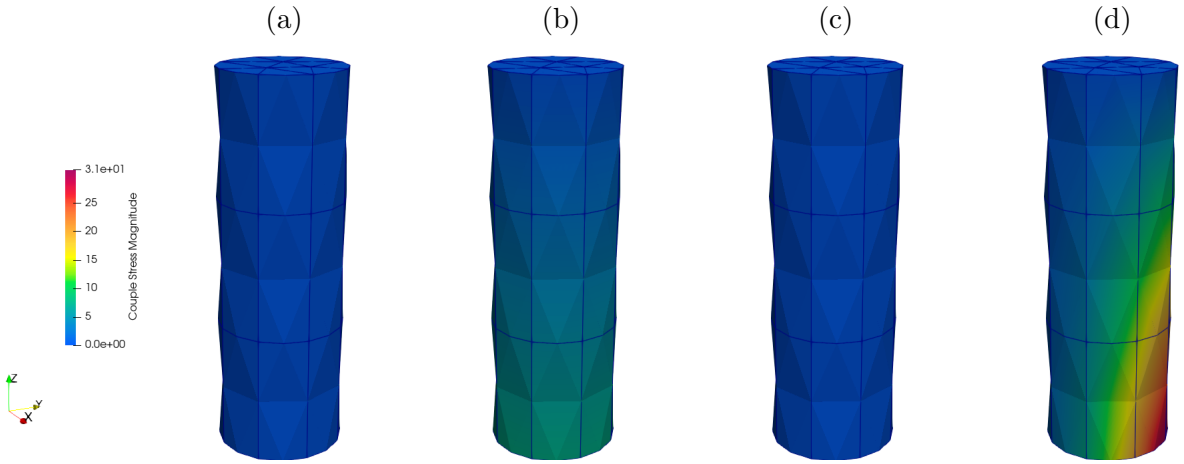

Figure B.55: Comparison of nodal couple stresses vector magnitude for (a) classical, (b) Cosserat, (c) functionally graded, and (d) functionally graded with Cosserat effects cases for a wedge element assembly in shear

B.4.3 Torsion

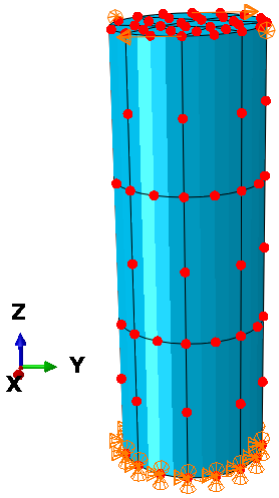

Figure B.56: Boundary conditions and loading for cylindrical wedge element assembly in torsion

Table B.12: Ranges for magnitudes of tensors of interest for cylindrical wedge element assembly in torsion

Tensor Magnitude	**Classical**	**Cosserat**	**Exponential Grading**	**Exponential Grading with Cosserat**
$\|\vec{\boldsymbol{u}}\|_{min}\,(mm)$	0	0	0	0
$\|\vec{\boldsymbol{u}}\|_{max}\,(mm)$	0.1046	0.1	0.1008	0.1044
$\|\vec{\boldsymbol{\varphi}}\|_{min}\,(rad)$	0	0	0	0
$\|\vec{\boldsymbol{\varphi}}\|_{max}\,(rad)$	0	0.0678	0	0.0635
$\|\vec{\boldsymbol{\sigma}}\|_{min}\,(MPa)$	0.9384	1.0787	0.6026	1.3333
$\|\vec{\boldsymbol{\sigma}}\|_{max}\,(MPa)$	24.3715	90.4330	35.3645	110.3864
$\|\vec{\boldsymbol{\mu}}\|_{min}\,(MPa \cdot mm)$	0	8.5542	0	2.8222
$\|\vec{\boldsymbol{\mu}}\|_{max}\,(MPa \cdot mm)$	0	17.5964	0	64.5506

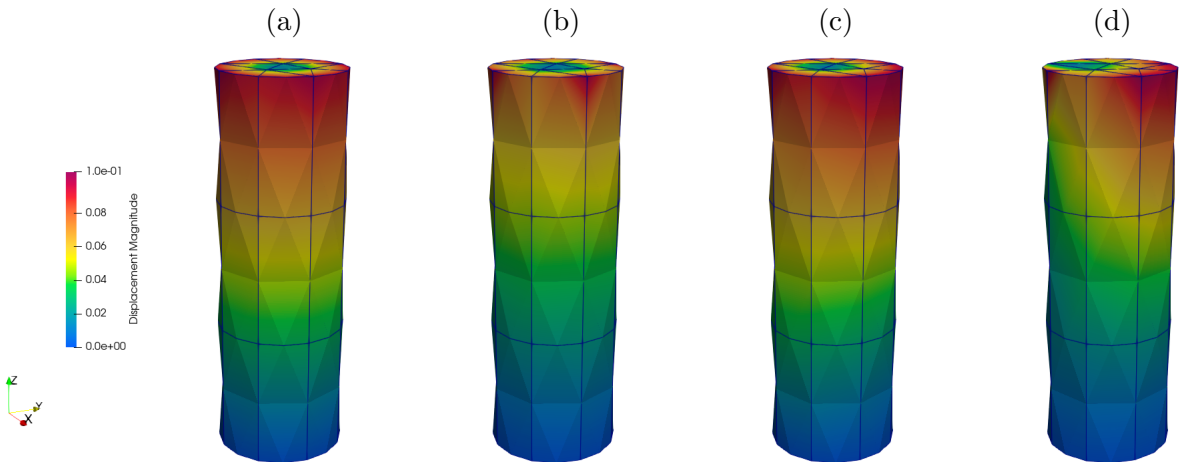

Figure B.57: Comparison of nodal displacements vector magnitude for (a) classical, (b) Cosserat, (c) functionally graded, and (d) functionally graded with Cosserat effects cases for a wedge element assembly in torsion

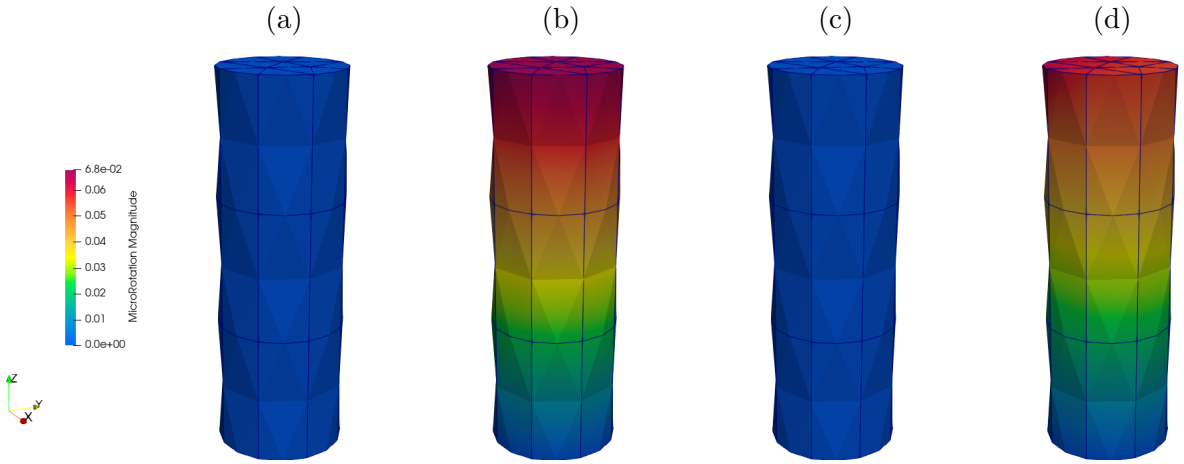

Figure B.58: Comparison of nodal rotations vector magnitude for (a) classical, (b) Cosserat, (c) functionally graded, and (d) functionally graded with Cosserat effects cases for a wedge element assembly in torsion

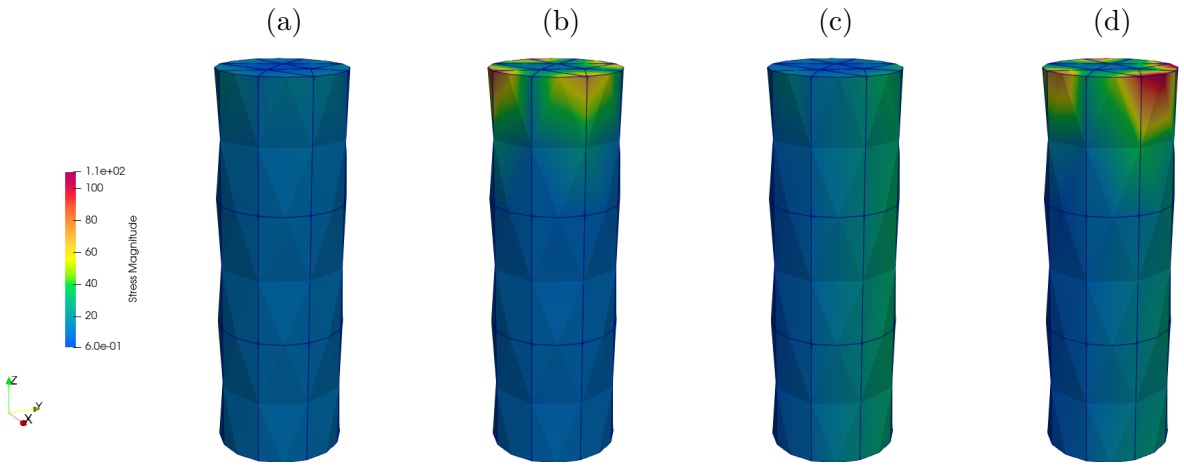

Figure B.59: Comparison of nodal stresses vector magnitude for (a) classical, (b) Cosserat, (c) functionally graded, and (d) functionally graded with Cosserat effects cases for a wedge element assembly in torsion

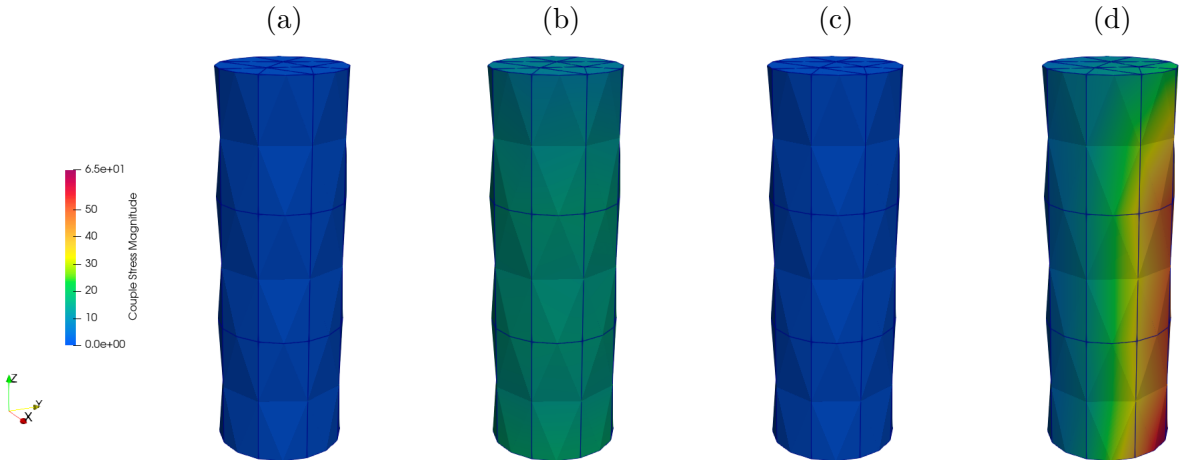

Figure B.60: Comparison of nodal couple stresses vector magnitude for (a) classical, (b) Cosserat, (c) functionally graded, and (d) functionally graded with Cosserat effects cases for a wedge element assembly in torsion